Graph-matching and FEM-based Registration of Computed Tomographies for Outcome Validation of Liver Interventions

dem Fachbereich Informatik
der Technischen Universität Darmstadt
genehmigte

DISSERTATION

zur Erlangung des akademischen Grades eines
Doktor-Ingenieurs (Dr.-Ing.)
von

Ing. Cristina Oyarzun Laura

geboren in Irún, Spanien

Referenten der Arbeit:	Prof. Dr.-Ing. Georgios Sakas Technische Universität Darmstadt Prof. Dr. techn. Dieter W. Fellner Technische Universität Darmstadt Prof. Dr. Reto Bale, MD Medizinische Universität Innsbruck
Tag der Einreichung:	17/09/2015
Tag der mündlichen Prüfung:	09/11/2015

Darmstadt 2016
D 17

Erklärung zur Dissertation

Hiermit versichere ich die vorliegende Dissertation selbständig nur mit den angegebenen Quellen und Hilfsmitteln angefertigt zu haben. Alle Stellen, die aus Quellen entnommen wurden, sind als solche kenntlich gemacht. Diese Arbeit hat in gleicher oder ähnlicher Form noch keiner Prüfungsbehörde vorgelegen.

Darmstadt, den 28.01.2015 Cristina Oyarzun Laura

A mi hermano

Acknowledgement

There are many persons who helped me during the completion of this work and it is time now to thank all of them for their invaluable help. First of all, I would like to thank my doctoral advisor Prof. Georgios Sakas for his supervision and comments that helped me to greatly improve this thesis.

In addition, I would like to thank Prof. Dieter Fellner for his support during this process and Prof. Reto Bale for sharing his medical expertise with me. This knowledge was of great importance given the topic of this work. Furthermore I would like to thank Prof. Arjan Kuijper for proofreading this thesis.

I had the opportunity to carry out my research work at the department of Visual Healthcare Technologies at Fraunhofer IGD, and I would like to thank Stefan Wesarg and my colleagues for the nice working atmosphere that always exists in the department. In particular, I would like to thank the colleagues that became my friends and with which I shared and continue sharing not only working time and discussions but also free time and activities: Klaus, Martin, Marius and more recently Andreas. I lost track of how many times Klaus and Andreas heard my presentation and how many comments they gave me to improve it. I would like to thank you for that!

I would also like to thank those students and grant holders that participated and contributed to this research project, namely, Simon, Pablo and Sergio.

Even if they have been far away during this process I would like to thank my friends in Irún that did not see me much during the last year, but did not forget me and will see me much more in the future.

My special thanks goes to Klaus for all his support, for the constructive discussions and specially for making it possible for me to have some life outside the thesis.

The acknowledgement section would be incomplete without thanking my parents and my brother for their unconditional support, love and help. Thank you for being always there!

Abstract

Liver cancer is one of the leading causes of death worldwide. One of the reasons for that is the high tumor recurrence rate. The only way to reduce the recurrence rate is to ensure that all carcinogenic cells are destroyed after intervention. Unfortunately, the information available to assess the outcome of an intervention is limited. In the clinical routine, a pair of pre- and post-operatively gathered computed tomographies (CT) of the abdomen are typically compared to decide whether the patient needs further treatment. However, the post-operative liver will be deformed due to breathing and intervention which will complicate the comparison task by simple inspection of both images.

The results presented in this thesis will support the physician during the outcome validation process after minimally invasive interventions and open liver surgeries. Therefore, the physician is provided with qualitative measures and visualizations that support him in the decision making task. The basis of a reliable outcome validation is an accurate non-rigid registration method.

This thesis proposes to combine internal correspondences at vessel ramifications and landmarks at the surface of the organ to increase the accuracy of the registration results. The internal correspondences are the result of a novel efficient and fully automatic graph matching method. Landmarks at the surface of the liver are given by a method that detects the organs that are adjacent to it at each surface point. Both types of landmarks are incorporated in a FEM-based registration. The registration method has been tested in 25 pairs of pre- and post-operative clinical CT images achieving an average accuracy of 1.22 mm and a positive predictive value of 0.95.

In consequence of the accuracy obtained with the proposed methods the physician is able to determine with certainty if the outcome of the intervention was satisfactory. Hence, he can without delay decide to re-treat the patient if needed to remove the remnant tumor. This fast response could at the end reduce the tumor recurrence rate.

Zusammenfassung

Leberkrebs ist eine der größten Todesursachen weltweit. Einer der Gründe dafür ist die hohe Rekurrenz. Um diese zu reduzieren, muss sichergestellt werden, dass alle karzinogenen Zellen nach dem Eingriff zerstört werden. Leider sind die verfügbaren Informationen, um das Resultat eines Eingriffes zu bewerten, begrenzt. Die Entscheidung, ob ein Patient weiter behandelt werden muss, basiert auf dem Vergleich von präoperativen und postoperativen Computertomographien (CT) des Abdomens. Allerdings wird die postoperative Leber aufgrund des Eingriffes und der Atmung stark deformiert, wodurch der visuelle Vergleich erschwert wird.

Die Ergebnisse dieser Arbeit unterstützen den Arzt bei der Bewertung minimalinvasiver und offener Lebereingriffe. Dafür werden dem Arzt quantitative Maße und Visualisierungen zur Verfügung gestellt. Eine genaue deformierbare Registrierung bildet die Grundlage für eine zuverlässige Bewertung.

Die in dieser Dissertation vorgeschlagene Methode verwendet anatomische Landmarken basierend auf den Gefäßen der Oberfläche der Leber, um eine hohe Genauigkeit zu erreichen. Landmarken innerhalb der Leber werden anhand einer neuartigen, effizienten und voll automatischen Graph-Matching Methode gefunden. Oberflächliche Landmarken werden anhand einer neuen Methode detektiert, die die Leberoberfläche anhand von benachbarten Organen einteilt. Beide Arten von Landmarken wurden in einer FEM-basierten Registrierungsmethode integriert. Für die Evaluierung wurden 25 CT Bildpaare bestehend aus jeweils einem prä- und einem postoperativen Datensatz verwendet. Die vorgestellte Methode erreicht eine mittlere Genauigkeit von 1.22 mm und einen positiven Vorhersagewert (PPV) von 0.95.

Aufgrund der hohen Genauigkeit der vorgestellten Methode kann der Arzt über den Erfolg des Eingriffes mit einem hohen Maß an Sicherheit entscheiden und den Patienten unverzüglich weiterbehandeln, falls der Tumor nicht vollständig beseitigt wurde. Dadurch kann letztendlich ein Wiederauftreten des Tumors vermieden oder reduziert werden.

Contents

1. Introduction

1.1. Motivation

According to the World Health Organization, cancer is the leading cause of death worldwide; it is responsible for a total of 13% of all deaths.[1] According to the statistics presented within the GLOBOCAN project, 11.3% of those deaths are due to liver cancer.[2] However, liver metastases are 20 times more common; these tumors can spread from any part of the body. Lung, breast, and colorectal cancers are the most common sources of liver metastases. Taking colorectal cancer as example, liver metastases will occur in 25% of the cases [MBZ13]. In the case of recurrent colorectal cancer, this can increase up to 75%.

Nowadays, different techniques exist to treat patients with primary or metastatic liver cancer. Often, chemotherapy is used first to reduce the size of the tumors. Then, the best technique to eliminate them will be chosen depending on the characteristics of the tumor (type, shape, and size) all the while trying to maximize the remaining healthy liver tissue.

One of those techniques is tumor resection that completely removes the tumor with a safety margin around it by cutting out the affected tissue. In 2004, Bentrem et al. [BDB05] pointed out that complete resection was only possible in less than 10% of colorectal liver metastases. When the first resections took place, the mortality rate of the patients that underwent the surgery was very high. But thanks to the advances in medical imaging, the mortality rate is continuously decreasing [RCLW12], and the number of resections per year is increasing. Nowadays, there are patients that will undergo a second resection due to recurrence. According to Rolff et al. [RCLW12], 70% of patients will develop recurrent colorectal liver metastases; 30% of them are candidates for a second liver resection.

Nevertheless, tumor resection is an invasive procedure and it is not always possible to do it. When the resection is not possible, minimally invasive therapies are chosen (e.g., radio frequency ablation). With this technique, the tumor cells are destroyed by application of high-frequency waves or gamma irradiation. Unfortunately, the tumor recurrence rate is still high; thus, it is important to ensure that after surgery, all of the carcinogenic cells are removed/destroyed.

To that end, the physician does not only remove the tumor itself but also a margin around it. After the surgery takes place, the physician needs to verify that the complete area including the margin has been removed/destroyed; therefore, the physician usually acquires two computed-tomography (CT) scans: a preoperative image that the physician uses to make the diagnosis and planning of the surgery [DOLW12] and another CT image acquired after surgery. Nevertheless, the comparison of both images is a difficult task, as physicians often have to overlap these images in their minds or by manually rotating and

[1] World Health Organization Fact Sheet 297. http://www.who.int/mediacentre/factsheets/fs297/en/
[2] GLOBOCAN Fact sheet 900. http://globocan.iarc.fr/factsheets/populations/factsheet.asp?uno=900

translating one of them. However, it is important to note that the liver is a soft tissue organ subject to deformations due to breathing. Interventions further change the shape of the organ as explained in detail in Section 1.2. All these deformations increase the difficulty of the overlapping task, and simple rotations and translations will not yield satisfying results.

Figure 1.1 shows two application scenarios (tumor ablation and resection) in which image registration plays an important role. The first image shows an abdominal CT scan in which the liver contains a tumor (darker region inside the red circle). The second CT scan shows an ablated area (dark area inside the red circle). The ablation can usually be recognized as a dark area with a (ideally) larger extension than the tumor. The patient of the third CT scan was treated by tumor resection. The area inside the red ellipse should usually contain liver tissue. However, that area has been resected. This can be recognized by the two bright structures (orange arrows) near the surface of the liver. This structures are the clips that were used to close the vessels cutted during surgery to prevent farther bleeding.

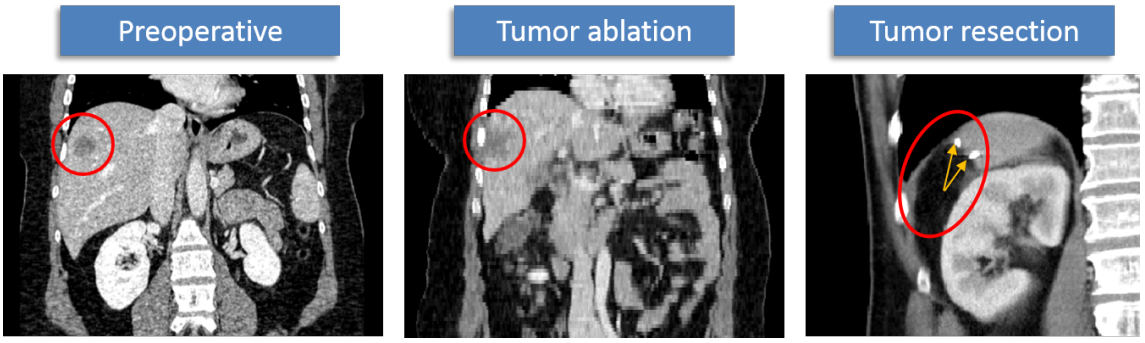

Figure 1.1.: Images acquired at different moments contain complementary information: while the preoperative images are used for diagnosis and show the tumor (dark area inside the red circle), the postoperative images (tumor ablation and resection) allow the physician to assess the outcome of a surgery. To take advantage of the information contained in both images, it is necessary to register both acquisitions.

1.2. Technical challenges

The technical challenges that will be solved in this thesis can be divided in two groups: challenges of the registration method and challenges of the identification of corresponding landmarks.

1.2.1. Registration

As previously mentioned, the liver is composed of soft tissue and it is prone to deformations. The sources of deformations are manifold:

- Breathing cycle. During inhalation, the lungs fill up with air. At the same time, the diaphragm and the ribcage move, causing the liver to deform. The opposite movements can be observed during exhalation.

- Ablation. The elasticity of the post-ablated area is much smaller than that of the parenchyma. This causes the area to react in a different way to the deformations caused by breathing.
- Resection. After a part of the liver has been resected, the surrounding organs may occupy the space where the liver was located before, exerting additional forces on the liver surface. In addition to this, the position of the liver inside the body can also change.
- Hypertrophy. The patient can also undergo a second resection. In that case, another deformation source arises, which is caused by the liver when it regrows (hypertrophy). The regenerated areas do not grow in the same way as the original liver.

Due to all of these possible deformations, rigid registration techniques (affine transformations) do not suffice for an accurate registration, and non-rigid registration has to be used.

Nevertheless, the results obtained with conventional non-rigid registration techniques (e.g., intensity based) under the presence of large deformations are not accurate. Under these circumstances, physical/anatomical information has to be added to the registration process to increase the precision of its results. One last constraint has to be considered for an appropriate registration. Tumors can be located anywhere in the liver; this means that accuracy is required not only on the superficial level of the organ but also the internal structures must be correctly registered.

Unfortunately, the methods proposed in the literature will not achieve accurate results in presence of large deformations and they concentrate their efforts to achieve accurate results in the interior or the surface of the organ but not in both areas. Thus, the main challenge is to conceive a deformable registration method that results in accurate results both in the interior and the surface of the organ in presence of large deformations.

1.2.2. Identification of corresponding landmarks

One technique to guide the registration process is to use landmarks. The liver vasculature is often used as anatomical landmark in the interior of the organ [LWRS09b, KKOLW13, CAM*05b]. It consists of three vessel systems (hepatic and portal veins and arteries). Before the CT acquisition, a contrast agent is injected. Vessels filled with it become visible as bright tubular structures in the CT images. These vessels are segmented in the pre- and postoperative images. Then, a graph representation of both hepatic and portal veins is generated. Finally, a graph-matching method is applied to find correspondences between them. However, finding these correspondences is not straightforward. Even if the anatomical vessel trees correspond to the same patient, the differences that can be observed between both of them are manifold. Some of these differences have their origin in imaging reasons:

- Missing branches. Due to inaccuracies of the segmentation methods, branches that are visible in one of the vessel trees (usually the preoperative one) might be missing in the other one. The situation gets worse due to different resolutions between pre-

and postoperative images. While the resolution of the preoperative image is usually high, the postoperative image is usually acquired with lower resolution in the clinical routine.

- Interconnecting vessel trees. Hepatic and portal veins are separate structures; however, in some areas where the vessels intertwine or artifacts are present, segmentation methods are not able to distinguish between them. Consequently, the generated graph will contain loops; this further complicates the process of finding correspondences.
- Missing tree parts. Depending on the exact moment in which the images are acquired with respect to the contrast agent injection, part of a vessel system might be invisible in one of the acquisitions. In an extreme case, no common structures will be visible between both acquisitions.
- Artifacts. Segmentation methods sometimes erroneously classify volume artifacts as part of the vessel trees.

Additional differences appear due to anatomic reasons:

- Hypertrophy. After a resection takes place, the liver starts regrowing. Nevertheless, the new vessels will not have the same length and topological structure as the original ones.
- Surgical segment removal/ablation. Changes in the topology of the trees appear in the neighborhood of treated areas.

To achieve a pose-independent and automatic method is still more challenging. As will be shown in Chapter 3 it is challenging to find a similarity metric for the liver vessels that is at the same time pose-independent and robust. Thus, existing methods, relax the pose-independence condition and ask the physician to manually preinitialize the images as input for the method. The physician will also need to provide at least one pair of preselected correspondences for the method to work. This is a hard and time-consuming task, since one of the trees (usually the postoperative one) contains a smaller number of bifurcations and sometimes even hypertrophic vessels; thus, it is not always easy to visually find correspondences.

As previously mentioned, the accuracy of the registration should not be restricted to a local area of the liver. The use of additional external landmarks will help to fulfill this constraint. In that sense, commonly used closest point distances between surfaces can work appropriately when the deformations are small. Nonetheless, their accuracy is reduced when deformations are large [NNSF09].

The main challenges related to the identification of corresponding landmarks are to conceive a pose-independent, automatic and efficient graph matching method able to deal with the aforementioned issues and to conceive a method to accurately detect correspondences on the surface of the organ in presence of large deformations.

1.3. Goals of the thesis

The goal of this work is to provide physicians with an automated tool for validation of liver surgery after tumor resection or ablation. The basis of such an approach is an accurate registration method.

Following the challenges mentioned in Section 1.2, the deformable registration method has to be able to handle large deformations and at the same time achieve accuracy in the interior and surface of the liver. Therefore, a physics based, non-rigid registration method is required. Such a method is able to better overcome large deformations (see Chapter 2). However, the main challenge of the registration is to achieve accuracy in the interior and surface of the organ instead of limiting the accuracy to a local area.

In this thesis a method is proposed that uses corresponding landmarks inside and on the surface of the liver to guide the registration process. It will be proven (see Section 5.5.3) that such an approach increases the achieved accuracy over state of the art methods. The method to detect corresponding landmarks inside the liver should be efficient and fully automatic to ensure that it can be used in all studied clinical scenarios. A pose-independent and fully automatic graph matching method has been conceived for this purpose.

To ensure the detection of correct correspondences on the surface of the organ in presence of large deformations (in some cases even resections) a method is proposed that uses prior knowledge of the human anatomy to detect those correspondences.

1.4. Contributions

The main contributions related to the identification of corresponding landmarks are as follows:

1. Survey and classification of graph-matching methods with application to medical imaging problems (see Chapter 2).

   Classification schemes were proposed in the literature to classify graph-matching methods for general/certain applications. But in spite of the high use of graph matching methods to solve medical imaging problems, none were proposed for that application. This thesis contains a survey and classification scheme that fills this gap. A special emphasis is put on the similarity metric used for each method and application, since the accuracy of the results will highly depend on this.

2. Root- and pose-independent efficient graph-matching method (see Chapter 4).

   Most state-of-the-art methods to find correspondences between vessel trees have some limitations that will be discussed in detail in Chapter 2: efficiency, root and pose dependency, and the inability to handle loops. When time is a constraint, the complicated task of preselecting a pair of roots can make the method unusable [OLDE*12]. On the other side, the inability to handle loops means that a previous tree separation has to take place for the method to work [DOOL11]. Furthermore, pose independence is a requirement for a fully automatic detection of correspondences. This thesis proposes an efficient graph-matching method that

solves these problems [OLD11c, OLD10]. In addition to this, an automatic statistical outlier detection is proposed to increase the accuracy of the results.

3. Interactive features (see Chapter 4).

   It is important to support the physicians (when necessary) to refine the results of the matching method. To this end, a series of interaction features are proposed that will help physicians influence the results of the method [DOLCE10, OLD11a].

4. Automatic extraction of liver surface landmarks (see Chapter 5).

   In order to achieve accurate results not limited to certain liver areas in which internal landmarks were found, liver surface landmarks are also needed. A method based on prior knowledge of the human anatomy is presented to extract liver surface landmarks from the anatomy surrounding the liver [OLDW14a]. A weighted histogram method is proposed to obtain a series of boundary classifiers that will automatically determine which organ is adjacent to the liver at each location.

The main registration related contributions are as follows:

1. Finite element method (FEM) based registration method using both anatomical internal and liver surface landmarks (see Chapter 5).

   A physics based approach is proposed that encompasses anatomical internal and liver surface landmarks [OLDW14b]. Therefore, a combination between finite element methods and thin plate splines is used. Furthermore, the liver model is divided into two tissue types: the parenchyma, which composes the majority of the liver, and Glisson's capsule [OLBPDW13].

2. Outcome validation tool (see Chapter 6).

   A tool to help physicians to visually inspect the outcome of the surgery is presented. The tool returns several volumetric measures for quantitative evaluation of the surgery.

3. Evaluation (see Chapters 5 and 6).

   The proposed methods are tested on a large number of clinical datasets to prove their accuracy. In addition to this, the evaluation is done on a surface level as well as in the interior of the organ. Therefore, an interactive tool is developed that allows the user to visualize the registered vessel systems and select corresponding point pairs. Then, the method returns quantitative measures on the accuracy of the registration.

1.5. Structure of the thesis

The thesis is structured as follows:

Chapter 2 reviews state-of-the-art methods. The chapter will focus on two main areas: image registration and matching methods. At the end of the chapter, an in depth discussion will show the open questions and challenges that this thesis will deal with.

Chapters 3 and 4 introduce the matching methods used for detection of internal correspondences. Chapters 4 also includes the description of a series of interaction features and a statistical outlier detector to automatically reduce the number of false matches.

Chapter 5 introduces the method to detect surface anatomical landmarks and describes the deformable registration method. Therefore, the used mesh generator method is introduced. This is followed by a literature study of the elasticity values that different tissue types in the liver can have. The rest of the chapter is dedicated to the registration itself.

The end of each chapter contains a thorough evaluation and discussion of the presented methods. The thesis concludes with applications of the proposed methods in Chapter 6 and conclusions and recommendations for future work in Chapter 7.

2. Related Work

Image registration is focus of research because of its importance to solve computer graphics problems, for instance, clinical applications. Despite the amount of work published in this field, there is still room for farther research as the advances in medical technology require higher speeds and accuracy. Besides, new imaging modalities require new registration methods.

Figure 2.1 shows the work flow of a typical registration process. It consists of two main steps: the initialization, which goal is to avoid the registration method to get stuck in local minima, and the registration itself. Features are often used to guide each step. Thus, the rest of the chapter is organized as follows. Section 2.2 gives an overview of initialization methods. Section 2.3 introduces state of the art methods on image registration. Section 2.4 introduces existing graph matching methods. The chapter concludes with a discussion of the introduced methods (Section 2.5).

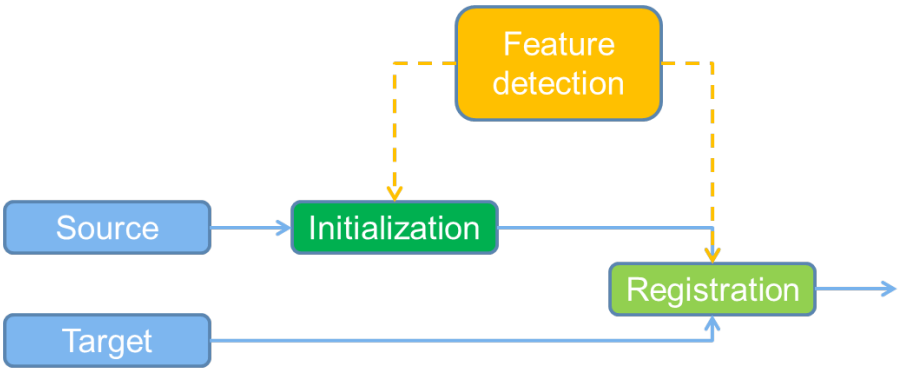

Figure 2.1.: Work flow of the registration process. The inputs to the registration are the source and target images, also known as moving and fixed images respectively. Usually an initialization of the images is necessary before further registration. In addition to this, several methods use landmarks as references to drive the transformations. This can happen either in the initialization process, in the registration process, or in both.

2.1. General concepts

Image registration is the process of transforming one image so that it shows an orientation similar to another image. The difficulty of the problem increases when one of the images contains deformations over the other one. In general the transformed image is known as **moving** or **source** image, and the one that remains intact **fixed** or **target** image. When the registration process finishes the two images are **registered**. If the

registration is done using translations and rotations, it is known as **rigid registration**. On the contrary, the transformations of **deformable** or **non-rigid registrations** contain deformations.

Features are structures (e.g., anatomical structures like vessels) or parts of the image that stand out against the rest of the image. Some registration methods use them as references to increase their accuracy. **Segmentation** methods can be used to extract these features. The goal of those methods is to divide the image into several regions (**labels**). Each region is represented by a different intensity value. Once the features are extracted, **landmarks** are detected (e.g., vessel bifurcations) and used to find correspondences between different images. Besides natural landmarks, many authors have used fiducial markers attached on the body of the patient as artificial markers. These markers can also be used for evaluation purposes.

2.2. Initialization

The images to be registered are acquired at different points in time. Under those circumstances, the positioning of the patient between acquisitions might vary. Images taken in prone and supine positions are an extreme example of this variation. Because of this, registration methods might fail if the underlying optimization methods get stuck in local minima. To solve this problem an initial placement of the images is done as pre-registration step. The goal of this placement is to bring the images closer to their final registered position. This is known as *initialization*.

In the application under study, the initialization method has to handle livers that underwent a tumor resection. Up to 80% of the liver might be resected during an intervention [MJM06], thus, the requirements of such a method differ from the approaches used to initialize complete livers.

Some initialization methods extract salient structures (features) in the images and use this information for the alignment. Darkner et al. [DVCL*06] initializes ear impressions rotating them around their orientation axis during impression scanning. Steger and Keil [SK10] use the tip of the chin as landmark to initialize CT and MR images of the head.

An often used technique to initialize livers is to align their centers. This is a valid approximation whenever the liver did not suffer a resection (e.g., surgery planning or after tumor ablation). It can also be valid after segmentectomy or bisegmentectomy [BCG*00] because of the relatively small size of the resected areas. Kainmueller et al. [KLL07] detect the lungs and uses the lower rim of the right lobe as reference to locate the liver. Kirschner and Wesarg [KW11] combine the ideas of Kainmueller et al. [KLL07] and Ruskó et al. [RBNF07], and initialize the liver model using the histogram of the liver as reference. Dos Santos et al. [dSSMMH10] propose to divide the liver surface meshes into a series of regions. They generate graphs of those regions and apply a graph matching method to find correspondences between the surfaces. These correspondences are the basis for their initialization. Clements et al. [CCD*08, CDC*11] use the falciform ligament and the inferior ridge as landmarks for a point based alignment of the liver surfaces. Therefore, they assume that both features can be identified in the preoperative and in the intraoperative liver volumes.

These methods solve the initialization problem for their particular applications. Nevertheless, they cannot initialize resected livers, especially after left or right hepatectomies, and extended left or right hepatectomies. Thus, specific methods have to be developed that provide a good initialization in presence of resections. Beuthien et al. [BPHF10] propose a solution to this problem. They initialize the two volumes matching their centers, and then carry out a rigid registration using the venous vessel system as reference. Their method has been tested in two datasets. Lange et al. [LWRS09a] use the vessel system as well. However, their method needs an interactive selection of correspondences between vessel trees. The task of manual selection of correspondences is tedious and difficult whenever the trees differ [OLD11a, OLDE*12]. Dumpuri et al. [DCL*09b] do not use the vessel system, but the iterative closest point (ICP) method to register both surfaces. However, they do not explain how do they handle the initialization problem, as ICP methods require a good initialization [DVCL*06].

Not all authors opt for landmarks to initialize the images. For example, Rhee et al. [RLNN07, RLNN08] initialize 3D knee MRI images manually. Other authors use intensity-based rigid registration techniques to initialize the two images. Anyway, the initialization method chosen should depend on the registration technique to be used afterward. In that sense, Cash et al. [CMS*05] point out that if the liver is going to be non-rigidly registered using a physics-based method (e.g., FEM), then the initialization should take into account which areas of the liver contain deformations, otherwise misregistrations might occur in initially not deformed areas. This is illustrated in Figure 2.2. In this figure the blue liver represents the preoperative liver and the red one the intraoperative one. The left lobe of the intraoperative liver presents deformations over the preoperative liver. A conventional registration method like, for example, ICP, would minimize the global distance between surfaces. However, this would lead to misalignments in the initially not deformed right lobe of the liver. Consequently, a physics-based deformable registration would exert forces to an area of the liver that should remain intact.

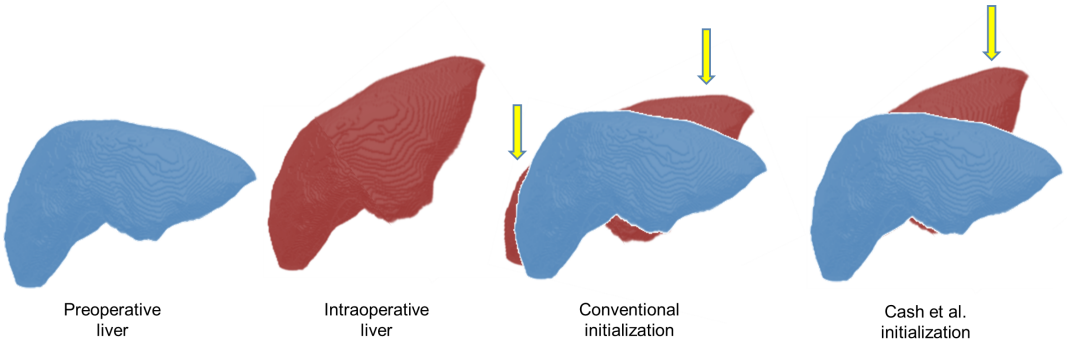

Figure 2.2.: Initialization of two liver volumes using a conventional approach (e.g., ICP) and using the idea proposed by Cash et al. [CMS*05]. In the former approach forces will be applied in initially not deformed areas leading to misregistrations.

2.3. Registration

In this section state of the art registration methods are introduced. Keeping in mind the goal of this thesis (developement of an outcome validation tool for liver tumor resection or ablation) an appropriate registration method should fulfill the next requirements:

- Capability to handle large deformations.
- Achievement of total organ accuracy.

Taxonomy Image registration is one of the main research topics in medical imaging. Proof of this is the number of review papers published about it. Among the most cited papers is the one by Maintz and Viergever [MV98]. Their taxonomy has served as basis for the classification schemes proposed by numerous authors (see Figure 2.3). While Maintz and Viergever present a complete and general scheme, other groups have a more specialized focus. Some authors, like Mäkelä et al. [MCS*02] or Kotsas and Dodd [KD11], focus on intrinsic registration for cardiac and 2D/3D registrations respectively. The same taxon has been chosen more recently by Oliveira and Tavares [OT12]. Pluim et al. [PMV03] has followed a classification scheme similar to that by Maintz and Viergever with the peculiarity to deal with registration methods that use mutual information as similarity metric.

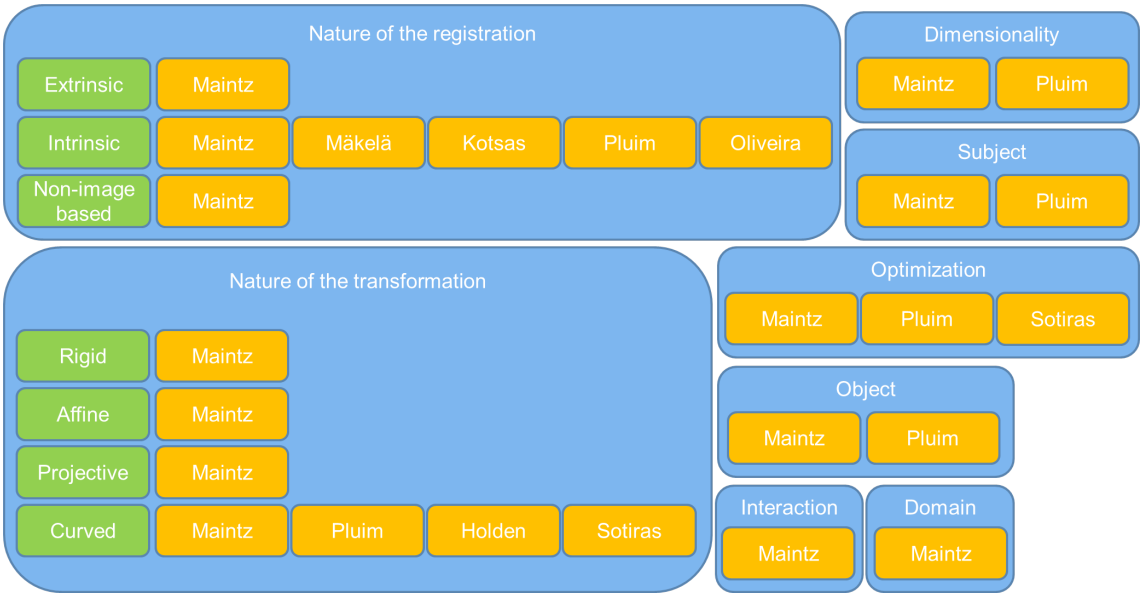

Figure 2.3.: The taxonomy proposed by Maintz and Viergever [MV98] has served as basis for several new classification schemes. This figure shows the main taxa (blue) proposed by Maintz and Viergever and their subdivisions (green). This taxonomy is very general and most of the authors have a focus on some of the taxa proposed by Maintz and Viergever. Authors (yellow) that are inside a concrete taxon (blue) have focused their work on it. If they concentrate their work in a concrete subdivision of the taxon, the author (yellow) appears to the right of the corresponding subdivision (green).

The taxonomies proposed by Holden [Hol08] and Sotiras et al. [SDP12] are of special interest for this thesis. Holden extends the curved (non-rigid) transformations taxon by Maintz and Viergever. According to him, this taxon includes: physical models, basis function expansions (renamed as "interpolation-based" by Sotiras and colleagues) and constraints of the transformation (renamed as "task specific constraints" by Sotiras and colleagues). Each taxon is then further subdivided. Sotiras and colleagues extend the subdivision of Holden and consider two additional aspects of the registration process, namely, objective functions and optimization strategies.

The taxonomy proposed in this thesis (Figure 2.4) is based on the one by Sotiras et al. [SDP12]. Opposite to the aforementioned taxonomy objective functions and optimization strategies will not be considered. The taxonomy proposed in this thesis will contain taxa common to Sotiras and colleagues and additional new taxa. Furthermore, some of the taxa proposed in the aforementioned taxonomy will be reorganized or ignored.

- *Common taxa.* The taxa common to Sotiras et al.'s [SDP12] taxonomy are shown in blue. As proposed by Sotiras and colleagues, non-rigid registration can be divided into physics based and interpolation based.

- *Reorganized taxa.* The yellow taxa are common to Sotiras et al.'s [SDP12] taxonomy but are reorganized in the proposed classification scheme. Papers classified as "knowledge-based" and "task-specific constraints" by Sotiras and colleagues can also be included either in "physics-based" or "interpolation-based" transformations. For example, a method that registers livers using the knowledge of the physiological motion of the lung is classified by Sotiras and colleagues in the group "knowledge based". To avoid ambiguities, this thesis classifies this method as physics- or interpolation based depending on the registration method used.

- *Ignored taxa (red).* Only a few papers can be classified as "curvature registration" and "basis functions from signal processing". Thus, they will be ignored in this thesis. The interested reader can find them in Sotiras et al. [SDP12].

- *New taxa.* This thesis introduces new taxa in the classification scheme (green). The methods contained in the "physics based" category are governed by physics equations. Opposite to "diffusion models" and "flows of diffeomorphisms", the equations that govern elastic and viscous fluid models derive from the same physics law, namely, Newton's second law of motion. Hence, this thesis groups them in the taxon "Models derived from Newton's second law". Besides, due to the continuous improvement of physical models this taxon is not complete by considering uniquely elastic and viscous fluid models. Thus, it is extended by including hyperelastic and viscoelastic models. Additional models have been developed, for example, porous models. Nevertheless, so far they have only been used for simulation but not for registration. Thus, they will not be included in the taxonomy. Finally, not only deformable registration techniques will be discussed in this chapter but also rigid registration techniques. They will be divided into intensity- and landmark-based.

There are two important aspects that were not taken into account in the previously mentioned taxonomies and will be considered in this thesis:

Figure 2.4.: Taxonomy of image registration methods. Blue: taxa common to the classification scheme by Sotiras et al. [SDP12]; Red: taxa included in Sotiras and colleagues but not in this thesis; Green: Taxa included in this thesis but not in Sotiras and colleagues; Yellow: taxa common to Sotiras and colleagues but reorganized in this thesis.

1. The region in which the accuracy is reached: local (inside the organ or on its surface), often achieved using landmarks, or total organ (inside and on the surface of the organ). For some applications global accuracy, extended to the body that surrounds the organ under study, can be important. Nevertheless, the region of interest of this thesis is reduced to the liver.

2. The amount of the deformations that the method can handle.

Some methods, especially those that use internal landmarks, will achieve high accuracy in the interior of the organ but not on its surface. The opposite happens with methods that register two images based on surfaces or external edges. This can be seen in Figure 2.5. The first image shows a preoperative CT of the liver. The second image shows a checkerboard visualization in which the postoperative (after tumor ablation) segmented CT image is registered to the preoperative CT image using internal landmarks. Note that the postoperative image has lower resolution. One can see, that the internal structures are correctly aligned but not the surfaces. A FEM method has been used in which internal landmarks have driven the registration. In the third image the opposite holds. In this case, the surface is correctly registered but not the internal structures. For this registration, a Demons based method has been used [ESH*11]. Thus, the methods can be further

classified according to their accuracy in: internal, surface or total organ accuracy. Finally, the methods are also classified according to the deformations that they can overcome. Figure 2.6 shows the classification according to those two aspects.

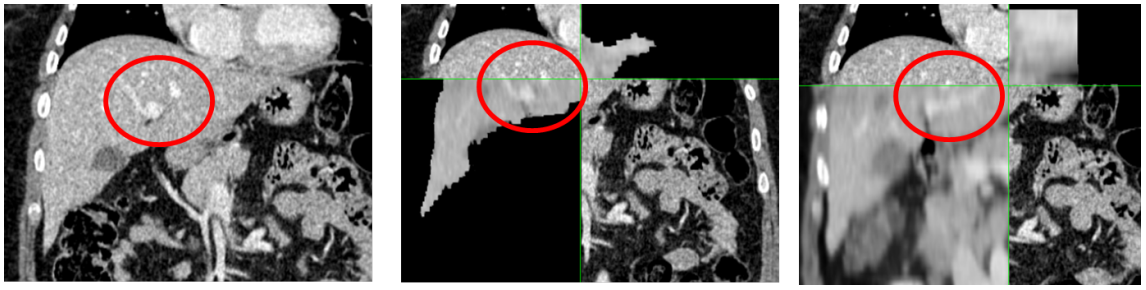

Figure 2.5.: Importance of taking organ internal and organ surface constraints into account. Left: Preoperative CT. Middle: Registration of pre- and postoperative livers with a FEM approach driven by internal landmarks. Accuracy is achieved inside the liver but not on the surface. Right: Registration with a Demons based method. Accuracy is achieved on the surface but not internally.

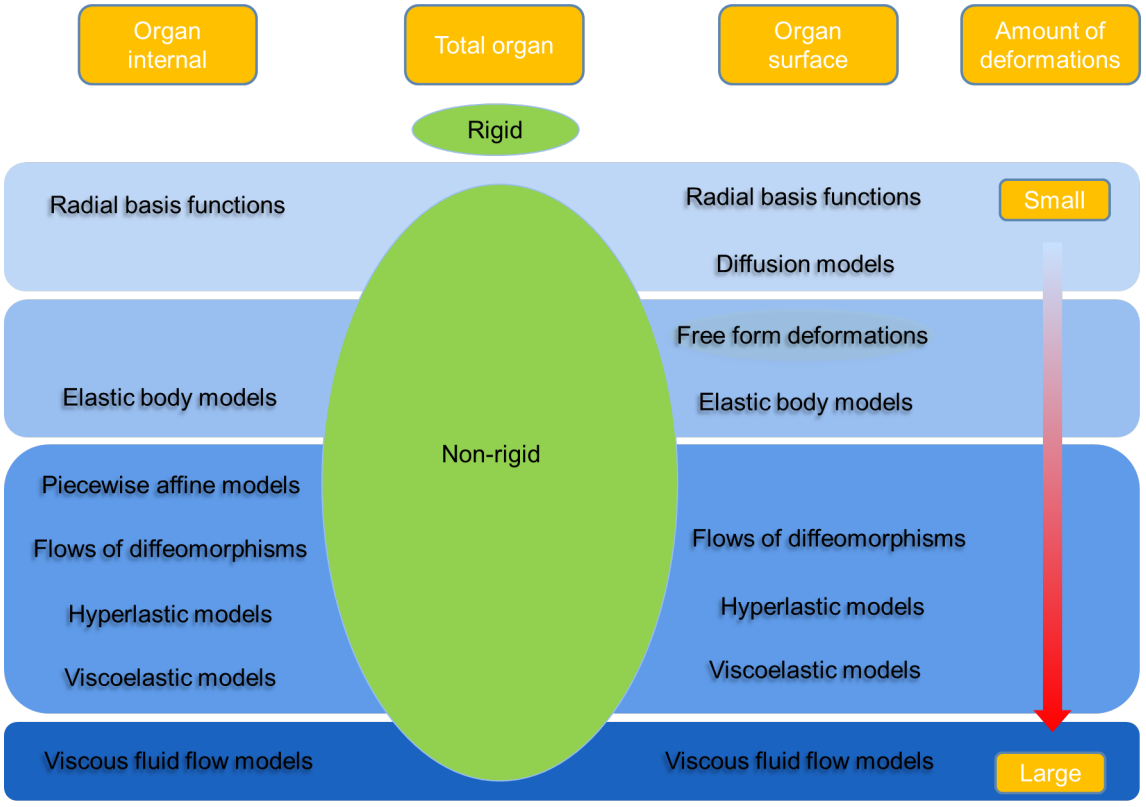

Figure 2.6.: Image registration taxonomy: The methods are classified according to the deformations that they can handle and the kind of constraints that they use to carry out the registration: organ internal, organ surface or total organ.

2.3.1. Rigid registration

Rigid registration methods (Figure 2.4) transform the moving image using translations and rotations. Occasionally, scaling is also used (affine transformations). These transformations are especially useful to register stiff structures, for instance, the bones. Rigid registration methods can be divided in intensity-based or landmark-based.

2.3.1.1. Intensity-based

This group contains rigid registration methods that find the optimal transformation by analyzing intensity similarities between voxels in the image. To this end, they optimize the metric that determines how similar the images are. Probably the most widely used metric for intensity-based rigid registration is mutual information. Carrillo et al. [CDLW00] use it as similarity metric to semiautomatically register different magnetic resonance imaging (MRI) acquisitions of the liver. Therefore, they carry out several preprocessing steps. An interactive selection of a mask removes certain structures on the MRI to avoid the failure of the method. They compare the results obtained using mutual information to those obtained using entropy, correlation, variance of the gray-scale ratio, and manual registration. The results show that the lower failure rate is given when mutual information or the variance of the gray-scale ratios are used as similarity. However, the former is more sensitive to a correct masking selection. Mutual information has also been used by van Dalen et al. [vDVH*04] to register computed tomography and positron emission tomography of the liver. They also propose to interactively select a region of interest prior to the registration. Finally, they compare the results with and without the region of interest, to a manual registration method, and to a landmark-based method in which the landmarks are manually selected. After analyzing the results, they conclude that mutual information focused on a region of interest provides the highest accuracy. Kuklisova-Murgasova et al. [KMQH*12] register fetal brain MRI and ultrasound data. Therefore, they propose to simulate a 3D ultrasound image from the MRI, and then register simulated and real ultrasounds images using normalized cross-correlation. The results in 5 pair of images using normalized cross-correlation showed to be more accurate than those using normalized mutual information. Stippel et al. [SEW*03] use Kullback-Leibler distance to register pairs of CT and intraoperative ultrasound acquisitions. Therefore, they use a liver phantom. First a pair of CT and ultrasound images is manually registered and their joint intensity histogram is calculated. Using this as reference the rest of the ultrasound images are automatically registered using the Kullback-Leibler distance between joint histograms. The algorithm has only been applied to the data generated from the liver phantom.

2.3.1.2. Landmark-based

The methods contained in this taxon use landmarks to drive the registration. As Maintz and Viergever [MV98] proposed the landmarks can be **extrinsic**, like fiducials or some kind of frames or structures placed in/on the patient, or **intrinsic**, like anatomical or geometrical landmarks that will be extracted from the image.

Hoßbach et al. [HGWG12, HGWG13] use several blue dots (fiducials) attached to the forehead of the patient to track the movement of the head during MR acquisitions. Thanks

to this, they can successfully remove the moving artifacts afterward as is it shown in the evaluation carried out on 3 volunteers. This is especially interesting for patients that due to certain sickness cannot stay still during the acquisition. Soft organs, for example, the liver, present difficulties to place fiducial markers on their surface. Under those circumstances, this technique is only used to measure the accuracy of a registration method on phantoms. On the other side landmarks placed on the outer surface of the body lead to inaccuracies as the liver is not fixed at the ribcage and will deform and move. For those organs, intrinsic landmarks are used.

Geometric landmarks (series of points located on the surface) have been combined with the widely used ICP method to register soft organs. Herline et al. [HHS*99] propose to use this method for intraoperative registration of the liver. Therefore, they generate a phantom containing six artificial tumors and collect a series of points in the surface of the liver. During surgery, corresponding points have to be detected using a tracked ultrasound probe. The ICP method is applied to both sets of points. They achieve an accuracy of 2.9 mm on the surface of the organ and 2.8 mm in the artificial tumors. Dumpuri et al. [DCL*09a] use ICP method to register preoperative and postoperative (post resection) CT acquisitions of the liver. Rigid registration methods lead to inaccurate results inside and outside the liver because the liver is made of soft tissue.

In addition to geometric landmarks, anatomical landmarks have also been used for rigid registration. Drechsler and Oyarzun Laura [DOL10b] carry out a 3D/2D rigid registration between computed tomography angiography and coronary angiographies. Therefore, a digitally reconstructed radiography is generated and point pairs are manually selected on the vessels of both images. The accuracy achieved with the proposed method is below 2 mm.

2.3.2. Non-rigid registration

Depending on the structure to be registered a transformation consisting only of translations and rotations will not return accurate results, for instance, registration of soft tissue. Thus, deformations are included in the registration process. The following sections will introduce state of the art methods that include deformations in the registration process.

2.3.2.1. Physics-based

This taxon encompasses the methods based on the laws of physics. It includes models governed by Newton's second law of motion, diffusion models and flows of diffeomorphisms.

Models derived from Newton's second law Newton's second law of motion states that the product of the mass m of an object and its acceleration a equals the net force F of the object:

$$F = m \cdot a \tag{2.1}$$

or

$$\nabla \cdot \sigma + F = \rho \ddot{u}. \tag{2.2}$$

In the last equation ü is the acceleration of the object, and u the displacement.

In the following, several concepts are introduced that help understand how an object will react to an exerted force. The **deformation gradient tensor** F is a measure of the change in shape of an object. Let dx be an infinitesimal element belonging to the original object and dx' the corresponding element after deformation, the deformation gradient tensor relates both elements as: $dx' = Fdx$. Similarly the volume change of the object is given by the **jacobian** J of F.

The **stress** in an object is known as the force per unit area. Different measures have been used to quantify the stress. In the following sections two of them will be used: Cauchy stress σ and First Piola-Kirschhoff stress P. The difference between them is that they measure the stress relative to the deformed and reference configurations respectively. This stress will cause a deformation of the object known as **strain**. The **Lagrangian strain tensor** E is used as measure of the strain. Under the presence of small deformations, E is replaced by the **infinitesimal strain tensor** ϵ. ϵ is a linear approximation for the measure of the deformation. The **strain energy density function** W constitutes the energy stored in the object per unit volume because of the applied deformations. Depending on the stress-strain relationship of the object it will react to the applied external force differently [Fun93].

This is illustrated in Figure 2.7. Linear elastic models (first row), represented usually by a spring, show a linear stress-strain relationship curve. The opposite holds for non-linear elastic models (usually known as hyperelastic models) for which the stress-strain relationship is non-linear. However, in both cases when the force applied (loading) to the object (a plane in the figure) is removed (unloading) the object returns to the initial state without deformations. When a viscous term is added to the equations (a dashpot in the model, see third row) time dependencies appear for the stress and for the strain. This means that an object under a constant stress will continue to deform. This effect is known as **creep** and it is illustrated as a green curve in the figure. On the other side if the object is subjected to a constant strain, the stress will diminish with time (**stress relaxation**). Finally, these models present a third phenomenon called **hysteresis**. According to this, the loading and unloading present differences (Figure 2.8). Due to the viscosity that these models contain the object will not return to their initial state after the load is released, but some deformation will remain. The fourth row of Figure 2.7 describes the behavior of fluid models. One can observe that the model does not contain an elastic term (spring) any longer, but it is purely viscous. This kind of models cannot overcome the deformation after the load is released.

Newton's second law has been transferred to the field of image registration and it is widely used. Therefore, the external force is determined by boundary conditions and assumptions (biomechanical models), or image similarity criteria.

This taxon will be further subdivided according to the mechanical behavior of the model in: elastic, hyperelastic, and viscoelastic, for solid models, and viscous fluid models. As the level of accuracy needed is increasing more complex models are studied, however, those models have not yet been used for registration purposes but for simulation. For

Figure 2.7.: Rheology. Rows from top to bottom: linear elastic, hyperelastic, viscoelastic and viscous fluid behaviors. The columns show: the model, stress-strain curves, and an illustration showing how a plane will recover from an applied load (first graphic) after the load is released (second graphic).

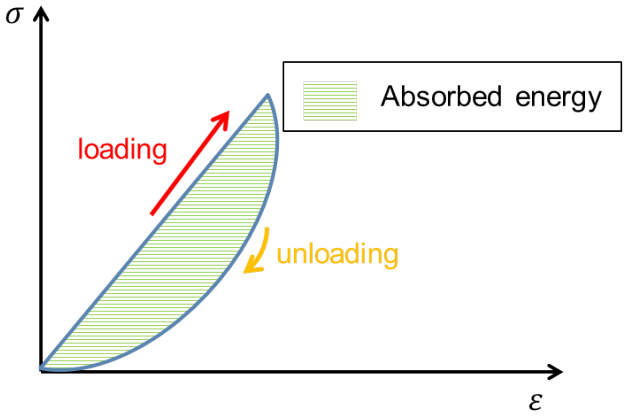

Figure 2.8.: Hysteresis phenomenon: the loading and unloading processes do not present the same stress-strain curves. Part of the energy is absorbed by the object.

instance, the liver model proposed by Maechesseau et al. [MHC*10], composed of viscosity, hyperelasticity, and porosity, has only been used for simulation.

Linear elastic models are the most widely used models derived from Newton's second law. They are less computationally expensive than those including non-linearities and viscous terms. The equation that governs the behavior of those models is given by the Hookean law:

$$\sigma = c\epsilon \tag{2.3}$$

where c is the stiffness tensor. In linear elastic models the deformations are assumed to be small. Thus, the infinitesimal strain tensor is used instead of E. Ferrant et al. [FWG*99] use homogeneous elastic models to register 3D brain MRI. They formulate the problem as an energy minimization procedure that combines the elastic behavior of the tissues with local image similarity constraints. A tetrahedral mesh of the object to be registered is generated. In the proposed method the external forces applied to the image are given by optical flow fields. A quantitative evaluation of the algorithm is not provided. Elastic body models have also been used to register liver volumes. Cash et al. [CMS*05] propose to use finite element methods (FEM) to simulate intraoperative deformations on the liver. Therefore, they introduce a novel initialization of the liver that takes into account which areas contain large deformations. The areas without deformations will drive the rigid registration. Consequently, during non-rigid registration forces will only be applied to the deformed areas. The registration is governed by three boundary conditions. The first one (a set of Dirichlet conditions) is applied to the areas of the liver assumed to be fixed. The second are stress-free boundary conditions. Finally, closest point boundary conditions are used: a combination between Dirichlet and Neumann conditions. The method has been evaluated using a liver phantom that contains artificial tumors resulting in an accuracy of 4 mm. Niculescu et al. [NFN07, NNSF09] register two liver surfaces using the ICP method and a finite element method. A closest point technique determines the forces that will deform the model. They use the direction similarity between the vectors normal to the surface to detect corresponding points. The method has been tested by

visual inspection in three datasets. Lee et al. [LLF08] use biomechanical elastic models of the prostate as evaluation tool for other registration methods. Boundary conditions based on the matching between surfaces can lead to physical inaccuracies. Instead, they propose to use the interaction between organs as boundary conditions. Therefore, they model the bones as fixed, and the bladder and rectum as hollow objects. Their interaction with the prostate will determine its deformation. The method has been used to compare fluid flow models, Demons method, and level sets. The authors state that although Demons method performs better in this example whenever deformations are large, fluid flow methods would be a better choice.

Even though FEM is widely used to solve the equation systems that describe the behavior of biomechanical models, sometimes a simplification of the problem is desirable. The consequences of this simplification will be a gain in speed and a loss of accuracy. Mass-spring methods simplify the model assuming it to be formed by masses connected by elastic springs. Conti et al. [CKB03] propose to use a mass-spring system to simulate soft tissue. This method has been used more recently by Dagon et al. [DBB08]. They extract the vessel tree skeletons from preoperative CT or MR liver acquisitions. Under the assumption that the liver parenchyma deformation correlates with that of the vessels, they define a vessel tree mass-spring model. In this model the masses are located at positions along the vessel skeleton. The elastic springs on the other side are given by the links between those points. During intervention, 2D tracked US acquisitions are taken. The vessels visible in those images are segmented using ellipse approximations and the center of each ellipse is converted into a 3D point using the referencial frame of the tracking probe. The final registration is achieved by applying forces to the mass-spring model of the preoperative images in the positions in which US points were detected. Evaluation on clinical data is not provided. This type of models has not only been used to register abdominal images. Lin et al. [LRQG13] used it to register cerebral MR images. They use sum of squared differences as similarity metric for the registration. The novelty of their work is the introduction of mass-springs analogies as regularization term to ensure the topology preservation of the method. This way they reduce the computational cost of other methods that force the Jacobian determinant to be positive as regularization. The mass-spring analogy includes the spatial relations between different voxels by limiting the deformation field to the movements of the mesh. They finally compare quantitatively their method to Demons method. The cross-correlation factor determines that the best results are obtained with the proposed method.

Even though linear elastic models can be appropriate to model the behavior of certain objects, sometimes the nonlinearity of the strain-stress relationship has to be taken into account. Then **hyperelasticity** is included in the model. The approximations done using ϵ in linear elastic models are not suitable any longer and the Lagrangian strain tensor is used instead. As shown in the stress-strain curves of Figure 2.7, the stress-strain relation will not depend on a constant factor any longer. It will be expressed as a function of the strain energy density function W. The first Piola-Kirchhoff stress tensor P of hyperelastic materials can be then defined as [MWTT98]

$$P = F\frac{\partial W}{\partial E} \tag{2.4}$$

which in terms of the Cauchy stress is expressed as

$$\sigma = \frac{1}{J} F \frac{\partial W}{\partial E} F^T. \tag{2.5}$$

Depending on the selected strain density energy function the object will have a different behavior (different stress-strain curve). Thus, the results of the registration will depend on that decision.

Johnsen et al. [JTT*11] use a Neo-Hookean hyperelastic model to describe the behavior of the liver under certain conditions (e.g., the deformations caused by a tool during intervention). They use collision detection to model the effect of tool-liver interactions, and ribcage-liver movement restrictions. In another experiment they drive the registration using internal constraints at points along the vessels. A thorough evaluation is planned as part of their future work. Another group working on the registration of livers using Neo-Hookean hyperelastic models is Suwelack et al. [STR*11, SRD*11]. They compare this model to a linear elastic model and two additional quasi-linear viscoelastic models. The latter will be further explained in the next subsection. The hyperelastic model returns similar accuracy to that obtained with the quasi-linear viscoelastic models. Linear elastic models show to work properly whenever an instrument indentation is simulated. But the accuracy is reduced in presence of breathing motion. All experiments have been done on phantom data. The authors further state that patient specific parametrization is not needed. Hamamci and Unal [HU13] use Neo-Hookean strain energy density as regularization for a hyperelastic registration. The goal of their method is to register MRI of the brain for tumor growing follow-up. Therefore, they propose to register the images using only the information contained in the healthy area of the brain. This way they can estimate the pressure produced by the tumor. Darkner et al. [DHLH11] use the strain energy function of Riemann elasticity as regularization for registration methods. They propose to decompose the left Cauchy-Green strain tensor and derive its eigenvalues to ensure diffeomorphism. They qualitatively evaluate their method in 2D cardiac MR and 3D ear surfaces.

Another organ that suffers from large deformations is the breast. Preoperative MR acquisitions of the breast are usually taken in prone position while breast surgeries are carried out in supine position. Carter et al. [CTBN*08] use a hyperelastic finite element model to register prone and supine images of the breast. Therefore, they apply to the model a force opposite to the gravity force to take away its influence. This way they reach the so-called reference state. Then, they apply gravity forces to the anterior direction to get the deformation of the model in supine position. To increase the accuracy of the model two tissue types (adipose and fibroglandular) are considered. Furthermore, a series of fiducial markers are attached to the skin and used for initialization and evaluation purposes. Once the biggest part of the deformation is recovered, a fluid based method is applied as final step of the registration. The method has been tested in the operating room resulting in an accuracy of around 5 mm. Lee et al. [LSR*10] propose another hybrid approach to register breast MR images. Opposite to the previous group, they consider the breast fixed at the ribs, which allow them to initialize the images using them as reference. After applying FEM, they use free form deformations (FFD) to refine the results. The method has been tested in one phantom data and 5 volunteers. Invariably

the hybrid approach outperforms FEM and FFD separately with an accuracy in the clinical datasets of 2.82 mm. Han et al. [HHM*11] accounts for the sliding of the breast against the chest wall by modeling the latter as a rigid surface, and adding a friction coefficient to the interface between them. In addition to this, they propose to update the model's parameter values iteratively until the best possible solution is achieved. They use free form deformations as final step to account for the approximations errors introduced by the finite element model. This method has been tested on one clinical dataset. The accuracy obtained calculating distances between fiducial markers was 2.8 mm.

Viscoelasticity constitutes another increase in the complexity of the solid models. Soft biological tissues, for example, the liver, do not behave as purely elastic but contain a viscous part [Hum03]. These models present some special behaviors called: stress relaxation, creep, and hysteresis, that show that the object deformation depends on the time and on the load history [Fun93]. This is reflected on the stress-strain relation of these models under linear conditions

$$\sigma(t) = \varphi(t)\,\epsilon(0) + \int_0^t \varphi(t-\tau)\,\frac{\partial \epsilon(\tau)}{\partial \tau} d\tau. \tag{2.6}$$

In this equation φ is the tensorial relaxation function that constitutes the previously explained relaxation effect (see the stress-strain curves in Figure 2.7). This time the stress-strain relation contains two terms. The first one is the deformation at the initial state given the strain $\epsilon(0)$. The second term represents the dependence of the stress on every previous strain. τ represents all previous times and t is the current time. Similarly to the effect of the different strain energy functions in hyperelastic models the behavior of the model will highly depend on the selection of the relaxation function.

However, the behavior of soft tissue is nonlinear. Thus, the relaxation function will not only depend on the time but also on the strain. To simplify the problem Fung [Fun93] propose to divide the relaxation function into two functions each dependent on one of the parameters (time and strain). This way the relaxation function is expressed as:

$$\varphi(\lambda, t) = G(t)\,T^{(e)}(\lambda), \tag{2.7}$$

where $G(t)$ is the reduced relaxation function that is only function of time. $T^{(e)}(\lambda)$ is the stress generated in the material by applying a strecht ratio of λ that can be defined in terms of the strain ϵ as $\lambda = 1 + \epsilon$. $T^{(e)}(\lambda)$ is a nonlinear function that takes care uniquely of the instantaneous elastic response of the material and not of the relaxation part. Then the stress-strain relation expressed in terms of the nominal stress T ($T = P^T$) is given by:

$$T(t) = \int_{-\infty}^t G(t-\tau)\frac{\partial T^{(e)}[\lambda(\tau)]}{\partial \tau} d\tau. \tag{2.8}$$

This is known as quasi-linear viscoelastic theory and has been the basis for several models. The most widely used one among them is Maxwell model that describes the dual behavior of some materials as combination of an elastic term (spring) and a viscous term (dashpot). This model has been used by Tang and Jiang [TJ04] and later by Yi and Wan [YW05] to register brain MR images. They compare the results of the viscoelastic method with fluid models and affine transformations. An improvement of the results is

achieved with the proposed method. A correlation coefficient of 0.9833 is reached. Models based on quasi-linear viscoelasticity for liver registration [STR*11, SRD*11] have been mentioned in the section about hyperelastic models.

Finally, some tissues are purely viscous, for instance, fluids. **Viscous fluid models** can handle larger deformations than those covered by the previous models. However, they do not describe the behavior of solid organs accurately [LLF08]. The objects included in this section are usually modeled as incompressible Newtonian fluids. In those models the stress is composed of two terms. The first one, called *internal stress*, is the one generated by the fluid pressure. The second one is the *viscous stress tensor* and it is related to the rate of deformation change (strain rate). In Newtonian fluids the viscous stress tensor is a linear function of the strain rate tensor (E) as shown in the next equation. According to Fung [Fun93] the stress-strain relation for incompressible Newtonian fluids is given by

$$\sigma = -pI + 2 \cdot \mu E \tag{2.9}$$

with [MWTT98]

$$E = \frac{(\nabla u + \nabla u^T)}{2}. \tag{2.10}$$

p is the pressure, I is the identity tensor, μ is the viscosity of the fluid and ∇u the displacement gradient tensor. From Equation 2.9 and 2.2 one can get the well-known Navier-Stokes equations that describe the behavior of the model for the registration methods in this section:

$$\dot{u} + (u \cdot \nabla) u = \frac{\mu}{\rho} \Delta u - \frac{\nabla p}{\rho} + f. \tag{2.11}$$

Wang and Staib [WS00] propose a method based of viscous fluid models for registration of 2D heart, and brain MR images. The novelty of the proposed method is that they incorporate statistical shape information in the boundary points. Thus, the results are more realistic. To incorporate this information in the viscous fluid model a Bayesian framework is used. The method is tested and compared to a linear elastic method. The used brain MR images contain small deformations while the deformations observed in the heart images are much larger. As it would be expected, because of the size of deformations fluid models outperform in the heart images but not in the brain images. D'Agostino et al. [DMVS02] use viscous fluid models as regularizer for a normalized mutual information based registration. The force field is defined by the image gradients and calculated using Parzen windowing. During the registration, the jacobian is not allowed to take negative values to preserve the topology of the image. The registration method is evaluated in brain MR images and artificially deformed brain MR images obtaining subvoxel accuracy (the dimention of each voxel was 2 mm^3). Christensens et al. [CRM96] is often cited. They use the Navier-Stokes equations to register CT aquisitions of cervix cancer patients and carry out the qualitative evaluation in one brain MRI. However, the proposed method has a drawback that is always pointed out, namely, the computation time required. Noe et al. [NTL*08] fix this drawback by using a GPU implementation of that method. In this implementation the external forces are calculated so that the sum of squared differences is minimized. Another group that tried to find a solution to the computational cost of Christensens and colleagues' method is Chengcheng et al. [CJLG08]. They propose to

simplify the calculation of the velocity field derivatives by representing the velocities as B-splines. Lepore et al. [LCL*08] propose an intensity based method derived from the simulation method by Bro-Nielsen and Gramkow [BnG96] to register brain MRI. As it was done by Christensens et al. [CRM96] only qualitative evaluation is provided.

Diffusion models Diffusion models are governed by the diffusion equation:

$$\frac{\partial u}{\partial t} = \Delta u. \tag{2.12}$$

In this equation u represents the variable object of diffusion. For an object undergoing diffusion, this equation describes the changes in its density that depend on the flux (inflow and outflow) of the material. For image registration it is not the density but the intensity what is isotropically diffused.

The most widely used method in this group is Demons method. It was introduced by Thirion [Thi98] and has been adapted many times for different applications. An adaptation of this method is used by Erdt et al. [ESH*11] to register multiphase liver CT images. During the liver segmentation process, a series of corresponding landmarks are detected. This information is used to align both images. Afterward, the arterial phase CT is deformed toward the portal phase image using the adapted Demons method. Therefore, they add a penalization term to the speed of the points according to their distance to the boundary. The results obtained for 11 patients have been evaluated by radiologists who gave a mark of 1.72 to the method (being 1 the best possible mark). Several other groups have used Demons method in the log-domain. Siless et al. [SGG*12], for example, propose a method combination of image-based and geometric-based to register T1 and brain fiber bundles. Geometric demons represented in the space of currents allows detecting misalignments and shape differences between bundles. The results obtained with the proposed method are more accurate than those obtained using non-linear T1, tensor, and multi-modal T1 Fractional Anisotropy. Risser et al. [RHMS12] propose a method that can be considered a hybrid between diffusion and flows of diffeomorphisms models. They combine a mutual information based log-Demons method with a novel detection of sliding motions to register 3D CT and MR of the lung. To deal with the sliding motions they divide the images into two domains, namely, the thoracic cage and the rest, and they use the heat equation to diffuse the velocity field in each domain. Finally, the calculated velocity fields and mutual information are combined to get the final registration between the two volumes. Similar results than those obtained using free form deformations are achieved. Cifor et al. [CRC*12] enhance the diffeomorphic Log-Demons to register 2D ultrasound images of the liver for tumor tracking. They propose a so-called Block-Matching Log-Demons in which besides local image features obtained through intensity similarities between voxels, and similarities between the features observed in the images, they add some regional spatial correspondences between neighboring blocks. Therefore, they divide the image into regular blocks. During the registration process, intensity similarity is used as metric and the most similar blocks are matched. The algorithm has been quantitatively evaluated on 8 clinical datasets. The results given in terms of the Dice coefficient are 90.8% $\pm$ 5. Diffusion models have also been enhanced to consider sliding geometries that can be found between adjacent organs. Schmidt-Richberg

et al. [SREWH09, SRWHE12], for example, takes into account the physiological motion of the lung for their registration. Therefore, they divide the image into the object (the lung in this case) and the background. The regularization is done separately in the normal and tangential directions to allow sliding between the object and the background. The results show that direction-dependent regularization outperforms diffusive regularization. However, this work assumes that discontinuities only occur in the tangential direction, which is false for lobar fissures. Yin et al. [YHL10] propose to use both discontinuities by applying the regularization only inside the objects but not in the interface of adjacent organs. Simultaneously, they avoid gaps between adjacent organs and achieve an average organ internal accuracy of 1.25 mm. The discontinuities handled in the previous methods are at nearly planar interfaces. However, some structures present tubular geometries (e.g., intraoperative tools) that present also discontinuities. To solve this problem Pace et al. [PNA11] propose a geometry conditional registration. Therefore, they divide the regularization term into intra-organ smoothness and inter-organ coupling. The diffusion tensor that smooths in the direction of the normal will have one, two, or three components depending on the local geometry of the object: planar, tubular or point-like. An accuracy if 10.82 ± 28.72 mm is achieved.

Flows of diffeomorphisms The name of this category helps understand the characteristics of its methods. On the one side "flow" refers to the variation of the velocity over time. To model this, the Lagrangian transport equation is used. Generally speaking, a deformation can be modeled based on the displacements u that caused it $x' = x + u$. This can also be expressed in terms of velocity vector field as

$$x' = x + \int_0^1 v_t dt. \tag{2.13}$$

The term "diffeomorphisms", refers to the type of used transformations. They are smoothly invertible, which means that anatomical features will be preserved in presence of large deformations. The goal of these methods is to minimize the energy function

$$E(v) = \int_0^1 \|v_t\|_V^2 dt + \lambda \|I_0 \circ \varphi_1^{-1} - I_1\|_{L^2}^2. \tag{2.14}$$

The first energy term means that the registration method searches for the transformation that minimizes the velocity field (or displacements). The second term minimizes the error produced registering the target image I_1 with the current transformed image $I_0 \circ \varphi_1^{-1}$. The moving image I_0 is transformed by the transformation φ_1. V is the space of velocity fields and L^2 is the space of square integrable functions.

The non-stationary approach proposed by Beg et al. [BMTY05] is often used. This method is commonly known as "Large Deformation Diffeomorphic Metric Mapping" (LDDMM).

In this approach the registration is done at the endpoint and it is therefore non-symmetric as only one of the images contributes to the registration. To solve this problem, Beg and Khan [BK07] propose to use two additional terms. The first term is called Consistent-Integral-Cost and is inspired by landmark matching. With this term, the registration error

is not only measured at the endpoint but also at every point along the flow. The second term is the Consistent-Midpoint-Cost in which each image is in charge of driving half of the flow. Another problem of the original LDDMM method is its memory consumption. Zhang et al. [ZNSY12] propose a solution for this problem that is aggravated when registering diffusion-weighted images (DWI). They first carry out a reorientation of the DWI images by decomposing them into fiber basis functions. Then they apply to the reoriented images affine transformations. The final registration is carried out by a LDDMM whose memory consumption is simplified. For this last step, they use a geodesic shooting method [AF11] that avoids the storage of every velocity field in the series.

2.3.2.2. Interpolation-based

Not all the registration methods are governed by the laws of physics. Several methods use interpolation or approximation techniques to propagate displacements known at certain image locations to the complete domain. This taxon can be further subdivided in: radial basis functions, B-splines, and piecewise affine models.

Radial basis functions Radial basis functions $\varphi(\|x - c_i\|)$ have been widely used for medical image registration. Given a set of known control points c_i the goal of the approximation function $f(x)$, combination of N radial basis functions, is to approximate the value of an unknown point x

$$f(x) = \sum_{i=1}^{N} \omega_i \varphi(\|x - c_i\|). \tag{2.15}$$

The set of weights w_i is precomputed using the set of known correspondences and the conditions:

$$\sum_{i=1}^{N} x_i \omega_i = 0 \tag{2.16}$$

and

$$\sum_{i=1}^{N} \omega_i = 0. \tag{2.17}$$

The goal of these weights is to scale the radial basis functions. During the interpolation process (Figure 2.9 (a)), a series of radial basis functions are placed each centered at one control point c_i. Each radial basis function has a different influence on the final interpolated curve. Their influence is determined by the scaling factors w_i.

The interpolation based on radial basis functions has the characteristic that the set of control points are known and the spacing between them can be non-uniform.

Among all radial basis functions the most popular for image registration are thin plate splines (TPS) [Boo89],

$$\varphi(r) = r^2 \ln(r), \tag{2.18}$$

where $r = \|x - p\|$. According to Figure 2.9 (a), using TPS for the interpolation means that the curve shown in Figure 2.9 (b) would be placed at each control point. To understand how TPS deform an image one can imagine it as an endless thin steel plate. Given two sets of corresponding points $X = x_1, ..., x_n$ and $Y = y_1, ..., y_n$ the plate (image) will bend

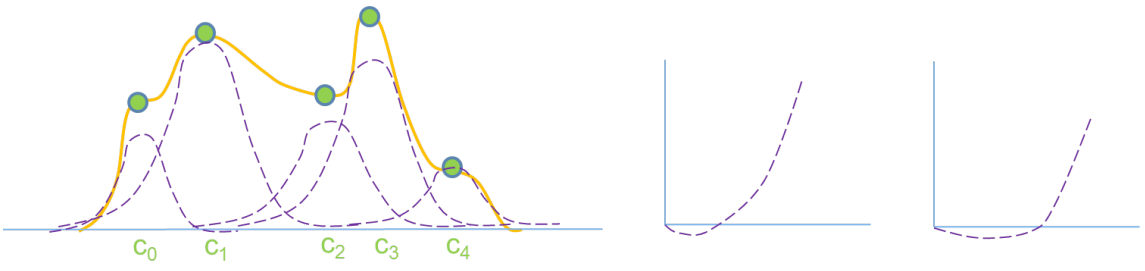

Figure 2.9.: Radial basis functions. (a) Interpolation: the interpolated curve (yellow) is obtained as linear combination of a series of radial basis functions (violet) centered in c_i and scaled by a factor ω_i. (b) Thin plate splines. (c) Elastic body splines.

influenced by the displacements of those points to match each other. The registration method minimizes the bending of the plate or in other words the total curvature of the plate [Kob98]:

$$E(S) = \int_S (\kappa_1^2 + \kappa_2^2) dS, \tag{2.19}$$

where κ_1 and κ_2 are the principal curvatures of the surface.

Thin plate splines have been broadly used for non-rigid registration of medical images. Rohr et al. [RFS99, RSS*01] use TPS to register 2D MR images of the brain. Statistical and geometric information is used to carry out the registration. The former one is achieved using an approximation scheme that deals with the uncertainties on the (semiautomatic) landmark selection. The latter is given by attributes that describe the orientation of the contour at the landmarks. This improves the registration in areas in which a rigid body is embedded in an elastic body according to the performed qualitative evaluation. Another organ in which TPS have been applied is the liver. Böttger et al. [BRS*03] propose to register abdominal 3D MR and CT in a two-step process. First the two volumes are rigidly registered using maximization of normalized mutual information. For the non-rigid registration TPS are used. They propose two ways to detect the control points that should drive the registration: one manual and one automatic. For the latter, they divide each volume in eight sub-volumes and rigidly register each pair of sub-volumes. The center of the sub-volumes will form the set of control points. After that, TPS are applied to the images and the process is repeated. An average mean square error of 15.7 mm is obtained after evaluation on two pairs of datasets. Noticing the limitations of TPS in the areas in which no landmarks are known, Lange et al. [LPH*09] propose a combination between landmark- and intensity-based registrations. They apply this method to the registration of 3D ultrasound and CT of the liver. The landmarks used to drive the registration are manually determined correspondences between the vessel trees of the liver. The method has been tested on three pairs of datasets obtaining an accuracy of 3 mm. More recently Keil et al. [KKOLW13] use the results of this thesis in another solution for ultrasound and CT registration of the liver. The novelty of their method is the introduction of automatically detected landmarks as control points for the registration. Therefore, a graph matching

method is used that finds correspondences between the vessel trees of the liver (See Chapter 4). Additional correspondences are detected to improve the accuracy of the results. The results show an improvement of 44 % using non-rigid registration over using rigid registration.

Elastic body splines (EBS) are splines built upon the physics of elastic body models. They take the form

$$\varphi(r) = [\alpha r^2 I - 3xx^T]r, \tag{2.20}$$

where I is the identity matrix and $\alpha = 12(1-\nu) - 1$ depends on the Poisson's ratio ν. Figure 2.9 (c) shows the shape of the spline that will be used for the interpolation in this case. As it was shown by Davis et al. [DKFH97], EBS have advantages (in terms of accuracy) over TPS in presence of a small number of control points. When the number of control points increases the accuracy of the results obtained with each spline will be similar. On the other side EBS are more computationally expensive than TPS.

The first authors introducing EBS for deformable registration were Davis et al. [DKFH97]. They propose to use as basis functions for the interpolation based registration method the analytical solutions of the Navier-Cauchy equations. The solutions are obtained after applying polynomial forces. Several groups have based their methods on this idea, enhancing it to work in their field of study. Kohlrausch et al. [KRS01] introduced a type of splines called Gaussian Elastic Body Splines based on the splines of Davis and colleagues. They apply an affine transformation to the images and use Gaussian forces instead of the previously proposed polynomial forces. The method has been used for the registration of 3D MR images of the brain showing to be more accurate than the previous one. Another group working on the registration (2D) of MR images of the brain is Wörz and Rohr. In their first work [WR06] they consider the uncertainties in the localization of landmarks using an approximation technique. Later [WR07], they enhance this using a combination between landmark and intensity information to drive the registration. This hybrid approach results in an improvement of the mean intensity error of 13 %. Gaussian elastic body splines are not exclusive for brain images. Lange et al. [LWRS09a] compare thin plate splines and gaussian elastic body splines to register preoperative and postoperative CT of the liver. In their approach they use two types of landmarks (branching and segment landmarks) extracted interactively from the liver vessels. The evaluation shows similar results using thin plate splines and gaussian elastic body splines.

B-splines B-splines B are univariate splines that have been widely used for medical image registration. Therefore, they are converted to multivariate functions

$$X(u,v) = \sum_{j=0}^{n} \sum_{i=0}^{m} B_i^m(u)\, B_j^n(v)\, P_{ij}, \tag{2.21}$$

through the spline tensor product that defines the deformation resulting from the popular free form deformation (FFD) transformation model. Free form deformations enclose the area to be deformed into a regular grid of control points, P_{ij} (also known as lattice). In 2D i and j are the indices of the control points, u and v are the local coordinates and n and m are the degrees of the B-splines. Note that in TPS and EBS the control points do

not need to be regularly spread. The set of control points have a similar goal as the set of weights in radial basis functions, namely, scaling each b-spline. As shown in Figure 2.10 (a), the set of control points form the control polygon approximated by the b-spline. Each interpolated segment is joined at the equally spaced knots u_i. Figure 2.10 (b) illustrates the interpolation process with a b-spline of order 1. The interpolation obtained using this b-spline is linear. Figure 2.10 (c) to (f) show the shape of b-splines of different orders. In order to obtain a smooth interpolation, cubic b-splines are often chosen. B-splines have the advantage over radial basis functions of being computationally more efficient [RSH*99]. Furthermore, the spacing of the regular lattice can be chosen to fulfill registration requirements: large spacing to cover global deformations and small spacing for local deformations.

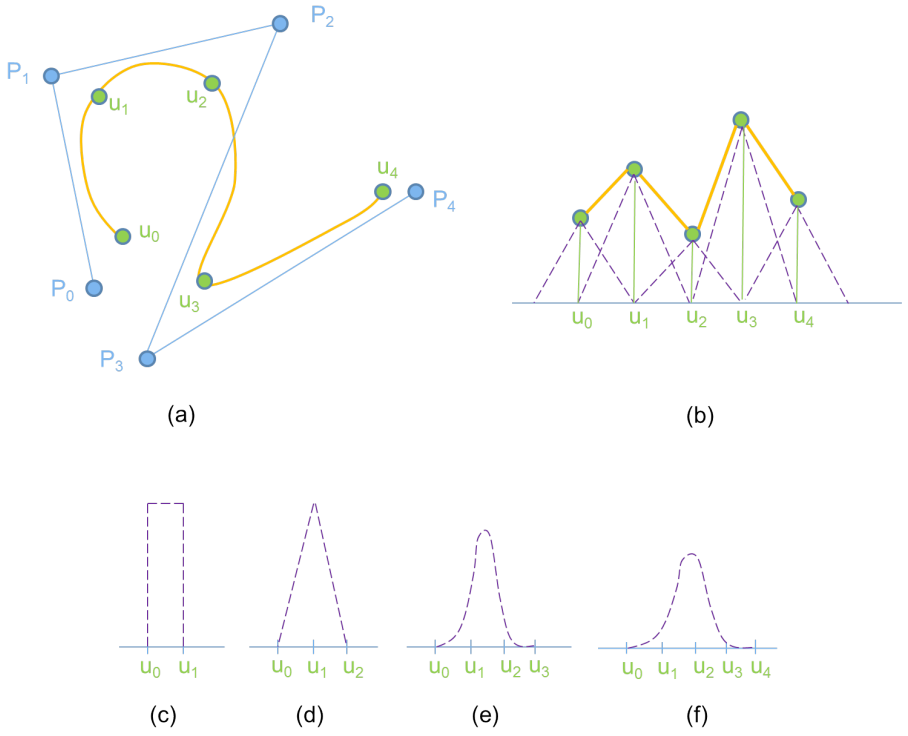

Figure 2.10.: (a) Interpolation with b-splines. The spline approximates a control polygon. (b) Linear interpolation using B-splines. (c) to (f) B-splines curves with increasing orders.

Rueckert et al. [RSH*99] use a combination between affine transformations and free form deformations to register 3D breast MR images. Affine transformations take care of the global motion of the breast and free form deformations of the local one. They propose to hierarchically carry out the registration to reduce the computational cost of the method. Their goal is to register pre-contrast enhanced MR images with post contrast enhanced images. Thus, they use normalized mutual information as similarity criterion for the registration. The algorithm has been evaluated on clinical data obtaining an accuracy in terms of the correlation coefficient of 0.8978. Mattes et al. [MHV*03] use free form deformations to register positron emission tomography (PET) and CT chest images. They do this through the registration of a transmission image aligned to the PET im-

age. In this case the global deformation is handled through a rigid registration and the local one through a free form deformation with cubic b-spline basis and mutual information. To reduce the computational cost they propose a multiresolution approach based on a limited-memory quasi-Newton optimization technique. Only qualitative evaluation has been provided. Several authors have based their work on the previously mentioned two methods. Loeckx et al. [LMVS04] enhance the method proposed by Rueckert and colleagues to handle local rigidities in the images. Therefore, they add a new penalty term to the cost function that ensures the local rigidity at specific locations by forcing the Jacobian matrix to be orthogonal. This effect should not affect in the same way to the complete image. Hence, a weight factor is added to control the amount of rigidity introduced according to the tissue type under study. The method has been applied to the registration of computed tomography angiographies and full body PETs but the results have only been visually evaluated. Other authors that based their work on the methods of Rueckert and colleagues, Mattes and colleagues, and Thévenaz and Unser [TU00] are Klein et al. [KSP07]. They focus their work on the optimization methods. Their experiments on CT scans of heart and chest, and on MR scans of the prostate show that depending on the application Robins-Monro method (in most cases), quasi-Newton method, or nonlinear conjugate gradient are the best choice. More recently Serag et al. [SAC*12] use the method by Rueckert and colleagues for longitudinal MR registration in brain development of infants. Therefore, they use spatio-temporal atlases that give prior information on missing anatomical structures between different acquisitions. The evaluation results vary between a Dice coefficient of 0.83 ± 0.05 and 0.95 ± 0.01 for different structures of the human brain. Shi et al. [SZP*12] introduce the concept of sparsity into free-form deformation methods. Their goal by doing that is to handle discontinuous motion in the images. Sparsity is included to automatically determine the control point spacing in multilevel free form deformations in the parametric space. The results in 2D and 3D MR of the heart show the improvement caused by sparse free-form deformations where discontinuous motions are.

Piecewise affine models Piecewise affine models divide the image into several parts. Each part is then registered using affine deformations. Erdt et al. [ESW12] use a patch-based approach to register Magnitude Diffusion Weighted Magnetic Resonance Imaging. The image is first divided in patches of different sizes. The patches that contain enough information are registered using the patch based registration of Söhn et al [SBC*08]. For the rest of the patches, the peakness of the metric gradient (the product of the eigenvalues of the Hessian matrix) is used as normalized quality measure. The method has been tested on 10 datasets of the abdomen resulting in an overlapping error of 8.21%. Commowick et al. [CWDP12] introduce an approach for patch-matching to solve the problems that arise when large rotation differences between the images exist. Therefore, they carry out a search over the local rigid-body transformations. The global rigid-body transformation will then be calculated from the local ones. To carry out the matching they propose to use the NEWUOA [WDYPB07] optimization technique. The method has been quantitatively evaluated in one pair of brain MRI datasets obtaining an accuracy of 0.12 ± 0.16. Piecewise rigid registrations have also been used for the registration of articulated objects

that suffer large rigid deformations, for example, bony structures. To solve for those deformations Smeets et al. [SKH*12] propose a two-step method in which first a series of key points are localized and matched in the images using Scale Invariant Feature Transform. Then, all the rigid motions are clustered using the mean shift clustering technique. The method has been evaluated on 2D knee fluoroscopy images. However, it can be used for n-D images. The accuracy of the results consists of a mean angular error of 0.39° and a mean translational error of 6.65 pixels.

2.4. Matching

As previously mentioned, features are often used as references during the registration process: during initialization, during registration, or in both. Although salient structures are frequently used for the initialization process (e.g., the chin [SK10]), the number of needed landmarks for deformable registration is high. This will allow a higher accuracy in the complete registered image.

Once the features have been detected and the landmarks extracted, correspondences between landmarks in different datasets have to be determined. Traditionally, either point cloud or graph matching methods have been used [Pin13] for that purpose. Point cloud matching methods contain well-known approaches like thin plate splines [ZCL13], coherent point drift [HRM*10], or ICP [EKB*12]. Despite the general interest of point cloud based matching for some applications, this thesis focuses on the matching of vessel-like structures. Using point clouds instead of graphs in this case would mean: not to take advantage of the topology of the vessel trees during the matching process. This would only increase the inherent difficulties of vessel tree matching. Thus, this chapter will focus on graph matching methods. The interested reader can find additional information about point cloud matching in [Pin13].

General concepts Given a set of V vertices (or nodes) and a set of E edges a **graph** is defined as $G = (V, E)$ where every edge $e \in E$ consist of a pair of vertices $(v_1, v_2) \in V$. One possible counterpart of vertices and edges in a graph representation of a vascular tree, for example, are the bifurcations and the vessel fractions between two bifurcations.

The graph is called **labeled**, $G = (V, E, l)$, if its nodes and/or edges are identified with a name, for example, the name of the anatomical structure they belong, and it is known as **attributed**, $G = (V, E, a)$, if its nodes and/or edges contain additional information, for instance, information of the structure's shape. These characteristics of the graph are widely used in medical imaging. Labeling of graphs is used to classify anatomical structures; attributes on the other side, are used to find similarities between two structures to be matched.

A graph that does not contain loops is known as **acyclic graph** or just **tree** (within this thesis the term tree will be used). If possible, using trees instead of graphs reduces the computational complexity of matching methods. Indeed, most state of the art methods that match vascular structures represent them as trees. A graph can be either **directed** or **undirected** depending on whether its edges have a direction. In a directed graph **parent** nodes are those from which other nodes derive. The latter are known as **children** of the

parent node. The **degree** of a node determines the number of children it has. A node that has not a parent is the **root** of the graph and the graph containing a root is known as **rooted graph**. The graph is **planted** if the root has degree 1. The end nodes with no children (degree 0) are the **leaves** of the graph. A **path** in the graph is a vector (v_1, v_2...v_n) that contains all the intermediate vertices traversed to connect two vertices, v_1 and v_n. In a tree there is only one possible path between two vertices, while in a graph there can be several possible paths. In this case the **shortest possible path** is defined as the path that contains the smallest number of vertices.

A **graph matching** method searches for similar nodes or edges in two graphs. Each found pair of nodes/edges is known as correspondence or **match**. Graph matching methods can be classified according to the type of pairings that they search for (Figure 2.11). Let's define two graphs G_1 and G_2. A graph matching method is **injective** when different nodes in G_1 cannot share a match in G_2, which means that many-to-one correspondences are not allowed. On the contrary, if every node in G_2 has at least one match in G_1 then the method is called **surjective**. If both conditions hold, the method is **bijective**. In this case each node in G_1 is matched to exactly one node in G_2. This requires that both graphs contain the same number of nodes. In other cases the goal is not to find one-to-one correspondences but many-to-many. When the two graphs to be matched contain different number of vertices, usual in medical imaging, the method will be **non-bijective**. Occasionally, the nodes that have no correspondences will be matched to **dummy** vertices.

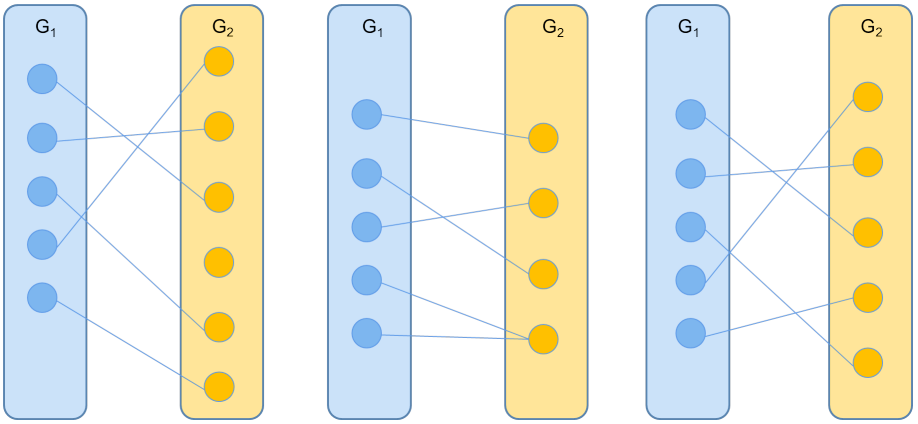

Figure 2.11.: Examples of injective, surjective, and bijective mapping.

An important concept of graph matching methods is **graph isomorphism**. Two graphs are isomorphic when there exists a bijective mapping between them. When the topological structure of the trees is also kept the match is called **homeomorphic**. Both concepts can be extended to subgraphs. If the vertices of a graph g_1 are a subset of the vertices of a graph G_1, $g_1 \subseteq G_1$, and g_1 contains all edges that connect those vertices then g_1 is called induced subgraph (of G_1). In this case the mapping is called **subgraph isomorphism**. Finally, the **maximum common subgraph** is the largest (in terms of number of nodes) possible common subgraph of two graphs.

In medical applications some factors have to be considered for the selection of an appropriate matching method, for example, artifacts. Under those circumstances, the

Bunke (2000)	Bengoetxea (2002)	Conte (2004)	Oyarzun Laura
TS		TS	TS
PR	PT	CO	PT
NN	NN	Other	NN
GA	GA	Other	EA
LP			
A			
	DT		
	CT		
		SM	SM
		Other	BM
			EGM

Table 2.1.: Comparison of the taxonomies used by other authors. The taxonomy presented in this thesis is specially thought for medical imaging applications. Acronyms stand for: Tree search (TS), Probabilistic relaxation (PR), Probability theory (PT), Continuous optimization (CO), Neural networks (NN), Genetic algorithms (GA), Evolutionary algorithms (EA), Linear programming (LP), Application(A), Decision trees (DT), Clustering techniques (CT), Spectral methods (SM), Bipartite matching (BM) and Elastic graph matching (EGM). Conte et al. [CFSV04] includes the taxa NN, GA, and BM in "others".

bijective constraint is too strong and it has to be softened to be more tolerant to some errors or differences between the graphs. Taking this into account graph matching methods can be **exact** when both graphs are identical, or **inexact** when they contain differences. Besides, the graphs representing anatomical structures do not necessarily share the orientation because of different body position during image acquisition. A graph matching method that does not require an initialization to return correct results is known as **pose-independent**.

Taxonomy The field of graph matching has been widely studied in the last decades. The classification schemes used by some authors are summarized in Table 2.1. The one who differs the most (excluded in the table) is Wu [Wu10] who classifies graph matching methods according to the similarity metric they use. Such a classification can also be found in Gallagher [Gal06]. However, most methods contained in his classification are exact matching methods, thus, not suitable for medical imaging purposes.

Most authors consider that the taxa "tree search" and "probabilistic relaxation" have to be included in every classification scheme. Nevertheless, nowadays other branches of probability theory have been used for matching purposes. That is the reason for Bengoetxea [Ben02] and Conte et al. [CFSV04] to change the name of the taxa to probability theory and continuous optimization respectively. Neural networks and genetic algorithms are also common to every review paper. Finally, some review papers focus on methods designed to solve a specific application. Rahm and Bernstein [RB01] review methods for automatic schema matching and Fan [Fan12] does it for social network analysis.

However, there is no survey paper dedicated to graph matching methods for medical imaging. In this chapter this gap is filled. In most medical applications exact match-

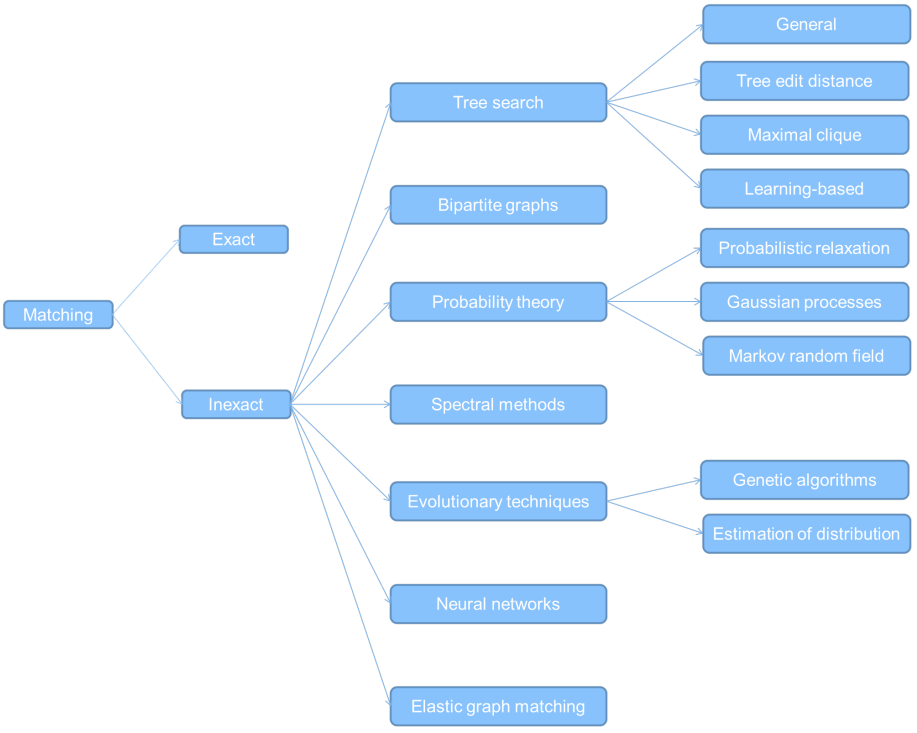

Figure 2.12.: Taxonomy of graph matching methods.

ing methods will not be flexible enough to provide accurate results. Nevertheless, this thesis includes the few exceptions and divides the methods as exact and inexact as Bengoetxea [Ben02] and Conte et al. [CFSV04] did before. Bengoetxea considers some graph matching techniques that do not have a big repercussion in medical imaging, for instance, clustering techniques. Conte and colleagues on the other side grouped many methods in a taxon called "other techniques". This taxon contains interesting approaches like evolutionary techniques or spectral methods.

The taxonomy in this thesis is a combination between both, removing those taxa not relevant to medical imaging applications. Figure 2.12 shows a diagram of the taxonomy. Most methods developed for graph matching in medical imaging belong to the taxa "tree search" and "probability theory". However, new methods are developed using evolutionary techniques like estimation of distribution algorithms or genetic algorithms. Neural networks and elastic graph matching methods are not so often used for medical imaging but are included in the taxonomy for completeness.

There are two aspects that will be focus of discussion in this thesis:

- Does the method find correspondences between graphs or trees?
- Are the trees/graphs rooted? In other words, is a preselection of roots necessary?

2.4.1. Exact

The concepts of graph isomorphism, bijective matching, and maximum common subgraph are the basis for exact matching methods. As previously mentioned, exact match-

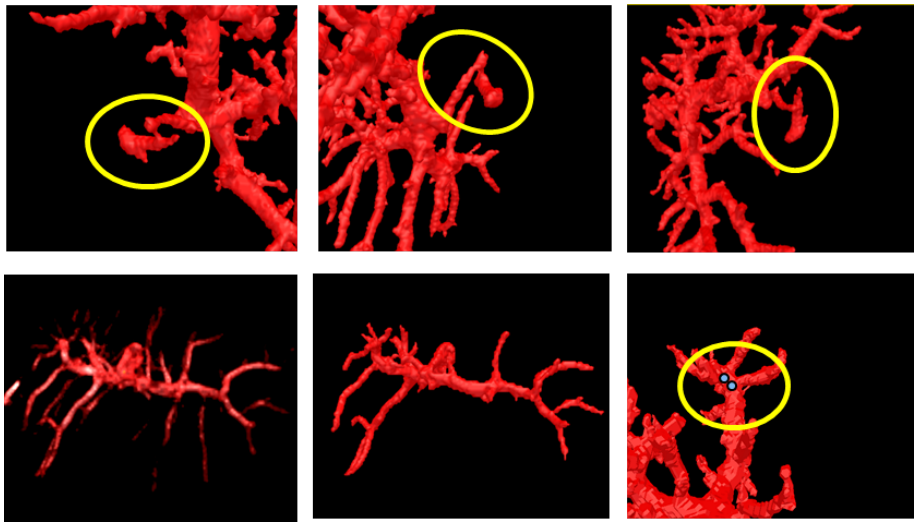

Figure 2.13.: Errors of segmentation or graph generation methods are some reasons for inexact matching methods to be needed in medical applications.

ing methods are not flexible enough to deal with the differences between trees that occur in medical imaging problems.

One of the few authors that present an exact matching method for medical imaging is Tsui et al. [TFV*13]. They search for correspondences between cortical surfaces. They can use an exact method because landmarks (at same locations) are selected by the medical doctors in every surface. Conformal transformations are used to map each surface.

2.4.2. Inexact

Although exact matching methods can be used for a few applications, in medical imaging the graphs tend to differ because of several factors, for example, noise. Figure 2.13 shows some examples in which unexpected structures in the vasculature system of the liver will result in inaccuracies in the underlying graph. The top images show some artifacts (yellow circle) that appear connected to the vasculature. The images in the bottom row show that depending on the used segmentation method more or less vessels will be visible. Finally, in the right most bottom image some graph generation method will detect two quite close nodes while other will find only one. Thus, the topology of the graphs varies from the real structure that they represent. In the following subsections state of the art methods able to deal with those inaccuracies are presented and discussed.

The usual way to find correspondences between two graphs is to use a similarity metric that determines the likelihood of two nodes to correspond. The choice of the metric is of high importance and will be responsible for the accuracy of the results. On the other side, depending on the metric used, the method will be more or less tolerant to pose changes. Figure 2.14 summarizes the similarity metrics used by state of the art authors cited throughout this subsection. The reader is encouraged to come back to that figure for a better understanding on the introduced methods.

2.4.2.1. Tree search

The methods in this group iterate through the complete graph adding new matches to the list of correspondences. A new pair of correspondences is added to the list if the value of the similarity resulting from its addition is above a certain threshold. Some methods presented in this section can be further subdivided into: tree edit distance, maximum clique and learning based. The methods that do not belong to any of those subdivisions will be included in the "General" group.

General Charnoz et al. [CAM*05b, CAM*05a] work on a series of hypothesis to find the best possible matches between liver vessel trees. Each hypothesis constitutes a combination of correspondences and has an associated cost. Starting from a known root, all out-edges are analyzed in search of the best combination of matches. The hypothesis chosen is then part of the final solution. The next depth level of the graph is analyzed and new sets of hypothesis are generated. This process is repeated until the whole tree is analyzed. The method has been tested on one clinical dataset and several artificially deformed ones. The evaluation shows that 95 % of the matches were detected, nevertheless, no information is provided about the percentage of errors. Nam et al. [NKL*12] introduce a method to register preoperative CT and intraoperative US of the liver using an edge matching method. The novelty of their approach is that it does not require an initialization of the images. Therefore, they carry out the matching method by using pose-independent metrics for the similarity calculation. These metrics are then introduced in a cost function that with an adapted Viterbi method provides as result the searched solution. The final registration is carried out using ICP method in which the surface of the liver is also considered. The accuracy of the matching method is only indirectly evaluated in terms of the registration accuracy (3 mm distance between fiducial points).

Another author that used such a method to find correspondences between human airways and liver vasculatures is dos Santos et al. [dSGMMH10]. They build up a matrix that contains topological and anatomical similarity scores. The former are determined by the similarity of the neighbors of the node under study. The latter is given by the similarity of certain properties, for example, diameter of the branches. This cost matrix will be maximized to solve the assignment problem using Munkres's algorithm [BL71]. After that, a pruning of the results is carried out to remove wrong matches. The results of the assignment are 3 % of false matches and 37 % of missing matches. The presented method is pose independent.

Lohe et al. [LKZ*08] introduce a hierarchical tree search method to find correspondences between human airways. First, they remove spurious branches and cycles. Then, the method proceeds hierarchically starting from the root and uses certain similarity metrics to find the correct matches (Figure 2.14). The method has been evaluated on 11 patients (human and pigs) and in two organs (lung and liver) giving an error rate of 19.1 % of the matches. Bülow et al. [BLWH06] propose another method for labeling human bronchial trees. They use the centerline points to avoid inaccuracies in the graph generation due to noise and low resolution. Two metrics are selected for the matching: the 3D shape context of the centerline points and their statistical moments. Then, the results obtained with both metrics are compared: 69% of successful matches with the former over

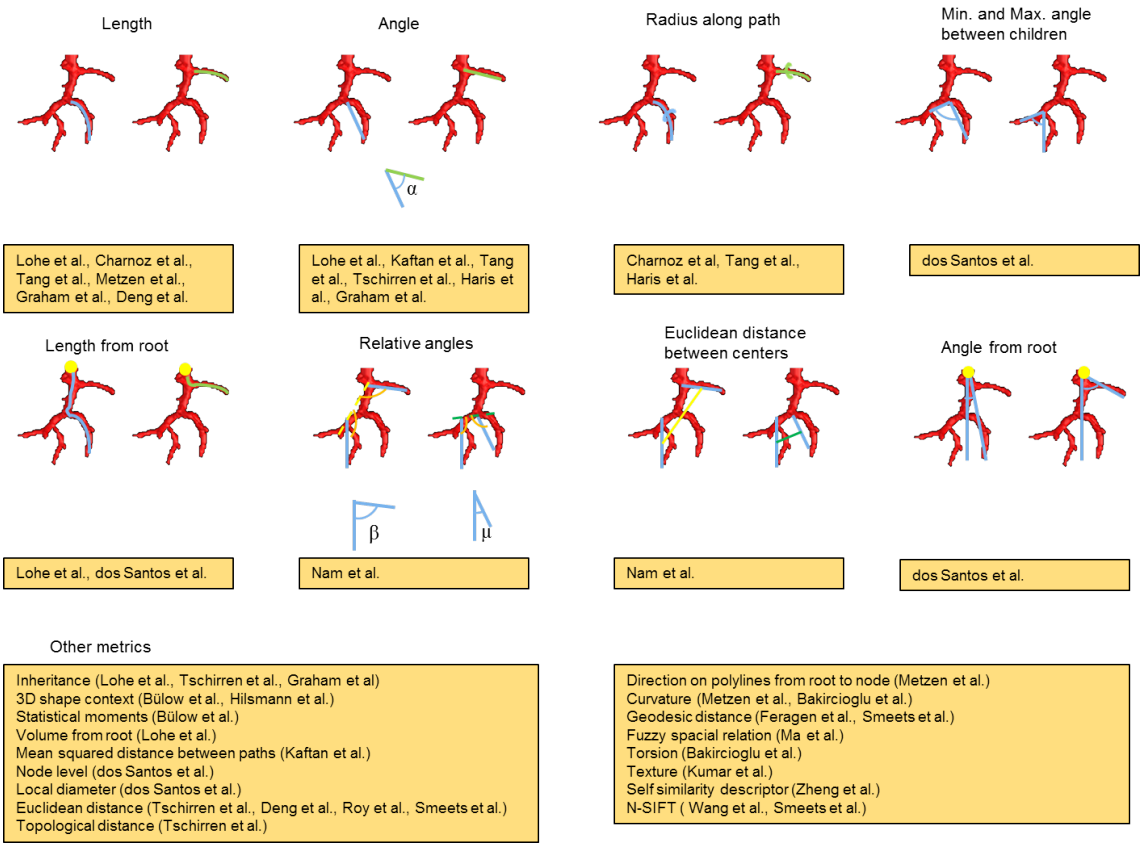

Figure 2.14.: Metrics used to calculate the similarity between nodes/edges by the authors cited in the state of the art section.

40% with the latter. This method has been reused by Hilsmann et al. [HVK*07] to register lung 4D CT of cancer patients. They chose to use only the 3D shape context as metric for the matching. They evaluate the method on datasets obtained from 10 patients. The matching method is again evaluated in terms of the registration accuracy (2.85 ± 2.11 mm).

Most authors try to find correspondences between edges or vertices. However, Kaftan et al. [KKNN06] match complete paths. They assume to have directed graphs previously aligned using the trachea and main bronchis as landmarks. These graphs may contain loops but this is solved by considering complete paths (without loops). They store all the calculated path-to-path similarities in a probability matrix that will favor those matches with a low similarity value constraint by a tolerance parameter. This way they ensure one-to-one matching. After evaluation of the method in 10 pairs of human airway trees, they show to have an error rate of 13% of the paths.

Tree edit distance Tree edit distance has been used for graph matching purposes for a long time. The goal of those methods is to find the minimum number of changes that have to be done to one of the graphs to be as similar as possible to the other graph.

Tang and Chung [TC06] developed a method to match cerebral vascular trees based on tree edit distances. The goal of the method is to match vascular trees of different pa-

tients to better determine the location of intracranial aneurysms. Therefore, the vascular trees are extracted from three-dimensional rotational angiographies. Then, a so-called theoretical tree is generated that contains information about the length, orientation and radii of the branches to be matched. To carry out the matching between two theoretical trees they calculate the tree edit distance using the method by Shasha et al. [SWZS94]. This method is prone to get stuck into local minima. Hence, the method is applied several times and the best result is kept. The authors note that the detection of the root is done automatically at the point at which the carotid artery and the image bounding box intersect. The work presented does not contain quantitative evaluation.

Maximum clique Another important concept of graph matching is the maximum clique. Figure 2.15 will clarify the following definitions. A clique of a graph *G* is a subgraph g $\subseteq$ G which edges connect every pair of vertices in *g*. Figure 2.15 (b) shows some cliques of a graph colored in yellow (3-clique), red (4-clique) and green (2-clique). Note that the 4-clique can be divided in additional 3-cliques. The maximum clique is the clique with the maximum number of vertices (Figure 2.15 (c)) and a clique which is not contained in any larger clique is called maximal clique. The three cliques marked in Figure 2.15 (d) are maximal cliques. However, the 3-cliques contained in the 4-clique cannot be considered maximal cliques as they are part of a larger clique. The search of maximum cliques has been widely used for graph matching purposes. Therefore, an association graph is generated. This graph contains a vertex for each possible pair of corresponding vertices. The vertices of the association graph are connected by an edge only if this relation exists in both graphs. The detection of the maximum clique contained in the association graph is the solution for the graph matching problem.

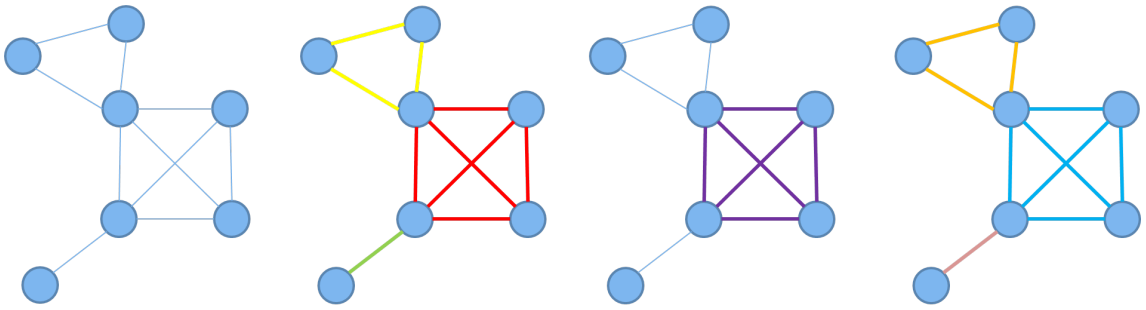

Figure 2.15.: (a) A graph. (b) Some of the cliques included in the graph: yellow (3-clique), red (4-clique) and green (2-clique). (c) Maximum clique. (d) Maximal cliques.

This approach has been chosen by Tschirren et al. [TMP*05] for anatomical labeling of the human airway. First, an initial pruning occurs to remove spurious branches that could lead to false matches. Then, the two trees are rigidly registered employing: the roots, the carina and main bronchi. The matching problem is divided into subproblems: first the major branchpoints are matched, then correspondences between the remaining subtrees are found. The method is efficient (1-3 seconds for trees containing up to 300 nodes) and

its error rate is 7.1 %.

Maximum cliques have also been applied to match liver trees. Metzen et al. [MKS*07] enhanced the method by Pelillo et al. [PSZ99] to work on the liver vasculature. Therefore, they defined additional constraints that the association graph should fulfill: unary constraints for its nodes and binary for its edges. The unary constraints measure the similarity of the paths in the trees. The binary constraints are determined by the lengths and curvatures of their branches. They evaluated the method in one pair of liver trees and one pair of bronchi trees. The mean runtime of the method was 288.29 seconds. The set of manually determined ground truth matches contained 34 matches. The mean number of correct and wrong matches according to the ground truth is 19 and 2 respectively. No information is given about the accuracy of the remaining matches. Ma et al. [MBB08] use an association graph based matching to detect tumors in mammograms. They use as similarity metrics the fuzzy spatial relations between the vertices and the breast boundaries. Thus, they avoid the need for an initial alignment of the mammograms. Finally, they use the backtracking method by Ullmann [Ull76] to find the correspondences. The authors of the paper classified 63.5 % of the matches as good matches by visual inspection.

Haris et al. [HEM*99] use maximal cliques instead of maximum cliques for labeling of coronary angiograms. First, a model of the coronary artery tree from a healthy heart is built. The generated 3D model is projected into the 2D space to show the same perspective of the angiogram. Two graphs are generated which nodes and edges represent arteries and parent-child relations between different arteries respectively. Finally, an association graph is generated and the maximal clique with the highest cost is chosen as the final solution. According to the opinion of expert cardiologists, the method results in 78.7 % of correct labels.

Learning-based approaches Those methods are based on the observation of several datasets from which a model can be generated.

Graham and Higgins [GH06a, GH06b] define a series of so-called primitives to handle the differences that can be frequently found among vascular trees (Figure 2.13), for instance, missing branches. Those primitives determine the set of valid matches. In addition to this a similarity measure is used that will favor similar lengths, parallel branches and parsimonious matches. Using all this information a tree search based method is applied to find the best global optimal set of matches between both trees. The method has been visually evaluated in 4 patients. The runtime of the method is 5 seconds to match trees with 341 and 131 nodes respectively.

Another method that belongs to this group is that by Feragen et al. [FPO*12]. They construct a tree space with 40 airway trees manually labeled by two experts. For every new tree, labels are assigned and the shortest path distance is computed. A hierarchical labeling is used to reduce the number of iterations. This approach uses the centerline geodesic distances as similarity metric. To avoid problems because of interpatient variability the trees are first scaled. The method has been tested in 19 patients obtaining an average of 83% of correctly labeled branches.

2.4.2.2. Bipartite graph matching

A graph that contains two disjoint sets of vertices is called bipartite graph. Every edge in this graph connects vertices belonging to different sets. This is illustrated in Figure 2.16. Matching methods based on bipartite graph matching find the set of connection edges between both sets of vertices.

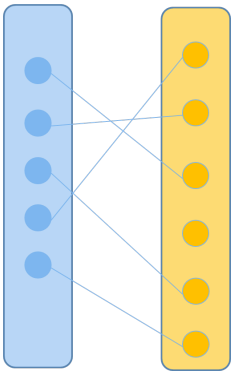

Figure 2.16.: Bipartite graph. The task of a graph matching method in this case is to find correspondences between the two disjoint sets.

Brain surfaces have been matched using bipartite graph matching by Bakircioğlu et al. [BGKM98]. Their goal is to study the variability of the human sulcus and its fissures. Therefore, they extract the fundus curves and define the distances between each pair of curves using Frenet equations. After sampling the curves to be matched, they have a set of points that lay on one curve and another set of points on the other curve. The bipartite graph matching [Sed83] finds the solution that minimizes a cost function determined by the speed, curvature and torsion of the curves. Only qualitative evaluation is provided.

Bipartite graph matching is used for another organ that has been focused of research in the last years, namely, the breast. Kumar et al. [KSG01] propose to use a weighted bipartite graph matching to find correspondences between mammograms. A weight is assigned to every edge connecting two nodes according to their similarity in a feature space. They combine the results given by the Hungarian minimum weight matching algorithm and the greedy algorithm introduced by Sallam and Bowyer [SB94]. Only those matches common to both algorithms are kept. Furthermore, they restrict the search of matches to a certain radius around the node to reduce multiple minima. The error rate of the hybrid method (3.14%) is lower than that of the two independent algorithms (7.91 % of incorrect matches with the Greedy algorithm and 10.14% with the Hungarian algorithm). The disadvantage of the presented method is that the number of detected matches is reduced in 8.6%.

2.4.2.3. Probability theory

This taxon contains graph matching methods that use concepts of probability theory to find the correct correspondences.

Probabilistic relaxation To this group belong methods that solve the matching problem in the continuous domain and translate then the results to the discrete domain. An advantage of those methods is that they are computationally more efficient although they have the risk of getting stuck into local minima.

The weighted graph matching problem is solved by minimizing the cost function [GR96]:

$$E(M) = -\frac{1}{2}\sum_{a=1}^{A}\sum_{i=1}^{I}\sum_{b=1}^{A}\sum_{j=1}^{I} M_{ai}M_{bj}C_{aibj}. \tag{2.22}$$

At this point, it is necessary to introduce some concepts often used in these methods. The first one is the assignment matrix M. If G_1 contains n vertices and G_2 m, M will be a *nxm* size matrix. Every element of M is assigned a value that represents how similar two vertices are. Several metrics can be used to determine the similarity between two vertices, for example, difference between the topological distances or radius. C is the compatibility matrix that determines which vertices can be matched and depends on the adjacency matrices of both graphs. In the general case, M will be assigned uniquely a 0 (non-similar) or a 1 (similar). This will lead to local minima. To solve this, the discrete optimization problem is converted into a continuous one using soft assign techniques. Therefore, the components of M will have values in the interval $m_j \in [0, 1]$:

$$m_j = \frac{\exp(\beta X_j)}{\sum_{i=1}^{I}\exp(\beta X_i)}. \tag{2.23}$$

The control parameter β is used to formulate the problem as continuous. As β keeps growing, the components of M that correspond to an assignment will approach the value of 1, and the others will get closer to 0. Another important characteristic of the method is that it ensures the two-way assignment by using the soft assign method by Sinkhorn [Sin64].

The graduated assignment method developed by Gold and Rangarajan [GR96] has been adapted several times for medical image applications. Deng et al. [DTZ*10] adapts the method to work with 2D retinal fundus images. Their goal is to register those images for a better disease diagnosis and treatment. After generating undirected graphs from the retinal vessels, two measures are assigned to each edge: the euclidean distance between the starting and end points of the edge and its vessel path distance. Compatibility and assignment matrices are built up and an objective quadratic function is minimized. The method returns several false matches (up to 80%) that are corrected with a local structure-based sample consensus method. Groher et al. [GZN09] uses the method by Gold and Rangarajan to find correspondences between 2D and 3D angiography scans. The graph matching step is done after projection of the 3D angiography graph into the 2D space. Then the matching method is applied and the 3D graph is deformed to fulfill certain conditions. The whole process is repeated several times until the desired deformation is reached. The accuracy of the method in terms of registration error is 3.8 cm.

Chui and Rangarajan [CR00] combines soft assign and deterministic annealing techniques with thin plate splines to register human brain sulci. The method iteratively finds correspondences and deforms the images until an energy function is minimized. They do

not guarantee to achieve a global optimal solution. The proposed method was compared with the conventional ICP outperforming the former one in all experiments. This method has also been used along with bipartite graph matching by Roy et al. [RPD09] to label the bronchial tree. Zheng et al. [ZIW*11] solve the problem of local minima with a method able to find simultaneously the proper correspondences and transformation using combinatorial optimization techniques. They test the method in 19 pairs of retinal images. In this kind of images the rotation observed between different acquisitions can be large. Thus, they develop a rotation invariant self-similarity descriptor. An accuracy of 1.2 ± 0.7 mm is achieved.

Gaussian processes Probabilistic relaxation is an established method for graph matching contemplated in most of proposed taxonomies. Nevertheless, nowadays other concepts of probability theory are also used for matching purposes, for example, Gaussian processes. Gaussian processes or in other words Gaussian random fields consist of a set of random variables distributed with a Gaussian distribution. Because of this reason, they are determined by their mean and covariance functions. Gaussian processes are often used to predict the value of unknown variables given a set of variables. Serradell et al. [SKMNF12] find a set of initial matches using a kalman-like scheme and affine transformations. Then, they introduce elastic graph matching concept to increase the set of correspondences. Therefore, Gaussian processes are used to model the deformations on the graphs. A branch-and-bound solver is used to find a set of edge matches consistent with the initial set of matches. The method is applied to find correspondences among retinal fundus vascular trees, X-ray angiographies, and 3D brain vascular trees. However, the proposed method cannot handle arbitrary and large deformations. Thus, Serradell et al. [SGK*12] introduce an approach based on non-linear regression to find correspondences among retinal fundus images, angiographies, and neuronal image stacks. The method selects two pairs of random matches. Then, it predicts the position (mean and variance) of the vertex in G_2 correspondent to a certain vertex in G_1. Between all the nodes that fulfill the estimation they choose a random one, and proceed. The method is repeated for every possible initial pairs of correspondences. Thus, the method is pose independent but slow (500 seconds for graphs with up to 100 nodes). However, they do not use any topological or geometrical similarity measures to carry out the matching, which makes the method prone to local minima. Pinheiro et al. [PSS*13b] enhanced the previous method. They divide the matching process into two steps. The so called active testing search does a coarse matching between a reduced number of selected points. Therefore, besides the non-linear regression introduced by Serradell et al. [SGK*12] they use a Bayesian model to find the correspondences. The final step is a fine alignment to increase the number of correspondences. The evaluation shows the algorithm to be faster than the one proposed by Serradell and colleagues.

Markov random fields Markov random fields are cyclic and undirected graphs. The nodes of those graphs are random variables with a Boltzman probability distribution. Each node has the property that the probability of a match given all possible matches is the same that its probability considering only the neighboring matches. The widely used

Ising model is a markov random field. It describes the interaction between magnetic spins [KS80].

Wang et al. [WPU*12] introduce a probabilistic graph matching method to register supine and prone computer tomographic colonographies. They present an iterative approach in which the most prominent matches are found first. They use the Ising model and mean field theory as computational method to simplify the calculations:

$$p(m) = \frac{\rho(m)}{Z(w,Q)} exp\left[\sum_{i<j} m_i Q_{ij} m_j + \sum_i w_i m_i\right]. \tag{2.24}$$

This equation returns the probability of a match given its neighboring matches. The probability function has the form of the normalized Boltzman probability distribution. In this equation m is the correspondence matrix, Q is the compatibility matrix and w is the similarity matrix. Thus, according to this probability function the probability of a match will be influenced by the similarity and compatibility matrices. On the other side ρ will ensure that all constraints are fulfilled, for example, that m is composed by discrete values. $Z(w,Q)$ is in charge of the normalization of the probability distribution. In the first iteration the problem is considered a one-to-many matching problem. Once the most prominent correspondences are determined, the one-to-one constraint is added by adapting w_i so those matches are favored. Thus, initially found matches are used as guidance in the next iterations of the method. The evaluation shows that the method increase accuracy against spectral methods (Section 2.4.2.4).

Ou et al. [OBB*10] find correspondences between brain images. A novelty that this method introduces is that instead of detecting the landmarks independently for each image to be registered (as usually done) they detect the landmarks pair-by-pair using a mutual-saliency measure. The result of the landmark detection is a set of possible not globally optimal correspondences. To solve this they generate a graph (Markov random field) and minimize a cost function that contains information about the location of each point pairs. Quantitative evaluation of the method is not provided. Hampshire et al. [HRH*11, HRH*13] have also used this kind of approach to find corresponding haustral folds between images taken in prone and supine positions. In this case the maximum a posteriori estimate is used to determine what is the best labeling for the folds. The matching process results in 102.5 haustral fold matches per case.

2.4.2.4. Spectral methods

The eigenvalues and eigenvectors of the adjacency matrices are invariant against node permutations. This is the basis for spectral methods. This means that two graphs will only be isomorphic if the eigenvalues and eigenvectors are the same [CFSV04]. The goal of these methods is to find the permutation matrix that returns the correct matches. Therefore, the function

$$J(P) = \|PA_G P^T - A_H\|^2 \tag{2.25}$$

has to be minimized. A_G and A_H are the adjacency matrices (of size nxn) of the graphs G and H respectively and P is a permutation matrix. Thus, the eigendecomposition of the

adjacency matrices is carried out:

$$A_G = U_G \Lambda_G U_G^T, \tag{2.26}$$

where U_G is an orthogonal matrix (U_H for A_H) and Λ_G is the diagonal matrix that contains the eigenvalues of A_G. Then it can be demonstrated [Ume88] that the sought permutation matrix is

$$P | tr \left(P^T \bar{U}_H \bar{U}_G^T \right) \leq n. \tag{2.27}$$

The first author presenting a spectral graph matching method was Umeyama [Ume88]. Several authors have taken his method as basis and adapted it to their particular problems. The constraint of isomorphic graphs has been relaxed for spectral methods to be used in more applications, for instance, medical. Smeets et al. [SBK10] build up the assignment matrix as a combination of two soft correspondence matrices and a local correspondence matrix. The first two matrices are constructed by calculating the probability of two bifurcations to correspond to another two of the second graph. This probability follows a Gaussian distribution. For the first matrix, geodesic distances are taken into account and for the second one euclidean distances. The third matrix contains information about the local similarity of the bifurcations and it is calculated using the n-SIFT descriptor. Once the combined assignment matrix is calculated, the spectral method by Scott and Longuet-Higgins [SLH91] is used to find the best solution to the problem. This method is applied to 3D lung vessel trees obtaining an average error of 1 ± 0.5 mm.

Spectral methods have also been used for sulcal graph matching by Im et al. [IPL*11]. The assignment matrix is built by calculating the individual and pairwise affinities of the assignments. To do this the sulcal position, depth, area of the basin and topology are considered. The assignment problem is solved by applying the spectral method by Leordeanu and Hebert [LH05]. According to this method, the eigenvectors of M provide a value to the confidence of an assignment. Using this information the final assignment matrix is calculated. The proposed method, evaluated in 48 subjects, results in a mismatching rate of about 0.15. Lombaert et al. [LGPC11] propose a method to match cerebral cortex. They also use a spectral method combined with similarities as the sulcal depth or curvature to find the correspondences. The validation of the method is done in terms of overlapping of sulcal regions resulting on a 88% overlapping.

Recently, Guo et al. [GWJS13] proposed a method to find correspondences between hand x-rays to be used in an age assessment system. Their method has as basis the spectral matching with affine constraint method [CSS06]. The novelty of their approach is that they generate a so-called line patch as similarity metric. This contains information about the intensity profile of the line that connects two points. Besides, they use the distances between points as second similarity metric. Their second contribution is to add a sparsity term to reduce the number of ambiguous matches. The sparse graph matching is hierarchically repeated. In every iteration the model graph is deformed using thin plate splines and new matches are selected. The average matching error on 8 hand x-rays is 0.81 ± 0.89 mm.

2.4.2.5. Evolutionary techniques

These taxa encompass methods based on evolutionary techniques to find correspondences. As it was proposed by Bengoetxea [Ben02], it will include Genetic algorithms and Estimation of distribution.

Genetic algorithms Genetic algorithms are based on the natural chromosomal evolution. These algorithms calculate a series of random populations that will be altered by using genetic operators like mutation or crossover to evolve into new populations until a solution is found. This will be repeated according to a so-called fitness function or until there are no more possible changes. The crossover is the process of mixing two sets of different solutions to create a new one. This operator is used to find a global optimal solution when there are two suboptimal matches. Figure 2.17 shows the effect of the crossover operator. The evolved children have part of the nodes from one parent and part from the other. The change is produced at the crossover point, visualized in red in the image. The same image shows the process of mutation of a graph. There a node (or more) is exchanged by a new one that is not part of the parent trees.

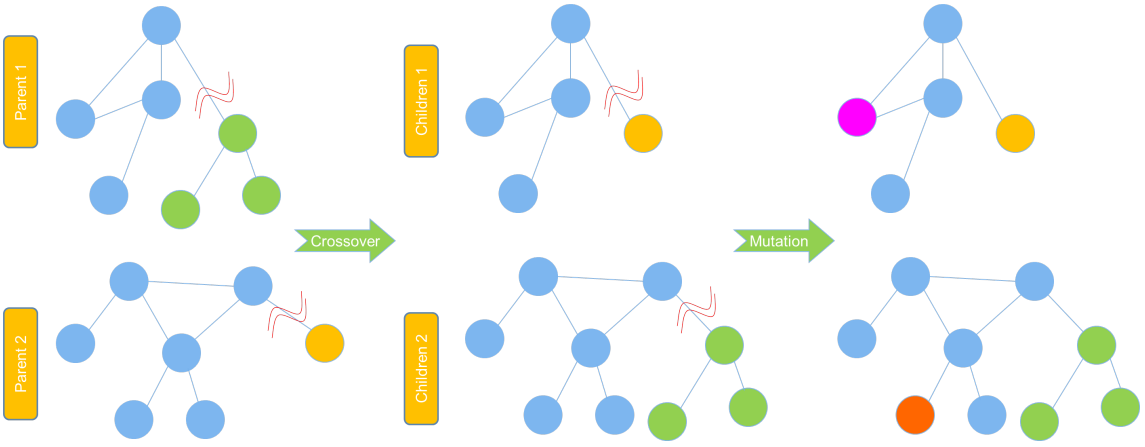

Figure 2.17.: Genetic operators: Crossover and mutation.

The first authors who used genetic algorithms for graph matching were Cross et al. [CWH97]. They use a bayesian consistency measure as fitness function and genetic search for the optimization of the problem. To speed up the process of convergence they use a deterministic hill-climbing process. In the field of medical imaging genetic algorithms have been used for labeling brain sulci by Yang and Kruggel [YK09]. First, they generate a model graph (using several training datasets) containing the brain sulci labeled by neuroanatomists. Graphs generated from new subjects are matched to the model graph. The feature space for the similarity calculation is given by neighborhood information and location, shape and orientation information. Then the fitness function is generated using that information and a genetic algorithm is used to optimize the problem. The method has been tested on 40 subjects obtaining a true positive rate between 85.0 and 94.5 for different sulci.

Estimation of distribution Estimation of distribution is another kind of evolutionary technique. Using this technique for graph matching was introduced by Bengoetxea et al. [BLBP01, Ben02]. Unlike genetic algorithms, estimation of distribution algorithms do not use the operators described before (reducing the number of parameters needed). They calculate the joint probability distribution of the individuals that best fit according to a fitness function and from this calculation the new set of individuals is evolved. Among other applications they apply this approach to the recognition of structures in brain MR images. The method has been compared with a genetic algorithm showing that estimation of distribution algorithms outperform genetic algorithms (0.6936 vs. 0.7480 best fitness value).

2.4.2.6. Neural networks

Genetic algorithms are not the only group of biologically inspired algorithms. Neural networks, for example, are based on biological neural networks. Generally speaking, artificial neural networks are mathematical models that describe the connection between different neural layers. These models are defined by a so-called neural function:

$$f(x) = k\left(\Sigma_i w_i g_i(x)\right). \tag{2.28}$$

Each term of this function represent the connection between two neurons. It contains a synaptic weight w_i and a function g_i. w_i is the weight given to the connection between two neurons and g_i the function that contains the data that the input neuron is sending to the output neuron. The neural function encompasses all the signals that the neuron received. This final signal is then transformed by the activation function into a signal that will be the input for the next neurons. The goal of the neural network algorithm is to find the set of weights w_i that lead to the optimal interconnection network. This is done by minimization of a cost function. The behavior of each single artificial neuron simulates the behavior of biological neurons as shown in Figure 2.18.

Riviere et al. [RMPO*02] use neural networks to label human cortical sulci. The cortex is represented by a graph in which each clique corresponds to a sulcus. Two types of neural networks are defined: those that study sulci (certain clique) and those that study the relation between two sulci. Each type of neural network receives a series of descriptors describing the shape (first type) or relation between sulci as input. 265 neural networks are necessary to study the complete cortex. Each one will contribute to the minimization of the cost function. The quantitative evaluation of the algorithm resulted in a mean recognition rate of 86% and 76% for the learning and generalization bases respectively. Fischer et al. [FTGL04] use a Hopfield-style neural network for medical image retrieval. Thus, a multiscale approach is used to analyze every region in the image. A graph that contains information about the different regions will be created and matched to the graph corresponding to the second image. Quantitative evaluation of the method is not provided.

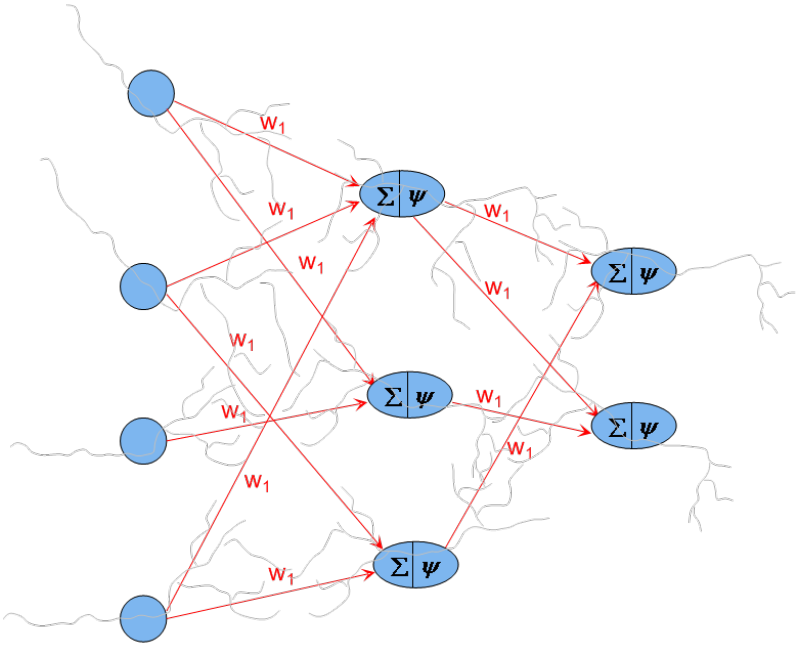

Figure 2.18.: Artificial neurons simulate the behavior of biological neurons.

2.4.2.7. Elastic graph matching

The problem of graph matching in presence of deformations is still a challenge. Elastic graph matching methods provide a solution for this when the deformations are small. This kind of methods has been used for face detection. Nevertheless, some elastic graph matching methods have been used for medical imaging. The usual process of elastic graph matching methods consists on constructing a grid that is aligned with the reference image. Then the grid is deformed so that it matches the image. Phang et al. [PBC06] use this kind of approach to track the deformation of the iris surface. Therefore, they extract a series of features from the iris. Their approach consists of two steps: a global move in which all the nodes of the grid are moved uniformly and a local move in which each node move to the neighborhood location with higher similarity. The similarity will be given by a combination between a Gabor wavelet response and the geometry topography. Finally, the cost function contains a weight that will determine how much can the nodes move, or in other words the allowed amount of deformations. The algorithm has been visually evaluated on synthetic iris images.

2.4.3. Manual/Visual

Not all matching methods are fully automatic. Some of them are completely manual and other have a manual refinement tool to improve the results of the method correcting false matches or adding matches. In either case it is necessary to have visualization features that make the interaction task user-friendlier. Lange et al. [LWRS09a] manually select a series of correspondences between liver vessel trees to register pre and postoperative liver CTs. They show that the interaction task is difficult and time-consuming. Hampshire

et al. [HHP*13] also opt for a manual approach to create a reference standard to find correspondences between prone and supine colonography images. Therefore, they develop a graphical user interface. It consists of two screens each one showing the external, internal and unfolded view of one of the images. The haustral folds are marked with white spheres. Once the physician has labeled a fold, a number will be assigned to it.

But this is not the only field in which manual graph matching has been used. Bremm et al. [BvLH*11] base their work on the visual comparison of biological trees that contain information such as DNA or protein sequences.

The results are often visualized using connecting lines between matches. This approach is used by Charnoz et al. [CAM*05b], Graham and Higgins [GH06a], Serradell et al. [SGK*12] or Smeets et al. [SBK10] among others. Other groups like Lohe et al. [LKZ*08] assign the same colors to corresponding paths. They use this approach for the human airway. The question remains whether this could work properly in other organs like the liver that contain more paths. This approach has been also used by authors whose goal is to label the brain sulci. For example, Rivière et al. [RMPO*02] gives different colors to the different sulci.

2.5. Discussion

In this section the methods introduced in the previous sections are discussed.

2.5.1. Registration

In the previous sections several registration and graph matching methods have been introduced. A method is more or less suitable for a particular application depending on its characteristics. Kashani et al. [KHB*08] did a multi-institution study to compare the accuracy of different registration methods. The evaluation of the study was done on phantoms simulating the human lungs. Methods based on thin plate splines, B-splines, Demons, Fluid flow and free form deformations were part of the study. Another study was presented by Brock [Bro10]. It was tested on clinical CT data of lungs and livers. 21 groups participated in the study. Compared to Kashani and colleagues viscous fluid, optical flow, linear elastic and juggler methods were added to the study. In spite of how useful this kind of studies is, there is not a method that is best suited for all kind of applications. Depending on factors like the speed or accuracy required by an application or the amount of the deformations that are present, a method suitable for one application can be inadequate for another one.

Outcome validation of tumor ablations and resections is the focus of research in this thesis. A registration method suitable for that application should be able to handle large deformations and should return total organ accuracy. In the next paragraphs registration methods are discussed with special emphasis on the amount of the deformations that they can handle and on the area (local or total organ) where they achieve the required accuracy.

Characteristics Table 2.2 shows a summary of the characteristics of each registration technique. Rigid registration techniques are appropriate to deal with images that do not contain large deformations. Under those circumstances, especially landmark based registration techniques are efficient. However, they are not suitable for images containing soft tissue (e.g., liver) unless the registration is considered a preprocessing step to align the images before the deformation occurs. Mass spring models are used to simplify the calculation of the equations. They might be used when efficiency is a bigger limiting factor than accuracy. They have the drawback that the number of parameters to be set is high. Interpolation based methods are in general less accurate than physics based methods and therefore not suitable to deal with large deformations. However, they depend on fewer parameters. Physics based methods can handle larger deformations at the price of a decrease in efficiency and an increase in the number of parameters. In this group, elastic models are the least accurate and the fastest. The accuracy keeps increasing as the complexity of the models increases: hyperelastic, viscoelastic... However, with the complexity, the processing time and the number of parameters also increase. The choice of a physics based approach highly depends on the tissue type to be modeled. Even though viscous fluid models can handle larger deformations than other physics based models, they do not correctly approximate the behavior of soft tissue [LLF08].

Category	Method	Efficiency	Big deformations	Accuracy	Parameters
Rigid	IB	+	–	+/-	+/-
	LB	++	-	+/-	+
Physics based	MSM	+/-	+/-	+/-	–
	LEM	+	+/-	+/-	+
	HM	+/-	+	+	+
	VM	-	+	+	-
	VFM	–	++	+	-
	DM	+	+/-	+/-	+
	FD	-	+	+/-	+
Interpolation based	RBF	+	-	-	++
	EBS	+/-	+/-	+/-	+/-
	FFD	+	+/-	+/-	+/-
	PAM	++	+	+/-	+

Table 2.2.: Characteristics of the different registration categories. Depending on the restrictions of the application one type of registration is more appropriate than other types. In the table ++ will be assigned to a method that is: efficient, robust against large deformations, accurate, and has a small number of parameters to be optimized. IB: intensity based, LB: landmark based, MSM: mass springs models, LEM: linear elastic models, HM: hyperelastic models, VM: viscoelastic models, VFM: viscous fluid models, DM: diffusion models, FD: flows of diffeomorphisms, RBF: radial basis functions, EBS: elastic body splines, FFD: Free-form deformatinons, PAM: Piecewise affine models.

An appropriate method for outcome validation of tumor ablation and resection should have the following characteristics:

- Capability to handle large deformations

- Total organ accuracy

Rigid registration methods cannot handle large deformations. Interpolation based methods return accurate results for images that do not contain large deformations. Nonetheless, the deformations considered in this thesis can be large, thus, it is interesting to incorporate information about the physiological behavior of the liver in the registration process. Physics based methods allow to do this. But as previously mentioned, one has to find a trade-off between model complexity and efficiency. Linear elastic models are the most efficient of physics based models. Nevertheless, just as viscous fluid models they do not accurately describe the behavior of the liver. Hyperelastic models and viscous elastic models can approximate this behavior better. Although in theory viscous elastic models should better describe this behavior [Hum03], a comparative study [STR*11, SRD*11] showed that in the practice no big changes in the results are observed. Hyperelastic models have the additional advantage of a higher efficiency and fewer parameters required. Thus, this thesis will carry out the registration using hyperelastic models.

Organ internal vs. organ surface accuracy In addition to the ability to handle large deformations, there is another factor that was not taken into account until now:

Is the accuracy achieved on the surface of the organ, in the internal structures or in both areas?

This information is important. Most authors pay more attention to the accuracy on the surface of the organ. However, to know the location of internal structures is crucial for the physicians. When they want to resect a tumor, for example, they need to know accurately where the surrounding vessels are.

Table 2.3 classifies the methods cited in the previous chapters according to the information that they use to carry out the registration: Organ internal, organ surface, or total organ. As it was mentioned before, physics based methods can achieve more accurate results in presence of large deformations. Thus, internal and surface constraints are further divided in three levels depending on how "physical" the applied constraints are: a "-" means that those methods did not use landmarks (they are mainly, intensity based methods), a "x" means that they used non-physical landmarks and a "+" means that they used physical landmarks. Thus, a method classified as "++" uses physical organ internal and organ surface landmarks along with a physics based registration method achieving a higher total organ accuracy as will be proven in the next Chapters. Note that this classification refers always to images containing large deformations. When this is not the case, intensity based methods can provide accurate results as well. In the following paragraphs each group is discussed.

Neither organ internal nor organ surface "- -" Most methods belong to this group. They use intensity based metrics such as (normalized) mutual information [DMVS02, RHMS12, KSP07, LMVS04, MHV*03, RCRMOZ04, RSH*99, SAC*12, SZP*12, EOLD*12] or gradients [PNA11, PEY*11, BK07] for the registration. The reached accuracy is achieved using uniquely local intensity similarity everywhere. That type of methods will fail in presence of large deformations and are therefore classified as - -. Schmidt et al. [SRWHE12] add to this similarity sliding geometries increasing the accuracy in some areas in which

Organ Surface \ Organ Internal	-	x	+
-	[FWG*99], [LRQG13], [DHLH11], [TJ04], [YW05], [CJLG08], [STR*11, SRD*11], [NTL*08], [DMVS02], [CRC*12], [SREWH09, SRWHE12], [PNA11, PEY*11], [BK07], [RHMS12], [BRS*03], [KSP07], [LMVS04], [MHV*03], [RCRMOZ04], [RSH*99], [SAC*12], [SZP*12], [CWDP12], [EOLD*12]	[SGG*12], [WR07]	[DBB08], [JTT*11], [HRM*10], [LWRS09b]
x	[DCL*09a], [NFN07, NNSF09], [HU13], [YHL10]	[ZCL13], [RFS99]	
+	[CMS*05], [LLF08], [CTBN*08], [HHM*11], [WS00], [ESH*11]		

Table 2.3.: Classification of the state of the art methods according of the information used for the registration: Organ internal or Organ surface. The colors represent the accuracy of the results that is expected according to the information used for the registration. The methods labelled as red did not use any extra information to drive the registration. The ideal case (green) would be to use both organ internal and surface information. The rest of the methods show an increasing expected accuracy in presence of large deformations as follows: dark orange, orange, yellow, light green.

interfaces between organs exist, for instance, lungs and ribs. However, because of the difficulties of these methods to overcome large deformations they are not suitable for the application under study.

Organ internal in some areas "x -" An increase in the accuracy can be observed in [SGG*12]. They take special care of the fibers that can be found in white matter. However, for the rest of the image they only use local intensity similarities. [WR07] also concentrates a series of landmarks in a small area, namely, the area in which a tumor is located. The idea of using landmarks to increase the accuracy in a local area inside the organ does not suffice to achieve the goals of the current work: total organ accuracy.

Non-physical organ surface "- x" On the other side some groups do not use the internal structures of the organs that they are registering, but the surfaces. They register them using closest point distances [DCL*09a, HU13, YHL10] or variations of it [NFN07,

NNSF09]. Even though this can lead to accurate results, the accuracy highly depends on the correctness of the alignment method used before the deformable registration takes place. If the latter is not correct, the surfaces will be matched to physically wrong places and the effect will be also extended to the internal structures. Using known correspondences between surfaces can partly solve the problem [ESH*11]. Similarly, as the previously discussed group, in this case only local accuracy is achieved, namely, in the areas near the surface.

Non-physical total organ "x x" These methods take care of internal structures and the surface but with non-physical registration methods. This is the case of [ZCL13] and [RFS99] that use landmarks spread along the skull and brain respectively. The methods in this group incorporate organ internal and organ surface landmarks. Nevertheless, the number of landmarks used for registration is in both cases small. In addition to this, the application under study requires a physics based method, opposite to the interpolation based methods used by the aforementioned authors. Thus, these methods are classified as "x x" and not as "+ +".

Physical organ surface "- +" Finally, some groups use physical constraints to deform the surfaces, for example, gravity forces to model the deformation of the breast [CTBN*08, LR10, HHM*11]. An interesting approach was proposed by Lee et al. [LLF08] that takes into account organ-to-organ interactions to match the surfaces of the prostate. In this approach the deformation of the organs surrounding the prostate is modeled. The deformation of the prostate is then induced by those deformations. Wang and Staib [WS00] introduce statistical shape information to the registration to have higher accuracy in the surface. Cash et al. [CMS*05] divide the liver surface in three parts and apply different boundary conditions to each one depending on the typical behavior of the liver in those areas. Finally, Erdt et al. [ESH*11] use known correspondences between liver surfaces to have a better registration of the surfaces. The methods in this group propose interesting ways to incorporate physical constraints to the organ deformations. Unfortunately, this constraints are focused on the surface of the organ.

Physical organ internal "+ -" Internal structures like vessels [DBB08,JTT*11,HRM*10, LWRS09b] have also been used to drive the registration. Depending on the approach used for the registration FEM [JTT*11], CPD [HRM*10], MSM [DBB08] or TPS [LWRS09b] the extrapolation of the deformation to the rest of the image is more or less accurate. However, in these methods landmarks are not spread in the complete image and the surfaces are not considered, which will reduce the achieved accuracy.

Physical total organ "+ +" So far, no authors have proposed to use physically based internal and external information with a physics based registration method to achieve more accurate registration results.

The methods classified as "- -" are a good choice when the deformations are small. However, landmarks (when available) are a good hint to carry out a more accurate registration. The methods classified as "- x" and "x -" guide the registration using a series

of landmarks. Nevertheless, the used landmarks are located only in certain area of the organ. The selection of one of these approaches would avoid the searched total organ accuracy. Similarly, the methods classified as "- +" and "+ -" do not allow for a total organ accuracy. Finally, the only disadvantage of the "x x" methods is that they do not use a physics based method for the registration. As it was discussed before, this would be desired for the application under study. Thus, this thesis proposes to incorporate physical internal organ and organ surface landmarks in a physics based registration method ("+ +").

Pre and postoperative liver registration A final important aspect should be discussed, namely, the application for which the registration method is developed in this thesis: outcome validation of liver surgery. Thus, registration methods for livers that underwent a resection or an ablation are discussed in the next paragraphs and classified in Table 2.4.

External \ Internal	-	x	+
-	[WCZ*98], [CDLW00], [WRK*07], [RWS*10, RWS*12], [GML*09], [FHI*06]	[BPHF10], [KLK*11]	[CAM*05a], [LWRS09a]
x	[DCL*09b], [NNSF09]		
+	[Bro10]		

Table 2.4.: Classification of the state of the art methods to register pre/post operative liver acquisitions. The same color code as in Table 2.3 is used.

The focus of the work by Wilson et al. [WCZ*98] is the registration of MR images acquired before and right after thermal ablation of tumors. They opt for a manual, rigid registration of the images. Therefore, they use a graphical user interface to ease the registration process and extracted isocontours to guide the user. Carrillo et al. [CDLW00] compared this manual method with a semiautomatic voxel based rigid registration one using four similarity metrics: mutual information, entropy, correlation and variance of gray scale ratio. They conclude that mutual information provides the best results, returning similar quantitative results that manual registration, but increasing its efficiency. Weihusen et al. [WRK*07] present another tool for visual assessment of radiofrequency ablation. They automatically initialize the preoperative and postoperative liver acquisitions by matching the center of the livers. Rigid registration is then performed manually. The same technique is used by Rieder et al. [RWS*10]. Fujioka et al. [FHI*06] present a semiautomatic rigid registration method that requires user interaction when the results are not as accurate as expected. Dumpuri et al. [DCL*09b] register CT acquisitions of the liver before and after tumor resection using the well-known iterative closest point to match the surfaces of both acquisitions. They do not quantitatively evaluate their method. Rieder et al. [RWS*12] propose an automatic rigid registration method focused on the lesion. They carry out the registration on a region of interest around the lesion. They mask the lesion so that it has no influence in the registration process and use local cross correlation to find the correct transformation. They compare the results of their method with a manual

registration carried out by expert. In 49 % of the cases the obtained results are similar. In 27 % of the cases they achieve more accurate results than the experts. Giesel et al. [GML*09] increase the number of degrees of freedom allowed by the transformation. They use affine transformations for outcome validation and follow up after radiofrequency ablation. Voxel similarity is used as metric for the registration. No quantitative evaluation of the method is provided.

However, not all the groups use rigid registration for that purpose. Some authors opt for deformable registration techniques to register liver acquisitions. Charnoz et al. [CAM*05a] proposed a tree matching method to find anatomical internal landmarks of the liver and they register the acquisitions by extrapolating the vector field generated by those correspondences. This method has only been tested on artificial data obtaining an accuracy of about 4 mm. Lange et al. [LWRS09a] focus their work on the registration of liver CTs pre and post tumor resection. As Charnoz and colleagues did before they use the vessels as internal landmarks, although they find the correspondences manually. They compare the registration results using thin plate splines, Gaussian elastic body splines and approximating Gaussian elastic body splines obtaining in every case similar results. Niculescu et al. [NNSF09] used external constraints instead of internal anatomical landmarks to guide the registration process using finite element methods obtaining 2 mm accuracy on 2D synthetic phantoms and 3D beef liver data. This technique is also used by Brock et al. [BDS*06]. However, they consider the interfaces between adjacent organs to match the surfaces and obtain an accuracy of 4.2 mm. 5 pairs of clinical datasets were used for the evaluation. Another approach that takes into account the elasticity properties of the liver is the one by Beuthien et al. [BPHF10]. In their work the resected liver is registered to the preoperative liver in a two-step process. First a rigid registration is carried out using the liver vasculature to determine a region of interest followed by a volume preserving elastic registration. They evaluate their method in one pair of CT images and conclude that non-rigid registration improves the results in 60 % over rigid registration. Kim et al. [KLK*11] enhance their non-rigid registration method with manually selected corresponding internal landmarks when the results are not accurate enough.

2.5.2. Matching

As previously mentioned, several authors opt for landmarks to carry out the registration. This has the advantage of having real knowledge of how the image should deform. On the other side the result will highly depend on the correctness and number of the detected landmarks.

Characteristics Table 2.5 summarizes the advantages and disadvantages of each type of matching method. In general, tree search methods perform slower than other approaches. However, as the search range is more exhaustive they are also more robust against local minima. On the other side, this type of methods need traditionally a known pair of preselected roots and two relatively well aligned trees. Nevertheless, the latter could be fixed by choosing rotation invariant similarity metrics. Probabilistic relaxation methods are in general efficient compared to the previous ones with the drawback of a bigger tendency to get stuck into local minima. In addition to this, they use to be pose

independent. However, the amount of the deformations that they can handle is small. The approaches presented using gaussian processes can handle larger deformations, but the time required to find the correspondences is increased again. Evolutionary techniques, neural networks and elastic graph matching methods perform well for certain applications but are not appropriate to match vessel like structures.

Due to the complexity of finding correspondences between vessel trees, it is not advisable to use methods based on probability theory. The generated trees contain often spurius branches that will increase the chances of the method to get stuck into local minima. Thus, spectral and tree search methods are the most appropriate approaches. Nevertheless, the robustness of tree search methods against getting stuck in local minima makes them more suitable for the application under study.

Method	Efficiency	Deformation sizes	Accuracy	Disadvantage	Advantage
Exact	-	-	+	No medical	
TS	+/-	+/-	+/-		Robust LM
BG	+	+/-	+/-	No vessel like	
PT	+	+/-	+/-	LM	NI (PR)
SM	+	+/-	+/-		
ET	+	+/-	+/-	No vessel like / LM	
NN	+	+/-	+/-	No vessel like	
EGM	+	+	+/-	No vessel like	

Table 2.5.: Characteristics of the different matching types. Depending on the restrictions of the application for which they are developed, one type of matching is more appropriate than other types. In the table ++ will be assigned to methods that are: efficient, accurate and can handle large deformations. Acronyms stand for: Tree search (TS), Bipartite graphs (BG), Probability theory (PT), Probabilistic relaxation (PR), Spectral methods (SM), Bipartite graphs (BP), Evolutionary techniques (ET), Neural networks (NN), Elastic graph matching (EGM), risk of local minima (LM), no initialization needed (NI). As in Tables 2.3 and 2.4 green is associated to advantages of the methods, red to disadvantages and yellow to intermediate of neutral characteristics of the method. A larger amount of colors is not required in this table.

Similarity metric The selection of an appropriate method is important. However, the final accuracy of the results will depend on the used similarity metric. This will also determine whether the method needs a pre initialization (alignment) of the graphs. It will also define whether known corresponding roots are necessary. Table 2.6 describes the influence of the similarity metric on the characteristics of the method. The selection of a metric will also depend on the structure to be matched. The last column of the table shows which structures have been matched using certain metric.

The metric that has shown to be more robust for vessel like structures is the length. It is pose invariant and is considered an isometry. Other metrics like radius, the diameter and the topological distances have the disadvantage not to be robust against errors produced by segmentation methods. On the other side, the direction is robust but has the drawback of not being pose invariant. The curvature might not be the most appropriate metric in

Metric	Pose invariant	Root	Organ
Length	Yes	No	Vessel (Liver, Lung, Retina)
Angle	Yes	No	Vessel (Liver, Lung, Retina)
Direction	No	No	Vessel (Liver, Lung, Retina)
Radius	Yes	No	Vessel (Liver, Brain, Heart)
Diameter	Yes	No	Vessel (Liver, Brain, Heart, Lung)
Angle between children	Yes	Yes	Vessel (Liver, Brain, Heart, Lung)
Length from root	Yes	Yes	Vessel (Liver, Lung)
Relative angles	Yes	No	Vessel (Liver)
Euclidean distance	Yes	No	Vessel (Liver, Lung, Retina)
Angle from root	Yes	Yes	Vessel (Liver, Lung)
Inheritance	Yes	No	Vessel (Lung)
Mean squared distance	No	No	Vessel (Lung)
Topological distance	Yes	No	Vessel (Lung)
Curvature	Yes	No	Brain surfaces, Vessel (Liver)
Volume from root	Yes	Yes	Vessel (Lung)
Node level	Yes	Yes	Vessel (Lung, Liver)
Fuzzy spatial relation	Yes	No	Breast
Torsion	Yes	No	Brain surfaces
Texture	Yes	No	Breast
Self similarity descriptor	Yes	No	Vessel (Retina)
N-SIFT	Yes	No	Colon, Vessel (lung)
Shape (thickness, depth)	Yes	No	Cortical sulci
Line patch	Yes	No	Hand

Table 2.6.: Characteristics of the method depending on the similarity metric used. The column root refers to the need of having known roots for the method to work. The colors in this table represent properties that the similarity metric should (green) or should not (red) have. In the column organ, green labels are assigned to similarity metrics that were used to find correspondences between vessel like structures.

presence of deformations.

Because of its robustness, the length is the most appropriate similarity metric to find correspondences between vessel like structures. However, during the matching process a combination of at least two attributes have to be used to solve ambiguities. To this end, Chapter 3.1 will evaluate the results of the combination of the length with other similarity metrics.

Point clouds vs. graphs A third factor has to be considered, namely, the selection of graph representations or point clouds. The choice highly depends on the organ or structure under study. In the liver vasculature the topology up to a certain point can be used to remove outliers. The number of nodes of the graph is high and in sometimes condensed. Furthermore, a one-to-one matching is desired. Thus, it is more appropriate to use graphs instead of point clouds.

Author	Type	Graph	Init	Root	3D	Fast	LM
Lohe et al. [LKZ*08]	TS	No	N/A	Yes	Yes	Yes	
Charnoz et al. [CAM*05b]	TS	No	Yes	Yes	Yes	No	
Feragen et al. [FPO*12]	TS	No	No	Yes	Yes	No	
Nam et al. [NKL*12]	TS	N/A	No	No	Yes	Yes	
Hilsman et al. [HVK*07]	TS	N/A	N/A	N/A	Yes	N/A	
Bülow et al. [BLWH06]	TS	N/A	N/A	N/A	Yes	N/A	
dos Santos et al. [dSGMMH10]	TS	No	No	Yes	Yes	Yes	
Kaftan et al. [KKNN06]	TS	Yes	Yes	Yes	Yes	N/A	
Tschirren et al. [TMP*05]	TS	No	Yes	Yes	Yes	Yes	
Metzen et al. [MKS*07]	TS	No	N/A(N)	Yes	Yes	Yes	
Ma et al. [MBB08]	TS	Yes	No	No	No	N/A	
Graham and Higgins [GH06b]	TS	No	Yes	Yes	Yes	Yes	
Tang and Chung [TC06]	TS	No	Yes	Yes	Yes	N/A	
Guo et al. [GWJS13]	SM	Yes	Yes	No	No	No	
Zheng et al. [ZIW*11]	PR	Yes	No	No	No	Yes	
Deng et al. [DTZ*10]	PR	Yes	Yes	No	No	Yes	
Groher et al. [GZN09]	PR	Yes	Yes	No	No	Yes	
Chui and Rangarajan [CR00]	PR	Yes	No	No	Yes	Yes	Yes
Serradell et al. [SGK*12]	GP	Yes	No	No	Yes	No	Yes
Pinheiro et al. [PSS*13b]	MRF	Yes	No	No	Yes	Yes	Yes
Roy et al. [RPD09]	PR	Yes	No	No	Yes	N/A	Yes
Smeets et al. [SBK10]	SM	Yes	No	No	Yes	N/A	

Table 2.7.: Characteristics of the graph matching method introduced in the previous sections. Only methods used to match vessel like structures are included in this table. As in previous tables green colors are assigned to properties that a method appropriate for this thesis should have. Init: Need for initialization, LM: Local minima, TS: Tree search, SM: Spectral methods, PR: Probabilistic relaxation, GP: Gaussian processes, MRF: Markov random fields.

Methods for vessel like structures In this section the methods used to find correspondences between vessel like structures will be discussed. The main characteristics of those methods are summarized in Table 2.7.

Most tree search based methods are meant to work on trees instead of graphs. With this they assume that the vasculature will not contain loops [LKZ*08, CAM*05b, FPO*12, dSGMMH10, TMP*05, MKS*07, GH06a, TC06]. This is true in the ideal case in which segmentation and graph generation methods would not be error prone. Unfortunately, due to image artifacts or low resolutions the result of the segmentation method will show vessel structures that intertwine and contain loops. Thus, tree matching methods that make this assumption require of a tree separation method before the matching process. Exceptions within this group are Kaftan et al. [KKNN06] that divide the graph into complete paths without loops even if the graph contains them. This method (as most tree search based ones) depends on a known pair of preselected roots and on two initially aligned graphs. Dos Santos et al. [dSGMMH10] present a pose independent method but like most of them it works on trees. Ma et al. [MBB08] present a tree search based method able to find correspondences in 2D images. Three additional methods are included in the

table [NKL*12, HVK*07, BLWH06] because they were used to find correspondences between vascular trees. However, they do not provide enough information to classify them correctly in the terms discussed in this work.

Probability relaxation methods have also been used to match vessel like structures. These methods find correspondences between cyclic graphs without the need of preselected roots with the disadvantage of being prone to get stuck into local minima [CR00, RPD09]. Most methods presented have been developed for 2D images [GWJS13,ZIW*11, DTZ*10, GZN09]. The non-linear regression based method by Serradell et al. [SGK*12] can find correspondences between 3D graphs without the need of an initialization and known roots. The disadvantage of this method is that it is much slower than other approaches and it is prone to get stuck into local minima. Recently, Pinheiro et al. [PSS*13b] used Markov random fields to speed up the method proposed by Serradell and colleagues, unfortunately the local minima problem is still present in their method.

The method presented by Smeets et al. [SBK10] eliminates most mentioned limiting factors. However, it depends on the intensity similarity between the two images. This makes the method monomodal, and not so robust in presence of noise.

2.6. Conclusion

A deformable registration method able to handle large deformations and at the same achieve accuracy in the interior and surface of the organ is an open research question (Table 2.3 bottom right). A liver that underwent tumor ablation and/or resection will present large deformations over the preoperative liver. The source of those deformations is not only due to breathing: When a tumor is ablated the elasticity of the treated area will change. Hence, it will react differently to forces exerted by the surrounding organs. Furthermore, when a tumor is resected the organs surrounding the liver will slightly move especially kidneys and intestine. Thus, forces are exerted at new positions of the surface the liver. In addition to this, the liver will re-grow. All these factors add deformations to the scenario.

Deformations are not the only constraint to pay attention to. Physicians need accuracy after registration and this cannot just be restricted to the surface of the liver, but it should be accurately extended to the interior of the organ. The liver vasculature is the anatomical feature of the liver that is most easily identifiable between different image acquisitions and even different modalities. Many methods have been proposed to find correspondences between vessel trees. However, as analyzed in Table 2.7 they lack some important characteristics:

1. Capability of matching cyclic graphs (no need for tree separation)
2. Independence of preselected roots
3. Robustness against local minima
4. Pose independence

As it was previously discussed, manual selection of matches is difficult and time-consuming. Interaction features could ease this task. Furthermore, an automatic outlier

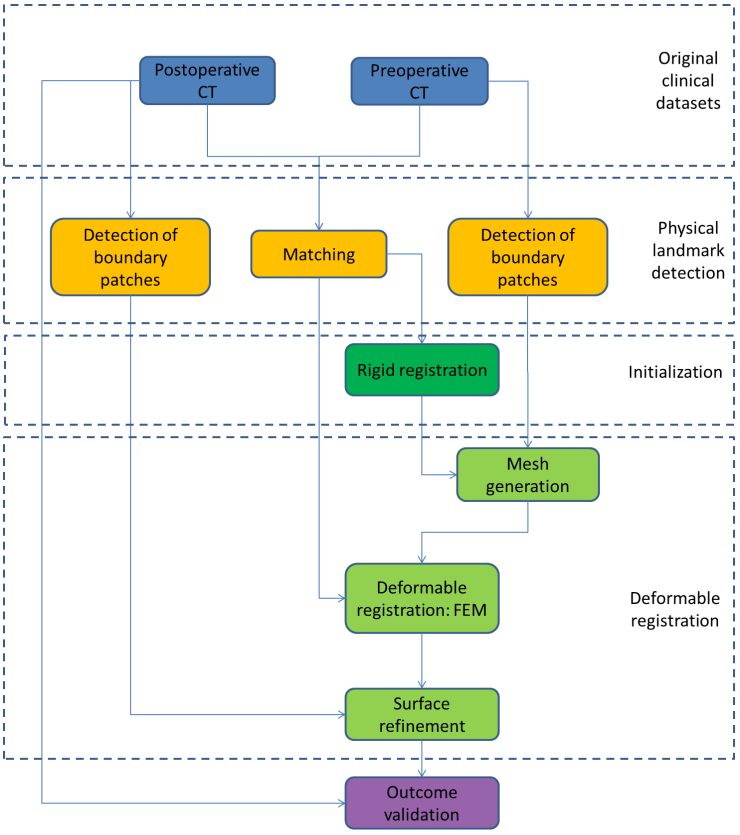

Figure 2.19.: Methods proposed in this thesis.

detector to avoid the need to refine the matching results would save additional time to the physician.

Physics based methods are more appropriate to recover from large deformations (Table 2.2). While linear elastic models can recover relatively small deformations, viscous fluids models are characterized for recovering large deformations. However, the latter do not follow the behavior observed in solid organs [LLF08]. Soft tissues usually have a non-linear, inelastic, heterogeneous, and anisotropic behavior [Hum03], which makes linear elastic models inappropriate to model the liver behavior. Hyperelasctic models can be a good compromise between complexity and size of deformations to be handled.

This thesis proposes a method that combines physical organ internal and organ surface landmarks and a physics based registration method. In accordance with the discussion the proposed registration method is based on hyperelastic models. As it is shown in Figure 2.19, the detection of landmarks will be composed of two methods. The first one will be a tree search based graph matching method that is simultaneously root and pose independent, efficient and suitable for cyclic graphs. This method is proposed for the detection of organ internal landmarks. The second method will be used to detect the organ surface landmarks. Therefore, a series of boundary patches will be introduced in the process that allow to enhance the registration with prior anatomical knowledge. Both types of landmarks will be incorporated in the registration process. As it will be proven the results obtained with such an approach achieve a higher total organ accuracy than state of the art methods.

3. Internal landmarks: Tree matching

According to the conclusions of Chapter 2 landmarks increase the accuracy of registration methods. In this thesis the use of physical landmarks inside the organ and on its surface is proposed to further increase this accuracy. This chapter focuses on the extraction of internal anatomical landmarks. Therefore, it is necessary to find structures that are easily identifiable in different acquisitions. In the case of the liver there are mainly two anatomical structures that fulfill that condition: the vasculature and the ligamentum falciforme. However, after a surgery (the clinical scenario of this thesis) the ligamentum falciforme will not necessarily remain attached to the liver. Moreover, the liver vasculature is spread through the whole liver increasing the number of landmarks that can be used for the registration and covering a higher area of the liver. Thus, this is the structure chosen for this thesis.

Tree matching has shown to be effective to find correspondences between vascular trees (see Chapter 2). Hence, it will be used to detect the corresponding landmarks that are required to register liver CT images. Although the work of this chapter has been carried out with a clinical scenario in mind (surgery and outcome validation), this chapter (together with the solution for cyclic graphs presented in Chapter 4) can also be seen as an independent solution for matching problems that can be used in other organs and different applications.

Tree isomorphismus is a recurrent concept in graph theory that has been successfully employed in applications that require exact matching [RW02, BGP*13]. However, inexact matching is needed to match trees representing the anatomical vasculature (see Chapter 2). The trees will not be isomorphic but will contain differences that will complicate the matching process:

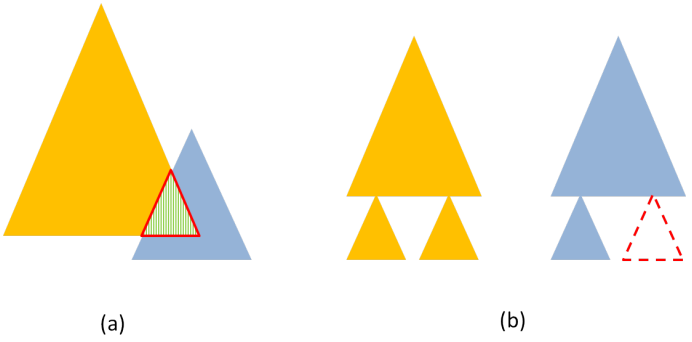

Figure 3.1.: Challenges. (a) Both trees (orange and blue) might have different sizes and share only a small subset of vertices (red triangle). (b) Part of a tree might be missing in one of the trees (red triangle in the blue tree).

(1) **Different sizes.** In general, the size of the two trees to be matched will differ. Note

that this condition does not exclude by itself the use of subtree isomorphism to solve the matching process. However, it cannot be ensured that one of the trees is completely contained in the other tree. They could actually share a small subset of vertices (see Figure 3.1 (a)).

(2) **Different topology.** It cannot be assumed that two corresponding nodes share the topology. Imaging artifacs and/or surgery will include topological variations in the tree. Consequently, two corresponding nodes could form ramifications of different sizes (e.g., a bifurcation and a trifurcation). To farther complicate the matching process, a single node in one tree could be represented by too close nodes in the second tree.

(3) **Missing subtrees.** During an intervention some vessels will be resected or ablated, consequently, they will not be present in the postoperative tree (see Figure 3.1 (b)).

Let T_1 and T_2 be two trees that represent the liver vasculature of the same patient acquired at two different points in time. Due to the aforementioned reasons both trees contain differences, for instance, missing or spurious branches. However, since they represent the same structure, they will also contain a common structure of nodes and branches. Thus, T_c is the tree common to T_1 and T_2 (see Figure 3.2). The goal of the tree matching method is to find the nodes of T_c.

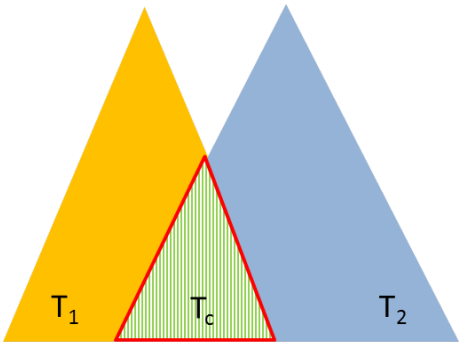

Figure 3.2.: Goal of the matching method. The trees T_1 and T_2 come from the same anatomical structure. Both trees contain differences (e.g., spurious and missing branches). However, they will also have common nodes. The goal of the matching method is to find a tree T_c containing the common nodes of both tree representations.

From the methods presented in the state of the art chapter (Chapter 2) the one proposed by Graham and Higgins [GH06a, GH06b] stands out in terms of efficiency. It will be used as starting point in this thesis. In general, tree matching methods consist of two main parts: the search technique to find matches (e.g., tree search) and the similarity metric used to determine which pair of nodes are actually corresponding nodes.

- Local similarity. As stated in Chapter 2, the selection of the similarity metric is crucial to achieve a high number of correct matches and not every metric is appropriate for every organ. Metrics based on geometric characteristics of nodes and branches

will be used to describe their local similarity. The results using different similarity metrics are evaluated in Section 3.1.

- Topological similarity. A key aspect of the method are the topological variations that are relevant in trees generated from the liver vasculature. The topological similarity (see Section 3.2) of the trees will be used in two ways. First, it will allow to restrict the search and therefore accelerate the method. Second, it will allow to consider as potential matches also node pairs that contain topological differences. The latter will allow for a more generic method that can handle real clinical challenges. Six topological variations relevant for the human airway were explicitly formulated by Graham and Higgins in [GH06a]. In this chapter 17 additional topological variations are explicitly formulated. Those topological variations can be often found in medical applications and result in an increased number of detected correspondences in the liver.

- Correspondence search. As mentioned before the method proposed by Graham and Higgins [GH06a, GH06b] is used as basis for the correspondence search. Opposite to the definition provided by Graham in [Gra08], the formal definition proposed in this chapter (Sections 3.3 and 3.4) focuses on the characteristics of the desired solution of the problem, namely, a topologically consistent injective solution to the matching problem. Therefore, the problem is defined using well known graph theory concepts. This formal definition of the problem allows its extension to cyclic graphs in Chapter 4. Furthermore, the complexity of the method is reduced with the introduction of two accelerators (Section 3.5).

- Manual preselection of node pairs (Section 3.6). The efficiency of the method is farther increased by subdividing the matching problem using a series of preselected node pairs.

The work presented in this chapter is partially covered in the author's previous publications [OLD11a, OLD10, DOLCE10].

3.1. Local similarity

The similarity metric has to be carefully selected. Depending on the similarity metric used the results obtained will vary as well as the characteristics of the method. Within this chapter the results achieved using metrics such as length, euclidean distance, mean radius, angle, radius, and direction are discussed.

In the remaining of the thesis the following notation will be used to describe potential matches. In general, given a node u in T_1, the notation $\phi(u)$ represents a potential correspondence to u in T_2. This notation will be specially used in pseudocodes and general definitions. For concrete examples the nodes will be labeled for a better understanding, for instance, $a \in T_1$ and $1 \in T_2$.

The most widely used attribute for matching of vascular trees is the length of the vessels (see Figure 3.3). This length refers to the geodesic distance (along the vessel centerline)

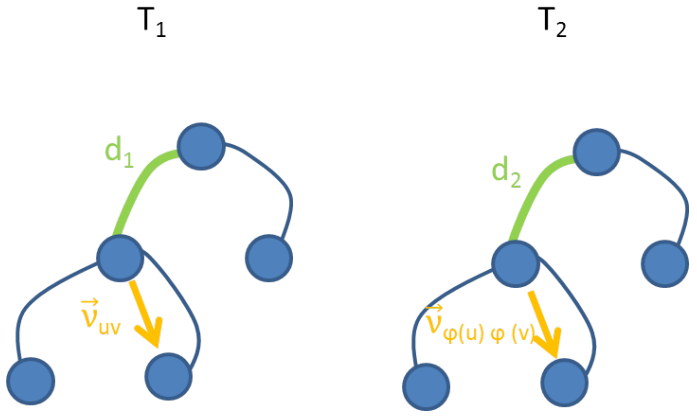

Figure 3.3.: Illustration of the geodesic length and direction attributes used as similarity metrics. In this example the length d_1 in T_1 will be compared to the length d_2 in T_2, and the direction vector $\vec{\nu}_{uv}$ in T_1 will be compared to the direction vector $\vec{\nu}_{\phi(u)\phi(v)}$ in T_2.

between two bifurcation points and not to their Euclidean distance (prone to differences due to deformations). The similarity measure using the length as attribute:

$$S_l = \begin{cases} -1 & \text{if } R > Th_l \\ \frac{-2R}{Th_l - 1} + \frac{Th_l + 1}{Th_l - 1} & \text{if } R \leq Th_l \end{cases}, \tag{3.1}$$

depends on a threshold Th_l that determines the tolerance of the method to variations of the length of two branches (u, v) in T_1 and $(\phi(u), \phi(v))$ in T_1 [GH06a]. The evaluation has shown that a threshold of 1.5 returns satisfactory results. The term R represents the ratio between length differences and is expressed as follows:

$$R = \max\left(\frac{d_1}{d_2}, \frac{d_2}{d_1}\right). \tag{3.2}$$

In this equation d_1 is the length between (u, v) and d_2 the one between $(\phi(u), \phi(v))$ (Figure 3.3). The maximum ratio between both of them is chosen for the calculations. Figure 3.4 (a) shows a plot of the Function 3.1 as the ratio R increases from 1 (minimum possible value for the ratio) to 2. For the generation of the curve the threshold Th_l was fixed to 1.5. One can observe that as R increases S_l decreases. When the threshold value is achieved (1.5) the value of S_l is -1. Since the threshold determines the maximum allowed difference between lengths, the rest of the values lack importance. Thus, they are set to the achieved minimum (-1).

The radius ratio between two bifurcations can also be used in a similar way as metric to find correspondences. In this case r_1 and r_2 are the radii of the two bifurcations and the ratio Q is given by:

$$Q = \max\left(\frac{r_1}{r_2}, \frac{r_2}{r_1}\right). \tag{3.3}$$

This is the only one of the studied attributes that belongs inherently to a vertex and not to a branch. While the radius can be found by inspecting the vessel at the position

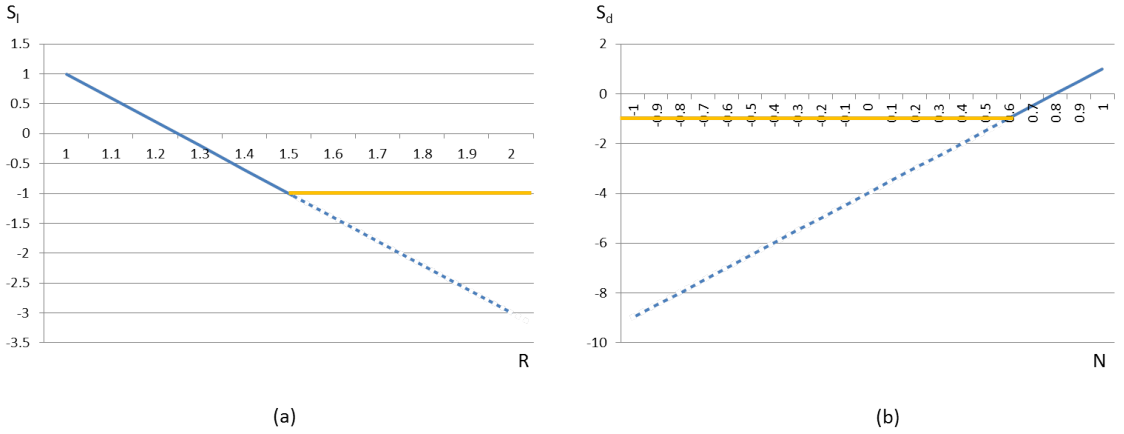

Figure 3.4.: Functions for the calculation of (a) the length (S_l) and (b) the direction (S_d) similarity metrics. For the generation of the curves a fixed value of the length and direction thresholds of 1.5 and 0.6 has been used. As Equations 3.1 and 3.4 suggest, when the threshold is reached, the similarity value is fixed to -1 (orange).

where the vertex is located, the rest of the attributes (e.g., angle) need two vertices (a branch) to be defined. A similar attribute is the mean radius, but in this case the value is calculated as a mean of the radius seen along the branch. For both radius and mean radius a threshold of 1.4 is used. The last attribute that can be analyzed using the same equation is the angle between two branches. A threshold of 0.2 returns the best results with this attribute.

For the calculation of the direction attribute the equation changes slightly. The direction is a vector and has the advantage against the angle to be oriented in space. While a single angle can be pointing in endless directions in 3D, the direction is fully defined given a known orientation. Thus, the angle will be in some cases unable to solve ambiguous matches. Ambiguities would still be a problem if the angle between children would be used instead, having the additional disadvantage of requiring a root dependent method. On the other side the angle would result in a method less tolerant to topology changes. The direction is pose dependent unless it is calculated related to a certain known position in space, for instance, a pair of know roots. The similarity S_d [GH06a] can be calculated in a similar way as it was done with the previous metrics:

$$S_d = \begin{cases} -1 & \text{if } N < Th_d \\ \frac{-2N}{Th_d - 1} + \frac{Th_d + 1}{Th_d - 1} & \text{if } N \geq Th_d \end{cases}. \tag{3.4}$$

As in previous cases there is a threshold Th_d (0.6) to control the maximum tolerable difference between the directions. The ratio N is given by:

$$N = \frac{\vec{\nu}_{uv} \cdot \vec{\nu}_{\phi(u)\phi(v)}}{\|\vec{\nu}_{uv}\| \cdot \|\vec{\nu}_{\phi(u)\phi(v)}\|}, \tag{3.5}$$

where $\vec{\nu_{uv}}$ is the direction vector between two branching points u and v and $\|\vec{\nu_{uv}}\|$ is the norm of the vector (Figure 3.3). The ratio N is the cosine of the angle between both

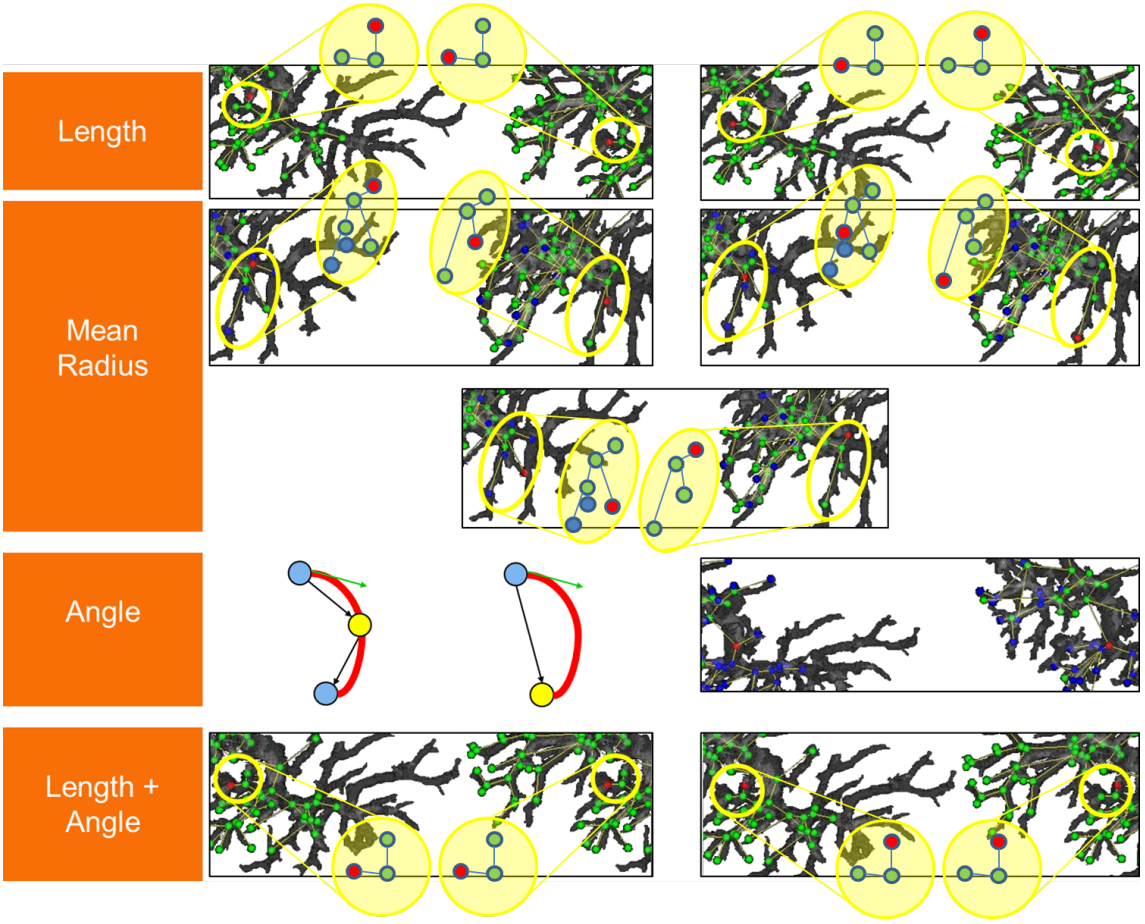

Figure 3.5.: Inaccuracies in the results appear when only one attribute is used for the similarity metric calculation (see highlighted red correspondences). A combination of two attributes improve the results in structure locations that are prone to errors due to ambiguities.

vectors. Figure 3.4 (b) shows a plot of the function for the calculation of S_d. Taking into account that N is the cosine of the aforementioned angle, a large N represents a small angle between the direction vectors, thus, a higher similarity S_d. When N equals 0.6 the threshold Th_d is achieved, thus, the rest of the values are fixed again to -1.

The total local similarity (SL) between a pair of nodes is the combination of several metrics and will be given by:

$$SL = \sum_{a \in A} w_a * S_a \tag{3.6}$$

and

$$\sum_{a \in A} w_a = 1, \tag{3.7}$$

where w_a is the weight given to the similarity metric a and A is the set of similarity metrics. In Section 3.7 the best value given to those weights is studied.

Attributes \ % of removed nodes		0	5	10	20	30	40	50
Length	Matches/Total matches	101/101	95/95	74/90	66/81	60/70	42/60	30/49
	No. wrong matches	2	2	2	3	1	1	0
Mean radius	Matches/Total matches	101/101	95/95	74/90	59/81	60/70	37/60	22/49
	No. wrong matches	0	2	1	11	16	12	6
Angle	Matches/Total matches	101/101	87/95	40/90	33/81	24/70	16/60	8/49
	No. wrong matches	0	3	1	4	8	5	4
Radius	Matches/Total matches	84/101	79/95	63/90	62/81	60/70	39/60	23/49
	No. wrong matches	33	22	27	29	30	27	15
0.8*Length + 0.2*Angle		0	0	0	2			
0.9*Length + 0.1*Angle					1	3		
0.95*Length + 0.05*Angle		0				2		
0.99*Length + 0.01*Angle		0	0	0	2	1	1	0
0.999*Length + 0.001*Angle		0	0	0	2	0	1	0

Table 3.1.: Evaluation of the accuracy of the method depending on the attribute used for the similarity measure calculation.

Evaluation To see the effect of the chosen attributes in the matching process a vessel tree has been extracted from a clinical CT image of the liver. Then an artificial tree has been created to ensure that ground truth data is available. For the artificial tree generation nodes have been randomly removed from the original tree. Note that even if some nodes have been removed, the ground truth result of the matching is still known. Thus, up to 50% of the nodes are removed. The removal technique will be further explained in the evaluation chapter.

Figure 3.5 shows the problems arose from using a single attribute as similarity metric. In each figure the red nodes have been matched to each other. Making the assumption [SBK10] that the vessels deform isometrically (the length of the vessels does not change significantly), the length should be the most trustful attribute. But in spite of being the most robust attribute for vessel like structures, it introduces inaccurate results in areas in which ambiguous structures are present (Figure 3.5 first).

As it is shown in Table 3.1 the mean radius performs nicely up to 20% of removed nodes. Then, the number of wrong matches increases greatly (up to 23% wrong matches detected). However it is still more accurate than the radius attribute (in the order of 43% wrong matches). The latter does not only contain a larger number of wrong correspondences, but it also hardly detects a high number of correspondences. A combination between the angle and length attribute seems to be a good option. However, the problem remains that the angle cannot handle all ambiguities correctly (up to 11% wrong matches).

Table 3.2 summarizes the advantages and disadvantages of the different similarity metrics. One can observe that those similarity metrics that are pose independent have the

Attribute	Advantage	Disadvantage
Length	Pose independent	Ambiguous matches
Radius	Pose independent	Ambiguous matches –
Mean radius	Pose independent	Ambiguous matches -
Angle	Pose independent	Ambiguous matches Deformations
Euclidean distance	Pose independent	Ambiguous matches Deformations
Direction	No ambiguous matches High number of correct matches	Pose dependent

Table 3.2.: Advantages and disadvantages of the different similarity metrics.

disadvantage of returning wrong matches due to ambiguities in the trees. Among them, radius (–) and mean radius (-) produce more wrong matches. The direction on the contrary is robust over ambiguities but is pose dependent.

The length and direction are the most appropriate attribute combination. This combination returns the highest number of correct matches. A thorough evaluation of the accuracy of the method using this combination can be found in Section 3.7. However, this combination results in a pose dependent method. In Section 4.3 a pose independent solution that encompasses the advantages of pose independent attributes (e.g., angle, length) and of robust attributes (e.g., direction) is proposed.

3.2. Topological similarity

As it was mentioned before topological and geometrical similarities will be used to find the final set of matches. In order to take into account the topological changes derived from problems 1 to 3 (see introduction) in the matching process a series of so-called primitives are defined. The primitives were initially defined by Graham and Higgins [GH06a, GH06b] and describe the topologies and topological changes (e.g., missing branches) that can be observed in trees derived from medical structures. Figure 3.6 serves to explain the initial set of primitives considered by Graham and Higgins. Let T_1 and T_2 be the two trees to be matched. The rows and columns of the figure show the topological structures that can be observed in T_1 and T_2 respectively. Following this figure one can see that each primitive is in charge of comparing two topological structures. In each structure the yellow node represents the nodes under study. This means that the topological similarity of the yellow nodes in T_1 and T_2 will be investigated. Two yellow nodes in the same structure represent nodes that are close and therefore can be merged. The motivation for merging nodes will be discussed in the next paragraphs. Thus, the set of primitives introduced by Graham and Higgins in [GH06a] (blue in the figure) contain:

1. Leaves in both trees (primitive 0).
2. Planted roots in both trees (primitive 1).
3. Bifurcations in both trees (primitive 2).

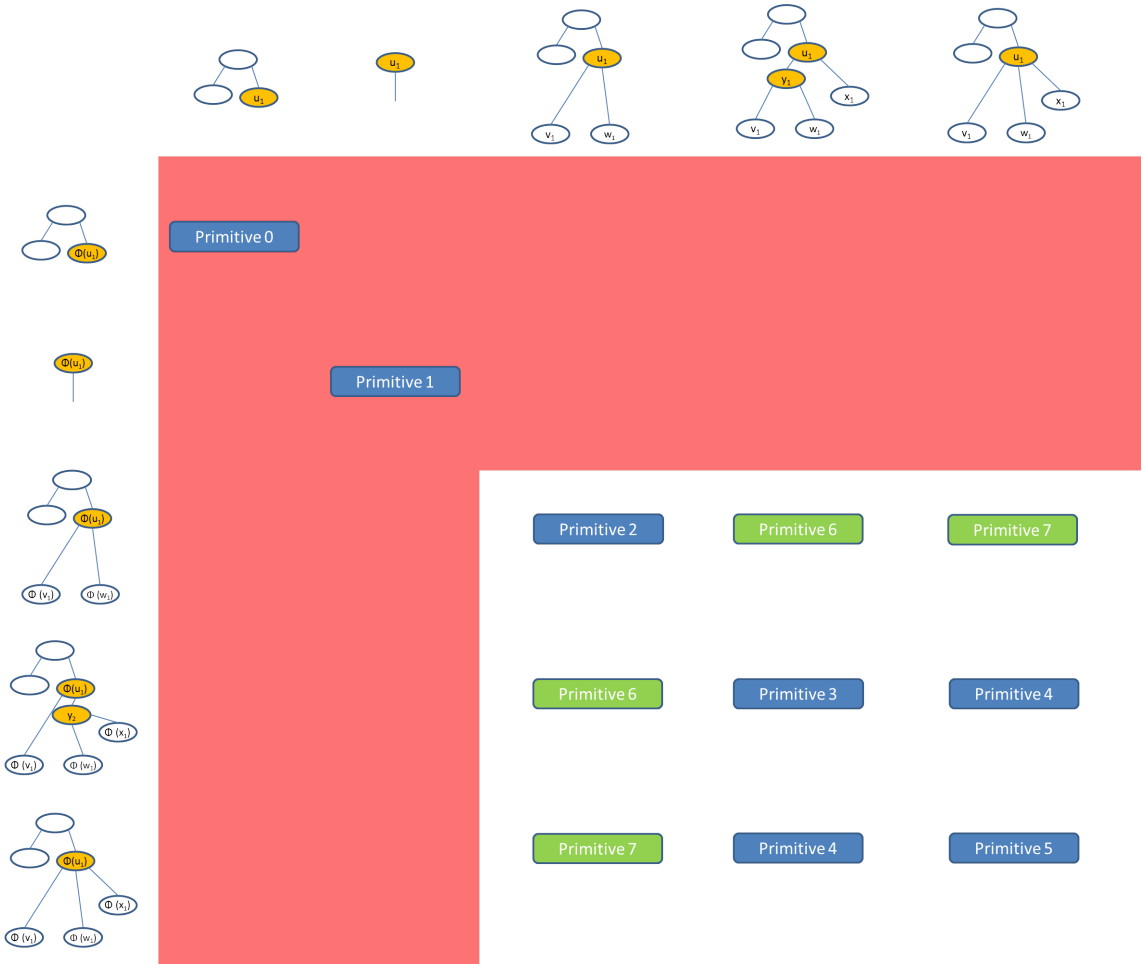

Figure 3.6.: Initial set of primitives. The first row and column show the structures that can be found in the first and second trees respectively. Each primitive is in charge of the comparison of two topological structures. The topologies in blue were introduced by Graham and Higgins in [GH06a], the green ones will be formulated in this chapter. As it is explained in the text the red area corresponds to topological structure comparisons that can be ignored in the proposed method.

4. Trifurcations in both trees (primitive 5).

5. A trifurcation derived from merging two close bifurcations in both trees where the ordering of the branches is reversed (primitive 3).

6. A trifurcation derived from merging two close bifurcations in one of the trees (T_1) and a trifurcation in the other tree (T_2) (primitive 4).

However, this initial set of primitives that was defined to find correspondences between human airways does not suffice for the liver vasculature. While in the human airway trifurcations are the larger ramifications that can be found, in the liver ramifications of up to 4 nodes are usual. Furthermore, the hard constraint of having planted roots cannot be assumed when matching liver trees. For instance, trees extracted from intraoperative

images will not necessarily contain the physical root of the liver vascular system. Thus, the combinations of other topological structures with the planted root are ignored (see red area in the figure). Finally, the topology of a node is determined by its children. Leaves do not have children and thus, can be ignored from a topological point of view. They will be matched using local similarity (Section 3.1).

In the following paragraphs the required primitives are explicitly formulated. For a definition of the six primitives specific for the human airway the reader is encouraged to read [GH06a].

The structures derived from medical vascular trees can be divided in three groups:

- Direct. Those structures show the same topology in both trees, e.g., a trifurcation in both trees. This group encompasses primitives 0, 1, 2, 5 in Figure 3.6 and primitive 8 in Figure 3.7.
- Close nodes. The presence of two close ramifications can be due two reasons: the real structure contains actually two close ramifications, or they appear slightly separated because of inaccuracies in the previous segmentation or graph generation methods. In the second case the real structure will contain one single ramification, but its graph representation will contain two very close nodes. To solve this inaccuracy and get as many correspondences as possible, these ramifications can be merged. Primitives 3 and 4 in Figure 3.6 and primitives 9, 10, 11, 12 and 13 in Figure 3.7 belong to this group. Note that the effect of merging nodes in the matching process will mean a higher amount of reduced trees in the set of reduced trees (see Section 3.3.1).
- Missing and spurious branches. Imaging artifacts will also be responsible for the appearance of spurious branches in one of the trees. In that case ramifications of different degrees might actually correspond (e.g., a bifurcation and a trifurcation). The goal is to ignore the spurious branch and match the other. Those structures might also contain nodes to be merged, but even after merging the spurious branches should be detected and ignored. This topological structures are represented by primitives 6 and 7 in Figure 3.6 and all primitives in Figure 3.8. The explicit formulation of those primitives is included for completeness, however the topological changes due to spurious branches are already incorporated in the formal definition of the matching problem (see Section 3.3.1).

Note that the 17 primitives that are formulated in the next paragraphs significantly extend the role of the original primitives. Initially [GH06a], they were used to restrict the set of valid matches according to their topology (e.g., two bifurcations). However, the set of meaningful combinations taking into account all existing challenges (missing branches, close nodes and combinations of both) is larger. **The primitives shown in Figure 3.8 allow to match alternative topologies, for instance, a ramification of four nodes with a bifurcation, or two close bifurcations with a ramification of 4 nodes.** These topologies, that might be rarely seen in other applications, are common in medical imaging. If they are not considered, two ramifications could be completely ignored due to their topology differences although they actually correspond. The clinical scenario studied in this

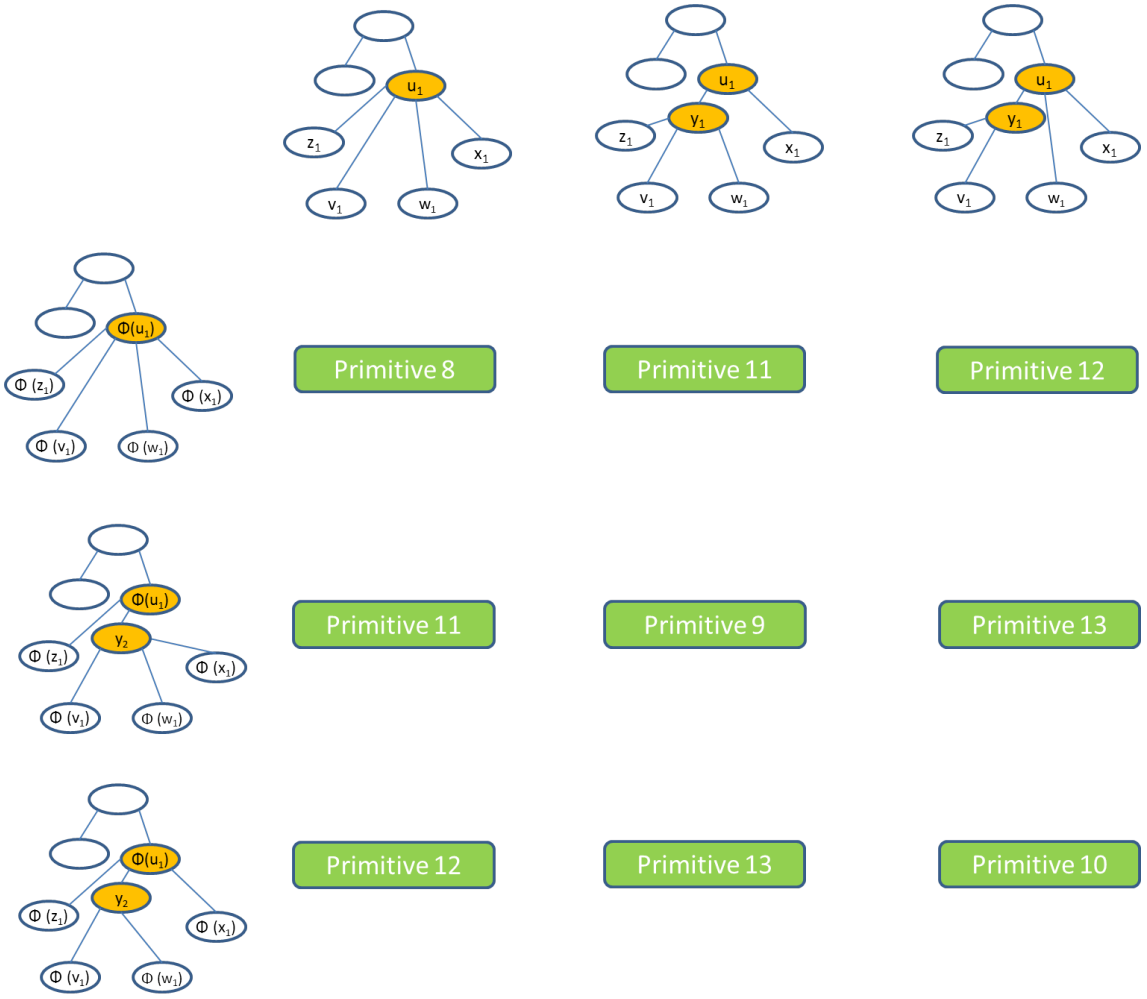

Figure 3.7.: Direct and close node primitives derived from the ramifications of 4 nodes.

thesis (liver resection) increases the need to handle those topological differences appropriately. If this is not the case, a high number of correct matches could be ignored, which at the end would lead to a reduced registration accuracy. Thus, this set of primitives mean a closer representation of trees coming from vascular trees and the final set of matches will contain correspondences that could not be found with the original set of primitives.

In the following $\Psi^{(i)}(T_1^{u_1}, T_2^{\phi(u_1)})$ denotes the set of i primitives that fulfill certain mathematical conditions. Let T_1 and T_2 be the two trees to be matched. $T_1^{u_1} \in T_1$ and $T_2^{\phi(u_1)} \in T_2$ are two subtrees with roots u_1 and $\phi(u_1)$ respectively. The notation $\phi(u_1)$ means that the node $u_1 \in T_1$ will be matched to $\phi(u_1) \in T_2$. Thus, $\phi = (u_1, \phi(u_1), ...(u_n, \phi(u_n))$ is a matching function that maps the nodes in T_1 to the nodes in T_2. $\psi_\phi^{u_1}$ is the restriction of ϕ when only the subtree with root u_1 is considered. The number of children of a node u_1 (degree of u_1) is denoted as $\delta(u_1)$. $lca(u_1, u_2)$ is the least common ancestor of the nodes $u_1 \in T_1$ and $u_2 \in T_1$, and $E(T_1)$ the set of branches of the tree T_1.

3.2.1. Direct

The direct primitive that has to be taken into account to match liver trees corresponds to a ramification of 4 nodes in both trees (primitive 8 in Figure 3.7). In this case no nodes have to be merged. The mathematical definition of the primitive follows:

$$\psi_{\phi}^{u_1} \in \Psi^{(8)}(T_1^{u_1}, T_2^{\phi(u_1)}) \text{ if:} \tag{3.8}$$

(1) $\psi_{\phi}^{u_1} = \{(u_1, \phi(u_1)), (v_1, \phi(v_1)), (w_1, \phi(w_1)), (x_1, \phi(x_1)), (z_1, \phi(z_1))\}$

(2) $lca(v_1, w_1) = lca(v_1, z_1) = lca(v_1, x_1) = lca(w_1, z_1) = lca(w_1, x_1) = lca(z_1, x_1) = u_1$ *in* T_1

(3) $lca(\phi(v_1), \phi(w_1)) = lca(\phi(v_1), \phi(z_1)) = lca(\phi(v_1), \phi(x_1)) = lca(\phi(w_1), \phi(z_1)) = lca(\phi(w_1), \phi(x_1)) = lca(\phi(z_1), \phi(x_1)) = \phi(u_1)$ *in* T_2

The first condition shows that the goal of this primitive is to find 5 matches. Condition (2) and (3) describe the topological structure of $T_1^{u_1}$ and $T_2^{\phi(u_1)}$ respectively.

3.2.2. Close nodes

In primitive 9 both trees contain a bifurcation close to a trifurcation but the ordering of their branches is reversed as illustrated in Figure 3.7. This is mathematically defined as follows:

$$\psi_{\phi}^{u_1} \in \Psi^{(9)}(T_1^{u_1}, T_2^{\phi(u_1)}) \text{ if:} \tag{3.9}$$

(1) $\psi_{\phi}^{u_1} = \{(u_1, \phi(u_1)), (v_1, \phi(v_1)), (w_1, \phi(w_1)), (x_1, \phi(x_1)), (z_1, \phi(z_1))\}$

(2) $\delta(u_1) = 2$ *in* T_1, $\delta(\phi(u_1)) = 2$ *in* T_2

(3) $lca(v_1, w_1) = lca(v_1, z_1) = lca(w_1, z_1) = y_1$ *in* T_1, *where* $(u_1, y_1) \in E(T_1)$

(4) $lca(\phi(v_1), \phi(w_1)) = lca(\phi(v_1), \phi(x_1)) = lca(\phi(w_1), \phi(x_1)) = y_2$ *in* T_2, *where* $(\phi(u_1), y_2) \in E(T_2)$

(5) $lca(z_1, x_1) = lca(v_1, x_1) = lca(w_1, x_1) = u_1$ *in* T_1

(6) $lca(\phi(z_1), \phi(v_1)) = lca(\phi(z_1), \phi(w_1)) = lca(\phi(z_1), \phi(x_1)) = \phi(u_1)$ *in* T_2

Without merging u_1 and y_1 in $T_1^{u_1}$ and $\phi(u_1)$ and y_2 in $T_1^{\phi(u_1)}$ 3 of the potential matches cannot be detected due to the topology of the trees (see reversed order of the branches in the figure). Thanks to the merging step all matches can be topologically found.

A similar case can be observed in primitive 10. Opposite to primitive 9 the degree of u_1 and ϕu_1 is now 3. Again, if u_1 and y_1, and $\phi(u_1)$ and y_2 are merged every node from both trees could be matched (Figure 3.7 primitive 10). Nevertheless, if the merging would not take place, v_1 would remain unmatched. Again the structure needs to be mathematically defined as follows:

$$\psi_{\phi}^{u_1} \in \Psi^{(10)}(T_1^{u_1}, T_2^{\phi(u_1)}) \text{ if:} \tag{3.10}$$

(1) $\psi_{\phi}^{u_1} = \{(u_1, \phi(u_1)), (v_1, \phi(v_1)), (w_1, \phi(w_1)), (x_1, \phi(x_1)), (z_1, \phi(z_1))\}$

(2) $\delta(u_1) = 3$ *in* T_1, $\delta(\phi(u_1)) = 3$ *in* T_2

(3) $lca(z_1, v_1) = y_1$ *in* T_1, *where* $(u_1, y_1) \in E(T_1)$

(4) $lca(\phi(v_1), \phi(w_1)) = y_2$ *in* T_2, *where* $(\phi(u_1), y_2) \in E(T_2)$

(5) $lca(z_1, w_1) = lca(z_1, x_1) = lca(v_1, w_1) = lca(v_1, x_1) = lca(w_1, x_1) = u_1$ *in* T_1

(6) $lca(\phi(z_1), \phi(v_1)) = lca(\phi(z_1), \phi(w_1)) = lca(\phi(z_1), \phi(x_1)) = lca(\phi(v_1), \phi(x_1)) = lca(\phi(w_1), \phi(x_1)) = \phi(u_1)$ *in* T_2

Merging is again important when one of the trees contains a bifurcation close to a trifurcation and the other one contains a ramification of 4 nodes. As can be seen in Figure 3.7 (Primitive 11), if nodes u_1 and y_1 are not merged, only two nodes could be matched due to topological reasons ($(x_1, \phi(x_1))and(z_1, \phi(z_1)), (v_1, \phi(v_1))or(w_1, \phi(w_1))$). If they are merged, on the other side, 2 additional matches could be detected.

The conditions that this primitive should fulfill are expressed as follows:

$$\psi_{\phi}^{u_1} \in \Psi^{(11)}(T_1^{u_1}, T_2^{\phi(u_1)}) \text{ if:} \tag{3.11}$$

(1) $\psi_{\phi}^{u_1} = \{(u_1, \phi(u_1)), (v_1, \phi(v_1)), (w_1, \phi(w_1)), (x_1, \phi(x_1)), (z_1, \phi(z_1))\}$

(2) $\delta(u_1) = 4$ *in* T_1, $\delta(\phi(u_1)) = 2$ *in* T_2

(3) $lca(\phi(v_1), \phi(w_1)) = lca(\phi(v_1), \phi(x_1)) = lca(\phi(w_1), \phi(x_1)) = y_2$ *in* T_2, *where* $(\phi(u_1), y_2) \in E(T_2)$

(4) $lca(v_1, w_1) = lca(v_1, z_1) = lca(v_1, x_1) = lca(w_1, z_1) = lca(w_1, x_1) = lca(z_1, x_1) = u_1$ *in* T_1

(5) $lca(\phi(z_1), \phi(v_1)) = lca(\phi(z_1), \phi(w_1)) = lca(\phi(z_1), \phi(x_1)) = \phi(u_1)$ *in* T_2

Primitive 12 handles a similar situation. In this case one of the trees has a trifurcation close to a bifurcation. The second tree has a ramification of 4 nodes. Note that the difference is the degree of u_1 or $\phi(u_1)$. While in primitive 11 $\delta(u_1) = 2$, in primitive 12 $\delta(u_1) = 3$. The final effect of the merging in both cases is similar as can be seen in Figure 3.7. Nevertheless, in the case of primitive 12 the solution without merging would return one additional match compared to primitive 11. The conditions for this primitive have to be adapted accordingly:

$$\psi_{\phi}^{u_1} \in \Psi^{(12)}(T_1^{u_1}, T_2^{\phi(u_1)}) \text{ if:} \tag{3.12}$$

(1) $\psi_{\phi}^{u_1} = \{(u_1, \phi(u_1)), (v_1, \phi(v_1)), (w_1, \phi(w_1)), (x_1, \phi(x_1)), (z_1, \phi(z_1))\}$

(2) $\delta(u_1) = 4$ *in* T_1, $\delta(\phi(u_1)) = 3$ *in* T_2

(3) $lca(\phi(v_1), \phi(w_1)) = y_2$ *in* T_2, *where* $(\phi(u_1), y_2) \in E(T_2)$

(4) $lca(v_1, w_1) = lca(v_1, z_1) = lca(v_1, x_1) = lca(w_1, z_1) = lca(w_1, x_1) = lca(z_1, x_1) = u_1$ *in* T_1

(5) $lca(\phi(z_1), \phi(v_1)) = lca(\phi(z_1), \phi(w_1)) = lca(\phi(z_1), \phi(x_1)) = lca(\phi(v_1), \phi(x_1)) = lca(\phi(w_1), \phi(x_1)) = \phi(u_1)$ *in* T_2

Primitive 13 describes the structure in which one of the trees contains a bifurcation close to a trifurcation and the other tree contains a trifurcation close to a trifurcation as illustrated in Figure 3.7. This is mathematically defined as follows:

$$\psi_{\phi}^{u_1} \in \Psi^{(13)}(T_1^{u_1}, T_2^{\phi(u_1)}) \text{ if:} \tag{3.13}$$

(1) $\psi_{\phi}^{u_1} = \{(u_1, \phi(u_1)), (v_1, \phi(v_1)), (w_1, \phi(w_1)), (x_1, \phi(x_1)), (z_1, \phi(z_1))\}$

(2) $\delta(u_1) = 3$ *in* T_1, $\delta(\phi(u_1)) = 2$ *in* T_2

(3) $lca(z_1, v_1) = y_1$ *in* T_1, *where* $(u_1, y_1) \in E(T_1)$

(4) $lca(\phi(v_1), \phi(w_1)) = lca(\phi(v_1), \phi(x_1)) = lca(\phi(w_1), \phi(x_1)) = y_2$ *in* T_2, *where* $(\phi(u_1), y_2) \in E(T_2)$

(5) $lca(z_1, w_1) = lca(z_1, x_1) = lca(v_1, w_1) = lca(v_1, x_1) = lca(w_1, x_1) = u_1$ *in* T_1

(6) $lca(\phi(z_1), \phi(v_1)) = lca(\phi(z_1), \phi(w_1)) = lca(\phi(z_1), \phi(x_1)) = \phi(u_1)$ *in* T_2

3.2.3. Missing and spurious branches

Due to missing branches sometimes one of the trees will contain less children than the other one. This can be observed in the primitives of Figure 3.6 (green) and in Figure 3.8. Note that for visualization purposes the matrix shown in Figure 3.8 has not been mirrored, i.e., the topologies in the rows and columns have to be seen as a pair. A pair of bifurcation and ramification of four nodes, for instance, is independent of which one of the trees contains the bifurcation (T_1 or T_2). In both cases the same primitive will represent this pair.

Primitive 6 deals with the case in which one of the trees contains two close bifurcations and the other one a bifurcation. With this combination of topological structures there will be one node (x_1) that will remain unmatched after merging. This corresponds to a spurious branch that appears attached to the structure due to noise or artifacts in the image. Figure 3.6 illustrates this primitive and the mathematical conditions that it should fulfill are expressed as:

$$\psi_{\phi}^{u_1} \in \Psi^{(6)}(T_1^{u_1}, T_2^{\phi(u_1)}) \text{ if:} \tag{3.14}$$

(1) $\psi_{\phi}^{u_1} = \{(u_1, \phi(u_1)), (v_1, \phi(v_1)), (w_1, \phi(w_1))\}$

(2) $\delta(u_1) = 2$ *in* T_1, $\delta(\phi(u_1)) = 2$ *in* T_2

(3) $lca(v_1, w_1) = y_1$ *in* T_1, *where* $(u_1, y_1) \in E(T_1)$

(4) $lca(v_1, x_1) = lca(w_1, x_1) = u_1$ *in* T_1

(5) $lca(\phi(v_1), \phi(w_1)) = \phi(u_1)$ *in* T_2

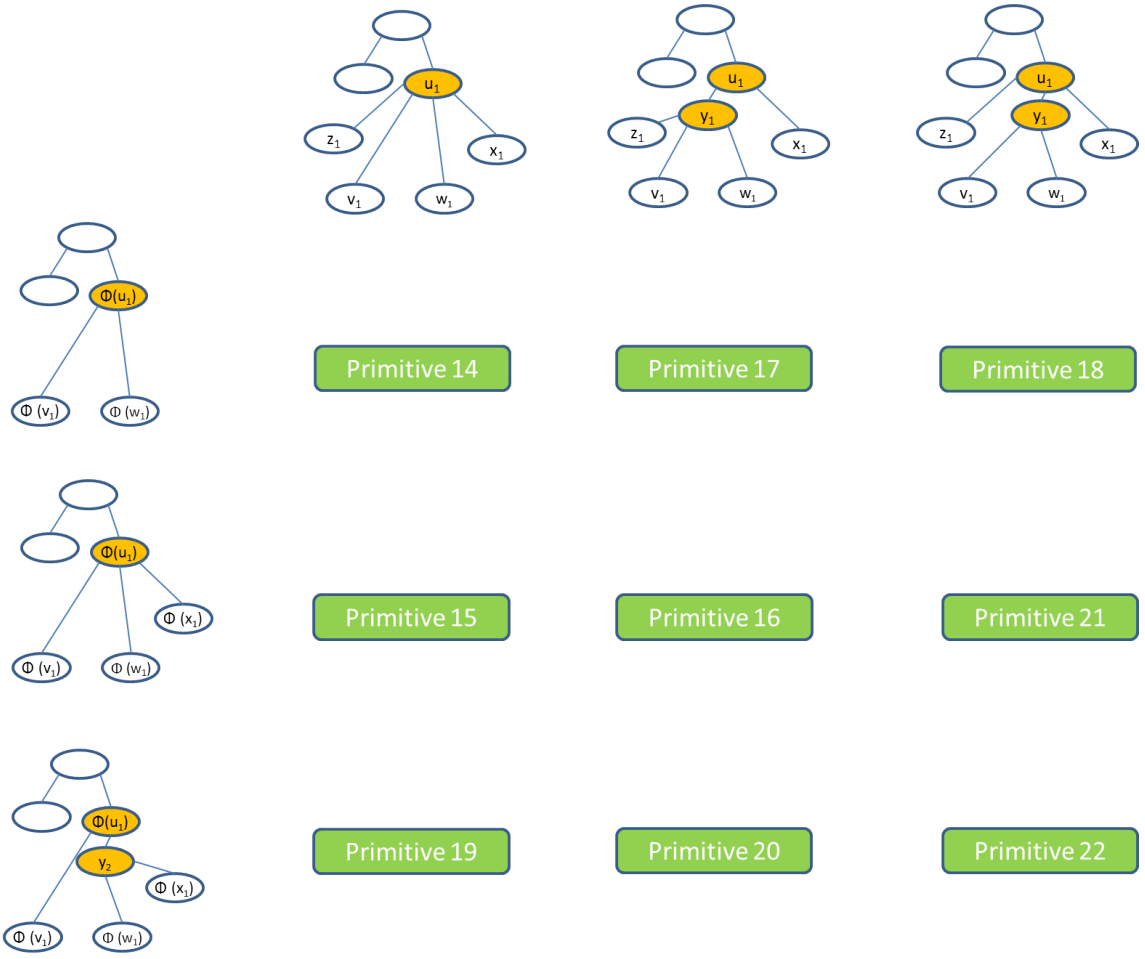

Figure 3.8.: Primitives caused by missing and spurious branches.

Primitive 7 (Figure 3.6) represents the topological structure combination in which one of the trees contains a trifurcation and the other one a bifurcation. Again node x_1 represents the spurious branch. This can be mathematically expressed as follows:

$$\psi_{\phi}^{u_1} \in \Psi^{(7)}(T_1^{u_1}, T_2^{\phi(u_1)}) \text{ if:} \tag{3.15}$$

(1) $\psi_{\phi}^{u_1} = \{(u_1, \phi(u_1)), (v_1, \phi(v_1)), (w_1, \phi(w_1))\}$

(2) $\delta(u_1) = 3$ *in* T_1, $\delta(\phi(u_1)) = 2$ *in* T_2

(3) $lca(v_1, w_1) = lca(v_1, x_1) = lca(w_1, x_1) = u_1$ *in* T_1

(4) $lca(\phi(v_1), \phi(w_1)) = \phi(u_1)$ *in* T_2

The next primitives represent spurious and missing branches contained in ramifications of 4 nodes. When two of the branches are spurious in the ramification of 4 nodes (z_1 and x_1) a bifurcation could actually correspond to the ramification of 4 nodes. This is represented in primitive 14 (Figure 3.8):

$$\psi_{\phi}^{u_1} \in \Psi^{(14)}(T_1^{u_1}, T_2^{\phi(u_1)}) \text{ if:} \tag{3.16}$$

(1) $\psi_{\phi}^{u_1} = \{(u_1, \phi(u_1)), (v_1, \phi(v_1)), (w_1, \phi(w_1))\}$

(2) $\delta(u_1) = 4$ *in* T_1, $\delta(\phi(u_1)) = 2$ *in* T_2

(3) $lca(z_1, v_1) = lca(z_1, w_1) = lca(z_1, x_1) = lca(v_1, w_1) = lca(v_1, x_1) = lca(w_1, x_1) = u_1$ *in* T_1

(4) $lca(\phi(v_1), \phi(w_1)) = \phi(u_1)$ *in* T_2

A similar effect occur when there is only one spurious branch (z_1), i.e., the second tree contains a trifurcation (Figure 3.8). This is incorporated in primitive 15:

$$\psi_{\phi}^{u_1} \in \Psi^{(15)}(T_1^{u_1}, T_2^{\phi(u_1)}) \text{ if:} \tag{3.17}$$

(1) $\psi_{\phi}^{u_1} = \{(u_1, \phi(u_1)), (v_1, \phi(v_1)), (w_1, \phi(w_1)), (x_1, \phi(x_1))\}$

(2) $\delta(u_1) = 4$ *in* T_1, $\delta(\phi(u_1)) = 3$ *in* T_2

(3) $lca(z_1, v_1) = lca(z_1, w_1) = lca(z_1, x_1) = lca(v_1, w_1) = lca(v_1, x_1) = lca(w_1, x_1) = u_1$ *in* T_1

(4) $lca(\phi(v_1), \phi(w_1)) = lca(\phi(v_1), \phi(x_1)) = lca(\phi(w_1), \phi(x_1)) = \phi(u_1)$ *in* T_2

As it was mentioned before in some cases after merging some spurious branches will also be present. Primitive 16 deals with this effect when one of the trees contains a bifurcation close to a trifurcation (resulting in a ramification of 4 nodes after merging), and the other tree consists of a trifurcation. In the example shown in Figure 3.8 z_1 correspond to the spurious branch. The mathematical description of this primitive is:

$$\psi_{\phi}^{u_1} \in \Psi^{(16)}(T_1^{u_1}, T_2^{\phi(u_1)}) \text{ if:} \tag{3.18}$$

(1) $\psi_{\phi}^{u_1} = \{(u_1, \phi(u_1)), (v_1, \phi(v_1)), (w_1, \phi(w_1)), (x_1, \phi(x_1)))\}$

(2) $\delta(u_1) = 2$ *in* T_1, $\delta(\phi(u_1)) = 3$ *in* T_2

(3) $lca(z_1, v_1) = lca(z_1, w_1) = lca(v_1, w_1) = y_1$ *in* T_1, *where* $(u_1, y_1) \in E(T_1)$

(4) $lca(z_1, x_1) = lca(v_1, x_1) = lca(w_1, x_1) = u_1$ *in* T_1

(5) $lca(\phi(v_1), \phi(w_1)) = lca(\phi(v_1), \phi(x_1)) = lca(\phi(w_1), \phi(x_1)) = \phi(u_1)$ *in* T_2

Similarly, primitive 17 deals with this effect when one of the trees contains a bifurcation close to a trifurcation (resulting in a ramification of 4 nodes after merging), and the other tree consists of a bifurcation. According to Figure 3.8 z_1 and x_1 correspond to spurious branches. The mathematical description of this primitive is:

$$\psi_{\phi}^{u_1} \in \Psi^{(17)}(T_1^{u_1}, T_2^{\phi(u_1)}) \text{ if:} \tag{3.19}$$

(1) $\psi_{\phi}^{u_1} = \{(u_1, \phi(u_1)), (v_1, \phi(v_1)), (w_1, \phi(w_1))\}$

(2) $\delta(u_1) = 2$ *in* T_1, $\delta(\phi(u_1)) = 2$ *in* T_2

(3) $lca(z_1, v_1) = lca(z_1, w_1) = lca(v_1, w_1) = y_1$ *in* T_1, *where* $(u_1, y_1) \in E(T_1)$

(4) $lca(z_1, x_1) = lca(v_1, x_1) = lca(w_1, x_1) = u_1$ *in* T_1

(5) $lca(\phi(v_1), \phi(w_1)) = \phi(u_1)$ *in* T_2

Primitive 18 will be used when on tree contains a trifurcation close to a bifurcation and the other tree contains a bifurcation. Again, z_1 and x_1 represent the spurious branches in Figure 3.8. The mathematical description of this primitive is:

$$\psi_{\phi}^{u_1} \in \Psi^{(18)}(T_1^{u_1}, T_2^{\phi(u_1)}) \text{ if:} \tag{3.20}$$

(1) $\psi_{\phi}^{u_1} = \{(u_1, \phi(u_1)), (v_1, \phi(v_1)), (w_1, \phi(w_1))\}$

(2) $\delta(u_1) = 3$ *in* T_1, $\delta(\phi(u_1)) = 2$ *in* T_2

(3) $lca(v_1, w_1) = y_1$ *in* T_1, *where* $(u_1, y_1) \in E(T_1)$

(4) $lca(z_1, v_1) = lca(z_1, w_1) = lca(z_1, x_1) = lca(v_1, x_1) = lca(w_1, x_1) = u_1$ *in* T_1

(5) $lca(\phi(v_1), \phi(w_1)) = \phi(u_1)$ *in* T_2

Primitive 19 deals with the topologies of a ramification of 4 nodes and a bifurcation close to a trifurcation. Considering this structures there is one single spurious branch, namely, the one corresponding to the node z_1 (Figure 3.8). The mathematical description of this primitive is:

$$\psi_{\phi}^{u_1} \in \Psi^{(19)}(T_1^{u_1}, T_2^{\phi(u_1)}) \text{ if:} \tag{3.21}$$

(1) $\psi_{\phi}^{u_1} = \{(u_1, \phi(u_1)), (v_1, \phi(v_1)), (w_1, \phi(w_1)), (x_1, \phi(x_1))\}$

(2) $\delta(u_1) = 4$ *in* T_1, $\delta(\phi(u_1)) = 2$ *in* T_2

(3) $lca(\phi(w_1), \phi(x_1)) = y_2$ *in* T_2, *where* $(\phi(u_1), y_2) \in E(T_2)$

(4) $lca(z_1, v_1) = lca(z_1, w_1) = lca(z_1, x_1) = lca(v_1, w_1) = lca(v_1, x_1) = lca(w_1, x_1) = u_1$ *in* T_1

(5) $lca(\phi(v_1), \phi(w_1)) = lca(\phi(v_1), \phi(x_1)) = \phi(u_1)$ *in* T_2

In primitive 20 two close bifurcation are present in one tree and a trifurcation and a bifurcation in the other tree. As in previous primitives z_1 represents the spurious branch in Figure 3.8. The mathematical description of this primitive is:

$$\psi_{\phi}^{u_1} \in \Psi^{(20)}(T_1^{u_1}, T_2^{\phi(u_1)}) \text{ if:} \tag{3.22}$$

(1) $\psi_{\phi}^{u_1} = \{(u_1, \phi(u_1)), (v_1, \phi(v_1)), (w_1, \phi(w_1)), (x_1, \phi(x_1))\}$

(2) $\delta(u_1) = 2$ *in* T_1, $\delta(\phi(u_1)) = 2$ *in* T_2

(3) $lca(z_1, v_1) = lca(z_1, w_1) = lca(v_1, w_1) = y_1$ *in* T_1, *where* $(u_1, y_1) \in E(T_1)$

(4) $lca(\phi(w_1), \phi(x_1)) = y_2$ *in* T_2, *where* $(\phi(u_1), y_2) \in E(T_2)$

(5) $lca(z_1, x_1) = lca(v_1, x_1) = lca(w_1, x_1) = u_1$ *in* T_1

(6) $lca(\phi(v_1), \phi(w_1)) = lca(\phi(v_1), \phi(x_1)) = \phi(u_1)$ *in* T_2

It is also possible that a trifurcation close to a bifurcation in one tree corresponds to a trifurcation in the second tree (primitive 21). The mathematical description of this primitive is:

$$\psi_\phi^{u_1} \in \Psi^{(21)}(T_1^{u_1}, T_2^{\phi(u_1)}) \text{ if:} \tag{3.23}$$

(1) $\psi_\phi^{u_1} = \{(u_1, \phi(u_1)), (v_1, \phi(v_1)), (w_1, \phi(w_1)), (x_1, \phi(x_1))\}$

(2) $\delta(u_1) = 3$ *in* T_1, $\delta(\phi(u_1)) = 3$ *in* T_2

(3) $lca(v_1, w_1) = y_1$ *in* T_1, *where* $(u_1, y_1) \in E(T_1)$

(4) $lca(z_1, v_1) = lca(z_1, w_1) = lca(z_1, x_1) = lca(v_1, x_1) = lca(w_1, x_1) = u_1$ *in* T_1

(5) $lca(\phi(v_1), \phi(w_1)) = lca(\phi(v_1), \phi(x_1)) = lca(\phi(w_1), \phi(x_1)) = \phi(u_1)$ *in* T_2

The last primitive corresponds to two close bifurcations in one tree and a bifurcation close to a trifurcation in the second tree (primitive 22):

$$\psi_\phi^{u_1} \in \Psi^{(22)}(T_1^{u_1}, T_2^{\phi(u_1)}) \text{ if:} \tag{3.24}$$

(1) $\psi_\phi^{u_1} = \{(u_1, \phi(u_1)), (v_1, \phi(v_1)), (w_1, \phi(w_1)), (x_1, \phi(x_1))\}$

(2) $\delta(u_1) = 3$ *in* T_1, $\delta(\phi(u_1)) = 2$ *in* T_2

(3) $lca(v_1, w_1) = y_1$ *in* T_1, *where* $(u_1, y_1) \in E(T_1)$

(4) $lca(\phi(w_1), \phi(x_1)) = y_2$ *in* T_2, *where* $(\phi(u_1), y_2) \in E(T_2)$

(5) $lca(z_1, v_1) = lca(z_1, w_1) = lca(z_1, x_1) = lca(v_1, x_1) = lca(w_1, x_1) = u_1$ *in* T_1

(6) $lca(\phi(v_1), \phi(w_1)) = lca(\phi(v_1), \phi(x_1)) = \phi(u_1)$ *in* T_2

The merging process occurs on-the-fly, i.e. during the matching when a pair of close nodes are detected. In that case, the similarity obtained merging and without merging the nodes will be calculated and the highest will be chosen. Alternatively, one could feel tempted to merge all very close nodes as a preprocessing step before the method takes place. However, in some cases the two slightly separated nodes represent the real structure and such a merging would introduce inaccuracies in the tree. This is visualized in Figure 3.9. In every figure green nodes are matched, blue nodes unmatched and red nodes highlight a correspondence. The first two figures represent an example in which thanks to the merging (during the matching process) more matches have been detected. In the first figure the highlighted nodes represent a wrong correspondence. Due to this error the blue nodes were not matched. This problem is solved using merging of close nodes as shown in the second figure. There two additional matches (green nodes in yellow circle) are added to the final set of correspondences. However, if the merging process is carried out as preprocessing step (last figure) some nodes are incorrectly matched, for instance, the selected red correspondence.

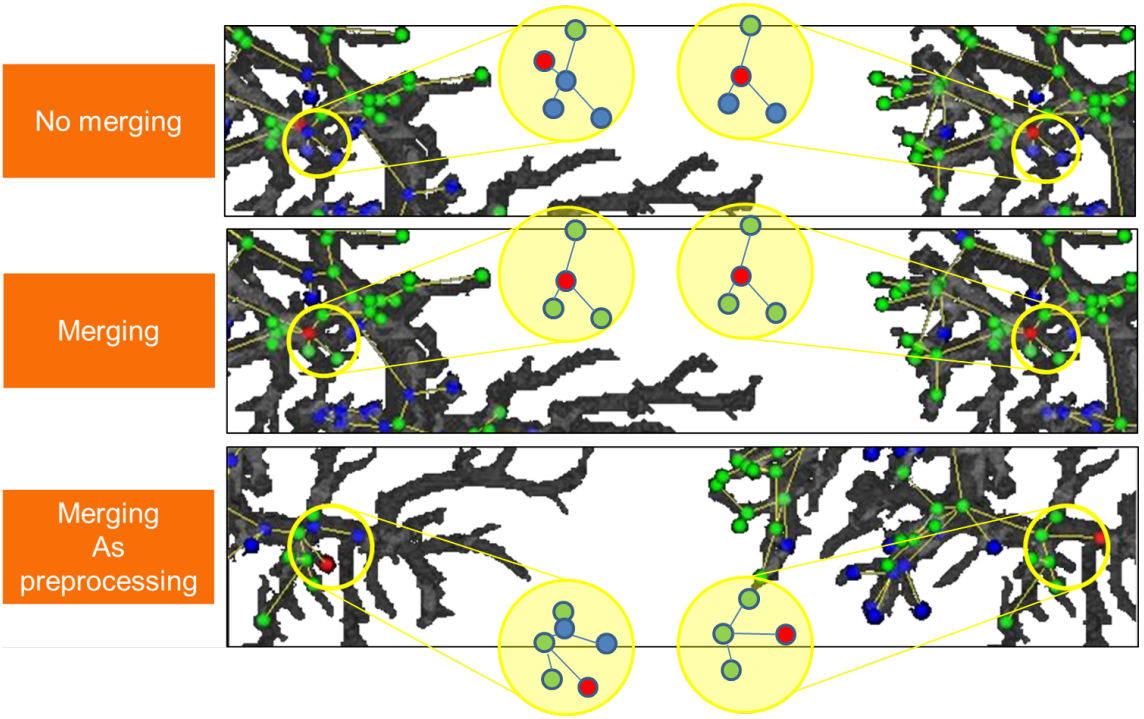

Figure 3.9.: Merging primitives. First figure: without merging some of the correspondences are not detected (blue nodes inside the yellow circle). Second figure: if merging is taken into account (during the matching process) those nodes are matched (green nodes in the yellow circle). Third figure: considering the merging process as a preprocessing step can lead to inaccuracies in some cases (correspondence highlighted in red).

3.3. Computation of the optimal solution

Let's define two trees T_1 and T_2 that have to be matched. The common tree T_c can be seen as an initial structure that contains nodes that are common to both trees. T_c can lead to T_1 or T_2 after undergoing certain deformations. The goal is to find the nodes of T_c.

If the set of common nodes (matches) would be known, the total pairwise similarity (ST) of two trees would simply be given by the addition of the local pairwise similarities (SL) of all the correspondences. In Figure 3.10 (a), if the set of correspondences $\{(a,1)(b,2)(c,3)\}$ are known, the total similarity of T_1 and T_2 would be:

$$ST = SL(a,1) + SL(b,2) + SL(c,3). \tag{3.25}$$

Unfortunately, the set of correspondences is unknown. In general, it is desired to find the set of correspondences that results in the highest possible total similarity. Let T_1 and T_2 be the two trees shown in Figure 3.10 (a). Their total similarity consist of:

(1) The local similarity of their roots ($SL(a,1)$). It can be directly obtained using Equation 3.6 (Section 3.1).

(2) The highest local similarity obtained by matching their children. Since the set of

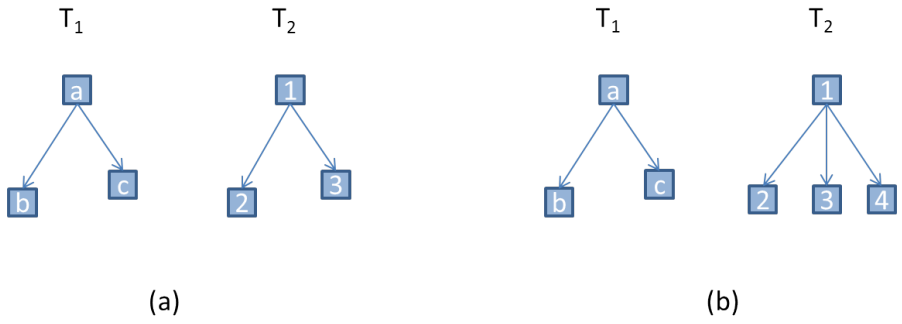

Figure 3.10.: Two trees to be matched. (a) The trees have the same topology. (b) The trees have different topology.

correspondences is unknown all possible combinations have to be calculated. For the example this value is calculated as:

$$max\{SL(b,2) + SL(c,3); SL(b,3) + SL(c,2)\}. \tag{3.26}$$

However, as mentioned in the introduction, it cannot be assumed that two corresponding nodes will share the topology (see Figure 3.10 (b)). In that case the calculation of (2) will be more complex, since the number of possible combinations will increase. The concrete amount and characteristics of those combinations will be mathematically defined in the next Section.

When the size of the trees increases (Figure 3.11 (a)), recursion can be used to solve the problem. The total similarity can be defined as:

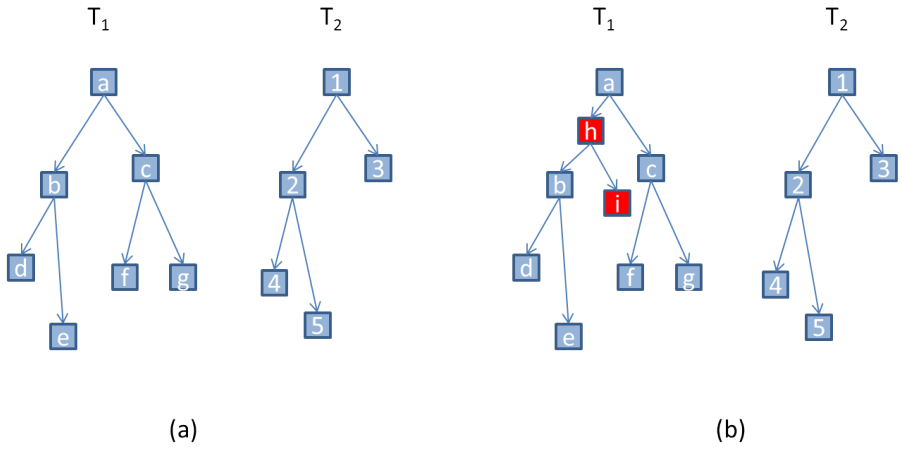

Figure 3.11.: Two trees to be matched. (a) Ideal case. (b) Real-world case.

$$ST(a,1) = SL(a,1) + max\{ST(b,2) + ST(c,3); ST(b,3) + ST(c,2)\}. \tag{3.27}$$

Since the children of b, c and d are leaves the recursion will end in the next iteration. For larger trees, the process will continue until the leaves are reached.

The previous equation covers an ideal case in which no spurious branches are considered. However, as discussed in the introduction, as consequence of imaging artifacts and surgeries, spurious branches are actually common (Figure 3.11 (b)). To incorporate this problem in the matching process, the second term of the equation will not be composed uniquely by the combinations that can be obtained with the children of a and 1, but also with the rest of their descendant. Thus, the combination $(h, 2)$ in Figure 3.11 (b) will be calculated, but the combination $(b, 2)$ that returns a higher similarity will be chosen. The mathematical expression of the total similarity calculation that incorporates this concept will be elaborated in the next section.

3.3.1. Formal definition of the problem

According to the previous paragraphs the matches that lead to the highest total similarity form the final set of matches. Therefore,

(1) all possible node combinations are generated,

(2) the amount of combinations is reduced by considering only topologically possible and meaningful matches and

(3) their similarities are compared to find the highest value.

The generation of the set of valid combinations requires the next two definitions. First, a set of tuples that contains all possible node combinations is generated.

Definition 3.1. The n-fold Cartesian product of n sets $X_1, X_2, ..., X_n$ can be defined as:

$$X_1 \times X_2 \times ... \times X_n = \{(x_1, x_2, ..., x_n) | x_i \in X_i, \quad \forall i = 1, ..., n\}. \tag{3.28}$$

The cardinality (number of n-tuples) of the Cartesian product is determined by the product of the sizes of the sets,

$$|X_1 \times X_2 \times ... \times X_n| = \prod_{i=1}^{n} |X_j|. \tag{3.29}$$

According to this definition the Cartesian product generates a set of n-tuples containing all possible combinations between the elements of the input sets. In the example tree of Figure 3.10 (a), two sets of nodes can be generated. The first set contains the children of a ($\{b, c\}$) and the second one the children of 1 ($\{2, 3\}$). The result of the Cartesian product would be the set $\{(b, 2)(c, 3)(b, 3)(c, 2)\}$. Note that each tuple will contain one element of each input set (e.g., $(b, 2)$). Definition 3.1 can be used to define the n-fold Cartesian product of n graphs.

Definition 3.2. The n-fold Cartesian product of n graphs $G_1, G_2, ..., G_n$ is a graph G. The set of vertices of G is given by the Cartesian product of vertices in the input graphs:

$$V(G) = V(G_1) \times V(G_2) \times ... \times V(G_n). \tag{3.30}$$

The adjacency of the vertices in G is determined by the corresponding adjacencies in $G_1, G_2, ..., G_n$.

Figure 3.12 shows the result of a Cartesian product of two graphs G_1 and G_2. G is composed of all possible nodes pairs between G_1 and G_2. However, from a matching point of view not all the vertices of G can be used simultaneously. The final set of matches should not contain nodes of G_2 that are matched to more than one node in G_1. For instance, a final set of matches that contain (b,2) and (b,3) is not considered in this thesis. Thus, only certain combinations of vertices in G can be part of the final set of matches. The conditions to be fulfilled and the number of vertices of G that fulfill those conditions can be defined as follows in Definition 3.3.

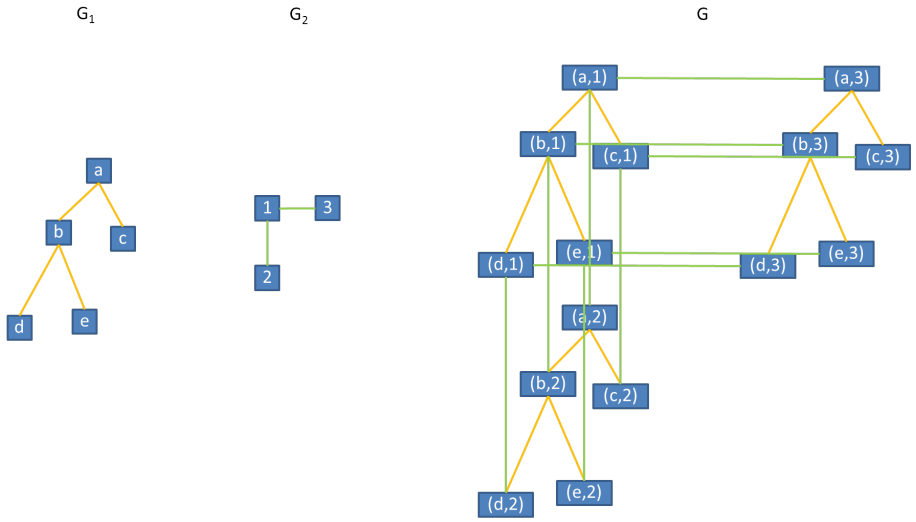

Figure 3.12.: Cartesian product of two graphs G_1 and G_2. The orange and green edges come from the adjacencies of G_1 and G_2 respectively. The resulting graph has one vertex for each pair of vertices in G_1 and G_2.

Definition 3.3. Let G_1 and G_2 be two graphs. The result of a graph matching method forms an injective relation between G_1 and G_2 when different nodes in G_1 cannot share a match in G_2. Hence many-to-one correspondences are not allowed.

The number of all possible injections between the two sets of vertices $V(G_1)$ and $V(G_2)$ such that $|V(G_1)| < |V(G_2)|$, is given by the falling factorial power:

$$|V(G_2)|^{\underline{|V(G_1)|}} = \prod_{i=0}^{|V(G_1)|-1} (|V(G_2)| - i). \tag{3.31}$$

Definitions 3.1 to 3.3 describe how to generate all possible sets of matches. The result of this step following the example of Figure 3.10 (a) would be a set of the form {(b,2),(c,3),(b,3),(c,2)}. Taking into account Definition 3.3, only combinations {(b,2),(c,3)} or {(b,3),(c,2)} will be further studied.

So far, no solution is given to the necessity to determine which one of the sets results in the highest similarity. As it was mentioned before, the solution should allow the detection of spurious branches (Figure 3.11 (b)). As it is shown in Figure 3.13, a series of graphs derived from G can be generated (orange) that take care of potential spurious branches. Each generated graph (reduced graph) results from removing at least one potential spu-

rious branch from the original graph G.

Definition 3.4. Let G be a graph and r the root of the graph. A reduced graph G^* of G with root r^* is a graph such that:

- G and G^* have the same root: $r^* = r$.
- The set of vertices of G^* is a subset of the vertices of G: $V(G^*) \subset V(G)$.
- If there exist a path between r^* and any vertex in G^*, a path should exist between r and the same vertex in G:

$$\forall v \in V(G^*), r^* \rightarrow v \Rightarrow r \rightarrow v. \tag{3.32}$$

- r in G and r^* in G^* have the same number of children.

Let $C = \{c_1, c_2, ..., c_m\}$ be the set of m children of r. The number of reduced graphs of G can be calculated using Equation 3.29 as:

$$|V(G^{c_1}) \times V(G^{c_2}) \times ... \times V(G^{c_m})| = \prod_{i=1}^{m} |V(G^{c_i})|. \tag{3.33}$$

Given the root r of the graph, a set of nodes will be generated for each subgraph rooted at all of the children of r. Thus, the number of sets will equal the number of children of r. Each set contains all vertices that belong to the subgraph rooted at the corresponding children. Then, the number of reduced graphs would equal the size of the Cartesian product of all sets. For example, in Figure 3.13 left, the subgraph of G rooted at b has three vertices. The three vertices can be seen in the aforementioned equation as a set. The subgraph rooted at c has 1 vertex. Thus, according to the equation the number of reduced graphs is 3. The next two definitions will be used to incorporate this idea in the matching process.

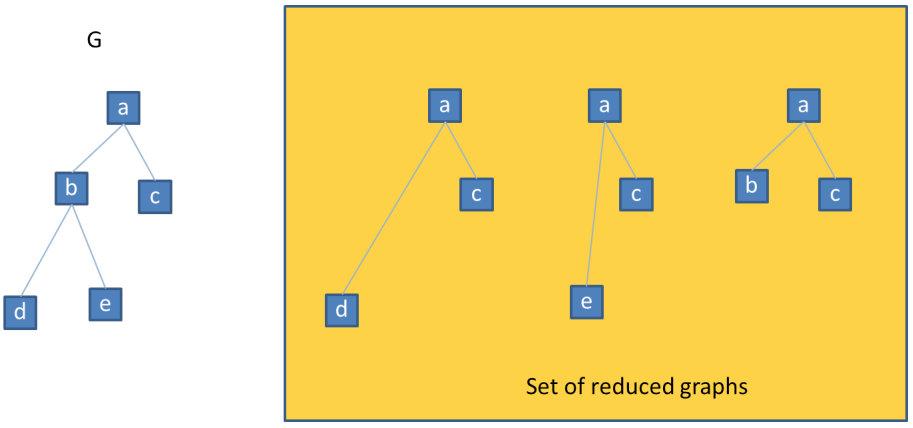

Figure 3.13.: Set of reduced graphs generated by removing branches from a graph G.

Definition 3.5. The set of reduced graphs F contains all possible reduced graphs of G.

Definitions 3.4 and 3.5 incorporate the possibility of detecting spurious branches in the matching process. Definitions 3.1 to 3.5 are used to calculate the solution of the tree matching problem in a recursive manner.

Definition 3.6. Let T_1 and T_2 be the two rooted trees to be matched. Let F_1^u and $F_2^{\phi(u)}$ be two sets of reduced trees such that F_1^u contains the set of reduced trees rooted at $u \in T_1$ and $F_2^{\phi(u)}$ contains the set of reduced trees rooted at $\phi(u) \in T_2$. The set of possible combinations of matches can be obtained as the subset of the Cartesian product of all elements of F_1^u and $F_2^{\phi(u)}$ that fulfill Definition 3.3.

Let n and m be the number of children of u and $\phi(u)$ respectively such that $m > n$, and let A be the set that contains all injective relations between the two subtrees rooted at u and $\phi(u)$. There are $|F_1^u||F_2^{\phi(u)}|m^{\underline{n}}$ combinations that fulfill that condition (see Equation 3.31). Each one of the combinations represent a set A_i of $min(n, m)$ matches.

Definition 3.7. The pairwise similarity of two rooted trees can be recursively defined as follows:

- Basis step: The similarity of all leaves is a plain local similarity that can be calculated with Equation 3.6.
- Recursive step: Let $z = min(n, m)$ be the number of matches in the set A_i with $i \in q$, and q the number of sets (see Definition 3.6) at a recursion step. The total similarity between any other pair of nodes (u and $\phi(u)$) can be calculated as:

$$ST(u, \phi(u)) = SL(u, \phi(u)) + max\{\sum_{j=1}^{z} ST(A_{1_j}); \sum_{j=1}^{z} ST(A_{2_j}); ...; \sum_{j=1}^{z} ST(A_{q_j})\}. \quad (3.34)$$

3.3.2. Example

Let T_1 and T_2 be the two rooted trees shown in Figure 3.14. The initial step of the matching process consists of generating the sets of reduced trees derived from T_1 and T_2. The generated sets are visualized in Figure 3.14 in a yellow square. Note that as anticipated in Definition 3.1, the number of components of F_1^a and F_2^1 are 9 (3×3) and 3 ($1 \times 3 \times 1$) respectively.

The Cartesian product for each pair of elements (one in F_1^a and one in F_2^1) is calculated. From all the possible sets of matches, only those corresponding to an injective match are stored. In Figure 3.15 the process for the first two elements of F_1^a and F_2^1 is illustrated. The set A shows the sets of matches that form an injective relation between both trees. Note that the number of injections (number of elements of the set A) is 6. This can be calculated using Equation 3.31. To decide which one of the elements (subsets of A), results in the highest total similarity, the total similarity of each one of them has to be calculated. However, unless one component of the tuple is a leave, a new recursion step is needed. Figure 3.15 shows that for the calculation of the similarity of the pair $(c, 3)$ a new pair of sets has to be generated. Now the children of all the components of the sets are leaves, thus, the recursion terminates and the similarity can be calculated. This process has to be repeated for every pair of elements in the initial sets of reduced trees and for every pair of nodes. The subset A_i leading to the highest total similarity will be part of the final set of matches, and so will be matches obtained in father recursion steps.

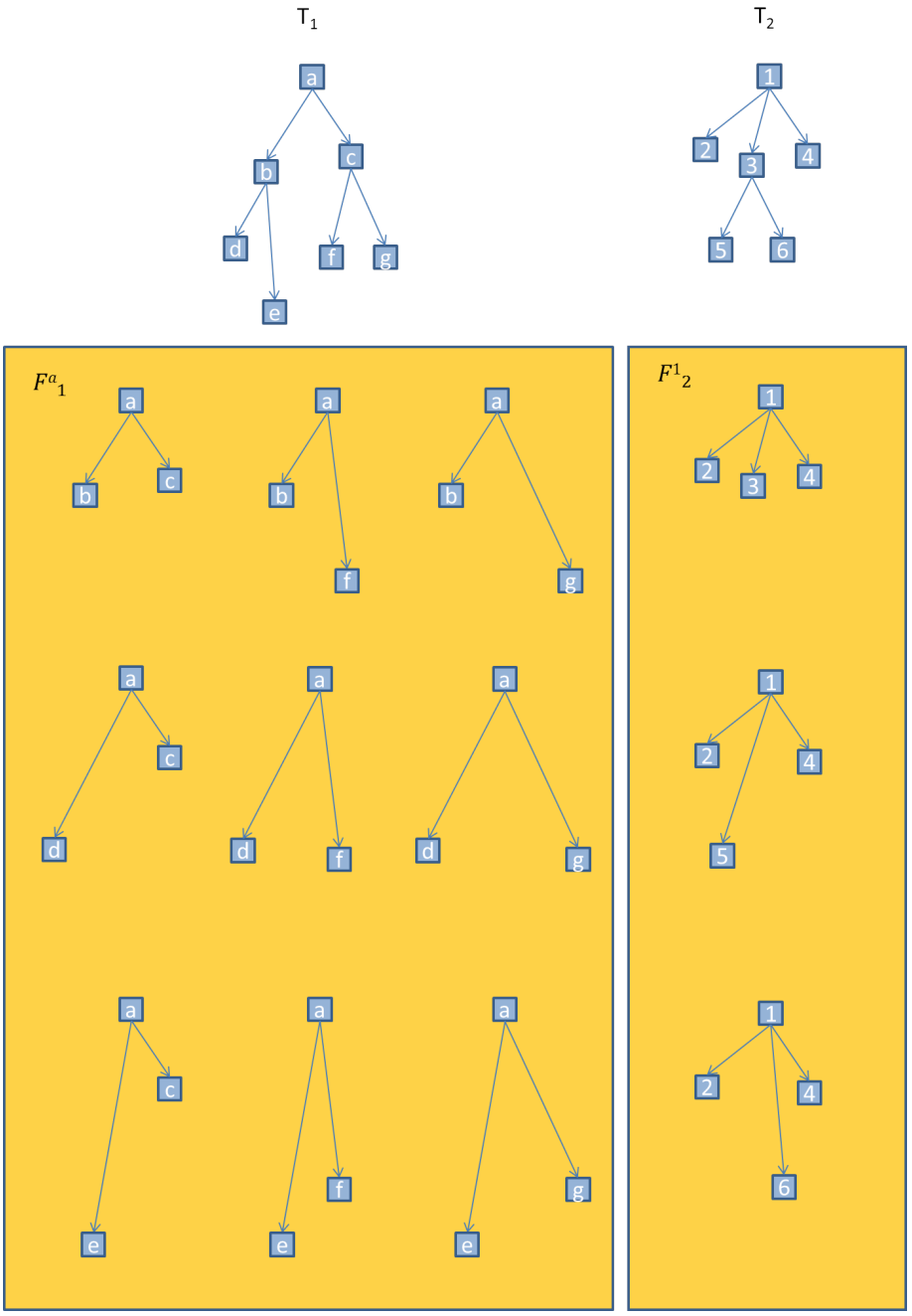

Figure 3.14.: Two trees to be matched and their corresponding sets of reduced trees (yellow square).

3.3.3. Pseudocode

Algorithm 1 presents the described method. The recursion is visible in line 11. As it was described in the formal definition of the problem, a series of sets are generated (lines 8-9) to allow the method to consider topological variations (e.g., spurious branches). All node combinations between those sets will be calculated and filtered in the "FIND COMBINATIONS(F_1^u,$F_2^{\phi(u)}$)" procedure (line 10).

One key aspect of the method is the generation of the sets of reduced graphs (see Defi-

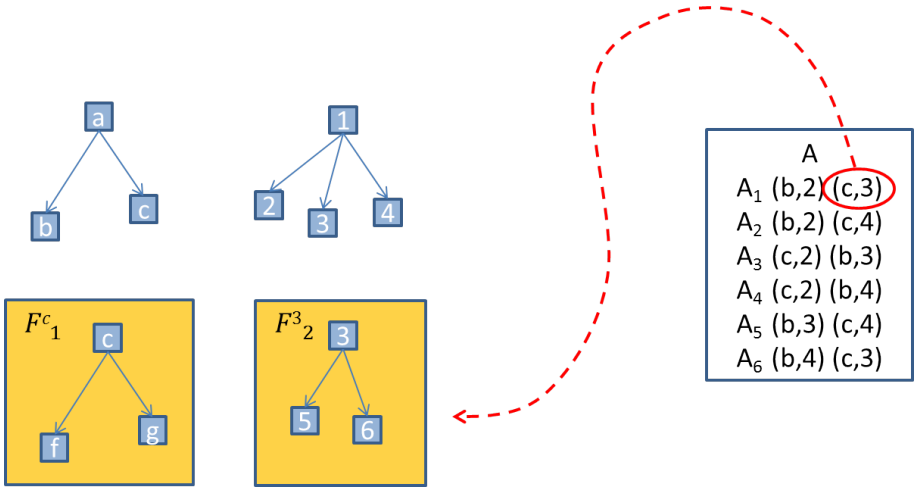

Figure 3.15.: The recursion proceeds until the leaves are reached. The pairwise similarity of all tuples in A has to be calculated. If those nodes are not leaves sets need to be generated.

Algorithm 1 Recursive tree matching

1: Let T_1 and T_2 be two trees rooted at r and $\phi(r)$
2: ST(r,$\phi(r)$)
3: **procedure** ST(u,$\phi(u)$)
4: Let s be a variable
5: **if** u and/or $\phi(u)$ is a leaf
6: $s \leftarrow SL(u, \phi(u))$
7: **else**
8: $F_1^u \leftarrow$ GENERATE SET(u,T_1)
9: $F_2^{\phi(u)} \leftarrow$ GENERATE SET($\phi(u)$,T_2)
10: A $\leftarrow$ FIND COMBINATIONS(F_1^u,$F_2^{\phi(u)}$)
11: $s \leftarrow SL(u, \phi(u)) + max\{\sum_{j=1}^{z} ST(A_{1_j}[0], A_{1_j}[1]); ...; \sum_{j=1}^{z} ST(A_{q_j}[0], A_{q_j}[1])\}$
12: **end if**
13: **return** s
14: **end procedure**

nitions 3.4 and 3.5). Algorithm 2 (Generation of sets) describes this process. Initially (see Figure 3.16), all subtrees rooted at the children of a are generated (lines 4-6). Then, the Cartesian product of the generated subtrees is calculated (line 7). The result is a graph *GCP* (see Definition 3.2) that contains all possible node tuples between the subtrees. A new tree is generated with each one of the node-tuples contained in *GCP* (line 8). The new trees are the elements of the set of reduced trees.

The main goal of the previous algorithm is to incorporate the detection of spurious branches in the method. Once this is ensured, the set of possible injective combinations (Definition 3.6) has to be found. This process is described in Algorithm 3. Each element of the set is compared to all elements of the second set (lines 2-3). For each pair of elements the Cartesian product between their children is calculated. Then, among all

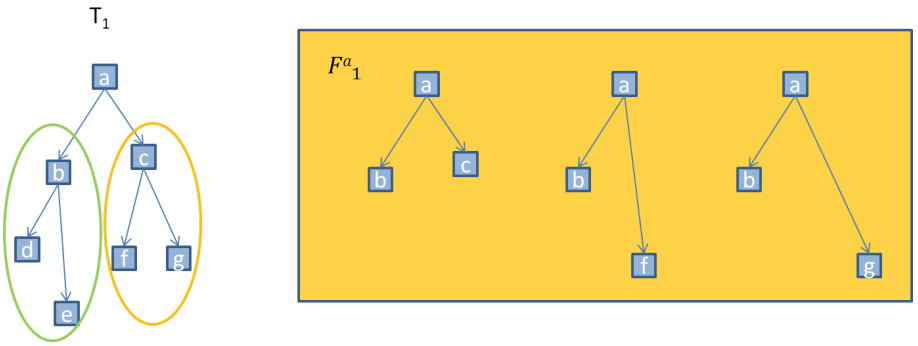

Figure 3.16.: Generation of reduced trees. Subtrees rooted at the children of a are generated (green and orange). From the definition of Cartesian product it is known that each tuple will contain one node of each subtree. Thus, the reduced tree can be generated taking a as root and the elements of the tuple as children. In the figure thre example reduced trees are shown.

Algorithm 2 Generation of sets

```
1:  procedure GENERATE SET(v, T)
2:      Let C be the set of children of a
3:      Let U be an empty set of trees
4:      for i ← 1, |C|
5:          U ← BUILD TREE(C_i, V(T^v)
6:      end for
7:      GCP ← CALCULATE GRAPH CARTESIAN PRODUCT(U)
8:      for j ← 0, |V(GCP)|
9:          F ← BUILD TREE(v, V(GCP_j))
10:     end for
11:     return F
12: end procedure
```

calculated solutions only those fulfilling the injective relation between both sets will be stored as a potential set of matches.

Algorithm 3 Injective solutions

```
1:  procedure FIND COMBINATIONS(F_1^u, F_2^φ(u))
2:      for i ← 0, |F_1^u|
3:          for j ← 0, |F_2^φ(u)|
4:              D ← C(F_1i^u)
5:              E ← C(F_2j^φ(u))
6:              CP ← CALCULATE CARTESIAN PRODUCT(D,E)
7:              A ← SELECT INJECTIVE SOLUTIONS(CP)
8:          end for
9:      end for
10:     return A
11: end procedure
```

3.3.4. Computationally efficient algorithm

The set *A* in Figure 3.15 shows that even in sets of reduced graphs with a small number of elements similarities have to be recalculated. In Figure 3.15 **each tuple appears twice, thus, their similarity will be calculated twice. The same similarities will be part of sets of reduced graphs in other iterations, increasing the number of recalculations.**

A common technique to design efficient algorithms is to divide the problem to be solved into subproblems. An optimal solution to the problem is given as combination of the solutions to its subproblems. As proposed in the literature [TMP*05], tree matching can follow this idea. In tree matching, the problem is to find the correspondences between two complete trees and the subproblems consist of dividing the trees into subtrees and finding their optimal solution. Then, the solutions (optimal sets of matches) to the subtree matching processes will contribute to the calculation of the final set of optimal matches.

The technique to be used to solve a problem based on its subproblems depends on the characteristics of the latter [CLRS09]. When each subproblem is going to be visited only once during the whole process (disjoint subproblems) recursion techniques can be efficiently used. However, when the subproblems overlap, i.e., each subtree has to be revisited several times until the optimal solution is found, recursion becomes an inefficient technique because each time it re-calculates values that were already calculated in an earlier step. As it was shown in Figure 3.15, this is the case in the described matching method. Dynamic programming has been designed to avoid recalculations. This is illustrated in Figure 3.17. Each time a new subproblem is visited, its solution is every time stored. Subproblems 1 and 2 contribute to the solution of subproblem 3, but if precalculated and stored, they do not have to be re-calculated, it suffices to recover their solution from the storage. Dynamic programming applied to tree matching means that each time a new pair of subtrees is visited (one in T_1 and one in T_2), its optimal calculated solution (similarity) is stored. When the subtrees are revisited no recalculations are necessary. This can reduce the runtime of the approach from exponential (recursion) to polynomial time (dynamic programming) [CLRS09].

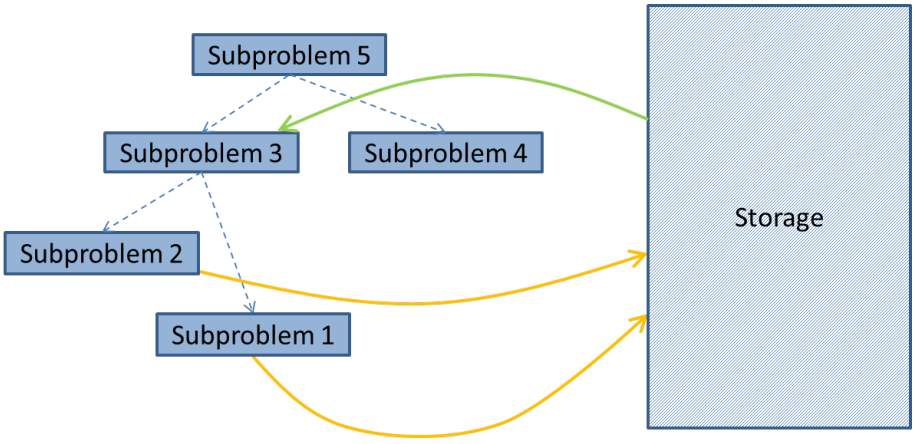

Figure 3.17.: Dynamic programming. The problem is divided into subproblems. The optimal solution for each subproblem is stored and read from storage when needed. This avoids unnecessary recalculations and as a matter of fact reduces the runtime.

Dynamic programming allows two traversing directions: top-down and bottom-up. Let $V(T^u)$ be the set of vertices in T^u and $|V(T^u)|$ be the size of a subtree (number of vertices of the subtree) rooted at u as shown in Figure 3.18. Using a bottom-up strategy $|V(T^u)|$ can determine the order in which the subtrees will be visited: smaller subtrees will be visited first. This ensures that in farther steps the required information is already stored. The size of the smallest subtrees is 1, and is assigned to all subtrees rooted at a leaf.

The method follows a hybrid bottom-up/top-down strategy. The bottom-up strategy will determine the global traversal direction of the trees [GH06a]. A top-down strategy will serve to incorporate a series of accelerators in the matching process. This hybrid strategy will be explained in detail in Section 3.5. In the following paragraphs the bottom-up matching mechanism is explained.

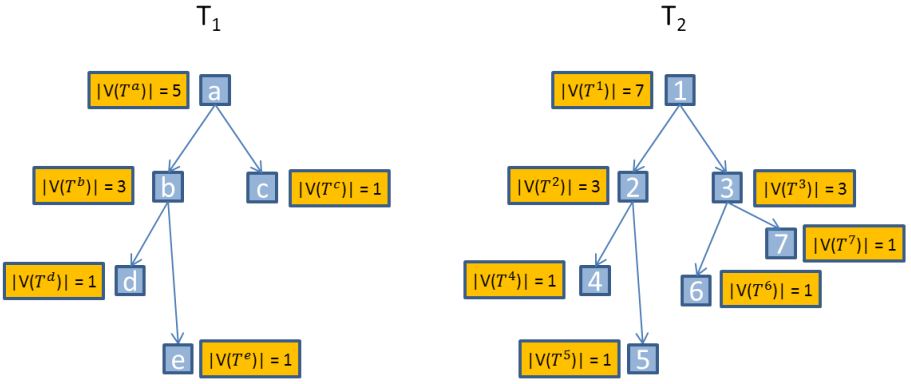

Figure 3.18.: Two example trees and their labeling according to their subtrees sizes.

Case $|\mathbf{V(T^u)}| = 1$ Each leaf $u \in V(T_1)$ is compared to all nodes $\phi(u) \in V(T_2)$ and similarities to all nodes in $|T_2^{\phi(u)}|$ are calculated and stored in a matrix as explained in detail in Section 3.4.

Case $|\mathbf{V(T^u)}| = 2$ A subtree of size 2 represents a node with one child as shown in Figure 3.19. This topological structure does not represent ramifications but intermediate nodes along vessel branches. While ramifications are easily identifiable in different trees, intermediate nodes do not necessarily have a correspondence in the second tree and are more likely to introduce inaccuracies. It is possible to increase the number of correspondences by introducing intermediate correspondences along branches. Therefore, in a post processing step refinement techniques are used to define additional correspondences based on the detected matches. This idea has already been applied to the graph matching method proposed in the next Chapter [KKOLW13]. However, the chapter focuses in the detection of the initial set of correspondences. Thus, this set of clinically impossible nodes is ignored.

Case $|\mathbf{V(T^u)}| = 3$ Each node $u \in V(T_1)$ with 2 children is compared to $|T_2^{\phi(u)}|$ and pairwise similarities are calculated. Not only the local similarity between nodes is calculated,

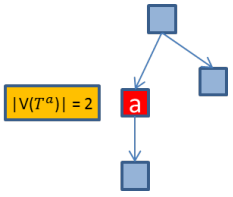

Figure 3.19.: Topology of a node (red) with one child.

but also the descendants of the pair of nodes u and $\phi(u)$ will contribute to the similarity value calculation. This highlights the advantage of dynamic programming, as the required descendant contributions were already calculated and stored in step $|V(T^u)| = 1$. Figure 3.20 helps to understand this contribution.

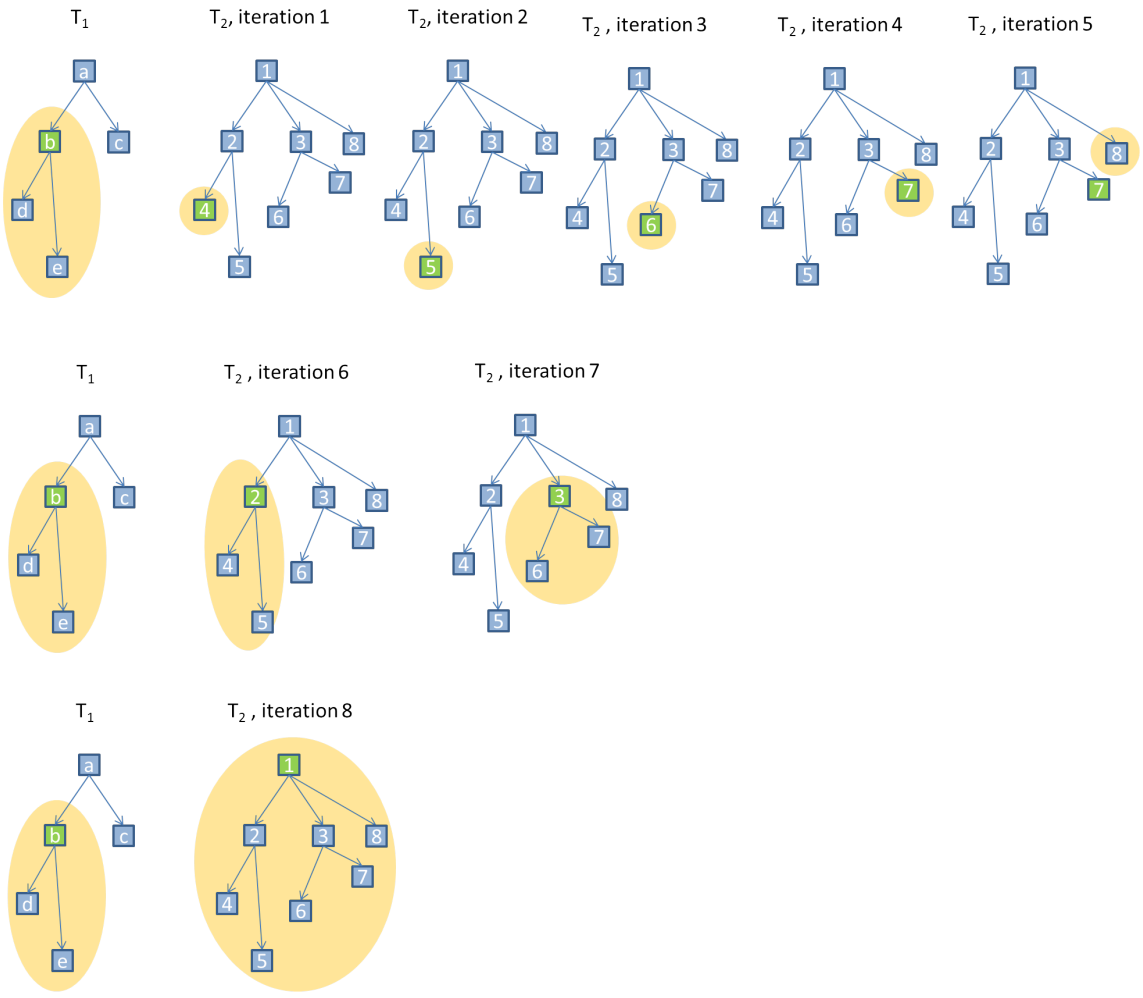

Figure 3.20.: Matching process when $|V(T^u)| = 3$.

In the first iterations (iterations 1 to 5) the node b ($|V(T^u)| = 3$) will be compared to all the leaves of T_2. As the leaves of T_2 have $|V(T^{\phi(u)})| = 1$ this process will return a plain local similarity for each compared node pairs.

The next group of iterations (6 and 7) correspond to nodes $\phi(u) \in T_2 : |V(T^{\phi(u)})| = 3$. Note again that the pairwise similarity of all pair of nodes in those subtrees is known. The

size of the subtrees rooted at those nodes is lower than 3 and thus, their similarities have been calculated in previous steps. Because of dynamic programming, those intermediate solutions will contribute to the computation of the optimal set of matches in farther iterations. Therefore, all possible descendant combinations of matches (Cartesian product of reduced trees) are studied in search of the highest achievable similarity. In Figure 3.20 the highest similarity of the descendant of the subtrees rooted at *b* and 2 respectively will be obtained by matching *d* to 4 and *e* to 5. This solution is obtained after comparing it to the combination of matching *d* to 5 and *e* to 4. Thus, the similarity obtained matching *d* to 4 and *e* to 5 will be the contribution of the descendant to the similarity of matching *b* and 2. The accumulated similarity value of matching *b* and 2 will be the addition of their local similarity and the contributed similarity from both subtrees.

In iteration 8, *b* is compared to 1. In this case $T_2^{\phi(u)}$ has more than 2 descendant, namely, 7. Furthermore, the number of children of *b* (2) and 1 (3) differ. Thus, the calculation of the contributed similarity is more complex. In this case, the descendant of *b* can be potentially matched to all descendant of 1, with the only restriction for those matches not to introduce topological inconsistencies (Figure 3.21). Now *b* and 1 have a different number of children. All possible combinations between them will be checked ((b,2),(c,3) or (b,2),(c,8), or (b,3),(c,8)). The maximum pairwise similarity will decide which node pairs will be part of the set of matches. The remaining subtree (subtree rooted at 8 in the figure) will be ignored.

Definition 3.8. Let $u \in V(T_1)$, $v \in V(T_1)$, and $w \in V(T_1)$ be three nodes of a directed tree $V(T_1)$ and $\phi(u) \in V(T_2)$, $\phi(v) \in V(T_2)$, and $\phi(w) \in V(T_2)$ be its corresponding nodes in a second directed tree T_2. Let $u \rightarrow^* v$ be a directed path between u and v and $lca(u, v)$ the lowest common ancestor of two nodes. A topological consistent match $(u, \phi(u))$ must fulfill the following conditions:

(1) **Path rule:** If u is a descendant of v in T_1, $\phi(u)$ must be a descendant of $\phi(v)$ in T_2. In other words, a directed path between them should exist:
$$v \rightarrow^* u \Rightarrow \phi(v) \rightarrow^* \phi(u).$$

(2) **Lowest common ancestor rule:** If w is the lowest common ancestor of two nodes u and v, $\phi(w)$ should be the lowest common ancestor of $\phi(u)$ and $\phi(v)$:
$$\forall u, v | lca(u, v) = w, lca(\phi(u), \phi(v)) = \phi(w).$$

Case $|\mathbf{V}(\mathbf{T^u})| > 3$ The process continues until the root is reached. The combination of matches that leads to the highest similarity in the last iteration will form the final set of matches.

3.4. Reconstruction of the optimal solution

Storage The storage mechanism used in this thesis consists of storing previously calculated subtree accumulated similarity values in an assignment matrix (Figure 3.22). In an assignment matrix all nodes of both trees T_1 (columns) and T_2 (rows) are represented. This means that if the number of nodes of T_1 and T_2 are n and m respectively, the size

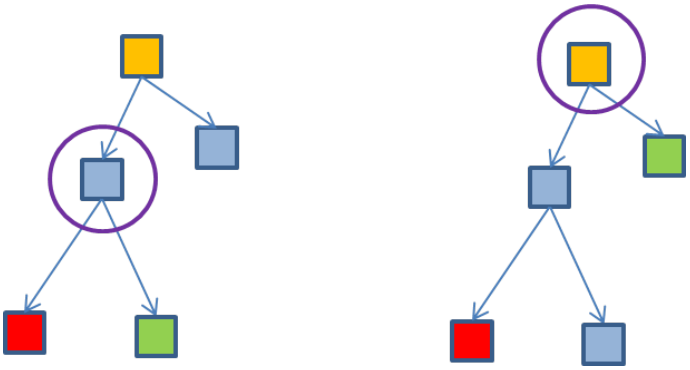

Figure 3.21.: Topologically inconsistent matches. Nodes with the same color are matched. Given the yellow match (root of the tree), matching the red and green nodes would lead to topological inconsistencies. Note that the least common ancestor (violet circle) in the second tree is its root but this is not the case in the first tree.

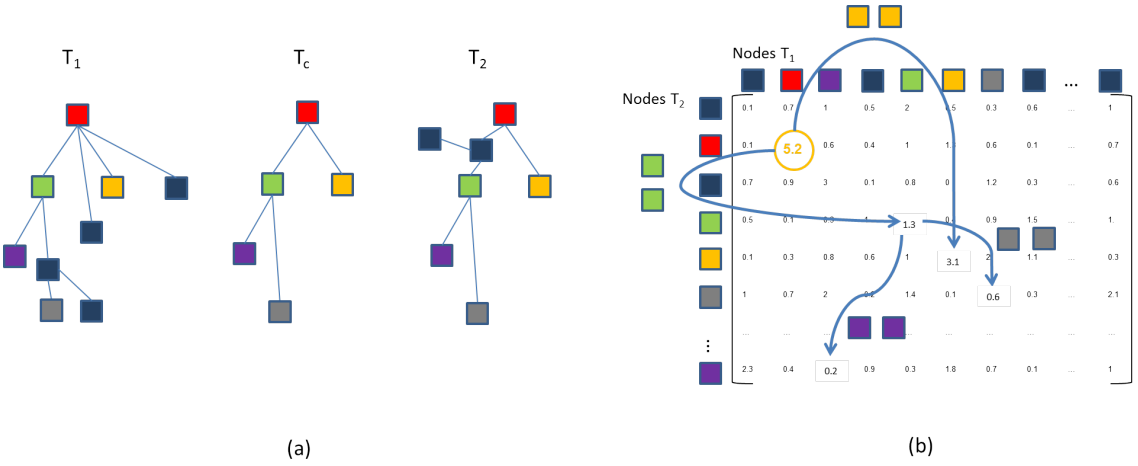

Figure 3.22.: (a) Trees to be matched T_1 and T_2 and common tree T_c that contains all nodes common to both trees. (b) Storage and recovery of matches and similarity values in an assignment matrix.

of the assignment matrix will be *nxm*. The element *ij* of the matrix will contain the accumulated similarity of matching the subtree $T_1^{u_i}$ and the subtree $T_2^{u_j}$. Since all calculated similarity values are stored in the matrix, recalculations are not necessary. Every time a new pair of nodes ($u_1 \in T_1$ and $u_2 \in T_2$) is visited, the similarity values of their descendant nodes will already be stored in the matrix (bottom-up). The highest value within the complete matrix corresponds to the optimal matching between both trees T_1 and T_2.

Reconstruction The goal of the matching method is to find nodes of the common tree. To this end, it should be possible to reconstruct from the matrix also the topological structure of the matches that led to the optimal similarity. Therefore, every time a pair of nodes is visited, the indices of their children (common tree) will also be stored. In the case of the red nodes in Figure 3.22 (a), for instance, the assignment matrix will contain the similarity

value (5.2 in Figure 3.22 (b)) and the indices to the green and yellow nodes (see common tree).

This makes the reconstruction task that will occur at the end of the algorithm straight forward. The goal is to find the final set of optimal matches (the matches of the common tree). After each iteration (subtree matching) an intermediate set of optimal matches is generated. Instead of storing all matches that lead to the highest similarity measure of those subtrees only the indices of their closest matched descendants (children in the common tree) will be stored reducing the memory consumption. Figure 3.22 illustrates the reconstruction problem. The assignment matrix (b) contains all subtree accumulated similarity values of matching the trees in (a). If the highest similarity value for all nodes is obtained matching the red nodes, the corresponding matrix element will contain the aforementioned value as well as the indices of the green and yellow nodes that lead to the optimal match. At the same time the green nodes contain the indices of the gray and violet nodes and so on. This way, the set of matches can be reconstructed until all the nodes of the common tree are found. This system will also be used for the detection of secondary roots in Section 4.2.6.

3.5. Complexity

The pseudocode of the described method (see Algorithm 4) helps to analyze the computational complexity of the proposed method. A series of matrices will be created (M_{l_1}, M_{l_2}, M_{d_1}, and M_{d_2}). The goal of those matrices is to precompute the geometric length (lines 4-5) and direction (lines 6-7) attributes between every pair of vertices. This will avoid recalculations during the "COMPUTE OPTIMAL MATCH" procedure (line 10). The calculation of all pairwise attributes will result in a computational complexity of $\mathcal{O}(|V(T_1)|^2)$ or $\mathcal{O}(|V(T_2)|^2)$ depending on the tree under study. The sizes of the subtrees contained in T_1 and T_2 have to be computed (lines 8-9). This will determine the order to visit the nodes of the trees. During this procedure each node is visited once, thus, their computational complexity is $\mathcal{O}(|V(T_1)|)$ or $\mathcal{O}(|V(T_2)|)$ depending on the tree under study.

Algorithm 4 Tree matching

1:	Let T_1 and T_2 be two trees	
2:	Let M_{l_1}, M_{l_2}, M_{d_1}, M_{d_2} and M be five new matrices	
3:	Let r be a new array	
4:	$M_{l_1} \leftarrow \forall u, v \in V(T_1)$, *GetGeodesicLength*$(u, v)$	$\triangleright\ \mathcal{O}(\|V(T_1)\|^2)$
5:	$M_{l_2} \leftarrow \forall u, v \in V(T_2)$, *GetGeodesicLength*$(u, v)$	$\triangleright\ \mathcal{O}(\|V(T_2)\|^2)$
6:	$M_{d_1} \leftarrow \forall u, v \in V(T_1)$, *GetDirection*$(u, v)$	$\triangleright\ \mathcal{O}(\|V(T_1)\|^2)$
7:	$M_{d_2} \leftarrow \forall u, v \in V(T_2)$, *GetDirection*$(u, v)$	$\triangleright\ \mathcal{O}(\|V(T_2)\|^2)$
8:	CalculateSubtreeSizes(T_1)	$\triangleright\ \mathcal{O}(\|V(T_1)\|)$
9:	CalculateSubtreeSizes(T_2)	$\triangleright\ \mathcal{O}(\|V(T_2)\|)$
10:	COMPUTE OPTIMAL MATCH($T_1, T_2, M_{l_1}, M_{l_2}, M_{d_1}, M_{d_2}, M$)	$\triangleright\ \mathcal{O}(\|V(T_1)\|^2 \|V(T_2)\|^2)$

During the "Compute optimal match" procedure the dynamic programming takes place (see Algorithm 5). Each call to ComputeHighestSimilarity (line 6), will find the optimal matches of two subtrees. Therefore, the association matrix M will be accessed to re-

cover the contributions of all subtree pairs contained in the current subtrees. The set of optimal matches changes dynamically depending on the current achievable highest similarity. This way errors are not accumulated. The computational complexity of the "Compute optimal match" procedure is ruled by the for loops in lines 2-5 that determine the number of times that ComputeHighestSimilarity will be called ($|V(T_1)||V(T_2)|$) and those included in ComputeHighestSimilarity. An overall complexity of $\mathcal{O}(|V(T_1)|^2|V(T_2)|^2)$ can be achieved [GH06a] with the unoptimized algorithm. Note that dynamic programming allows this complexity to remain in polynomial order.

Algorithm 5 Compute optimal match

```
1: procedure COMPUTE OPTIMAL MATCH(T1, T2, Ml1, Ml2, Md1, Md2, M)
2:     for i ← 1, |V(T1)|
3:         for j ← 1, |V(T2)|
4:             for all T1^u : |V(T1^u)| = i
5:                 for all T2^φ(u) : |V(T2^φ(u))| = j
6:                     M ← ComputeHighestSimilarity(T1^u, T2^φ(u), M)
7:                     r ← GetChildrenOptimalMatch(T1^u, T2^φ(u))
8:                 end for
9:             end for
10:        end for
11:    end for
12:    return M and r
13: end procedure
```

Two accelerators are used to farther reduce the computational complexity of the method. The pair of known corresponding roots serves to restrict the set of valid matches according to their distance to the root. In other words, let dr_1 be the geodesic distance between the root r_1 and a node u_1 in the first tree and let dr_2 be the distance between the root $\phi(r_1)$ and a node $\phi(u_1)$ in the second tree. If the ratio

$$max(\frac{dr_1}{dr_2}, \frac{dr_2}{dr_1}) > \epsilon \tag{3.35}$$

between both geodesic distances is greater than ϵ, the pair of nodes $(u_1, \phi(u_1))$ will not belong to the set of valid matches. The accelerated "Compute optimal match" procedure is shown in Algorithm 6. In line 6 the geodesic distances between the nodes and the root will be compared. Only if the required condition is fulfilled the remaining computations will take place. With this condition the computational complexity contributed by lines 6-7 in the basic approach ($\mathcal{O}(|V(T_1)||V(T_2)|)$) is reduced.

Similarly, the geodesic distance between the nodes and their descendant will restrict the amount of descendant that will be checked. According to Figure 3.23 when the pair of nodes $(b, 2)$ is under study only a reduced number of descendants will be compared. Let dn_1 be the geodesic distance between a node under study and one of its descendant in T_1, and dn_2 the corresponding geodesic distance in T_2, if the ratio of the geodesic distances between two branches (e.g., (b, e) and $(2, 9)$) is above ϵ

$$max(\frac{dn_1}{dn_2}, \frac{dn_2}{dn_1}) > \epsilon \tag{3.36}$$

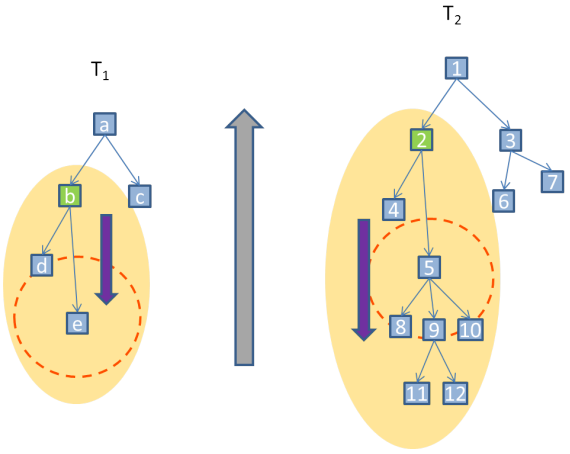

Figure 3.23.: Hybrid strategy. A bottom-up strategy is used (grey arrow) to determine the order to traverse the trees. This order ensures that all similarities required are calculated in previous steps. A top-down strategy (violet arrow) is used to compute the current subtree similarity. If the similarity of matching e and 9 is low there is no need to study the descendant of 9. The red circle illustrates the area in which matches will be considered.

those nodes are too far apart. Consequently all nodes that are farther apart can be ignored. In the example, 11 and 12 and their potential subtrees are ignored. Note that therefore, a top-down traversing order is more appropriate (see Figure 3.23). Thus, the computation of optimal matches inside a subtree will follow a top-down strategy. This accelerator reduces the number of reduced trees in the set of reduced graphs. The second accelerator has a similar effect on the computational complexity. In general, the reduction rate will depend on the density of the trees and the chosen value of ϵ.

It has been empirically found that a value $\epsilon = 1.15$ is a good threshold for both accelerators.

Algorithm 6 Computation optimal match with accelerators

```
1:  procedure COMPUTE OPTIMAL MATCH(T1, T2, Ml1, Ml2, Md1, Md2, M)
2:      for i ← 1, |V(T1)|
3:          for j ← 1, |V(T2)|
4:              for all T1^u : |V(T1^u)| = i
5:                  for all T2^φ(u) : |V(T2^φ(u))| = j
6:                      if CompareGeodesicDistancesToRoot(u, φ(u)) < ε
7:                          M ← ComputeHighestSimilarity(T1^u, T2^φ(u), M)
8:                          r ← GetChildrenOptimalMatch(T1^u, T2^φ(u))
9:                      end if
10:                 end for
11:             end for
12:         end for
13:     end for
14:     return M and r
15: end procedure
```

3.6. Manual preselection of matches

For some applications in which time is a constraint, it is desirable to further increase the efficiency of the method. Several authors have shown that tree matching methods are error prone. That is why some authors opt for manually selecting the matches. In this chapter a series of interactive features have been developed to help the user refine the matching results (4.4). In addition to this, the physician can set a series of input matches to guide the automatic matching process.

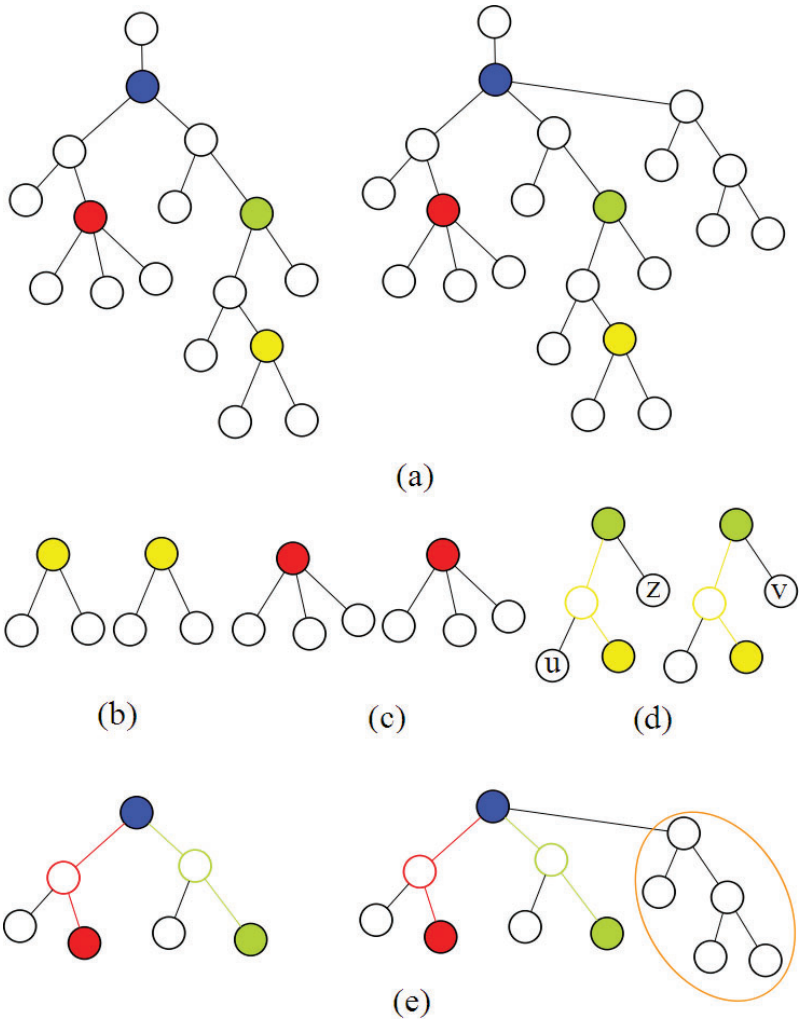

Figure 3.24.: Tree matching with preselection of nodes. The preselected nodes are visualized in red, yellow, green and blue. The tree matching problem is divided into a subtree matching problem. For the subtrees containing more than one preselected points (c,d) additional conditions should hold to ensure that the topology of the tree is preserved [OLD11a].

Figure 3.24 serves to clarify the speed-up process. The method works as follows:

Preselection The physician manually preselects a series of node pairs. After this is done, the preselected nodes will be checked. If the matches are topologically consistent

(see definition of impossible matches below), they will constitute a hard constrain, else the physician will be required to repeat the preselection. They are visualized in Figure 3.24 (a) using different colors. In the example the user has selected 4 node pairs. After the selection is done, the automatic tree matching takes place.

Impossible matches The preselected nodes might lead to topological inconsistencies (Figure 3.25). Before the automatic method takes place, the preselected node pairs are analyzed in search for inconsistencies. In case that an impossible combination of matches is detected, the user is requested to repeat the selection process. Inconsistencies are detected based on the next rule:

1. If a preselected node v in T_1^u is a descendant of another preselected node w in T_1^u its correspondence $\phi(v)$ in $T_2^{\phi(u)}$ must be descendant of $\phi(w)$ in $T_2^{\phi(u)}$.
2. If a preselected node v in T_1^u is a descendant of more than one preselected nodes w and z in T_1^u, being w in turn descendant of z, the descendants order in $T_2^{\phi(u)}$ has to be kept.

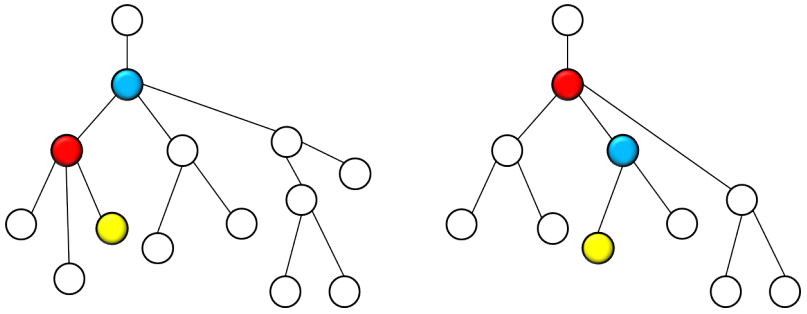

Figure 3.25.: Example of topologically inconsistent preselection of nodes. It topologically is not possible to keep all the nodes pairs selected by the user in the final set of matches.

Subtree matching containing one preselected node The tree matching problem is converted into a subtree matching problem. Every pair of nodes selected by the user is considered as a pair of roots of the corresponding subtrees. The preselected nodes are visited according to their level. The search starts from the leaves to the root. Thus, the order of detection of the nodes in Figure 3.24 will be: yellow, red, green and blue. Once the order is determined, the subtrees (T_1^u and $T_2^{\phi(u)}$) rooted at nodes (u and $\phi(u)$) are extracted and the automatic matching is carried out in that pair of subtrees (Figure 3.24 (b)). The set of nodes that lead to the highest similarity value, as well as, the similarity value are stored. The process is repeated until all preselected nodes are analyzed (Figure 3.24 (c)).

Subtree containing two preselected nodes When the subtree contains more than one preselected nodes, the method has to be adapted so that both preselected nodes

remain as final matches and at the same time the topology of the tree is preserved. This step of the process is illustrated in Figure 3.24 (d). In this case, both the yellow and green (root) nodes belong to the subtree. One can observe that the nodes below the yellow nodes in Figure 3.24 (b) are not further considered. The reason for that is that the optimal set of matches for the yellow nodes is already calculated in a previous step (b). The yellow match acts as a black box which contains the similarity measure previously found. The yellow node should remain to ensure that every preselected node will be part of the final set of matches without breaking the topological rules. To this end an imaginary line (yellow) is drawn along the path between the two preselected points (being one of them the root of the subtree). To ensure that the topology of the tree is preserved and at the same time the preselections remain part of the final set of matches, every branch derived from the imaginary line must be matched to branches derived from the corresponding imaginary line in the second subtree $T_2^{\phi(u)}$). This means that in Figure 3.24 (d) node u cannot be matched to node v, else the yellow node would need to be removed from the set of matches.

Subtree containing more than two preselected nodes The way to proceed when more than two preselections exist is similar. In this case, there will be as many imaginary lines as preselected nodes. Mathematically speaking, each line is the path that joins one of the preselected nodes with the root node. As before, nodes that are descendant of one path will only be matched to nodes descendant from the corresponding path and not from any other. To ensure this the next statement should hold:

$$\forall v | lca(v, a_i) \in P_1(r, a_i), \phi(v) \in P_2(\phi(r), \phi(a_i)). \tag{3.37}$$

v is a node of T_1. a_i is one of the preselected nodes where $i = [0, n]$ and n is the number of preselected nodes. $P_1(r, a_i)$ and $P_2(\phi(r), \phi(a_i)$ are the paths connecting a preselected node and the root, and its corresponding nodes respectively. This is illustrated in Figure 3.24 (d). Note that this enhancements speed-up greatly the method as the number of valid matches is highly reduced. The speed-up will be quantitatively evaluated later in this chapter.

3.7. Evaluation

The tree matching method has been evaluated with artificial and real data. This section explains the evaluation method and discusses the obtained results. All experiments have been carried out on a PC equipped with an AMD Athlon 2.41 GHz 64 X2 Dual Core Processor 4600+, 3.25 GB RAM and Windows Vista x64 as operating system. A single clinical dataset was the basis for the generation of the artificial data. It was acquired with a GE Medical Systems LightSpeed 16 CT Scanner (dimension: 512x512x291, spacing: 0.64x0.64x1.0 mm, slice thickness: 1.25 mm).

Efficiency To evaluate the runtime of the tree matching algorithm a series of trees with different sizes were selected. The first column in Table 3.3 shows the sizes of the trees

No. nodes	0 Input	1 Input	2 Input	3 Input
192-192	7.45	2.56	1.41	0.74
192-101	2.84	1	0.48	0.32
192-52	0.95	0.46	0.22	0.21
192-11	0.15	0.12	0.12	0.13
101-101	0.96	0.45	0.24	0.19
101-52	0.35	0.18	0.11	0.1
101-11	0.1	0.07	0.08	0.07
52-52	0.14	0.13	0.09	0.1
52-11	0.03	0.04	0.04	0.05

Table 3.3.: Efficiency. Time in seconds that the tree matching algorithm needs to find correspondences between trees of different sizes and with a different number of preselected correspondences.

that were matched. For every pair of trees 4 experiments were carried out changing the number of preselected points that were used. Note that since the tree matching method needs the root to be known, the 0 Input column shows the results for those trees in which only that pair of nodes were known. In the cases of 1, 2 and 3 input correspondences, nodes were selected that were close to main branches because it is assumed that the physician will more likely select those nodes instead of leaves. The slowest runtime takes place for bigger trees 192-192 as expected. But even for those trees the preselection of one additional node pair brings the time required from 7.45 seconds down to 2.56 seconds.

Artificial data The artificial data for the evaluation has been obtained from a real clinical vessel tree extracted from an abdominal CT acquisition. Changes have been made on the original tree T_1 to generate the second tree T_2. The idea for the first experiment was to simulate the effect of liver resection [CAM*05b]. To this end, nodes have been randomly removed and also every branch derived from the removed node. Figure 3.26 (a) shows an example the generation of artificial trees following this method. A node is removed and so they are all the branches and nodes that are descendant from that node. In other words, all the nodes that belong to the subtree that has that node as root are removed. The remaining tree is the one in the right. This experiment has been carried out in 60 different pair of trees, 30 in which 25% of all nodes were removed and another 30 in which 50% of all nodes were removed. Note that the problem of tree matching in this case is not as complicated as with experiment number 2 because the topology in most of the areas of the tree remains untouched. Table 3.4 summarizes the results of the experiments as an average of all the experiments that were carried out. The table shows the number of matches that were found, the number of wrong matches, the maximum and minimum number of matches detected between all experiments as well as the number of experiments that contained wrong matches. The number in parenthesis, if they exist, is the maximum number of wrong matches that were found in a tree pair. Thus, one can see that all the correspondences were found for each one of the 30 pairs of trees both with 25 and with 50% of the nodes removed. None of the 60 experiments contained wrong matches.

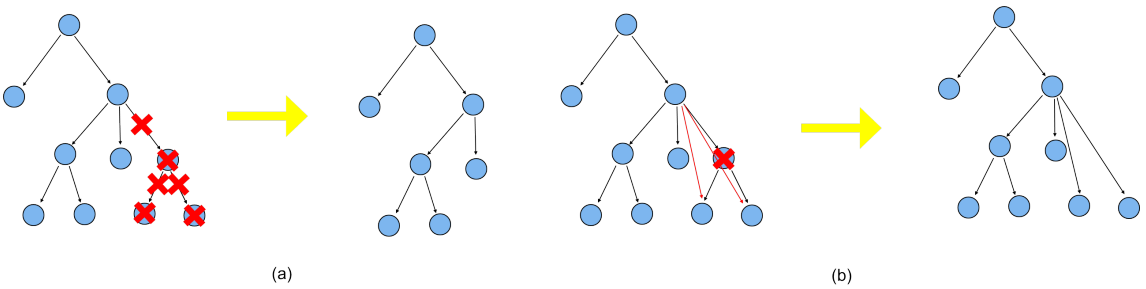

Figure 3.26.: Generation of artificial trees from real ones. (a) A random node is removed and so they are all the nodes and branches descendant from it. (b) A random node is removed and as consequence all its children become children of its first ancestor (parent).

Experiment	Rem (%)	Matches	Wrong	Max	Min	Wrong exp
1	25	144	0	144	144	0
	50	96	0	96	96	0
2	25	103.82	1.17(2)	131	62	6
	50	46.59	1.4(3)	68	22	7

Table 3.4.: Topological experiments. Average result of experiment 1 and 2. For each experiment and each percentage of removed nodes 30 tree pairs were matched. Matches: number of matches found. Wrong: number of wrong matches, in parenthesis the maximum number of wrong matches. Max/Min: Maximum/minimum number of found matches. Wrong exp: Number of experiments containing wrong matches.

The tree generation for the second experiment was more complex. In this case, every time a random node was selected only that single node was removed. All children from that node became automatically children of its parent. As a result topological variations were introduced in the trees. Figure 3.26 (b) shows an example of this. One can notice that due to those changes the topology of the tree varies much more than in the previous experiment. When a high number of nodes are removed (25-50%) the trees are highly different (Figure 3.27). Again 30 pair of trees have been matched with 25% of the nodes removed and another 30 with 50% removed. The results summarized in Table 3.4 show the robustness of the method towards topological variations. Even with 50% of the nodes removed the maximum number of wrong matches is 3 with a mean of 1.4 matches. One can see that in this case the number of detected correspondences is lower. This is on the one side due to the large topological variations between both trees which make the problem harder. But the reason is also that with this artificial removal, ramifications of more than 4 nodes are present, which are not considered by the method. Certain new primitives would be necessary to detect a bigger number of matches, but it is out of focus within this thesis due to its irrelevance for its application to match liver vasculatures.

Attribute experiments Not only the topology may differ between trees but also the attributes might have slightly different values. To evaluate the effect of the variation of the attributes, uniformly distributed noise is added to the edges and nodes of one of the

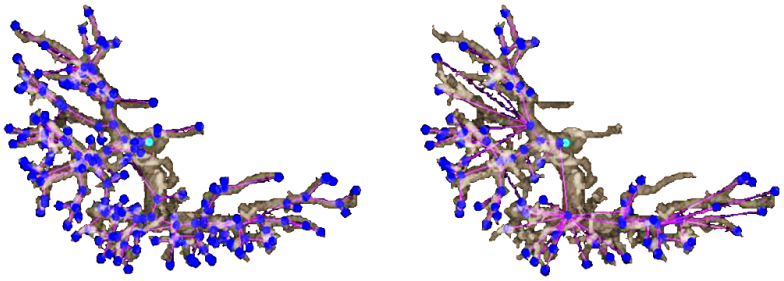

Figure 3.27.: Experiment 2. After removal of 50% of the nodes the second tree is highly different compared to the first tree [OLD11a].

trees:

$$\sigma = \frac{b-a}{\sqrt{12}}. \tag{3.38}$$

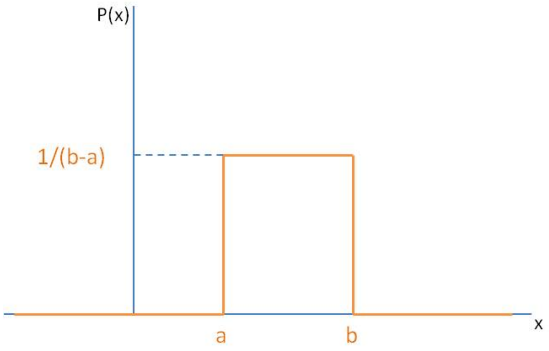

Figure 3.28.: Probability density function of uniformly distributed noise [OLD11a].

σ is the standard deviation, which is varied during the experiments to evaluate the tolerance of the method to changes in the attributes. According to the definition of uniformly distributed noise, all values of the probability density function $P(x)$ that lie between a minimum a and a maximum b are equally probable (Figure 3.28). To the attributes of each node of the tree, a random value between a and b is added or subtracted. σ varies from 0.2 to 0.8 (distance between a and b is increased), and for each different value of σ 30 pairs of trees are matched. Table 3.5 summarizes the results of the attribute experiments. A maximum of 1 wrong match was detected and no less than 184 nodes were matched (from 192 possible matches). Even with the highest standard deviation only 2 experiments returned errors.

Figure 3.29 is a summary of the evaluation performed on artificial data. One can see the low number of wrong matches. The worst results are obtained for topological variations with up to 50% of the nodes removed. However, as previously mentioned the deformations seen in these extreme cases will not appear in abdominal clinical data.

Realistic experiments Two experiments have been carried out based on real data. A tree generated from a clinical dataset has been cropped. In a second experiment the tree

σ	Matches	Wrong	Max.	Min.	Wrong exp.
0.2	192	0	192	192	0
0.4	191.47	0	192	189	0
0.6	189.83	1	192	184	1
0.8	183.13	1	192	174	2

Table 3.5.: Attribute experiments. σ: standard deviation. Matches: number of matches found. Wrong: number of wrong matches. Max/Min: Maximum/minimum number of found matches. Wrong exp: Number of experiments containing wrong matches.

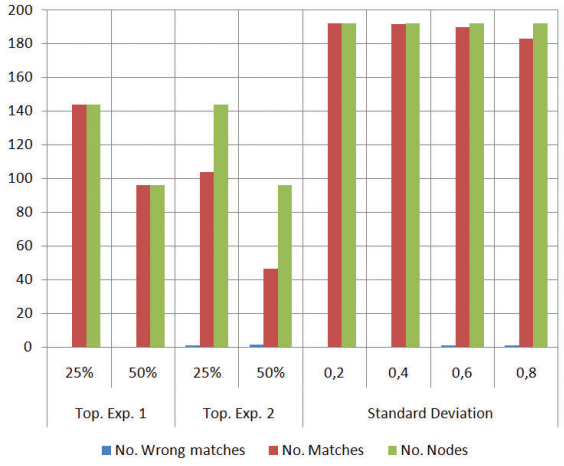

Figure 3.29.: Summary of the results obtained after topological and attribute variations [OLD11a].

has been cropped twice and the resulting trees were matched. In both cases 0 to 3 nodes were considered as wrong. Note that in this case the decision of which nodes are correct or not is more complicated as ground truth results are missing. The decision has been taken after evaluation of each pair of node one-by-one. It is important to notice that the results agree with those obtained with the artificial data. In the first tree 63 out of 78 were matched and in the second 83 out of 129.

Clinical data One real clinical data have been used for evaluation. The preoperatively gathered data contained a tumor. In the postoperative data the tumor was ablated. Due to the ablation a big amount of vessels are missing in the second tree. After one-by-one evaluation of the resulting matches one wrong match was detected. The evaluation of tree matching results on clinical data is a difficult task as ground truth is not available. Nevertheless, the internal accuracy obtained after registration in Chapter 5 is a proof of the correctness of the matching results.

3.8. Discussion

Even though the tree-to-tree matching method is efficient and appropriate for pre/post clinical applications, there are two limiting factors that make it inappropriate for certain applications:

1. Shared traversal direction required and
2. the portal and hepatic trees have to be separated.

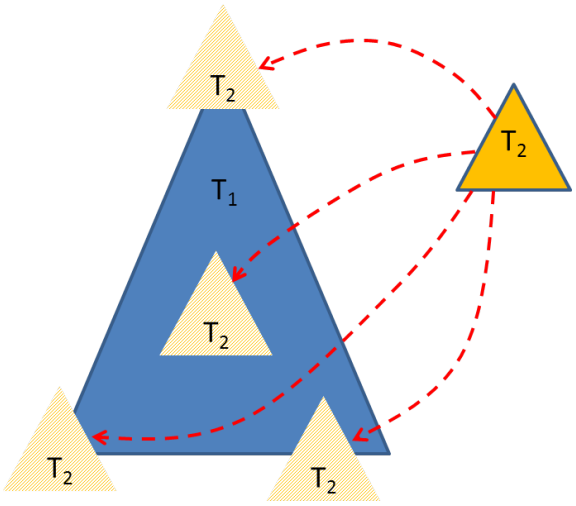

Figure 3.30.: T_1 can be spatially located anywhere in relation to T_2.

Shared traversal direction The method proposed in the previous sections requires a pair of known correspondences (roots) that determine the traversal directions of the trees. However, in some cases the roots might not correspond. They could even be located in an area outside the common tree (see Figure 3.30). If the pair of roots does not correspond, the optimal solution can still be detected as far as the traversal direction in both trees is still the same. This ideal case is illustrated in Figure 3.31 (a). The roots do not correspond (orange nodes), but the optimal set of matches (red) can still be detected. The distance to root accelerator cannot be used under those circumstances since no corresponding roots are known. If the traversal direction in one of the trees differs the set of optimal matches will not be detected (see Figure 3.31 (b)).

The manual selection of roots is not a straightforward task. The greatest challenge is to find the correspondences between different modalities (e.g., CT/US). In that case, in addition to the different resolution between acquisitions, some of them might not even show the root of the tree. Even between acquisitions of the same modality, especially after tumor resection, the portal/hepatic vein root is not always visible to the user. Furthermore, up to 80% of the liver can be resected during a surgery. This means that only a small part of the vessel tree will remain. This complicates the task of finding the needed pairs of correspondences.

On the other side, the CT images used for vessel segmentation purposes are contrast enhanced. However, the contrast agent is not always homogeneously spread. In some

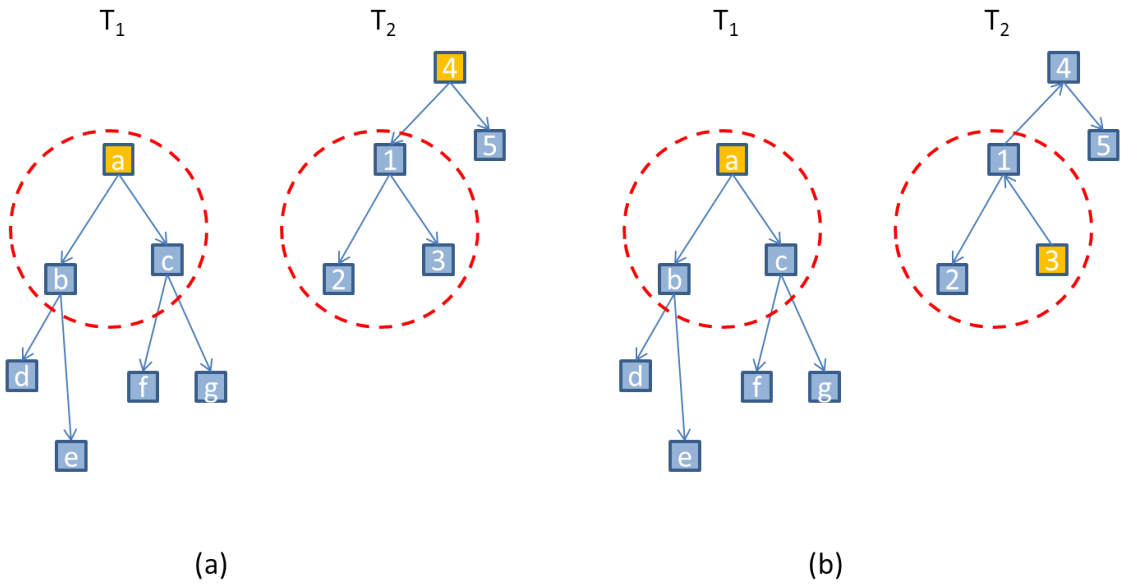

Figure 3.31.: (a) The set of optimal matches (red) can be detected when the roots do not correspond as far as the traversal directions are the same. (b) If the traversal directions change the set of optimal matches will not be found.

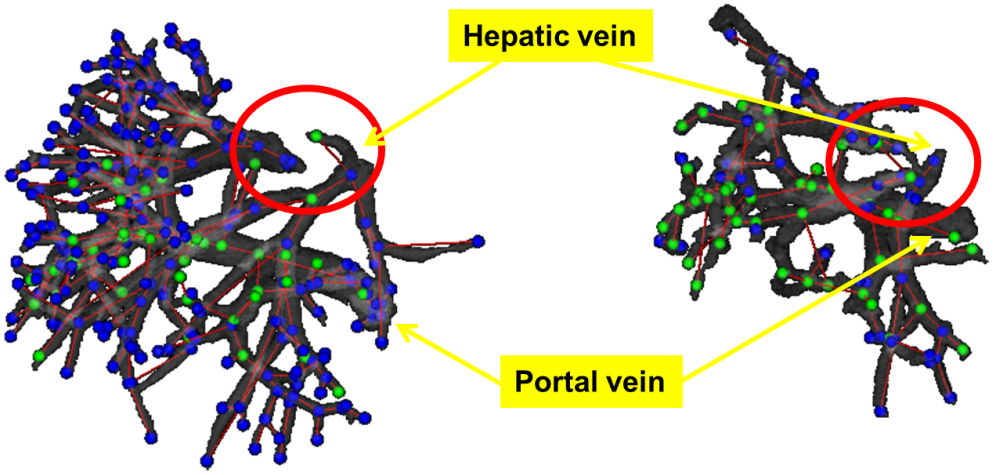

Figure 3.32.: Vessels segmented from CT images of the same patient. The hepatic vein appears separated in two in the left (preoperative) tree but not in the right (postoperative) one.

cases there are areas that are not contrast enhanced. In other cases due to segmentation reasons parts of the trees are missing. This is shown in Figure 3.32. It can be seen that the hepatic vein is divided in two pieces in the left segmentation. The problem arises when the trees/graphs considered are directed, as it often happens in tree search based methods. In that case a root is selected (Figure 3.33 red) and a directed tree is generated starting from that root. The trees appear connected at different positions (green circles in the figure). The effect of that is that the directions of the edges of one tree are opposite

to those of the other tree. This means that those nodes (yellow circle in Figure 3.33) that according to their spatial location are correspondent do not share the same topology and using a conventional tree matching method will not be matched.

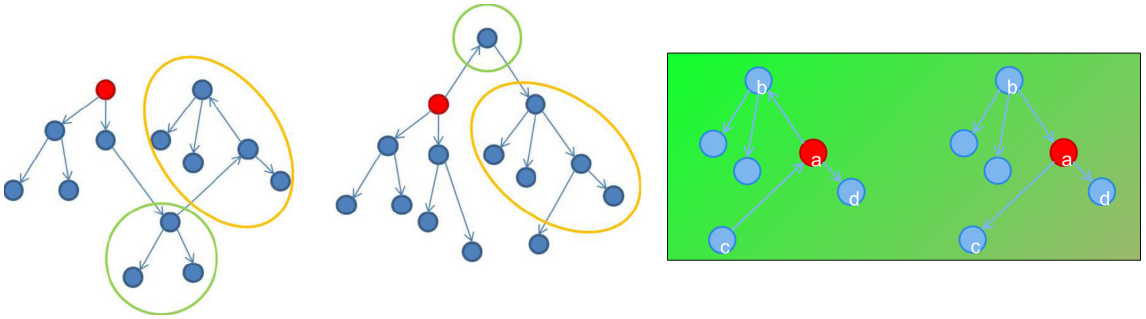

Figure 3.33.: Part of the tree representation of Figure 3.32 in which the preoperative and the postoperative trees have topological differences that complicate the matching process and reduce the possible number of matches [OLD11c].

Separation of portal and hepatic trees Even if in reality portal and hepatic veins are two separated vessel systems, the trees appear intertwined at some positions due to segmentation errors. Thus, opposite to what most of the authors assume, the structures generated from the segmented vessels are not trees. They contain cycles. Hence, a tree separation tool [DOOL11] is necessary as preprocessing step of the matching process.

3.9. Summary

In this chapter, an efficient and robust tree matching method has been proposed. This method is a solution for the set of challenges enumerated in the introduction of this chapter and it sets the basis for the graph matching method that is proposed in Chapter 4. Therefore, the method has been formally defined in such a way that allows its extension to cyclic unrooted graphs as it will be shown in the next chapter. However, the detection of correspondences in cyclic graphs presents new challenges that were not considered in this chapter as shortly mentioned in the discussion (see Section 3.8). All these new aspects will be considered in the next chapter.

4. Internal landmarks: Graph matching

Tree matching methods have some limitations in the clinical practice (Section 3.8). Thus, a generalized graph to graph matching method is needed that can deal with those limitations, in addition to challenges (1) to (3) enumerated in the introduction of the previous chapter.

(4) **Root independence.** Most state of the art methods depend on a known reference point to perform appropriately. However, it cannot be assumed that a known root exists. Moreover, time limitations during an intervention will make the selection of roots during surgery unsuitable.

(5) **Cyclic graphs.** While in theory the vessels do not form loops, due to imaging artifacts the graphs generated from them will actually contain loops. Most of state of the art methods are based on the assumption that no loops exist.

(6) **Pose independence.** Due to the difficulty of finding robust similarity metrics that are at the same time pose independent, several state of the art methods are pose dependent as shown in Table 2.7. In the clinical scenarios under study it cannot be assumed that both imaging acquisitions share the orientation. Thus, pose independence is an additional requirement.

(7) **Efficient.** While this is not a hard constraint for the outcome validation of a surgery, the proposed methods are meant to be used in other applications, for example, intra-operative navigation, in which time is a limiting factor.

As it was shown in Chapter 2, several graph matching methods have been proposed. Probabilistic relaxation based methods are specially interesting due to their efficiency and pose independence. However, their drawback is that they are prone to get stuck into local minima. The incorporation of topological information makes tree search based methods robust against local minima, but until now those methods where developed for acyclic graphs with a known root.

In this chapter a novel graph matching method is proposed that incorporates the advantages of probabilistic relaxation methods (efficiency and pose independence) and those of tree search methods (robustness thanks to the use of topologies). In some clinical scenarios (e.g., intervention) preselection of roots is not suitable. Thus, a novel graph matching method will be presented (Section 4.2) that is root independent, efficient and can handle loops. Finally, a solution for the pose dependency problem is proposed (Section 4.3).

Graph matching methods are always to a greater or lesser extent error prone. That is the reason why appropriate interaction features could be of a great help to refine the matching results or manually increase the amount of matches (Section 4.4). On the other

hand, in some cases in which efficiency is a limiting factor, an approach that automatically detects and removes wrong matches from the total set of matches is desirable. In Section 4.5 a statistical approach for outlier detection is introduced for that purpose. Finally, all presented methods are evaluated in Section 4.6.

The contributions that go beyond the state of the art included in this chapter are:

- Fully automatic, pose independent, graph-to-graph matching method that supports loops and does not need preselected roots. The improvements proposed for the tree to tree matching are incorporated in the graph matching method.
- Detection of secondary roots. Most of state of the art methods that depend on the topology of the graphs, consider an ideal case in which the root is known and both graphs present a similar topology. Unfortunately, due to imaging artifacts and/or contrast this assumption does not necessarily hold. In some cases, parts of the graphs will be missing leading to different topologies. In this chapter a technique is proposed that will detect not only the matches achieved given the main root of the graphs but also those obtained at secondary roots. This technique will increase the final set of matches with matches that would be ignored otherwise.
- Interaction features containing color codes to reduce the search range.
- Statistical outlier detection for automatic removal of wrong matches.

The work presented in this chapter is partially covered in the author's previous publications [OLD11a, OLD11c, OLDE*12].

4.1. Root independence

As it is illustrated in Figure 4.1 given two graphs G_1 and G_2 under root independence conditions (no corresponding roots are initially known) the common area between both graphs is unknown. Any of the nodes of both graphs is a potential root.

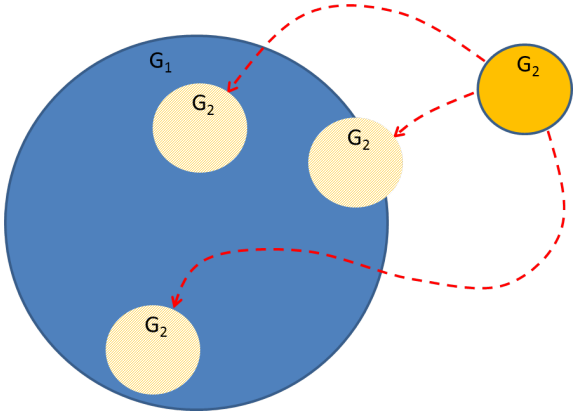

Figure 4.1.: Given two graphs G_1 and G_2, the area shared by both graphs is initially unknown.

4.1.1. Computation of the optimal solution

Manual detection of roots is often problematic. However, roots allow to determine the traverse direction of the method. The goals of the root independence are therefore:

- No need for preselection of correspondences
- Known traverse direction

In the proposed method the traverse direction will be given by a randomly selected node in one graph. This "root" is the starting point to convert the graph into a directed graph. Figure 4.3 shows an initial undirected graph G_1. A node is randomly labeled as root node. Then G_1 is converted into a directed graph G'_1 starting from the selected root node. The matching process seen from G'_1's perspective will follow the strategy proposed in the previous chapter. The order to visit its nodes will depend on the size of the subgraph rooted at them (first the leaves that have a subgraph size of 1), and they will be compared to all nodes in G_2.

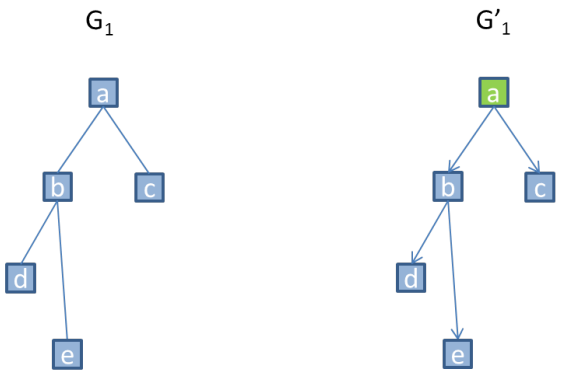

Figure 4.2.: First step of the root independent approach. G_1 is converted into a directed graph G'_1 starting from a randomly selected node.

Since initially no correspondences are known, the second graph remains undirected. However, during the matching process all nodes in the second graph will be seen as potential roots. As it is shown in Figure 4.3, G_2 is an undirected graph. Opposite to the tree matching process described in the previous chapter, the lack of a correspondence eliminates the possibility for the nodes in G_2 to be traversed in an order determined by the root. Instead, the nodes in G_2 will be visited in an arbitrary order. Note that regardless of that order, dynamic programming is still possible thanks to the traversing order given by G'_1.

During the matching process nodes of G'_1 will be compared to nodes in G_2. Each time a node in G_2 is under study, it will be temporarily seen by the method as a root. Then, that node in G_2 will define the traverse direction in G_2. Figure 4.3 shows this process for two nodes 2 and 7 at two different iterations. If G_1 and G_2 are acyclic graphs (all considerations about cyclic graphs will be given in Section 4.2), once the traverse directions in both graphs is known, the matching process will proceed as explained in the previous chapter (see Section 4.1.3 for an example). The sets of reduced graphs will be

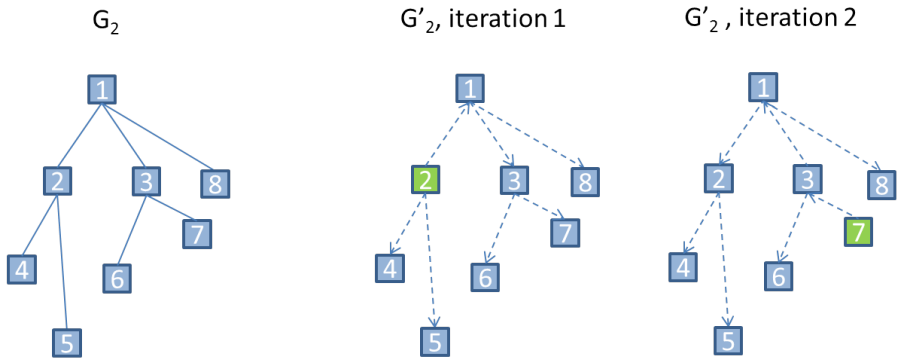

Figure 4.3.: During the matching process all nodes in G_2 will be seen as potential roots. When a node in G_2 is under study, it will determine the traverse direction inside G_2.

generated and the combinations fulfilling the injection relation will be calculated. When the matching process is over (the root of G_1' is reached), the matrix will be analyzed in search for the maximum similarity value, and the reconstruction of the final set of matches will take place.

In Figure 4.4 a small part of the graphs in Figure 3.33 is shown and serves to motivate the need to keep the second graph undirected. The first subgraph G_1' has been converted into a directed graph. The second graph is represented as a directed G_2' and an undirected G_2 graph. The observation of the sets of reduced graphs of G_1', G_2' and G_2 highlights the advantages of keeping the second graph undirected. The set of matches will be given by the Cartesian product between $F_{1'}^{a}$, and $F_{2'}^{\phi(a)}$ or $F_{2}^{\phi(a)}$. The final set of correct matches should be composed of $\{(a,\phi(a)),(b,\phi(b)),(c,\phi(c)),(d,\phi(d)),(e,\phi(e),(f,\phi(f))\}$. The Cartesian product of the elements of $F_{1'}^{a}$ and $F_{2'}^{\phi(a)}$ would include (among other combinations) $\{(a,\phi(a)),(d,\phi(d))\}$. The reason for this is that the amount of nodes of G_2' that is studied is constraint by the direction of the edges. The Cartesian product of $F_{1'}^{a}$ and $F_{2}^{\phi(a)}$, on the contrary, would include $\{(a,\phi(a)),(b,\phi(b)),(d,\phi(d)),(e,\phi(e)),(f,\phi(f))\}$ (i.e. all the nodes of G_2 are studied). The match $(c,\phi(c))$ would be included in the set of matches in the next iteration of the method.

Topological inconsistencies Thanks to the proposed approach there is no need for root preselection or directed graphs. However, some difficulties arise from that lack of constraints. In fact topological inconsistencies can happen and they have to be detected and resolved properly to ensure the validity of the obtained results. The two subgraphs shown in Figure 4.5 are again taken from real clinical datasets (the orange ellipse highlights a spurious branch in G_1' and c in G_2 introduces topological differences between both graphs). Taking into account the bottom-up strategy, initially the leaves will be matched and the process will continue until a in G_1' is reached. Let's assume that up to node f in G_1 the best similarity measure has been achieved by matching the set of nodes $\{(f,f),(d,d),(e,e),(g,g)\}$. According to the bottom-up strategy, the next node to be studied will be j, that will produce low similarity values taking into account its condition as spurious branch. In the next iteration the node a in G_1' will be studied. It would be topo-

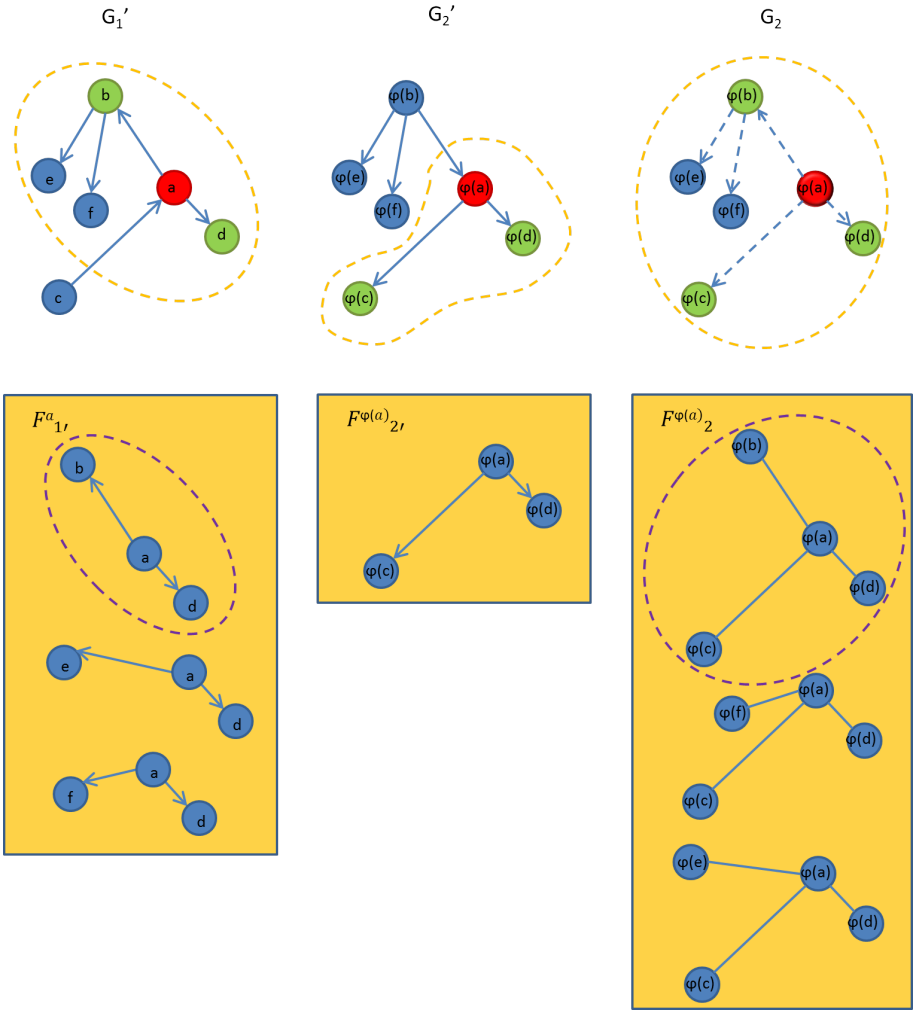

Figure 4.4.: Difference in the final set of matches if directed or undirected graphs are taken into account. The figure shows a small part of the graph shown in Figure 3.33. The red nodes are the ones under study and the green ones those that are considered as valid matches in the current iteration. The set of reduced graphs obtained in each case is shown in orange squares. The first element of set of G_2 allows to consider the combination $\{(b, \phi(b))(d, \phi(d))\}$ that would not be considered otherwise.

logically inconsistent to match (a, a) while keeping $\{(f, f), (d, d), (e, e), (g, g)\}$. The only way to consider all the matches would be by merging c and f in the second graph. This is visually clarified with the colored lines. Each colored line shows the shortest path from f to the matched descendant. One can see that in the second graph two paths (red and violet) are overlapping over the path connecting c and f, which is topologically impossible.

Let $p_1 = [a, j, f]$ be the blue path between the node under study a and the child f in G_1' and $p_2 = [a, c, f]$ its counterpart in G_2. And let $B_1 = \{[e, f], [g, f], [d, f]\}$ in G_1' be the set of paths between that child f and all node pairs that were matched to achieve the highest similarity value at (f, f), and $B_2 = \{[e, f], [g, f], [d, c, f]\}$ its counterpart in G_2. To ensure that there will not be topological errors there should not exist intersections between p_1

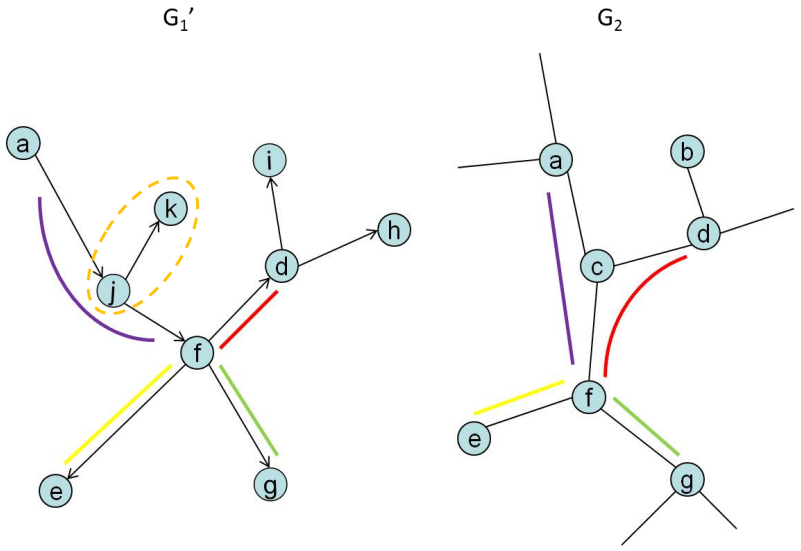

Figure 4.5.: Topological inconsistencies that have to be taken into account. It is not topologically impossible to match nodes (a,a) and [(f,f),(d,d),(e,e),(g,g)] at the same time [OLD11c].

and B_1 and between p_2 and B_2.

When the node *a* in Figure 4.5 is visited, the combination of matches that fulfills the previous condition and leads to the highest similarity measure will be chosen (either nodes *a*, *f*, *e* and *g*, *a* and *d* or *a*, *f*, *e*, *g* and *d* if *f* and *c* in G_2 are merged using the corresponding primitives). The unmatched nodes will then be considered spurious nodes.

4.1.2. Formal definition of the problem

This section updates the formal definition of the problem with the considerations required for root independence.

(1) The input graphs are undirected unrooted acyclic graphs.

(2) Matches should fulfill the topological consistency condition (see Definition 4.1).

Note that even if this search strategy can be (and will be) used for cyclic graphs, the formal definition will first be defined for acyclic graphs. The definition will be updated to consider cyclic graphs in Section 4.2.3, when all the new challenges related to cycles have been introduced.

Definitions 3.1 to 3.5 will remain unchanged in the presence of acyclic and undirected graphs. The Cartesian product, injective relations and reduced graphs can be generated similarly as done with rooted directed trees. Note that even if the graphs are undirected, the generation of reduced graphs is produced when G_2 (and G_1) has a temporary direction given by the visited node (temporary root). Thus, in every sense the generation of reduced graphs is equivalent to the generation when the input graphs are rooted directed trees.

Definition 3.6 defines how to generate the sets of valid matches according to the injection definition (Definition 3.3). The injective relation should still be fulfilled for the set

of matches to be valid. However, as mentioned before, indirection introduces potentially inconsistent matches in the process. Thus, a new definition is required that ensures that the set of valid matches will not contain inconsistent matches.

Definition 4.1. Let p_1 be a path between a node u and one of its children v in G_1' and p_2 a path between the corresponding nodes $\phi(u)$ and $\phi(v)$ in G_2. Let B_1 be the set of paths between v and its matched children in G_1', and B_2 its counterpart in G_2. To avoid topological inconsistencies there should not exist an intersection between p_1 and anyone of the paths contained in B_1, and also not between p_2 and anyone of the paths contained in B_2. Thus, the following rule

$$p_j \bigcap (B_j)_i = \emptyset \ \forall i \tag{4.1}$$

must hold. i is an integer that takes the values [1,n], where n is the number of paths in $(B_j)_i$ and $j = [1, 2]$.

This new definition further constrains the set of valid matches. Definition 3.6 has to be updated accordingly.

Definition 4.2. Let G_1 and G_2 be the two undirected acyclic graphs to be matched. Let F_1^u and $F_2^{\phi(u)}$ be two sets of reduced graphs such that F_1^u contains the set of reduced graphs rooted at $u \in G_1$ and $F_2^{\phi(u)}$ contains the set of reduced graphs rooted at $\phi(u) \in G_2$. The set of possible combinations of matches can be obtained as the subset of the Cartesian product of all elements of F_1^u and $F_2^{\phi(u)}$ that fulfill Definition 3.3 and Definition 4.1.

Let n and m be the number of children of u and $\phi(u)$ respectively such that $m > n$, and let A be the set that contains all injective relations between the two subgraphs rooted at u and $\phi(u)$. There are no more than $|F_1^u||F_2^{\phi(u)}|m^{\underline{n}}$ combinations that fulfill those conditions (see Equation 3.31). If no inconsistent combinations exist (see Equation 4.1), the number of valid combinations of matches will be $|F_1^u||F_2^{\phi(u)}|m^{\underline{n}}$. Each one of the combinations represent a set A_i of $min(n, m)$ matches.

The definition of the problem as a recursion (Definition 3.7) is still valid as far as the input graphs do not contain cycles.

4.1.3. Example

Figure 4.6 shows to graphs to be matched. Initially G_1 is converted into directed graph G_1'. In the example the node a has been used as root for that purpose, but any other node could have been used. First, the leaves (c, d and e) of G_1' will be compared to all nodes in G_2. As it was explained before, the similarity value given a leave is a plain similarity and can be directly calculated.

According to the size of the subgraphs included in G_1' the next node to be studied is b. b is not a leave thus the set of reduced graphs rooted at b has to be generated (see F_1^b in Figure 4.6). b has to be compared to all nodes in G_2. Since G_2 is an undirected graph, there is no special order to visit its nodes. The comparison process will end when all nodes of G_2 have been compared to b. Each time a node of G_2 is under study, (for instance, 2 in Figure 4.6), this node determines the temporary direction to traverse

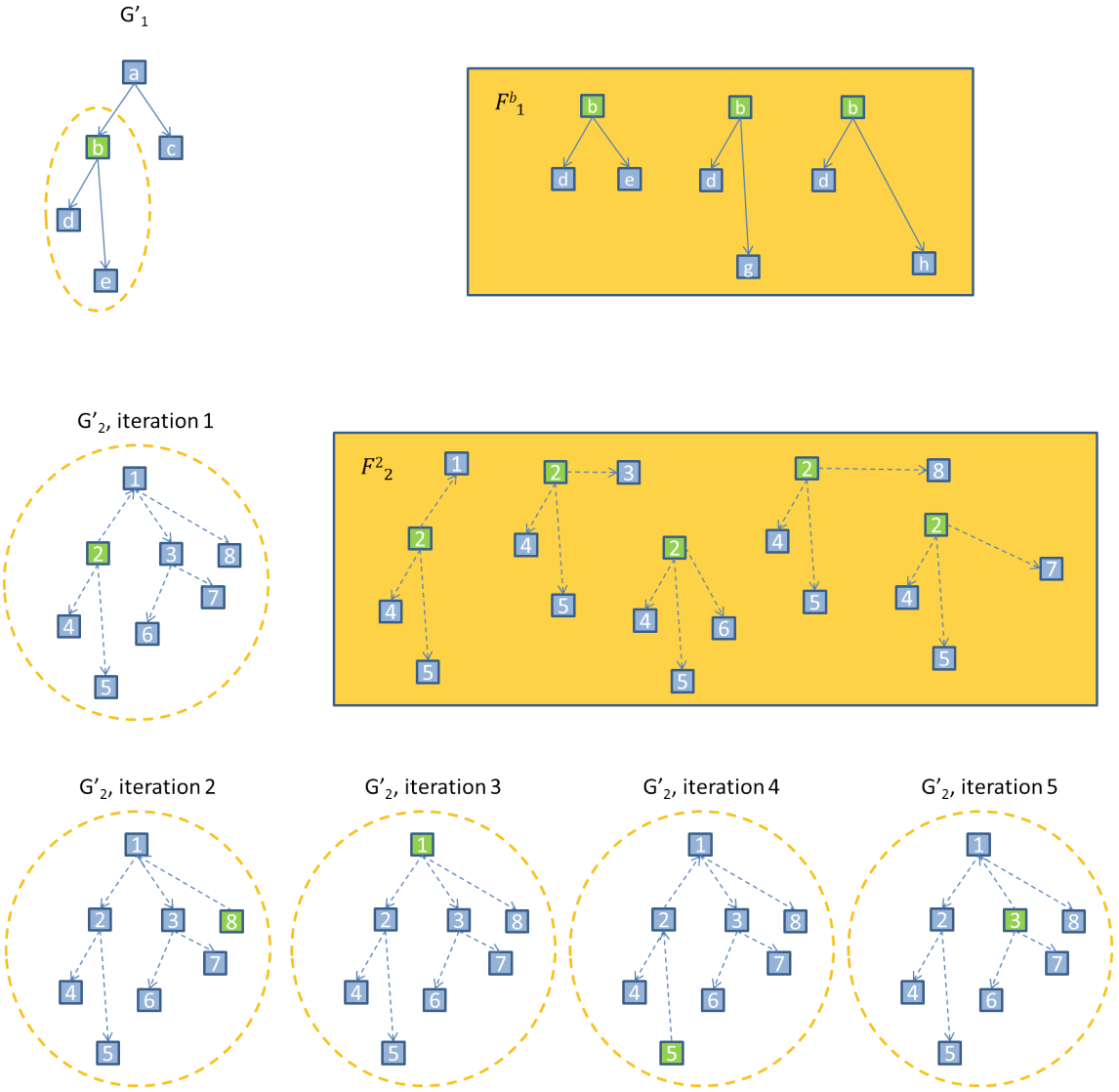

Figure 4.6.: Matching strategy when the input graphs are unrooted and undirected.

G_2. Then, the set F_2^2 of reduced graphs of G_2 rooted at 2 is generated. Once both sets of reduced graphs are generated, the Cartesian product between their elements is calculated and its solutions filtered according to the injection and topological consistency conditions. The maximum similarity value obtained among the remaining combinations will be stored in the association matrix.

Then, a new node in G_2 will be compared to b (8 in Figure 4.6). The traverse direction in G_2 will be now determined by the new root of G_2, namely 8, and the computation of the optimal match process will be repeated. This will happen until all nodes in G_2 have been visited. Then, the node a in G_1' will be compared to all nodes in G_2 and the process will finish. The final set of matches will be obtained according to the highest similarity value stored in the association matrix.

4.1.4. Pseudocode

Algorithm 7 is an update of the algorithm proposed for rooted directed trees. Let for the moment consider G_1 as an undirected acyclic graph. G_1 is initially converted into a directed graph (line 4). Similarly as it was done to find correspondences between rooted trees, the length and direction of all pair of nodes is pre-calculated (lines 5-8) to decrease the operations needed during the optimal match calculation (line 10). As it was mentioned before the traversing direction will be given by G'_1. Thus, the size of all subgraphs included in G'_1 has to be calculated (line 9).

Algorithm 7 Graph matching

1: Let G_1 and G_2 be two undirected graphs
2: Let M_{l_1}, M_{l_2}, M_{d_1}, M_{d_2} and M be five new matrices
3: Let p be a new array
4: $G'_1 \leftarrow$ GenerateDirectedGraph(G_1)
5: $M_{l_1} \leftarrow \forall u, v \in V(G'_1), \mathit{GetGeodesicLength}(u, v, p_1)$
6: $M_{l_2} \leftarrow \forall u, v \in V(G_2), \mathit{GetGeodesicLength}(u, v, p_2)$
7: $M_{d_1} \leftarrow \forall u, v \in V(G'_1), \mathit{GetDirection}(u, v, p_1)$
8: $M_{d_2} \leftarrow \forall u, v \in V(G_2), \mathit{GetDirection}(u, v, p_2)$
9: CalculateSubgraphSizes(G'_1)
10: COMPUTE OPTIMAL MATCH($G'_1, G_2, M_{l_1}, M_{l_2}, M_{d_1}, M_{d_2}, M$)

Opposite to the algorithm for rooted directed trees (see Algorithm 6), the traverse direction is guided by the sizes of the subgraphs of G'_1 as shown in Algorithm 8 line 4. The rest of the algorithm proceeds as expected, the sets of reduced graphs are generated (lines 9-10) and the highest similarity (line 12) between all valid combinations (line 11) is calculated.

The procedure to find combinations is enhanced with the topological inconsistence filter (line 8 in Algorithm 9). Once the injective solutions (line 7) of the Cartesian product (line 6) have been selected, the solutions that do not fulfill the consistency conditions are filtered out. Only those solutions that fulfill both conditions will be returned and considered in the similarity calculation.

Accelerators Opposite to Algorithm 6 the root distance accelerator cannot be used anymore as no corresponding roots are known initially (see Algorithm 8). However, the second accelerator introduced in Section 3.5 can still be used. This is illustrated in Figure 4.7. Even if the graphs do not have any initially known pair of correspondences that can be used as global roots, the current nodes under study (b in G'_1 and 2 in G'_2 in Figure 4.7) can be used as temporary correspondences. Then if the ratio between the geodesic distances of the nodes b and 2 to its descendants is higher than certain threshold, descendant that are farther away will be ignored. This in practice is translated into a decrease in the number of elements of the set of reduced graphs.

Algorithm 8 Compute optimal match

procedure COMPUTE OPTIMAL MATCH($G'_1, G_2, M_{l_1}, M_{l_2}, M_{d_1}, M_{d_2}, M$)
  for $i \leftarrow 1, |V(G'_1)|$
    for all $V(G_2)$
      for all $G'^{u}_1 : |V(G'^{u}_1)| = i$
        Let s be a variable
        if u and/or $\phi(u)$ is a leaf
          $s \leftarrow SL(u, \phi(u))$
        else
          $F^{u}_1 \leftarrow$ GENERATE SET(u)
          $F^{\phi(u)}_2 \leftarrow$ GENERATE SET($\phi(u)$)
          A $\leftarrow$ FIND COMBINATIONS(F^{u}_1,$F^{\phi(u)}_2$)
          $s \leftarrow SL(u, \phi(u))+max\{\sum_{j=1}^{z} ST(A_{1_j}[0], A_{1_j}[1]); ...; \sum_{j=1}^{z} ST(A_{q_j}[0], A_{q_j}[1])\}$
          $r \leftarrow GetChildrenOptimalMatch(G^{u}_1, G^{\phi(u)}_2)$
        end if
      end for
    end for
  end for
  return s and r
end procedure

Algorithm 9 Injective solutions

procedure FIND COMBINATIONS(F^{u}_1,$F^{\phi(u)}_2$)
  for $i \leftarrow 0, |F^{u}_1|$
    for $j \leftarrow 0, |F^{\phi(u)}_2|$
      $D \leftarrow C(F^{u}_{1_i})$
      $E \leftarrow C(F^{\phi(u)}_{2_j})$
      CP $\leftarrow$ CALCULATE CARTESIAN PRODUCT(D,E)
      A $\leftarrow$ SELECT INJECTIVE SOLUTIONS(CP)
      A $\leftarrow$ TOPOLOGICAL INCONSISTENCY FILTER(A)
    end for
  end for
  return A
end procedure

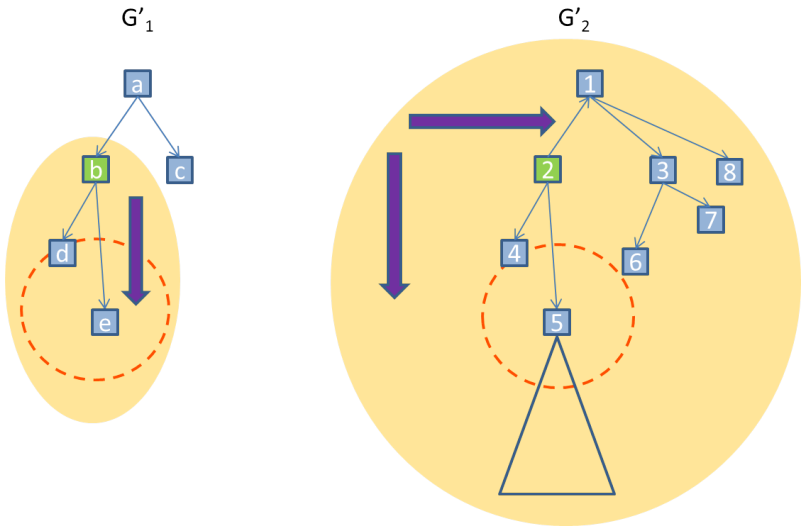

Figure 4.7.: The second accelerator can still be used. When the ratio between geodesic distances between a potential match an its temporary root is to high its descendants will not be checked anymore, reducing as consequence the size of set of reduced graphs.

4.2. Cyclic graphs

With the solutions presented up to this point it is possible to efficiently detect matches between two undirected unrooted acyclic graphs. This section will present a solution for the detection of correspondences in the presence of cyclic graphs (G_1 and/or G_2) that incorporates all the ideas previously presented.

Furthermore, since the roots are unknown (and probably inexistent) the reconstruction step cannot assume that the highest total similarity will be achieved matching the roots. This fact motivates the idea that due to topological differences the graphs might not only have a unique pair of corresponding roots, but also some secondary roots. The detection of all of them will increase the size of the final set of matches.

Finally, cyclic graphs will introduce the concepts of loops and shortest paths in the process.

4.2.1. Computation of the optimal solution

The detection of correspondences between two undirected unrooted cyclic graphs follows a bottom-up strategy. Concretely, the root independent solution presented in Section 4.1 is used as strategy to traverse the graphs. The considerations that has to be taken into account in the presence of cyclic graphs are explained in the next paragraphs. Then, the formal definition of the problem will be extended to incorporate these new considerations.

Cycles represent one step forward on the way from ideal to real-world graphs that represent anatomical structures. In Figure 3.11 (b) spurious branches were introduced in the matching problem. Now, cycles will also be introduced as shown in Figure 4.8. The introduction of cycles mean that there might be multiple paths connecting two nodes. Within the matching process this will have two consequences. First, opposite to the tree

to tree matching method the set of reduced graphs will contain elements (graphs) with different sizes. Second, shortest path assumptions appear to be helpful to calculate the length and direction similarity between two nodes.

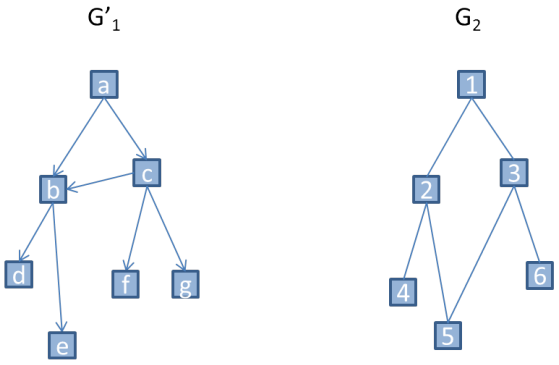

Figure 4.8.: In the real-world graphs will also contain cycles.

Sets of reduced graphs During the generation of the set of reduced graphs, G_1 and G_2 are directed. G_1 has been converted into a directed graph G'_1 at the beginning of the method, and G_2 has a traverse direction G'_2 each time one of its nodes is visited (that node will be labeled temporarily as root). Multiple paths connecting nodes result in reduced graphs that were not found in the tree matching process. Let G' be a directed graph (see Figure 4.9 (a)). The node a in G' has two children b and c. Opposite to the tree matching method, the subgraphs rooted at b and c will have a series of common nodes caused by the multiple paths (orange ellipse in Figure 4.9 (b)). According to the definition of reduced graph, a reduced graph will have $a \in G'$ as root and one node of G'^b and one node of G'^c as children (see dashed lines in Figure 4.9). However, multiple paths will cause two new types of structures during this process (see Figure 4.9 (c)).

A node b could appear two times in the reduced graph. In this case one of the connecting edges should be ignored to ensure that the injection condition is fulfilled. On the other side, the child e of b in G' could become a sibling of b in the reduced graph. Due to the cycles this is not necessarily topologically inconsistent. It can be observed that the elements of the set of reduced graphs under the condition of cyclic graphs do not necessarily have the same size.

Shortest path assumption The proposed method allows graphs to contain cycles. Nonetheless, cycles do not represent the real vascular structure but are caused by imaging artifacts. In theory, all the paths that connect two nodes should be taken into account by the method to find the highest optimal match. This, however, would increase the number of operations required. Since intra-operative registration is one the the potential scenarios in which the method can be used [OLDE*12], time is a constraint. Thus, in this chapter the assumption is made that the path that represents the correct underlying anatomical structure is the shortest path between two nodes. The evaluation results (Section 4.6) confirm that this assumption can be made.

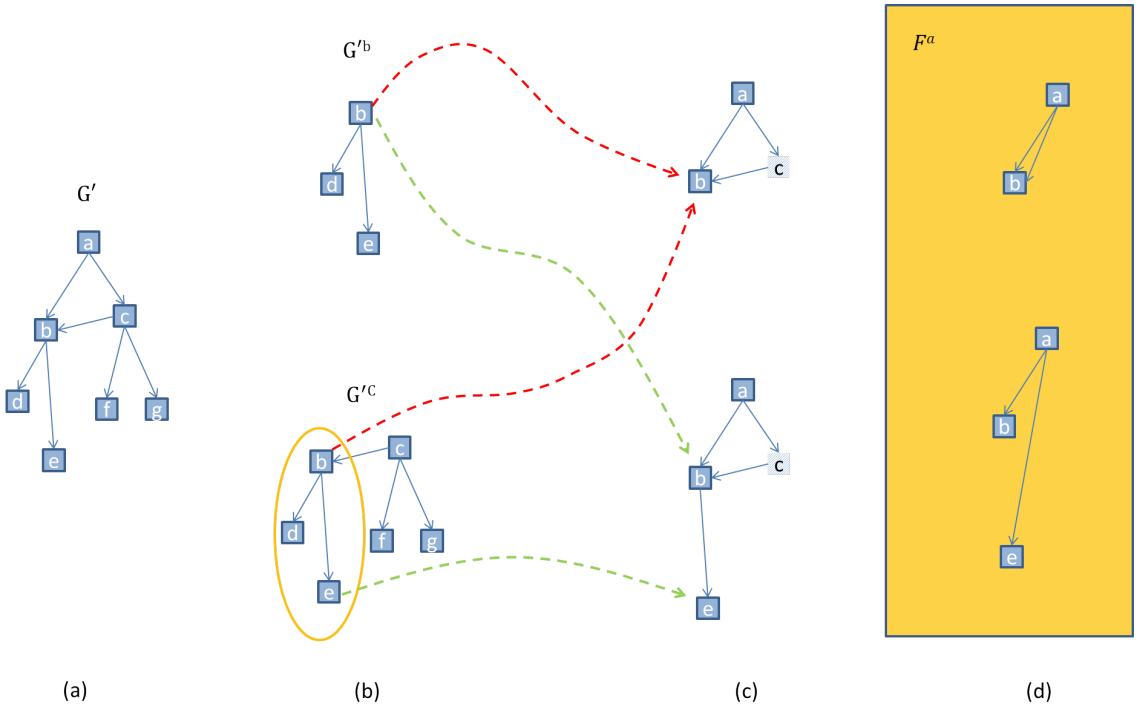

Figure 4.9.: (a) graph with multiple paths connecting *a* and *b*. (b) Subgraphs rooted at *b* and *c*. (c) Generation of reduced graphs. (d) Subset of the set of reduced graphs.

The shortest path problem is well known in graph theory and several methods have been developed to solve it. Among them the Dijkstra's method [Dij59] uses dynamic programing to solve the single-source path problem and it has shown to be robust and efficient. Opposite to the single-source path problem that calculates the shortest paths from a source node to the rest of the nodes, this chapter requires to have a solution for all-pair shortest paths. In this sense Dijkstra's method can be efficiently applied to each node of the graph to obtain all-pair shortest paths. The only restriction of Dijkstra's method is that no negative edges exist. However, since the weights of this chapter are given by the geodesic lengths between two nodes, the weights will be always non-negative and Dijkstra's method can be used.

Automatic detection of local minima The shortest path assumption has a disadvantage: It may make the graph method prone to get stuck into local minima. The illustration in Figure 4.10 clarifies this issue. There exist two paths that connect *a* and *b* in G'_1, while there exist only a single path that connects their corresponding nodes, 1 and 4 in G_2. According to the shortest path assumption, the shortest path in G'_1 will be taken as reference. Unfortunately, in the two graphs of the example this does not correspond to the correct corresponding path. It would be possible for another area of the graph to contain a structure that is more similar to that one leading to local minima if the size of the graph, and consequently the set of potential matches, is not large enough to compensate the local error.

To solve this problem the set of valid matches is restricted by removing matches with

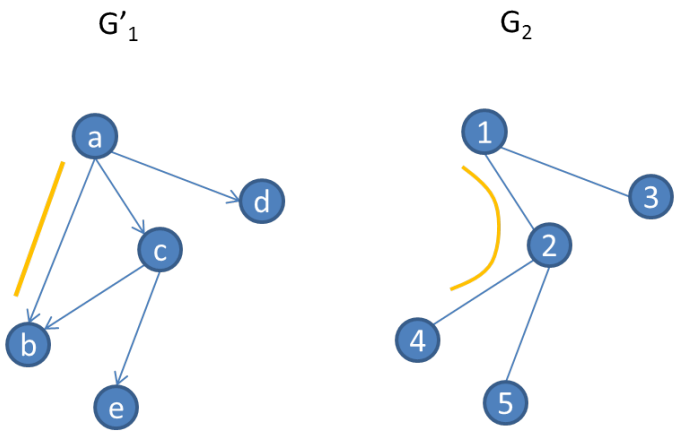

Figure 4.10.: Local minima. *a* and *b* in G'_1 are connected by two paths. The shortest path does not correspond to the actual path in G_2.

a small incremental contribution to the local actual similarity value. In the ideal case, given two identical graphs, the contribution of each new match to the maximum similarity value would be 1. However, this will not hold when both graphs are different. Let $N_{u,\phi(u)}$ be the number of nodes that were matched to achieve the maximum similarity value for $(G_1'^u, G_2^{\phi(u)})$, then only those nodes that fulfill that

$$ST(G_1'^u, G_2^{\phi(u)}) > \epsilon * N_{u,\phi(u)} \tag{4.2}$$

will be added to the final set of matches. ϵ is a threshold that has been experimentally determined and in this chapter takes the value of 0.68. Thus, every new match that is added to the set of optimal matches increases the similarity value in more than $\epsilon * N_{u,\phi(u)}$. The other matches do not contribute enough to the global similarity and are therefore discarded. The formal definition of the problem that follows (Section 4.2.3) will clarify how does Equation 4.2 affect the matching process.

4.2.2. Topological similarity

The set of primitives that were formulated in Section 3.2 are meant to be also used in the graph matching method. However, taking into account that the graphs that are considered may contain cycles, the process of merging nodes can result into undesired structures. Thus, several considerations have to be taken into account. In particular, the two structures shown in the first row of Figure 4.11 (a) have to be detected and corrected. The first structure would lead to a nonexistent cycle after merging. The second structure represent a double edge after merging that has to be eliminated for the generation of injective solutions between both graphs as explained before.

Merging nodes will have a different effect in G'_1 and G_2. G'_1 will be a directed graph already before the merging of nodes takes place. Let G'_1 be the graph shown in Figure 4.11 (b). If node number 3 is merged to node number 1 (c) or if node number 2 is merged to node number 1 (d) undesired structures appear. To solve this problem, the method detects those structures immediately after merging two nodes and removes the

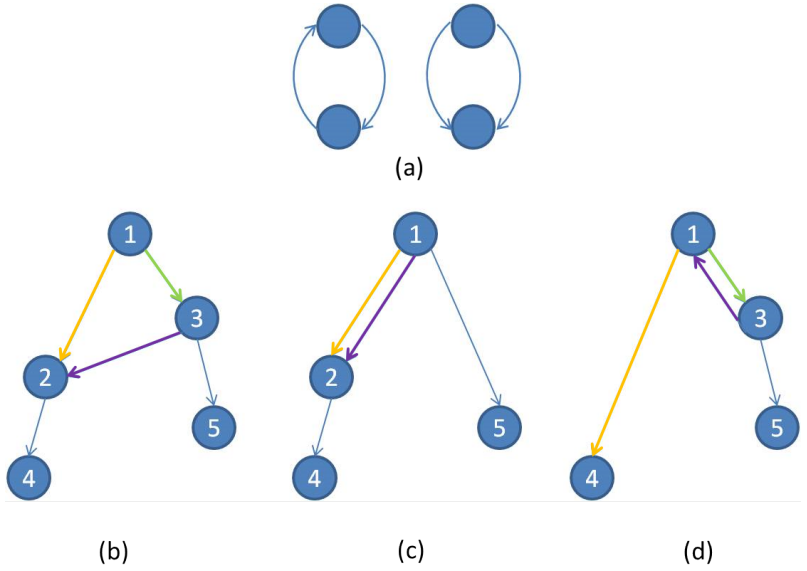

Figure 4.11.: Structures that appear in cyclic graphs after merging. Top: structures to be avoided. Bottom left: Example graph. Bottom middle: double edge after merging 3. Bottom right: cycle after merging 2 [OLD11c].

corresponding edge based on the direction of the graph prior merging. In the case of double edges, one of them will be removed, otherwise the edge pointing to the opposite direction is removed.

G_2 is an undirected graph, thus the effect of merging nodes will produce an undirected cycle. Since during the matching process the node under study in G_2 will act as temporary root to determine the traverse direction of G_2, the produced cycle will take the form seen in the second structure of Figure 4.11 (a). One of the generated edges will therefore be removed.

4.2.3. Formal definition of the problem

Four main considerations have to be included in the formal definition of the problem for graph to graph matching:

- The input to the method are unrooted undirected cyclic graphs.
- The elements of the set of reduced graphs will have different sizes.
- The detection of topological inconsistencies has to be adapted in the presence of multiple paths.
- Local minima is possible and has to be detected.

Definitions 3.1 and 3.2 remain unchanged. They correspond to the definition of n-fold Cartesian product and the Cartesian product of graphs and do not depend of the characteristics of the used input graphs. Similarly, the definition of an injective relation between two graphs will still hold (Definition 3.3).

Definition 4.3 has been used to define inconsistent topologies for undirected acyclic graphs. However, cycles mean that multiple paths can exist. According to the shortest path assumption, the shortest path between two nodes is considered to be the one that correctly represent the underlying anatomical structure. Thus, this will be the path that will be used for the detection and exclusion of topological inconsistencies.

Definition 4.3. Let p_1 be the shortest path between a node u and one of its children v in G_1' and p_2 the shortest path between the corresponding nodes $\phi(u)$ and $\phi(v)$ in G_2. Let B_1 be the set of shortest paths between v and its matched children in G_1', and B_2 its counterpart in G_2. To avoid topological inconsistencies there should not exist an intersection between p_1 and anyone of the shortest paths contained in B_1, and also not between p_2 and anyone of the shortest paths contained in B_2. Thus, the following rule

$$p_j \bigcap (B_j)_i = \emptyset \ \forall i \tag{4.3}$$

must hold. i is an integer that takes the values [1,n], where n is the number of shortest paths in $(B_j)_i$ and $j = [1, 2]$.

A reduced graph can still be defined using Definition 3.4, but the definition should be extended as follows:

Definition 4.4. A reduced graph generated from a cyclic graph G may contain double edges connecting the root and its children. In that case, only one edge will be included in the reduced graph.

Definition 4.5. The elements of set of reduced graphs generated from a cyclic graph do not necessarily have equal size.

According to the formal definition of rooted trees, the injective solutions of the Cartesian product are stored in a set A. Each A_i represent one the injective solutions. The number of matches contained in one A_i was given by $min(n, m)$, where n and m were the number of children of $u \in F_1^u$ and $v \in F_1^v$ respectively. Since all elements in F_1^u and in F_1^v had equal size the number of matches of all A_i was equal.

According to Definition 4.5 cycles will cause the elements of the sets of reduced graphs to have different sizes (see Figure 4.9). Thus, the size of each A_i will vary and will depend on the number of children of the concrete elements of F_1^u and F_1^v that lead to that solution.

Definition 4.6. Let G_1 and G_2 be the two graphs to be matched. Let F_1^u and $F_2^{\phi(u)}$ be two sets of reduced graphs such that F_1^u contains the set of reduced graphs rooted at $u \in G_1$ and $F_2^{\phi(u)}$ contains the set of reduced graphs rooted at $\phi(u) \in G_2$. The set of possible combinations of matches can be obtained as the subset of the Cartesian product of all elements of F_1^u and $F_2^{\phi(u)}$ that fulfill Definitions 3.3 and 4.3.

Let A be the set that contains all injective and topologically consistent relations between the two subgraphs rooted at u and $\phi(u)$. Let A_i be one injective and topologically consistent solution. Each A_i does not have the same number of matches since each element of F_1^u and $F_2^{\phi(u)}$ has not the same size. Let n and m be the number of children of u and $\phi(u)$ for a pair of elements in F_1^u and $F_2^{\phi(u)}$. For A_i corresponding to that pair of elements the number of matches is given by min(n,m).

The number of combinations that fulfill Definitions 3.3 and 4.3 is smaller or equal than $\sum_{i=1}^{F_1^u} \sum_{j=1}^{F_2^{\phi(u)}} m_j^{\underline{n_i}}$, given $m > n$. The equality will only hold if there are no inconsistent combinations.

The problem can then be defined in a recursive way taking into account that local minima has to be avoided, and that the number of matches of each solution will vary (see Definition 4.6).

Definition 4.7. The pairwise similarity of two graphs can be recursively defined as follows:

- Basis step: The similarity of all leaves is a plain local similarity that can be calculated with Equation 3.6.
- Recursive step: Let $z_i = min(n, m)$ be the number of matches in the set A_i with $i \in q$, and q the number of sets (see Definition 3.6) at a recursion step. The total similarity between any other pair of nodes (u and $\phi(u)$) can be calculated as:

$$ST(u, \phi(u)) = SL(u, \phi(u)) + max\{\sum_{j=1}^{z_1} ST(A_{1_j}); \sum_{j=1}^{z_2} ST(A_{2_j}); ...; \sum_{j=1}^{z_q} ST(A_{q_j})\}. \quad (4.4)$$

  For all the combinations considered in 4.4 the next equation should hold:

$$\forall A_i | \sum_{j=1}^{z_i} ST(A_{i_j}) > \epsilon * N_{u,\phi(u)}. \quad (4.5)$$

4.2.4. Example

Figure 4.12 shows two example graphs to be matched with the proposed method. The graph G_1' has already been converted into a directed graph. One can observe that nodes a and e are connected by two paths in G_1'. A cycle formed by the nodes 2,5 and 6 is visible in G_2. The process of matching both graphs will start at the leaves of G_1' and will proceed following a bottom-up strategy according to the size of the subgraphs that are found in G_1', exactly as proposed in Section 4.1.

Initially the leaves of G_1', namely, d, g, h and f, will be compared to all nodes in G_2. As it was previously explained, the similarity of the leaves will consist of a plain local similarity.

The matching process will be more challenging for the remaining recursion steps. In the next step the set of reduced graphs rooted at e should be generated and compared to the sets of reduced graphs generated on each node in G_2. Note however, that in this example G_2 contains a cycle.

Remember that the nodes in G_2 will be visited in an arbitrary order. Let $5 \in G_2$ be the node under study. Then, 5 will be labeled as temporary root of G_2. The cycle will cause the set of reduced graphs to contain reduced graphs that were not present with acyclic graphs, as explained in Section 4.2.1. In the first reduced graph of F_2^5 (see Figure 4.13) the node 2 has been reached directly through 5 and indirectly through 6. In the second reduced graph the nodes 2 and 1 are considered as siblings (they share the

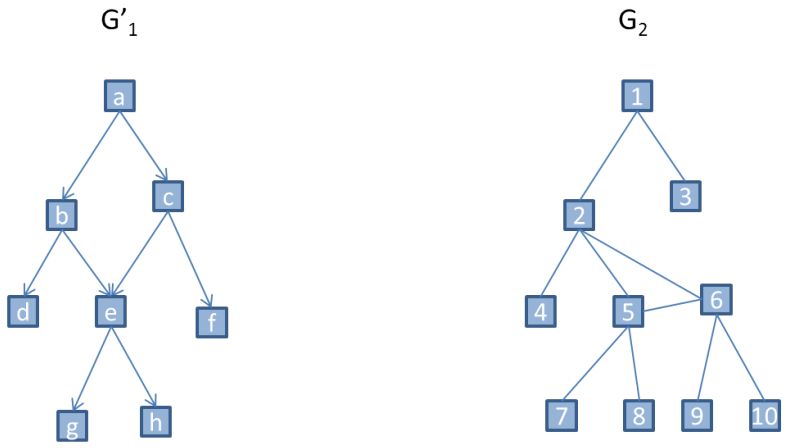

Figure 4.12.: Two example graphs to be matched.

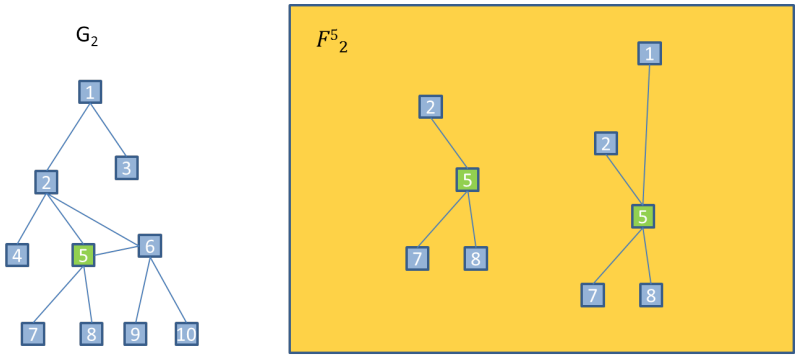

Figure 4.13.: Some interesting elements of the set of reduced graphs of G_2 with 5 being the node under study.

parent) although in the original graph they are neighboring nodes (nodes connected by and edge). In this sense Definition 4.3 will ensure that no topological inconsistencies exist in the final set of matches. Note that opposite to the initially presented method (Section 3.3.1), the elements of a set of reduced graphs are not equally large.

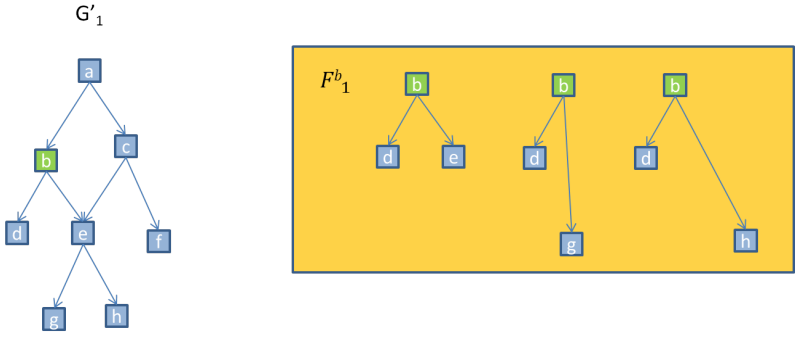

Figure 4.14.: Set of reduced graphs derived from b.

Once the node *e* is compared to all nodes in G_2, the process will proceed with nodes

b and *c*. Note that so far the sets of reduced graphs generated from G'_1 do not differ from those that would be generated if G'_1 would be an acyclic graph (see Figure 4.14). The difference arrives at *a*. The first element in F_1^a correspond to a graph with a single connection (see Figure 4.15). The reason for this is that starting at *a*, *e* can be reached through *b* and through *c*, resulting on that reduced graph. In the second subgraph *e* is considered a sibling of *g* (they share the parent) although in the original graph *e* is the parent node of *g*. A similar effect can be observed in the last element with *b* and *e* regarded as siblings, although in this case *b* is the parent of *e* in the original graph.

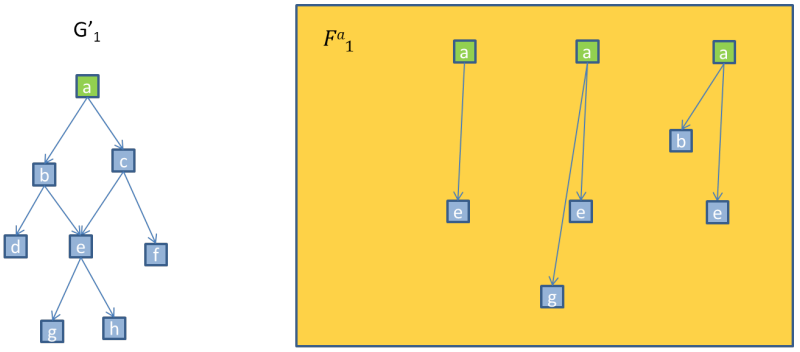

Figure 4.15.: Some interesting elements of the set of reduced graphs of G'_1 with *a* is under study.

Once *a* is reached and compared to all nodes in G_2, the association matrix contains all similarity values and the reconstruction of the optimal solution step can start.

4.2.5. Pseudocode

Algorithm 10 helps to clarify the graph matching process. The input to the algorithm are two undirected (unrooted) graphs. In line 4 G_1 is converted into a directed graph G'_1. Then, the shortest paths that connect each pair of nodes are precalculated (lines 5-6). Thanks to the shortest path assumption, the lengths and directions between each pair of nodes in G'_1 and G_2 respectively can be precalculated and stored in matrices (lines 7-10) to reduce the number of operations required during the matching process, when the pairwise similarity between nodes has to be calculated. The bottom-up strategy will be given by G'_1, and the order to visit its nodes will be determined by their correspondent subgraph size (line 11).

The "Compute optimal match" procedure is detailed in Algorithm 11. Note that the bottom-up strategy is now centered on G'_1 (lines 2 and 4) but the nodes in G_2 do not require any special order (line 3). For each pair of nodes to be matched the sets of reduced graphs rooted at those nodes are generated (lines 9-10). Then, the set of combinations are generated (line 11). These combinations will be filtered using the local minimum criterium that was previously defined (line 14). If the obtained similarity value does not fulfill the condition given in Equation 4.2, the pairwise similarity of those nodes will be set to 0.

Note that the distance to root accelerator cannot be used in the graph matching method since the pair of correspondent roots is unknown. The second accelerator that reduces number of descendant nodes to be considered can be still used. This accelerator will

Algorithm 10 Graph matching

1: Let G_1 and G_2 be two undirected graphs
2: Let M_{l_1}, M_{l_2}, M_{d_1}, M_{d_2} and M be five new matrices
3: Let p be a new array
4: $G'_1 \leftarrow$ GenerateDirectedGraph(G_1) ▷ $\mathcal{O}(|V(G_1)|)$
5: $p_1 \leftarrow$ CalculateShortestPaths(G'_1) ▷ $\mathcal{O}(|E(G'_1)||V(G'_1)| + |V(G'_1)|^2 log|V(G'_1)|)$
6: $p_2 \leftarrow$ CalculateShortestPaths(G_2) ▷ $\mathcal{O}(|E(G_2)||V(G_2)| + |V(G_2)|^2 log|V(G_2)|)$
7: $M_{l_1} \leftarrow \forall u, v \in V(G'_1)$, *GetGeodesicLength*$(u, v, p_1)$ ▷ $\mathcal{O}(|V(G'_1)|^2)$
8: $M_{l_2} \leftarrow \forall u, v \in V(G_2)$, *GetGeodesicLength*$(u, v, p_2)$ ▷ $\mathcal{O}(|V(G_2)|^2)$
9: $M_{d_1} \leftarrow \forall u, v \in V(G'_1)$, *GetDirection*$(u, v, p_1)$ ▷ $\mathcal{O}(|V(G'_1)|^2)$
10: $M_{d_2} \leftarrow \forall u, v \in V(G_2)$, *GetDirection*$(u, v, p_2)$ ▷ $\mathcal{O}(|V(G_2)|^2)$
11: CalculateSubgraphSizes(G'_1) ▷ $\mathcal{O}(|V(G'_1)|)$
12: COMPUTE OPTIMAL MATCH($G'_1, G_2, M_{l_1}, M_{l_2}, M_{d_1}, M_{d_2}, M$) ▷ $\mathcal{O}(|V(G'_1)|^2|V(G_2)|^2)$

reduce the number of elements (reduced graphs) contained in the set of reduced graphs. Consequently, the number of possible combinations and operations required will also be reduced.

The number of reduced graphs in the set can be farther reduced by ignoring the possibility of merging nodes during the matching process. The fact that the graph matching method is able to handle loops makes the algorithm slower in presence of large graphs. When nodes are merged, the number of reduced graphs increases and consequently the efficiency is further decreased. For applications in which time is a limiting factor nodes will not be merged.

Algorithm 12 highlights the need to constraint the set of combinations not only according the definition of injective solution (line 7), but also considering the definition of topological inconsistency that was defined in the previous section (line 8).

Complexity The computational complexity of each step of the algorithm is included in Algorithm 10. The complexity to generate the geodesic length and direction matrices ($\mathcal{O}(|V(G'_1)|^2)$ for G'_1 and $\mathcal{O}(|V(G_2)|^2)$ for G_2) and that needed to calculate all subgraph sizes in G'_1 ($\mathcal{O}(|V(G'_1)|)$) were already analyzed in the tree matching section 3.5. The complexity to calculate all-pair shortest paths using Dijkstra's method is well known [FT87] and given by $\mathcal{O}(|E(G'_1)||V(G'_1)| + |V(G'_1)|^2 log|V(G'_1)|)$, where $E(G'_1)$ represents the set of edges of G'_1. As in the tree matching method, the computational complexity of the algorithm is dominated by the compute optimal match procedure.

Algorithm 11 theoretically explains how to compute the optimal match. It is dominated by the "generate set" procedure (lines 9-10) and specifically be the computation of the Cartesian product that would result in a computational complexity of $\mathcal{O}(|V(G'_1)|^5|V(G_2)|)$. However, in the practical implementation of the algorithm injective solutions are directly searched (avoiding the computation of the Cartesian product) reducing the computational complexity to $\mathcal{O}(|V(G'_1)|^2|V(G_2)|^2)$, which is equivalent to the one obtained for tree to tree matching. Furthermore, the generation of reduced graphs occurs iteratively until the descendant accelerator determines that no farther nodes will be checked. Thus, the computational complexity of the "generate set" procedure is highly reduced and so will be the global complexity of the algorithm.

Algorithm 11 Compute optimal match

procedure COMPUTE OPTIMAL MATCH($G'_1, G_2, M_{l_1}, M_{l_2}, M_{d_1}, M_{d_2}, M$)
  for $i \leftarrow 1, |V(G'_1)|$
    for all $V(G_2)$
      for all $G'^{u}_1 : |V(G'^{u}_1)| = i$
        Let s be a variable
        if u and/or $\phi(u)$ is a leaf
          $s \leftarrow SL(u, \phi(u))$
        else
          $F^u_1 \leftarrow$ GENERATE SET(u)
          $F^{\phi(u)}_2 \leftarrow$ GENERATE SET($\phi(u)$)
          A $\leftarrow$ FIND COMBINATIONS(F^u_1,$F^{\phi(u)}_2$)
          $s \leftarrow SL(u, \phi(u))+max\{\sum_{j=1}^{z_1} ST(A_{1_j}[0], A_{1_j}[1]); ...; \sum_{j=1}^{z_q} ST(A_{q_j}[0], A_{q_j}[1])\}$
          $r \leftarrow GetChildrenOptimalMatch(T^u_1, T^{\phi(u)}_2)$
          if $s < \epsilon * N_{u,\phi(u)}$
            $s \leftarrow 0$
          end if
        end if
      end for
    end for
  end for
  return s and r
end procedure

Algorithm 12 Injective solutions

procedure FIND COMBINATIONS(F^u_1,$F^{\phi(u)}_2$)
  for $i \leftarrow 0, |F^u_1|$
    for $j \leftarrow 0, |F^{\phi(u)}_2|$
      $D \leftarrow C(F^u_{1_i})$
      $E \leftarrow C(F^{\phi(u)}_{2_j})$
      CP $\leftarrow$ CALCULATE CARTESIAN PRODUCT(D,E)
      A $\leftarrow$ SELECT INJECTIVE SOLUTIONS(CP)
      A $\leftarrow$ TOPOLOGICAL INCONSISTENCY FILTER(A)
    end for
  end for
  return A
end procedure

4.2.6. Reconstruction of the optimal solution

So far, a root independent graph matching method has been presented. But there is an issue that was explained in Section 3.8 and was not considered in the previous section. What happens when the graphs are wrongly connected due to imaging artifacts at different locations? Figure 4.16 shows what could in that situation.

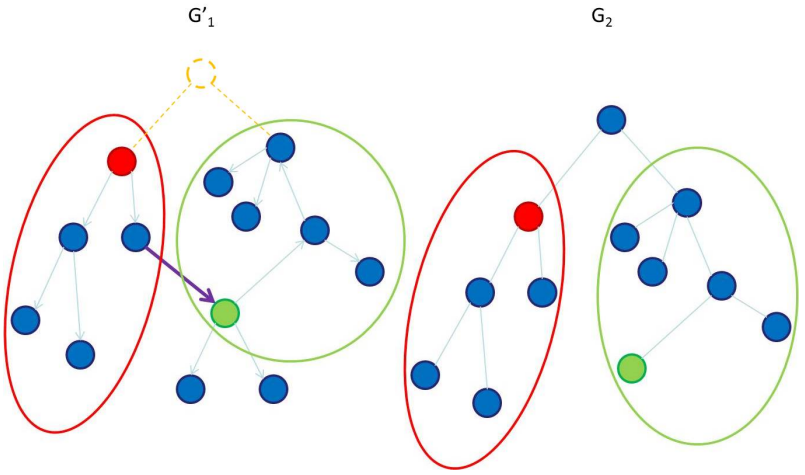

Figure 4.16.: When gaps appear in the two graphs in different places (orange) the set of final matches might contain only a smaller number of matches. In the figure only the matches in the red circle are found but not those in the green one due to impossible topologies [OLD11c].

The root (of the hepatic vein) of the graph is missing in the left graph (orange in Figure 4.16) and both parts of the hepatic vein are wrongly connected through the violet edge. This connection does not exist in the (correct) right graph. This example was obtained from vessels segmented from a clinical CT in which artifacts have caused this error. Let's assume that the highest similarity measure between two graphs is achieved when the red nodes (and their correspondent subgraphs) are matched. In that case, the set of final matches would contain the nodes inside the red circle. Nonetheless, one can observe that the nodes in the green circle should also be matched according to their spatial positions, and since the subgraph in that area is large, a substantial similarity value can be expected from those potential matches. But as the violet connection does not exist in the right graph, this is topologically not possible: There does not exist a common path that connects the green nodes in both graphs, since the root is missing in G'_1.

The solution can be found analyzing the assignment matrix (Figure 4.17). When the matching is done, the assignment matrix should contain the global maximum similarity value (red nodes in the example). Nevertheless, in cases like the discussed one, the assignment matrix does not only contain one global maximum, but also local maxima. In the particular example of Figure 4.16, there is one local maximum that comes from matching the green nodes. In order to detect such secondary matches after the matching process is completed, a search starts to find substantial matches that were not included in the final set of matches. Those matches can be: part of branches that do not exist in the other graph, or branches that were not considered due to topological problems like

Figure 4.17.: Detection of secondary roots using the assignment matrix. Each pair of correspondences is assigned a similarity value as well as the children that let to that value.

the mentioned before. Note that in the former case, the branch will be match to a wrong branch of the other graph. A threshold in the similarity value will be used to decide to which one of the cases holds for each branch. In general, the value of the threshold is calculated similarly to the threshold to avoid local minima (Section 4.2). Thus, the threshold is proportional to the number of nodes of the branch under study in the common graph. First of all, the minimum similarity value required for a subgraph to be considered as a secondary root is set to 5. If the value is smaller, the size of the subgraph is small and the branch could actually be located in a local minima (there is no enough information to ensure the robustness of such an small subgraph). Then the local minima equation (Equation 4.2) is used to ensure that the branch under study corresponds to a correct set of matches. Once a secondary root is detected, the method reconstructs the set of matched nodes that lead that similarity value. This is done similarly to the reconstruction method that was adopted to reconstruct the optimal set of matches given a known root in Section 3.4. The only difference will be that now instead of recovering the matches that lead to that similarity value, two independent reconstruction processes will start and the the final set of matches will be given by the union of both sets of matches.

4.3. Pose independence

In the previous sections solutions have been proposed for a root independent method that can handle cyclic graphs. However, nothing was yet proposed to solve the pose independence problem. While pose independence could be directly solved by combining the graph matching method with pose independent similarity metrics, the length and direction similarity metrics have shown to be more robust and allow a higher detection of matches (see Section 3.1). Since the direction is pose dependent, the robust pose independent detection of matches becomes challenging. In the clinical scenarios pro-

posed in this thesis, pose dependence is not a determinant factor as the patient during CT acquisition will be placed similarly. The small pose changes that can be observed can be overcome by adjusting accordingly the similarity metric thresholds from length and direction. Nevertheless, for completion of the work a solution is proposed that makes the matching method useful also for other applications in which pose independence is important, e.g., clinical intervention. The orientation of images acquired during intervention can greatly differ the orientation of preoperative images. Thus, the use of pose independent similarity metrics is crucial. However, it is desired to used similarity metrics that will result in robust matching results (length and direction).

As it was mentioned before the direction threshold has advantages (high number of matches and small number of ambiguities) that cannot be fulfilled with other metrics. However, it is pose dependent. On the contrary, other similarity metrics, for instance, the angle or the geodesic or euclidean distances, that are pose independent, will result in a high number of wrong matches in presence of ambiguous matches (nodes with comparable pairwise similarity values). This chapter proposes a method that incorporates the advantages of both type of attributes without their disadvantages. This methods works as follows:

Initial matching In the general case, one cannot assume that both graphs share the same orientation. Furthermore, the relative orientation is unknown. Thus, a pose independent initial match is carried out. Therefore, the graph matching method proposed in the previous section is combined (by means of Equation 3.6) with a similarity composed by maximum angle between branches, euclidean distance and length. Figure 4.18 shows that the combination of the three similarity metrics (d) returns more accurate results than those obtain using each similarity metric independently ((a) to (c)). To highlight the general use of this method the graphs of Figure 4.18 belong to a preoperative CT and a intra-operative US image. For visualization purposes both graphs appear with a similar orientation in the figure. However, the method has been tested by previous rotation of one of the graphs up to 180 degrees obtaining identical results.

In the proposed graph matching method the root is unknown. This means that it is not possible to determine which are the children of each node as no direction is known. Thus, instead of calculating the angle between root and certain node, or between children, like it was proposed in other state of the art methods, the maximum angle observed between all branches descendant from the studied nodes is calculated (Figure 4.19). The reason to use the maximum angle is that small branches (that usually form smaller angles) are more often missing than larger branches. Thus, the intolerance of the angle similarity metric to topology changes is minimized. The result of the initial matching is a relatively small set of matches containing some ambiguities.

Rigid transformation The initial set of matches contain only a small number of matches compared to those that could be obtained using the direction as similarity metric (see difference between (d) and (e) in Figure 4.18). Thus, a landmark based rigid transformation is carried out with the initial set of matches. The rigid transformation is calculated following the method by Horn [Hor87], which allows to find the correct transformation between

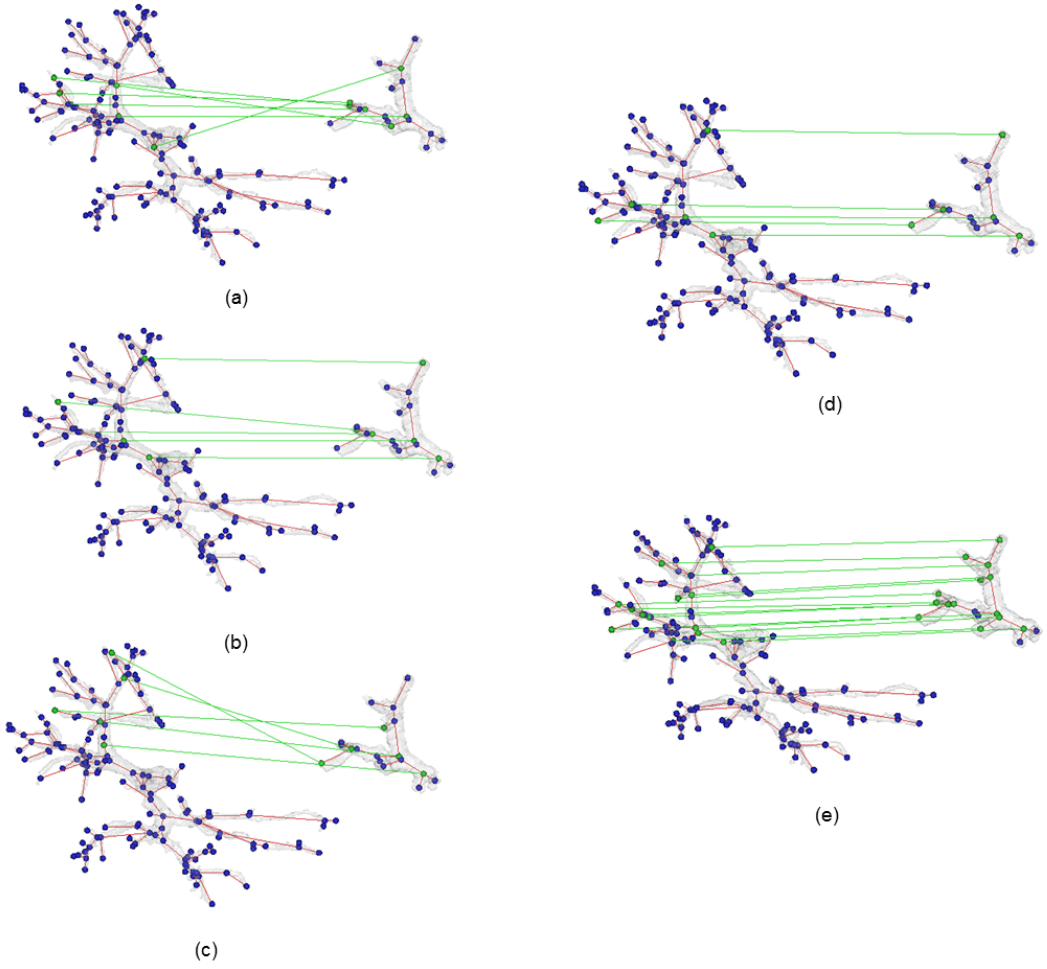

Figure 4.18.: Pose independent graph matching. (a) to (c) Results of the matching using the length, euclidean distance and angle as similarity. (d) Results of the matching using the combination between length, euclidean distance and angle as similarity. (e) Results of the last matching step. The combination of direction and length increases the number of matches after rigid registration.

two corresponding sets of points. Once this is done, both graphs will have the same pose. Thus, this step will allow a final matching step with the robust length and direction combination of similarity metrics.

Final matching Once both graphs share the same orientation, it is possible to apply the matching method using the direction (Figure 4.18 (e)). The result will contain a higher number of correct matches. Due to the efficiency of the proposed methods (Section 3.7) the application of the method a second time is not problematic, and has the advantage for the physician not to require any prealignment of both images.

The incorporation of deformations in the matching process can be advantageous in presence of larger deformations. This topic will be addressed by the author in the future.

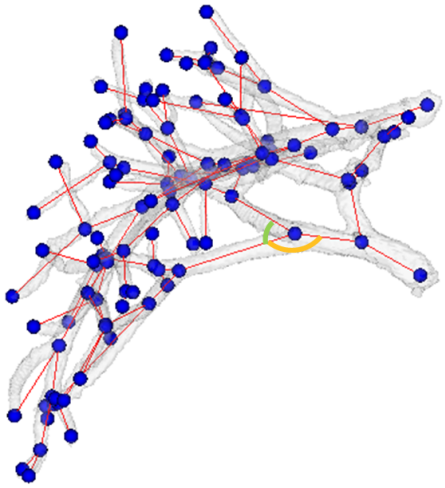

Figure 4.19.: Maximum angle between branches (orange) and angle between children (green).

4.4. Interaction features

As it was previously mentioned existing graph matching methods are error prone a need some interaction to refine the results. In addition to this, a preselection of nodes (roots) is often necessary before a matching takes place. A series of interaction features have been developed to facilitate and speed-up these tasks. This section is divided in two parts: the features designed for the preselection (Section 4.4.1) and those designed for the refinement of the results (Section 4.4.2). The visualizations needed in this section have been created using *Visualization Toolkit*.[1]

4.4.1. Preselection

The following interaction features have been developed and will be explained in detail in this section:

- Both graphs are visualized in 3D and they can be rotated and zoomed to better visualize the area of interest.
- 2D slices are shown overlapped on the 3D view.
- 2D views (sagittal, coronal and axial) are visible below the 3D view.
- The 3D view contains the 3D surface of the vessels as well as spheres and lines to represent nodes and edges in the graph respectively.
- Matches are visualized with lines joining the pair of nodes or with identical numbers next to both nodes.

[1] Visualization Toolkit (VTK). http://www.vtk.org/

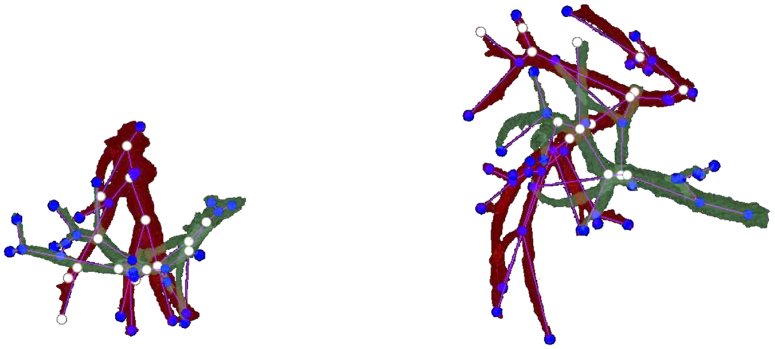

Figure 4.20.: Fully manual matching using the 3D view. The left graph belongs to a US image and the right one to an MR image [OLD11a].

- Part of the graphs can be hidden to have a better focus on a certain area of the graph.
- Portal and hepatic vein are visualized in red and blue respectively for the interaction with the matching method.

Figure 4.20 shows a 3D view in which portal and hepatic veins are visualized with different colors. It shows the results of a completely manual matching. The nodes that have not been matched are visualized as blue spheres, while the matched ones are visualized in white. The edges of the graph are visualized as violet lines and the vessel surface is also visualized to increase the sense of orientation in the 3D view.

Figure 4.21 and 4.22 show how this feature works to facilitate the user to concentrate in a specific area of the graph. Two criteria can be used to do this: to decrease the size of the graph according to the depth of the nodes inside the graph (Figure 4.21), or to do it using the diameter of the vessels as reference (Figure 4.22).

As previously mentioned the matches can be visualized using lines that join the two correspondences or with identical numbers next to the them as shown in Figure 4.23.

This 3D features serve to facilitate the interaction task but they still have a disadvantage. Physicians are used to work with 2D slices better than 3D views. Thus, it would be advisable to have an interaction tool that besides the interaction in the 3D view allows interacting in the 2D slices (Figure 4.24). With the tool developed within this chapter the interaction can be done in either view and the selection is automatically shown in the other one. To facilitate the selection task the vessels are highlighted in white in the 2D view. The physician can click at any location next to a vessel bifurcation and automatically the closest bifurcation will be selected. In Figure 4.24 the selected node appears highlighted in pink. In addition to this, the physician can change the 2D view from sagittal to axial or coronal. 2D slices can also be visualized in the 3D view to facilitate the orientation in space.

4.4.2. Refinement

The interaction is not only useful for preselection of nodes, but also for refinement of the results. Note that the number of matches provided by the automatic matching method can

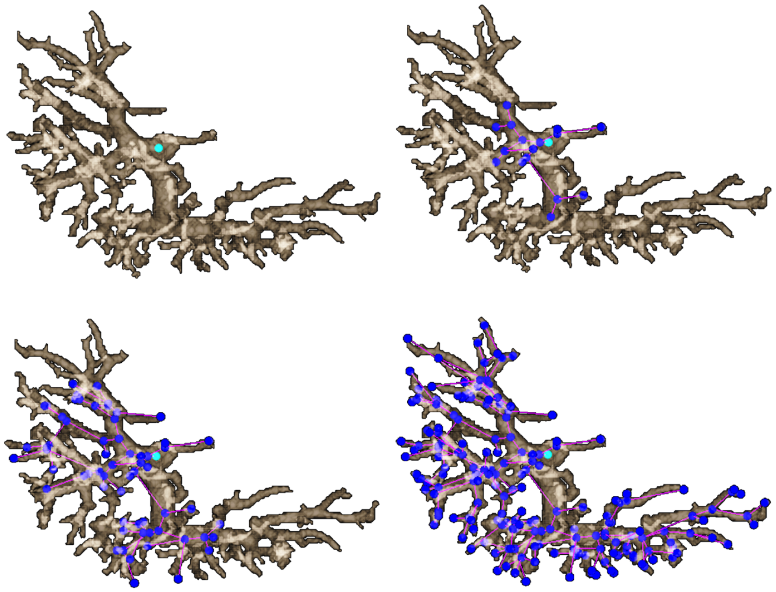

Figure 4.21.: Areas of the graph can be hidden using the depth of the nodes inside the graph as reference [DOLCE10].

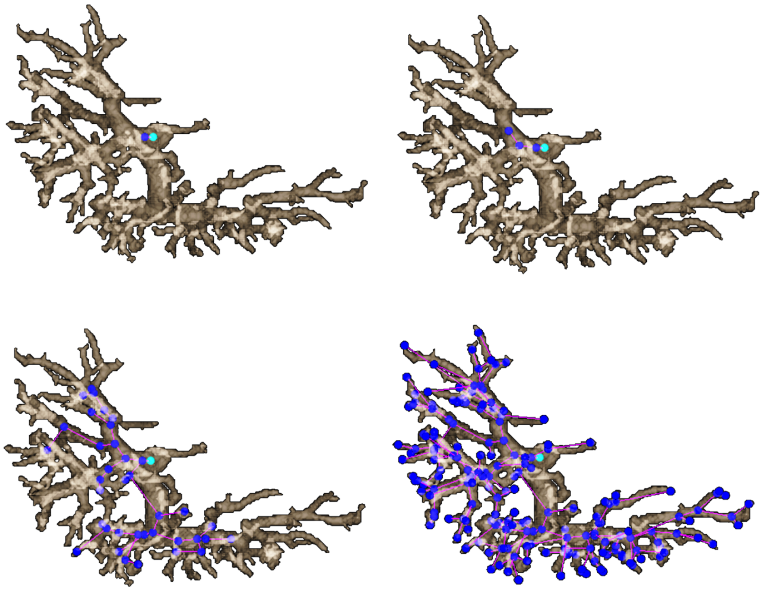

Figure 4.22.: Areas of the graph can be hidden using the diameter of the vessels as reference [DOLCE10].

be really high. This makes the task of finding wrong matches hard and time consuming (Figure 4.26 left).

This chapter proposes to classify the matches according to their probability to be correct. Thus, a color code is used to divide the nodes into correct (green), neutral (yellow) and wrong (red). Note that those nodes that are classified as red are not necessarily wrong: the color just means that if a match is wrong, it will belong to the set of red

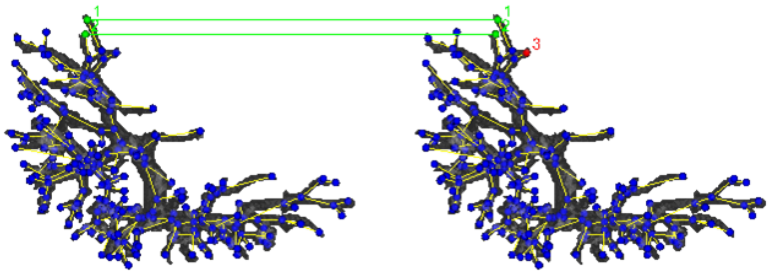

Figure 4.23.: Visualization of the matches using lines and numbers.

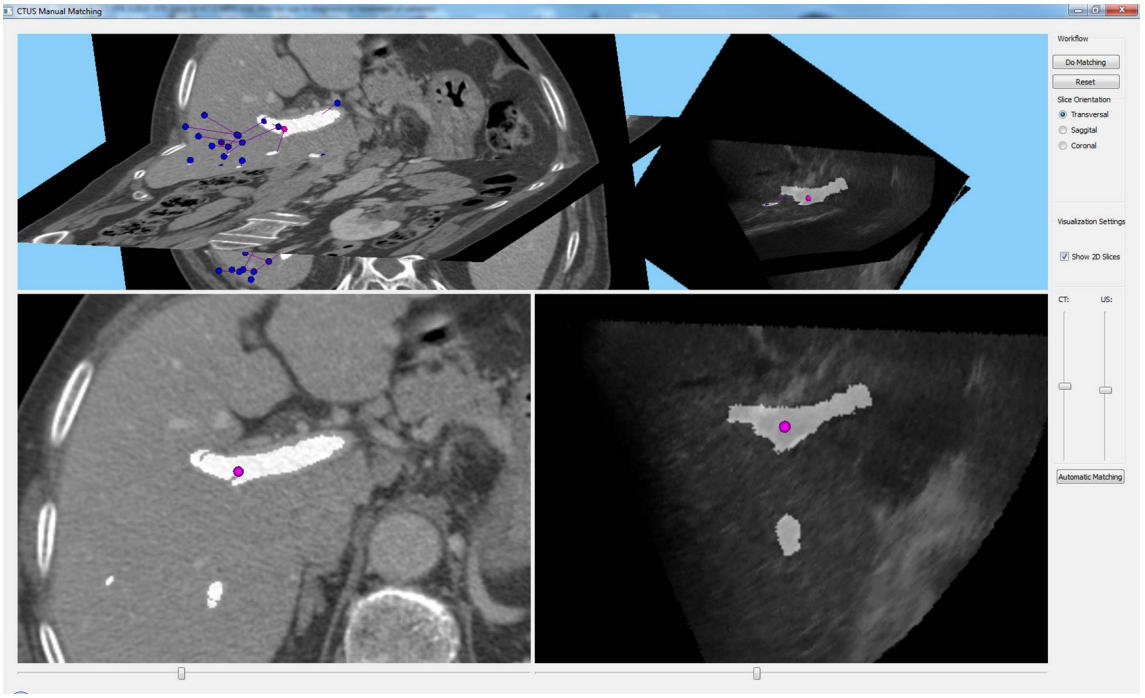

Figure 4.24.: The interaction can be done both in 3D or in 2D. The result of this interaction will automatically be shown in the opposite window [OLDE*12].

matches.

For the calculation of the probability of a match $(u, \phi(u))$ to be correct, the first matched ancestor $(v, \phi(v))$ is taken as reference (the parent in the common graph). Then, the length and direction similarities between the branches (u, v) and $(\phi(u), \phi(v))$ will be calculated. Depending on the similarity values obtained the match will be classified as red, green or yellow match. Let's assume that the red/green nodes in Figure 4.25 are matched. This figure illustrates why the first matched ancestor should be taken as reference to calculate the probability of the red nodes. The first matched ancestor (green) leads to a high similarity measure (direction arrow in (c)), while the selection of another reference node, like, e.g., the parent (violet (b)) of the red node would lead to a much smaller similarity value.

Once the reference node is determined, both similarity components are calculated, namely, the length S_l similarity and the direction S_d similarity. Colors will be assigned to the nodes following the next rule:

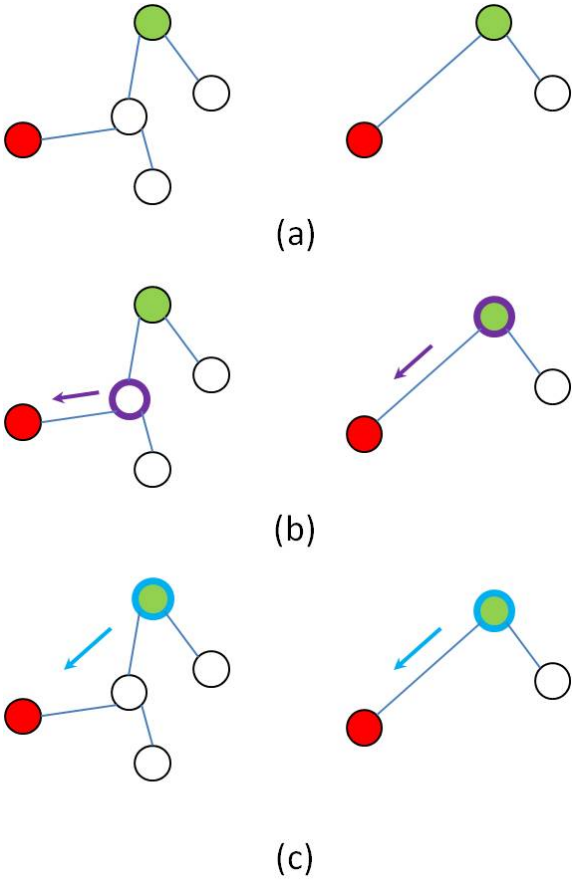

Figure 4.25.: Reference node for the calculation of the probability for a node to be correct [OLD11a]. (a) the red/green nodes of the two graphs are matched. (b) The similarity would be low if the parent (violet) is taken as reference. (c) The first matched ancestor provides a more accurate similarity value.

$$Color = \begin{cases} red & \text{if } S_l < Th_{l_1} \vee S_d < Th_{d_1} \\ yellow & \text{if } Th_{l_1} < S_l \leq Th_{l_2} \vee Th_{d_1} < S_d \leq Th_{d_2} \\ green & \text{if } Th_{l_2} \leq S_l \vee Th_{d_2} \leq S_d \end{cases}. \tag{4.6}$$

The new threshold values Th_{l_1}, Th_{l_2}, Th_{d_1} and Th_{d_2} determine how large/small the similarity value of a match must be to be considered as correct/wrong. They take the values -0.6, 0.5, 0.5 and 0.7 respectively. Thanks to this color code the task of detection of wrong matches is facilitated (Figure 4.26 right).

This differentiation into different colors facilitates the process. Nevertheless, all matches are still visible and it can be hard to distinguish the connection lines. Therefore, a last interaction feature is proposed. The nodes are visualized in groups of colors. In other words, green and yellow nodes (for example) can be hidden so that the user can concentrate only in the red ones. In addition to this, when a match is manually corrected, it will be set to a fourth group of nodes, visualized in white, so that the user does not have the risk to recheck the same nodes. When a node is selected, it will appear highlighted in pink. Finally, the matches can also be visualized one by one so that the user can completely

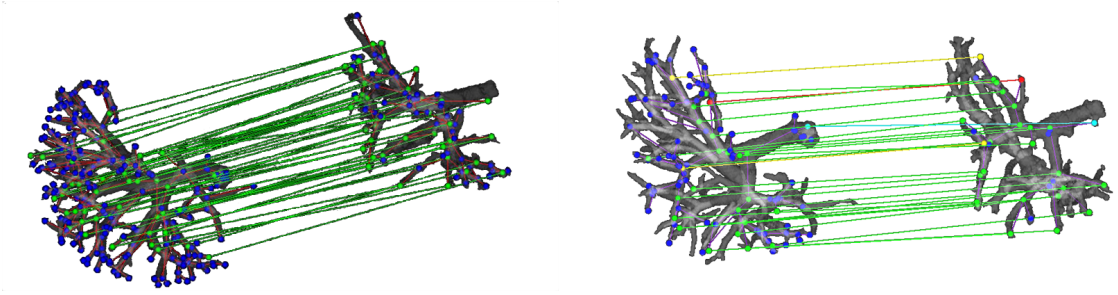

Figure 4.26.: Results of the matching method with and without probability differentiation [OLD11a].

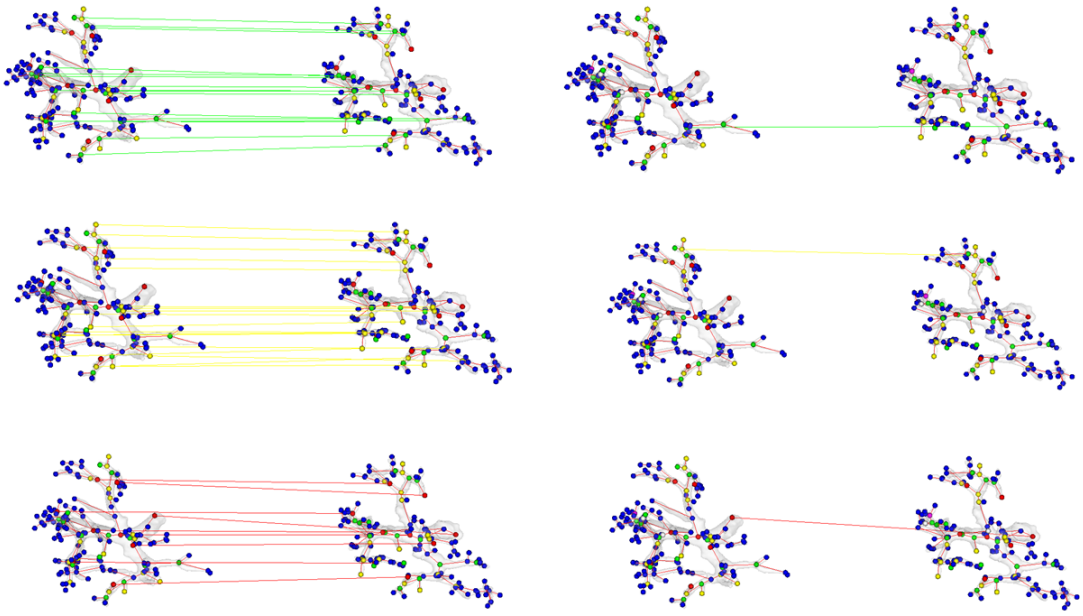

Figure 4.27.: First column: Division of matches in colors and groups according to their probability to be correct. Second column: visualization of the matches one by one.

focus on one of them without being distracted by any other match. Figure 4.27 shows an example of this.

4.5. Statistical outlier detection

In spite of the interaction features, manual refinement of the results of a graph matching method is time consuming. Thus, in cases in which time is a limiting factor, automatic approaches for detection and removal of wrong matches are desirable. In this section an automatic statistical outlier detector is proposed to automatically remove wrong matches from the total set of correspondences.

Let $U = \{u_j : j \in [0,k]\}$ and $\Phi(U) = \{\phi(u)_j : j \in [0,k]\}$ be the sets of matched nodes of the preoperative and postoperative graphs respectively. In both sets each matched

point is given by its 3 coordinates in physical space. Points that share the same index are detected correspondences.

Taking into account the low proportion of wrong matches (Section 4.6) these wrong matches can be considered as outliers. According to Chebyshev's inequality [Bie53] the maximum proportion of outliers in the set of matches can be determined as:

$$P(|X - \mu| \geq k\sigma) \leq \frac{1}{k^2}, \forall k \in \mathbb{N}. \tag{4.7}$$

All points that lie outside the range $(\mu - k\sigma, \mu + k\sigma)$ can be considered as outliers in the set. μ is the mean and σ the standard deviation of the distribution. A compromise has to be found to decide which value of k is more appropriate. While a small k ensures that no wrong matches are added to the final set, a certain number of correct matches might also be removed. On the contrary, a high value of k would not be able to remove all outliers.

The mean μ is defined as the mean of all euclidean distances d_i between corresponding points (A_i and B_i)

$$\mu = \frac{\sum_{i=1}^{m} d_i}{m}, \tag{4.8}$$

where m is the number of matches and $d_i = \|A_i - B_i\|$. Then the variance and standard deviation σ of the set of matches is given by:

$$\sigma = \sqrt{variance} = \sqrt{\frac{\sum_{i=1}^{m} (d_i - \mu)^2}{m}}. \tag{4.9}$$

The outlier detection works as follows:

Rigid transformation of the graphs Using the detected correspondences a landmark-based registration of both graphs is carried out. The final number of correct matches is much higher than the number of wrong ones. Thus, the influence of the latter in the transformation is minimal and it can be considered accurate enough for the purposes of the outlier detection. There are two main scenarios that make this rough pre-registration necessary. On the one hand the presence of resections that will not only deform the liver, but also displace it and rotate it. On the other hand in intra-operative interventions the positioning of acquired images is unknown. Thus, an euclidean distance based outlier detector would return false results without a pre-registration. Figure 4.28 illustrates the problem of the outlier detection without an initial rigid registration. The figure shows two vessel trees (red and blue). The distance between the vessels encircled in green is lower than the distance of the vessels encircled in orange, but this distance difference is not caused by wrong correspondences, but by a wrong alignment.

Determination of k and its role As it was mentioned before, the role of k in the outlier detector process is fundamental. Thus, it is important to select a value of k that is a good trade-off between removal of wrong matches and correct matches. The goal is to remove all wrong matches and as less correct matches as possible. Figure 4.29 shows

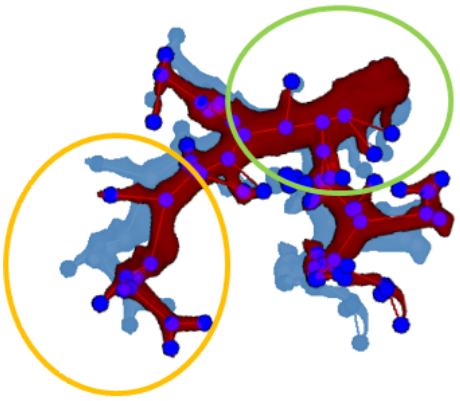

Figure 4.28.: Need of an initial registration for the outlier detection. The distances between the vessels might vary (green and orange circles) due to misalignments even though the detected correspondences are correct.

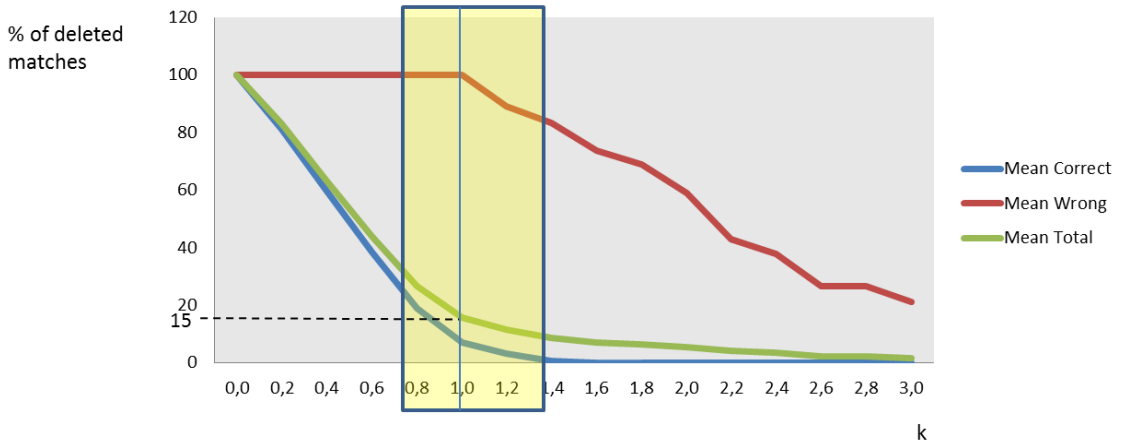

Figure 4.29.: Role of k. As k increases a smaller number of matches is removed.

the effect of increasing k between 0 and 3 in 0.2 steps. When k takes a value between 0.8 and 1.2 all wrong matches (red line) are removed in all tested graphs and only a minimal number of correct matches (blue line) are deleted. One can observe that the number of correct matches that are deleted decreases rapidly with the increase of k. During the matching process the number of wrong matches is unknown. Nevertheless, a removal of approximately 15% of the total set of matches (green line) is advisable so that all wrong matches and only a minimal number of correct matches will be removed. This corresponds to a k value of 1. The value can be made more restrictive if desired, but in that case the number of removed correct matches will increase rapidly. For the evaluation carried out in this Section a value of 1 is used.

Outlier detection Once the correct k is determined μ and σ are calculated and the outlier detection takes place. All matches outside the range $(\mu - k\sigma, \mu + k\sigma)$ will not be

part of the final set of matches.

4.6. Evaluation

This section evaluates the methods proposed in this chapter. On the one hand, the interaction features have been evaluated with the help of some volunteers. The results of this evaluation are shown in Section 4.6.1. Finally, the graph to graph matching method is also evaluated (Section 4.6.2).

4.6.1. Interaction features

For the evaluation of the interaction features a liver CT acquired with a GE Medical Systems LightSpeed 16 CT Scanner has been used. A group of 4 participants (computer scientists and engineers) have taken part in the experiments to find out how helpful the preselection and refinement features are.

4.6.1.1. Preselection

Two experiments have been carried out for evaluation of the preselection features: one with equal graphs and the other one with unequal graphs.

Equal graphs For each participant 8 different setups have been used. Each one of the setups has one or two features turned on or off. The participants are divided in two groups. For one of them the vessel surfaces are visualized in the background and for the other one the surfaces are hidden (feature D), which means that they uniquely see the graph representation of the segmented vessels. Figure 4.22 shows a graph in which not only the edges but also the vessel surfaces are visualized in the background. The features that are studied are: visible edges (feature A, see Figure 4.22), matches visualized as identical numbers next to the nodes (feature B, see Figure 4.23), matches visualized as connecting lines (feature C, see Figure 4.23 left).

The participants had two minutes to get familiar with the tool. After that they had one minute time to find as many correspondences as possible. When the minute was over the participants were asked which one the features was more helpful to detect correspondences. Table 4.1 shows the results obtained for every setup and every participant. The numbers represent the amount of matches that they were able to find in the given time.

The participants that had the segmented vessels visualized in the background recognized that this was helpful for them. However, the results show they found a smaller number of matches. In general, they all found easier to detect matches when feature A was on. Feature C (lines) was preferred against feature B. The usefulness of feature C according to the participants depended on the task: useful for validation after the matching, but confusing during the interaction. A single participant favored B over C.

Unequal graphs A second experiment was carried out. In this case, the graphs that were shown to the participants were different. A new constraint was included in the

Setup	D present			D absent		
	P1	P2	Avg.	P3	P4	Avg.
-	13	20	16.5	26	26	26
A	15	27	21	23	25	24
B	10	14(1)	12	22	22	22
AB	14	23	18.5	24	27	25.5
C	14	25	19.5	23	25	24
AC	16	24	20	24(1)	28	26
BC	17	27	22	23	26	24.5
ABC	17	23	20	22(2)	21	21.5

Table 4.1.: Results of the interaction on equal graphs. P1-P4: identification of the participants. A: edges between bifurcations on, B: number to identify matches on, C: connecting lines to identify matches on. The numbers represent the number of matches manually selected by the participants. Wrong matches are written in parenthesis.

Setup	D present			D absent		
	P1	P2	Avg.	P3	P4	Avg.
-	10	17	13.5	19	(1)	17
A	11	9	10	16	19	17.5
B	9	10	9.5	20	15	17.5
AB	8(1)	13	10.5	17	20	18.5
C	7(2)	18	12.5	20(1)	9(1)	14.5
AC	10(1)	18	14	14	19	16.5
BC	8	13	10.5	16	15	15.5
ABC	11	11(1)	11	14(1)	17	15.5

Table 4.2.: Results of the interaction on unequal graphs. P1-P4: identification of the participants. A: edges between bifurcations on, B: number to identify matches on, C: connecting lines to identify matches on. The numbers represent the number of matches manually selected by the participants. Wrong matches are written in parenthesis.

task: the participants were requested to start finding the correspondences in the inner nodes from the root to the leaves. Due to the increased complexity of the task the rate of number of matches per second was decreased. The number of matches obtained without any feature on, was surprisingly high. This is due to the structure of the graphs. Once one match was found it was easier to detect additional matches next to the previously detected ones (those graphs presented similar clusters). This is not the case in the clinical scenarios in which the graphs can vary significantly. In those cases, the features A and D might lead to significantly better results. In general features A and C showed to be the most helpful features.

After the experiments one can conclude that a rate of 10-15 manual matches per minute are practicable.

4.6.1.2. Refinement

It is important to facilitate the preselection task but also to help the user to correct inaccuracies of the automatic method if necessary. In the third experiment the automatic matching was applied to 3 different pair of graphs. The method produced a series of known mismatches. The participants were requested to correct the mismatches without knowing the number of wrong matches that were present in the results. After the experiments, the participants were only able to detect the most prominent wrong matches. Feature C was the most valuable help for the participants. Usually when the set of matches is visualized with connecting lines they appear to be nearly parallel to each other (Figure 4.23 left). In cases in which the match was far from being correct (spatially speaking), the direction of the line connecting the nodes was eye-catching. On the contrary, when the locations were not so far away, the lines were nearly parallel like when they are correct. The difficulty of finding wrong matches when the number of correspondences is high shows the need for more appropriate interaction features. Thus, 5 experiments have been carried out to evaluate the features based on the color code:

1. Without color code. Nodes are visualized in green (matched) or blue (unmatched). Participants can set on/off features B and C as desired.

2. Without color code but one by one. Nodes are visualized in green (matched) or blue (unmatched). Participants can set on/off features B and C and also one-by-one visualization.

3. Color code. The participants can choose the group of matches (according to the colors) that they want to analyze at each moment.

4. Color code one by one. The participant can check the matches one by one according to their colors.

5. Without color code. The nodes are visualized in green or blue but the depth of the graphs can be changed to hide part of the graphs.

Seven persons participated in these new experiments. From one clinical CT image a graph was generated. Then six artificial graphs were created by random removal of nodes in the original graph. Thanks to this artificial generation of the graphs, ground truth results of the matching were known. The experiments were carried out in similar conditions as the previous one. The results of the method containing certain number of mismatches were shown to each participant and they had to correct the results without knowing how many wrong correspondences were present. For every one of the experiments the liver vasculature was set to semitransparent in the background (feature D). A trained user can provide better results than an untrained one. Since the goal of the experiments was not to evaluate the performance depending on the expertise of users, but to test the usefulness of the different features, the experiments were carried out in different order for each one of the participants. This ensured that good results in certain experiments were not due to training gain after several tries. Another factor that could bias the results of the experiment was the bigger difficulty of some of the graphs against the others. To avoid this, the graphs were randomly reordered each time a new participant was doing

Experiment no.	Easy	Intermediate	Difficult	No. wrong found (%)	Mean time (s)
1	2	3	3	56.25	227
2	2	3	3	68.86	632
3	4	2	2	71.28	107
4	3	3	2	78.43	122
5	2	3	3	76	367

Table 4.3.: Results of the experiments to analyze the usability of the color code features. Easy, intermediate and difficult refers to the difficulty and amount of graphs that were employed in each experiment.

the experiments. In other words, the graphs assigned to each experiment were varying over the different participants. The graphs were classified according to their difficulty depending on: the number of wrong matches that they possess, the time elapsed by the participants to find the matches, and the number of wrong matches that were detected by the participants. Table 4.3 summarizes the difficulty of the graphs that were used for each experiment.

In average experiments 3 and 4 showed to be the favored ones. For them the biggest amount of wrong matches was detected in the lowest time. With the newly developed features the participants could focus on the matches that were most likely wrong. Experiment 2 required the longest time since the participants needed to check every node one by one without any exception. One of the participants who had carried out the experiments number 3 and 4, gave up while performing experiment 1. This gives the idea that after using the new features experiment 1 looks much harder. All the participants expressed their preference towards experiments 3 and 4 and more specially 4. At the same time they suggested that experiments 1, 2 and 5 looked more congested and it was more difficult to focus on a concrete pair of nodes. To the eyes of the participants experiment 5 was the most confusing one as with the change on the depth of the graphs the user was not sure of which nodes were already checked or not and they needed to recheck several nodes.

Taking into account the results of experiments, the use of colors to determine the likeliness of the matches to be correct speeds up the refinement process. In addition to this the possibility of showing those correspondences one by one eases the task of deciding which one should be removed from the final set of nodes. Other features like the identification of matches through numbers or hiding parts of the graphs according to their depth are not recommended.

4.6.2. Graph to graph matching

The graph to graph matching method has been evaluated both in pre and postoperative CT images as well as in preoperative CT and intra-operative US. Ground truth data is necessary for a good evaluation of a method. To this end the tree matching method has been applied to the portal and hepatic veins separately and the results have been used as ground truth data.

In the first experiment 3 pairs of trees have been matched. The first two pairs (Table 4.4) are identical trees. As expected all the correspondences have been found and no wrong

Graph 1	Graph 2	Matches	Wrong	Matches gap
253	253	253	0	
94	94	94	0	
253	94	43	2	11

Table 4.4.: Results of the graph matching method on real data.

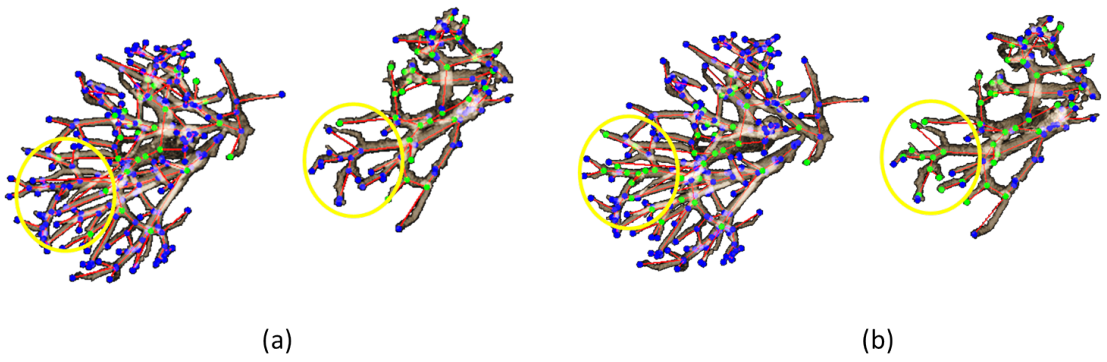

Figure 4.30.: The detection of secondary roots allows to find correspondences that would be missing else.

matches have been detected. For the third experiment the dataset that was analyzed in Section 4.2.6 was used. As it was mentioned this dataset contains a gap in the root of the hepatic vein of one of the graphs. Thanks to the secondary root detection 11 correspondences have been detected that would be let unmatched without this detection. This is also visualized in Figure 4.30. 2 wrong matches appear in the results. The number of correspondences detected (43 out of 94) is low. Nonetheless, the main reason for this is that most of the rest of the 94 nodes are unmatchable. From those 94 at least 27 belong to branches that do not exist in the other graph. In addition to this there are cases in which a leaf exists in both graphs but they cannot be matched because the length of their branches highly differs. Thus, even though the branches correspond to each other the nodes do not correspond.

The graph matching method has also been evaluated to match the vessels extracted from preoperative CT and intra-operative US. Table 4.5 summarizes the results obtained for four pair of graphs. The mean value of wrong matches is 0.75 nodes. The table shows the number of nodes of both graphs, the number of matches detected, and the number of impossible matches. Impossible matches belong to branches that are missing in one of the graphs, and to mis-segmentations or leakages.

Figure 4.31 shows the results of the graph matching method in four datasets. One can see that in the case of CT/US trees the size of the graphs greatly differs. The yellow circles show areas in which the segmentation method produces leakages into a tumor. The red circle shows a branch that is missing in the other graph. Even under those circumstances the graph matching method produces satisfactory results. The bottom left image shows the matching between a preoperative CT and a CT after liver resection.

	Graph 1	Graph 2	Matches	Wrong	Impossible
Patient 1	77	22	9	0	6 (tumor)
Patient 2	139	10	7	0	2
Patient 3	149	18	16	0	2
					32 (missegmentation)
Patient 4	44	67	16	1-2	5 (length)
					8 missing branch

Table 4.5.: Results of the graph matching method in graphs extracted from clinical CT and US images.

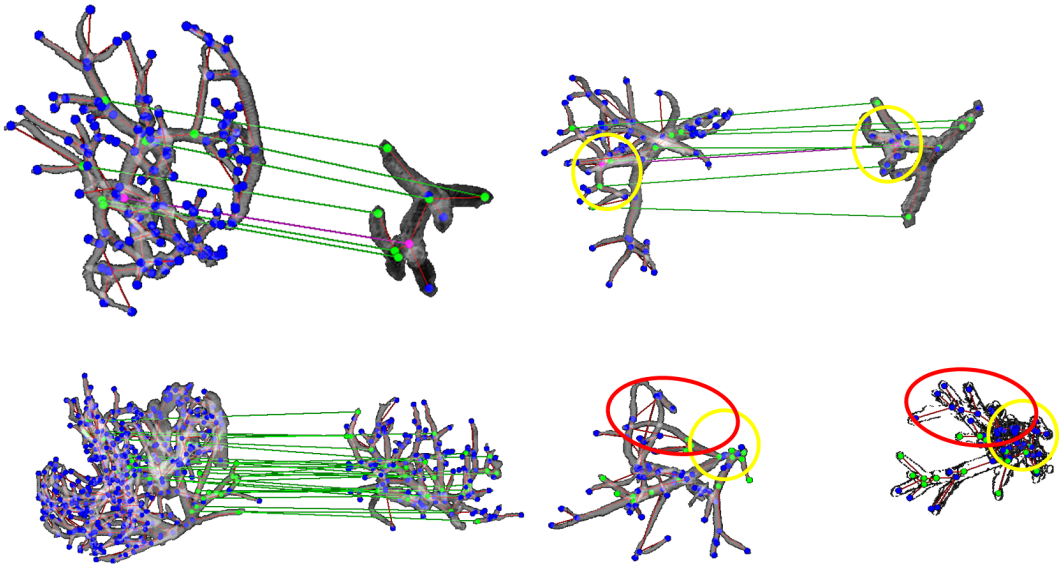

Figure 4.31.: Graph to graph matching results on 3 CT/US vessel trees and a CT/CT pre- and post-resection. The yellow circles show areas in which the segmentation produces leakages. The red circle shows a branch that it is missing in the other graph [OLDE*12].

4.7. Discussion

In this chapter four methods have been proposed:

- Two methods to find corresponding landmarks between liver vessels, namely, a tree- and a graph-matching methods.
- Two methods to refine the results obtained with the presented matching methods: interaction features and statistical outlier detection.

Each one of the methods has advantages and disadvantages that will be discussed in this section.

Similarity metrics for matching methods have to be chosen depending on the structures to be matched. Nevertheless, there are decisions that do not uniquely depend on the structure but also on the application for which the method is developed. The decision of using cyclic or acyclic graphs, for example, is restricted by the constraints of the

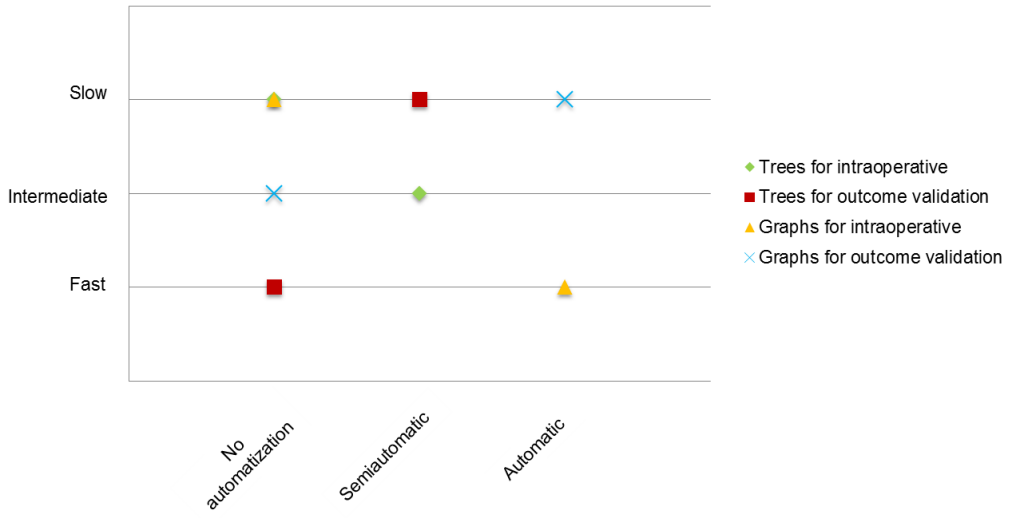

Figure 4.32.: Efficiency of graph and tree matching methods depending on the application and the automation level.

application.

In this thesis there are two main applications for which the proposed methods are especially useful: outcome validation of a surgery and intra-operative registration. Both applications have different requirements. The former uses for the comparison graphs extracted from clinical CT images. These graphs have usually a high number of nodes, in the range of 400. It can also be assumed that in the postoperative image the number of visible vessels is smaller due to lower resolution. While before a surgery high resolution images are used for a better diagnosis, after the surgery the resolution is lower to reduce the radiation dose in the patient. In addition to this, the vessels that were located in the treated area will disappear. Nevertheless, these graphs will still contain a not insignificant number of nodes.

The conditions present during surgery are different. In most of the cases, physicians use a pre-operatively acquired CT and intra-operatively acquired ultrasound images for the registration. There are some physicians that opt for acquiring CT images during intervention as well. In any case, during intervention time is a limiting factor. While the preoperative graph will remain large, the graphs that are found during intervention are much smaller than in outcome validation: the field of view of the ultrasound probe is usually reduced and the resulting image shows a very small part of the liver.

Figure 4.32 shows an efficiency vs. automation level graphic. The efficiency is divided into three conceptual values, namely, slow, intermediate and fast. The automation is also divided into three terms:

- No automation: preselected roots are requisite of the tree/graph matching method.
- Semiautomatic: preselected roots are not required. This term holds only for tree matching methods. Since these methods cannot deal with cyclic graphs the process will still not be fully automatic. Trees will need to be separated before the matching process starts.

- Automatic: the graph matching method does not require preselected roots. It is fully automatic.

Let's now analyze the different combinations of intra-operative or outcome validation with tree or graph matching:

Intra-operative registration using tree matching The proposed tree matching method can be used for intra-operative registration without any automation or as semiautomatic approach. The former would be, as a matter of fact, too slow for this application. Physicians request registration results in less than 3 minutes during intervention. No automation means in this case that the physician needs to separate the trees and then search for two pairs of corresponding roots, one for the hepatic vein and one for the portal vein. Similarly to the proposed graph matching method the root preselection step could be avoided. This would save the physician the time needed for the preselection. However, the tree separation step would still be a must. Thus, the use of tree matching for intra-operative registration is not advisable.

Intra-operative registration using graph matching The proposed graph matching method could have been made dependent on root preselections (no automation). Nevertheless, intra-operative preselection of correspondences is especially challenging. As it was mentioned before, the field of view of the intra-operative image is small. Often it is even hard to identify the concrete location of the structure shown in this image in the complete liver. Under those circumstances the preselection of matches would require time that is not available during surgery. Thus, the automation of preselection of nodes is a must for the intra-operative application. Opposite to the tree matching method, the number of nodes of the intra-operative graph is very small, which makes the increase in the complexity due to the automation insignificant. Furthermore, the proposed graph matching method is pose independent which saves the physician the need for manual initialization of the images. Thus, the use of graph matching for intra-operative registration is recommended.

Outcome validation using tree matching It has been shown in the evaluation section that the tree matching method is very efficient even for big trees. Again, the root preselection step could be skipped. But opposite to the previous application, this would not suppose an advantage. On the contrary, the trees are large and as consequence the complexity of the method would highly increase. Thus, the use of tree matching for outcome validation is recommended.

Outcome validation using graph matching In spite of the advantages that the automation means for intra-operative registration, the opposite effects can be seen for outcome validation. The proposed graph matching method has the clear advantage of handling cyclic graphs (no need for tree separation). Yet, this automation besides the large size of both graphs increase the complexity of the method greatly. Thus, the use of graph matching for outcome validation is possible, but not advisable.

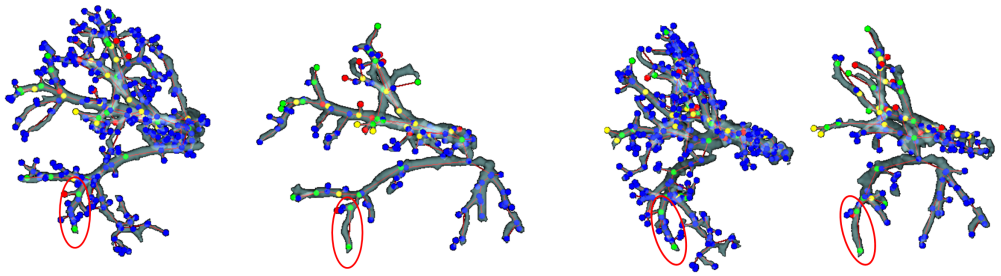

Figure 4.33.: Pre- and post-operative hepatic veins of a patient visualized from two different perspectives. The branch encircled in red contains deformations.

It can be concluded that for outcome validation purposes the proposed tree matching method is more appropriate. Exceptionally, the graph matching method can be preferable when the postoperative image belongs to a liver that underwent an extended hepatectomy. In that case only a small part of the liver remains and the resulting graph would again be small. Due to the intra-operative time limitations, the reduced size of the trees, and the difficulties to preselect nodes, the proposed graph matching method is preferable for intra-operative registration.

The automatic outlier detection is robust for the detection of wrong matches and it is advantageous when time is a limiting factor. Nevertheless, the value of k that ensures complete removal of wrong matches will at the same time remove some matches that should remain. Figure 4.33 shows the hepatic vein of a patient that underwent tumor ablation. The branch encircled in red is deformed. In spite of the deformation the matching method has been able to detect a correspondence. Nevertheless, this match will be removed by the statistical outlier detection. The interaction features are helpful to avoid the removal of correct matches. Thus, both the statistical outlier detector and the interaction features are complementary tools.

4.8. Summary

In this chapter, a novel cyclic graph matching method has been presented. The method is able to efficiently find correspondences between liver vessels in a fully automatic way: it is pose and root independent. Furthermore, an statistical outlier detector has been proposed to automatically refines the matching results. The results of this method will be used as references to guide the FEM-based registration method that is proposed in the next chapter.

5. Pre and post operative liver registration

This chapter focuses on the registration method that uses the landmarks obtained with the methods proposed in the previous chapters. It is important to introduce some concepts that are necessary to understand the clinical scenario that this chapter focuses on.

One of the goals of this thesis (see Chapter 6) is to provide the physician with a tool that allows him to easily evaluate the outcome of a surgery. In particular, two techniques for tumor removal are considered: **tumor ablation** and **resection**. The former consists in the application of high-frequency waves to the carcinogenic cells to destroy them. After the ablation process is over, the cells in that area are dead and the tumor cannot further grow. The ablated area loses elasticity, becoming a tissue that is stiffer than the surrounding parenchyma. The process of tumor ablation is minimal invasive. A clinical CT image of a liver that contains an ablation can be seen in Figure 5.1.

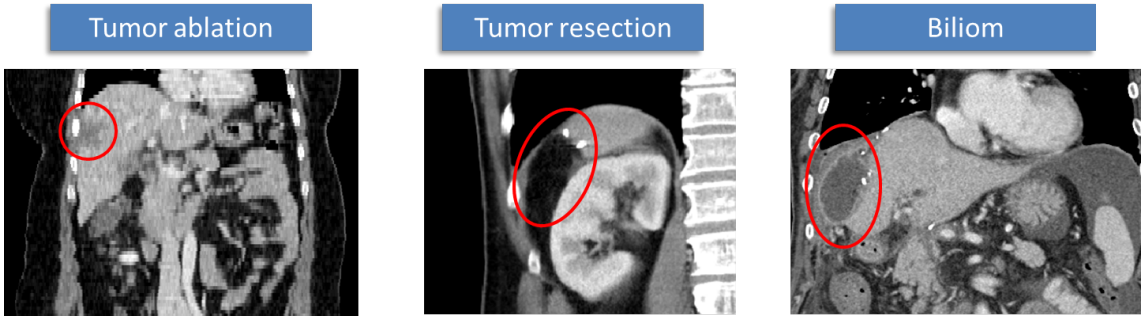

Figure 5.1.: Clinical CT images that contain the concepts of: tumor ablation, tumor resection, biliom and hypertrophy.

Opposite to tumor ablation, tumor resection is a procedure that requires open liver surgery. This technique consists of cutting the area in which the tumor is located and removing it from the body. The vessels that were cut during the process are closed with so called **clips** to avoid further bleeding of the patient. The removal of parts of the liver will have the effect of a slight movement of the organs adjacent to it. This is especially noticeable in the kidneys and intestine. The re-growing effect of the liver after a resection will introduce additional deformations on the liver.

Type of resections As it was explained in [Dre12] there are two possible types of liver tumor resections: typical and atypical. The first type consists of resecting the Couinaud segments that are affected by the tumor. During an atypical resection, on the other side, the tumor is resected as well as a safety margin around it. "The Brisbane 2000 terminology of liver anatomy and resections" [BCG*00] contains information about all possible types of segment based liver resections. The resections go from segmentectomies in which only one segment is resected up to extended hemihepatectomies in which only

two segments remain after resection. In extreme cases up to 80% of the liver can be resected. Figure 5.2 shows a representation of the segments that are removed during right and left (extended) hemihepatectomies. The illustration is done using the method of Drechsler [Dre12].

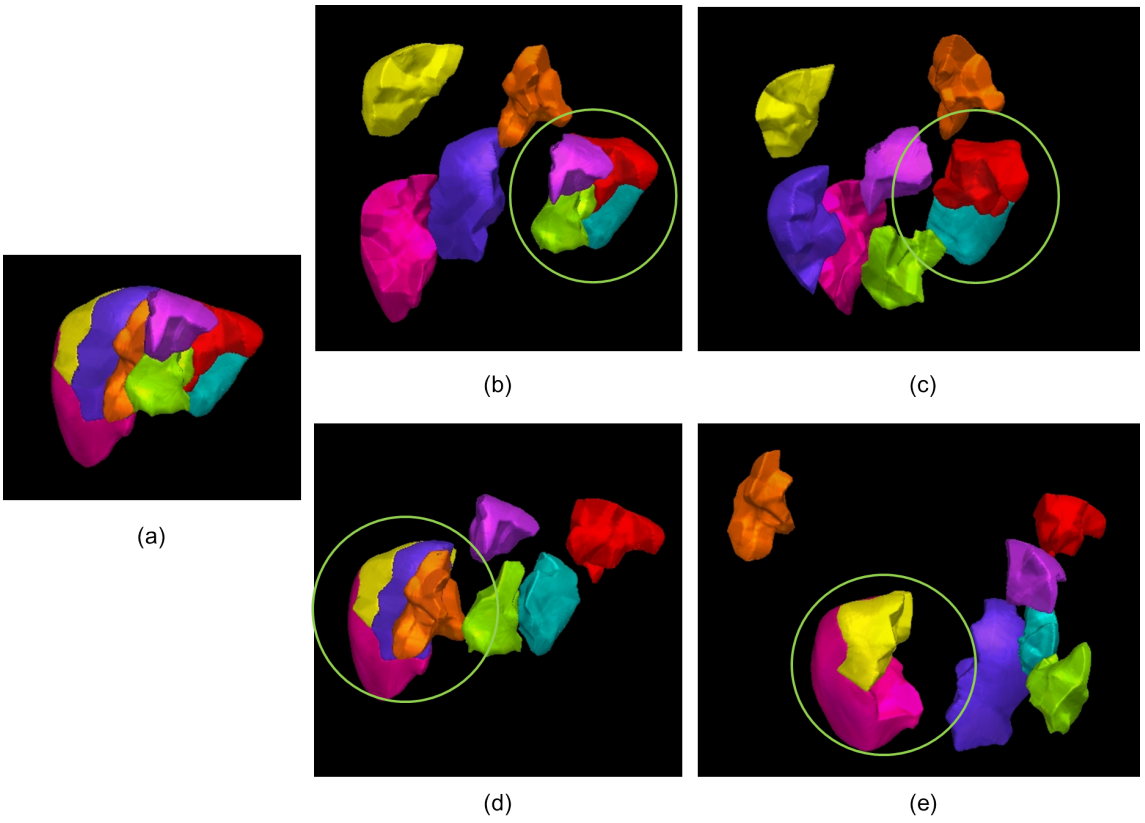

Figure 5.2.: Type of resections. (a) Division of the liver in Couinaud segments. (b) and (d): right and left hemihepatectomies. (c) and (d): extended right and left hemihepatectomies. The segments encircled in green remain after surgery. The illustrations were created using the method by Drechsler [Dre12].

While the ablated area is usually easily identifiable in every image as a darker area (Figure 5.1), resections present a higher variability. A resection can usually be identified as an area where the liver is missing and instead another organ (e.g., the intestine) is present. Nevertheless, in some cases a cyst is created after tumor resection in that area. This cyst is filled with gall. This phenomenon is called **biliom**. The biliom appears in the image as a dark area surrounded by a lighter ring attached to the liver. The last effect that can be observed after tumor resection is hypertrophy. **Hypertrophy** occurs when the cells of the liver grow in size after tumor resection. This derives in an enlargement of the liver that appears larger than the original one.

The physiological behavior of the lung will further deform the liver as shown in Figure 5.3. During inhalation the lung is filled with air and consequently it swells up. The surrounding organs are pushed and deformed accordingly. The liver is pushed downwards. However, this is not a free motion. It is limited by the resistance that the organs located below the liver, for instance the intestine and kidney, exert on it.

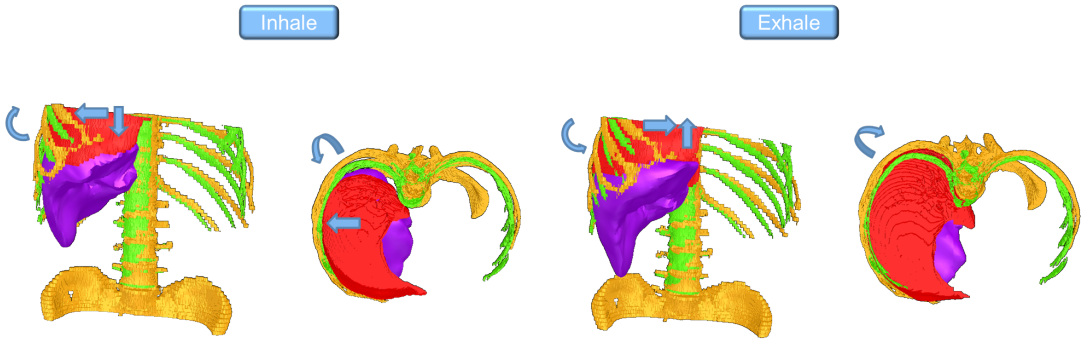

Figure 5.3.: Motion of the organs due to breathing. Both for inhale and exhale two views are shown. The organs of interest for this thesis have been segmented: liver (violet), lung (red), inhale ribcage (orange), exhale ribcage (green). The arrows show the direction of organ motion due to breathing.

The motion of the lungs does not solely have an effect in the liver. Despite the fact that the ribcage is known to be a hard tissue, it has certain flexibility. The swelling of the lungs pushes the ribcage, that consequently moves out and upwards. This biomechanical behavior of the ribcage is well known and usually explained as a "bucket-handle" motion. The reason for that is that each rib behaves similarly as a bucket-handle, in this case connected on one side to the spine and on the other to the sternum. This movement of the ribcage creates a space for the liver to deform in the direction of the ribcage. This can be seen in Figure 5.3. In the inhalation image, the liver and lung are visualized before air intake. At the same time, the ribcage before (green) and after (orange) air intake are visualized. One can see that the movement of the ribcage will leave some free space between the exhale liver and the inhale ribcage.

The opposite happens in the exhale process. In this case the lung motion induces the liver to move upwards. On the other side the ribcage will move inwards and downwards. The movement of the ribcage inwards will add an additional pressure to the liver.

The basis of a good outcome validation tool is an accurate pre and postoperative liver registration. However, as described in the previous paragraphs, the postoperatively acquired CT will contain deformations and differences with respect to the preoperative CT that will difficult the registration process.

As explained in Chapter 2, physics based registration methods result in more accurate results than interpolation based registration methods in presence of deformations. In particular, the liver can be modeled as a neo-Hookean hyperelastic model as a trade-off between efficiency (elastic models) and accuracy (viscoelastic models). The most widely used numerical technique to solve the equations that represent such a physical behavior are finite element methods. They will be the basis for the physics based registration method proposed in this thesis.

Figure 5.5 shows the work flow of the registration process. Given two CT images (pre and post operative), the liver is initially segmented [ESKW10]. Then, the vessels are segmented and their graph representation generated [DOLW12]. These steps are not part of the thesis and are therefore ignored in the presented work flow. The work presented in this chapter consists of the following steps:

(1) **Internal correspondences.** Internal correspondences (at corresponding vessel ramifications) will be used as references during the whole registration process. The methods proposed in Chapters 3 and 4 will be used to detect those internal correspondences

(2) **Boundary patches.** The boundary patches represent the organ that is adjacent to the liver at each surface point. They are used as additional surface references in addition to the internal correspondences during the registration process

(3) **Initial rigid registration.** In this step the pre- and postoperative images are rigidly registered

(4) **FEM-supported deformable registration.** This step deals with the largest deformations of liver. After this, the interior of the liver, including the vessels (internal landmarks) and their surrounding parenchyma, will be elastically registered. The liver resulting from this step will still contain deformations in areas near the surface of the liver, where no landmarks are known

(5) **Surface refinement.** Thin plate splines are used to refine the registration results in areas near the surface

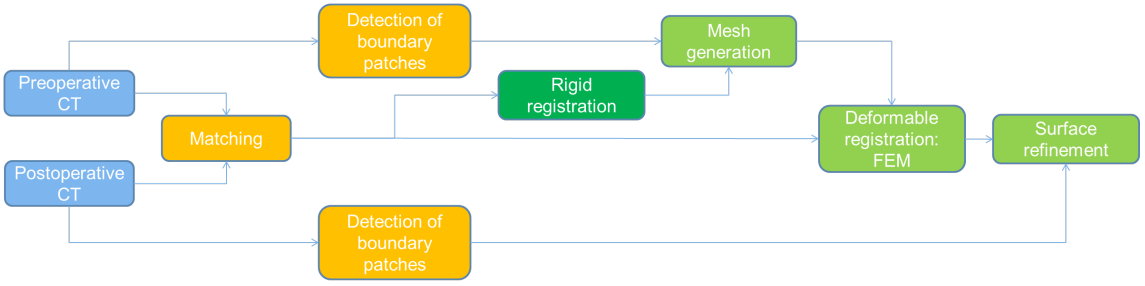

Figure 5.4.: Work flow of the methods proposed in this thesis. The colors represent a parallelism with Figure 5.5.

Solutions to all these concepts are proposed in this chapter that is structured as follows: Section 5.1 presents a solution for the detection of boundary patches. Section 5.2 and 5.3 present solutions for the initialization and deformable registration respectively. As usual, the chapter is finished with an in depth evaluation (Section 5.5) and a discussion of the presented methods (Section 5.6).

The contributions that go beyond the state of the art in this chapter are:

- Automatic detection of organs adjacent to the liver at each surface point
- Landmark-based initialization after extreme resections, namely, hemihepatectomy or extended hemihepatectomies
- Review of material parameters for simulation of liver deformations
- Registration of highly deformed liver volumes using both physical internal and on the surface constraints

- Evaluation of the methods in a high number of clinical datasets

The work presented in this chapter is based on the papers [OLDW14b, OLBPDW13, EOLD*12, OLDW14a, OLBPD13].

5.1. Detection of boundary patches

As it was mentioned before, a series of landmarks have to be defined on the surface of the organ. They will serve to drive the initialization process in absence of contrast agent and to drive the surface refinement step of the deformable registration. These landmarks will be given by the organs that are adjacent to the liver at each surface point. This section proposes a method to detect those landmarks.

Several authors have used closest point techniques to find correspondences and register the surface of the organs. Depending on the goal of the registration, this can provide results that are accurate enough. The problem arises when the organ contains large deformations where such techniques might not recover accurately the shape of the organ. For those cases, a physics based approach for organ shape registration would be more appropriate, namely, anatomical knowledge should be added to the calculations. Therefore, the organs that are adjacent to the liver at each point have to be determined.

Several methods have been developed to detect organs in the body. An method that has been widely used for face detection is that by Viola et al. [VJ04]. Their efficient method utilizes a cascade of classifiers to carry out the detection. Zhan et al. [ZZPK08] based on the work by Viola et al. detect the organs in whole body CT scans. Therefore, they generate a learning-based localizer. Besides learning-based techniques [ZGC09], regression techniques [ZZC07] have also been widely used for organ localization. Pauly et al. [PGC*11] detect multiple organs in MR Dixon sequences employing random ferns and forests. Criminisi et al. [CSRK10] utilize regression techniques to localize the organs in CT volumes. All these techniques localize the organs in the body, however, this is not enough for the application of this thesis: it is necessary to find out which concrete organ is adjacent to the liver at each surface point.

Ling et al. [LZZ*08] have proposed an approach to solve this problem, although with a different goal in mind. They divide the liver surface in boundary patches. Each patch represents the union interface between the liver and an adjacent organ. They use this information to refine the results of liver segmentation methods. The disadvantage of this approach is that it depends on known landmarks on the surface of the organ that should have their counterpart in every liver to be segmented. An atlas is generated with livers that have been manually labeled. Thus, the information of which surface landmark corresponds to which patch is available. But what happens if, like in the clinical scenarios that this thesis studies, the liver was subject to resections? In those cases there would be areas in which no corresponding landmarks would exist anymore. In addition to this, there are resections of all kind of sizes and locations. This complicates the process of the generation of a meaningful atlas.

This thesis proposes a method that does not require a set of training datasets, does not need corresponding landmarks and thus, can be used in pathological livers. The main ideas of the proposed method can be summarized as follows:

- A series of gray-level histograms are generated of the organs around the liver (Section 5.1).
- The intensity profile of the normals to the surface of the liver is generated and represented as a histogram.
- The histogram at each surface point is compared to the sample histograms to decide which organ is adjacent to the liver at that point.

The first step of the method is the extraction of the gray-level histograms of the organs that surround the liver. To this end, the liver is assumed to be surrounded by six organs. In the following each one of those organs will be identified with a concrete color: heart (yellow), lung (red), ribcage (green), intestine (blue), kidney (pink) and spine (white). Some other organs are located below the liver, for example, the pancreas. However, the effect of those organs in the deformation of the liver is similar to that of the intestine, namely, they exert a resistance to the movement of the liver downwards. Thus, they will be all encompassed in the intestine boundary patch.

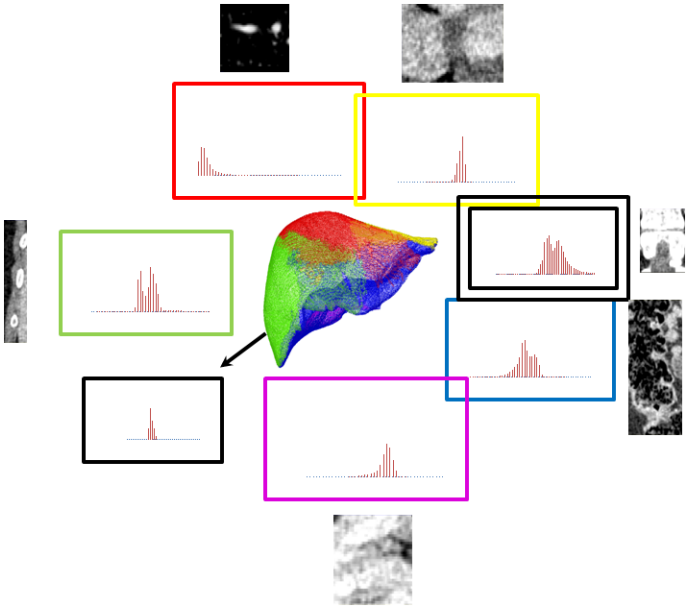

Figure 5.5.: Generation of samples histograms for the detection of organs adjacent to the liver [OLDW14a]. The liver is assumed to be surrounded by: heart, lung, ribcage, intestine, kidney and spine. An intensity histogram of each sample image is generated.

For the generation of histograms it is necessary to evaluate image samples of each of the organs mentioned before. This is done using a single abdominal dataset. Even though theoretically the use of multiple scans could improve the accuracy, the evaluation showed good results using a single one. Thus, the dataset is manually cropped six times (once per organ) so that the size of each one of the resulting samples (3D rectangular cropped images) is the largest possible box inside the organ (without having information of any other adjacent organ). A 2D slice of the cropped 3D image for each organ is shown in Figure 5.5.

Once the image samples have been defined, their histograms can be generated. Let H_s be the set of the six sample histograms $H_s = \{h_{o_1}, ...h_{o_6}\}$ and h_{o_i} the histogram of an organ o_i. Each histogram determines the frequency of appearance of each intensity I_s in the sample images. Thus, every voxel in the sample images will be considered for the calculation. The intensities are often grouped in so-called bins. This means that within the histogram, a certain bin returns the frequency of a set of intensities in the image. The number of bins can be defined as desired. The intensity values that are included in certain bin are determined with two values bin_{min} and bin_{max}.

The histogram of each organ is normalized and stored. These histograms are generated only once. Every time that the detection has to take place the stored histograms are loaded and used for the detection as shown in line 2 of Algorithm 13.

As mentioned before, the previous steps take place only once. The next steps including the preprocessing, however, take place every time the detection method has to be applied to a new dataset.

Algorithm 13 Generation of boundary patches

```
1: Let CT be the input image and I an empty image
2: H_s ← LoadSampleHistograms()
3: Liver ← SegmentLiver(CT)
4: Mesh ← GenerateMesh(Liver)
5: Mesh ← SmoothMesh(Mesh)
6: for i ← 0, MeshSize
7:     P ← SamplePointsAlongNormal()
8:     h_p ← GenerateHistogram(P)
9:     I ← CompareHistograms(H_s, h_p, normal)
10: end for
11: for w ← 1, 6
12:     Outliers ← BiggestConnectedComponent(I,w)
13: end for
14: for j ← 0, Outliers
15:     I ← CheckNeighborLabels(I)
16: end for
```

Preprocessing The detection method starts with the precondition that a segmentation of the liver exists. Thus, the liver has to be segmented from the CT image as a preprocessing step (line 3 in Algorithm 13). Then a surface mesh of the liver has to be generated (line 4). Note that an important factor of the method is the calculation of normals to the surface of the liver. The normals will be sensitive to inaccuracies in the segmented surfaces. That is why a smoothing filter is applied to the surfaces before further steps take place (line 5).

Detection The main idea of the detection process is to generate a series of normals along the surface of the liver. The intensity profile along each normal vector can then be compared to the pre-known organ histograms to decide which organ is adjacent to the liver at each surface point.

Thus, once the mesh is generated, the normal vectors ($\vec{n_i}$) to the surface are calculated. Therefore, every point in the mesh (Q_i) is iteratively visited (line 6 in Algorithm 13). For each point Q_i, $\vec{n_i}$ is calculated and a series of k points P_j along $\vec{n_i}$ are sampled that lay outside the liver (line 7). The optimal value for k is evaluated in Section 5.5.1. The sampling process is described in Equation 5.1.

$$P_j = j \frac{\vec{n_i}}{\|\vec{n_i}\|} d \tag{5.1}$$

As illustrated in Figure 5.6, d is the distance between sampled points. P is the set of all k sampled points $P = \{P_j : j \in [0, k]\}$ in the current iteration and $\frac{\vec{n_i}}{\|\vec{n_i}\|}$ the unit normal vector.

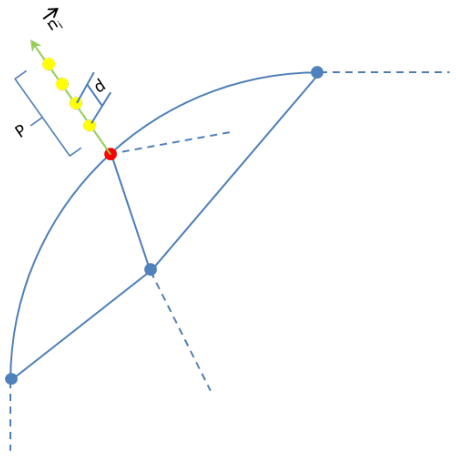

Figure 5.6.: Process of iterating along the mesh. Starting from every point on the mesh series of points P are sampled along the normal outside the liver.

For each sampled direction $\vec{n_i}$ a new histogram h_p is created using the sampled points (line 8 in Algorithm 13). This is shown in black in Figure 5.5. The histogram h_p has to be compared to the histograms in the set H_s to determine which organ has the most similar intensity profile to the current surface position. However, the position of the organs with respect to the liver does not have a large inter-patient variability. Thus, it is not necessary to compare the current h_p with all organ histograms h_{o_i}. The coordinate system that will be used in the method can be seen in Figure 5.7. According to the direction of $\vec{n_i}$, h_p will only be compared to those organs that are within a certain angle from the axis of the aforementioned coordinate system. Table 5.1 summarizes the angle ranges that have been used for each one of the organs. For example, if the normal vector, $\vec{n_i}$, is pointing in the direction from feet to head (y direction in Figure 5.7), only the histograms belonging to the heart and lung will be compared to h_p.

The similarity (S) between a sampled histogram h_p and the histogram of an organ h_{o_i} is calculated as their sum of the differences. Let n be the number of bins of a histogram, then the similarity is given by:

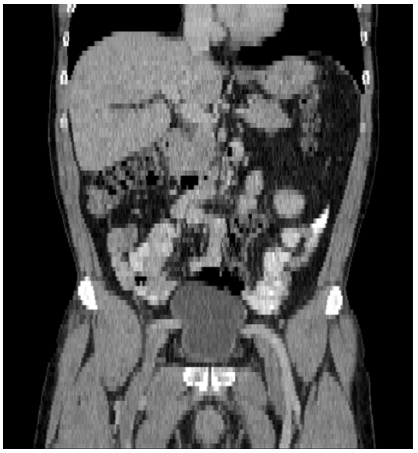

Figure 5.7.: Coordinate system used in the method.

	Angle (in degrees)		
Organ	x	y	z
Heart	$> 10, < 135$	$\geq 25, < 135$	< 90
Lung	-	< 160	≤ 90
Kidney	≤ 90	≤ 135	$> 100, \leq 180$
Ribcage	> 90	-	$< 135, > 45$
Spine	< 45	≤ 90	≤ 180
Intestine	-	-	$> 90, < 270$

Table 5.1.: Range of angles (in degrees) that determine whether a histogram h_p will be compared to a certain organ or not.

$$S = \sum_{bin=1}^{n} (h_{o_i}(bin) - h_p(bin)). \tag{5.2}$$

Two additional factors have to be taken into account:

(1) Only a small portion of intensities are represented in the histogram h_p due to the reduced amount of sampled points.

(2) Some organs have similar histograms.

As it is shown in Figure 5.8 (c) the histogram generated from the sampled points h_p contains a smaller amount of intensities than h_{o_1} and h_{o_2} (first factor). Bins that are not represented in h_p have therefore no relevance in the similarity calculation. Furthermore, the significance of the similarity would be reduced by including them in the calculations. Thus, the calculations are restricted to the bins that are represented in h_p:

$$A = \{\forall bin : h_p(bin) \neq 0 \wedge bin \in \mathbb{N} \wedge 0 \leq bin \leq c\}. \tag{5.3}$$

The second factor is given by organs that have similar histograms like for example the spine and kidney. They will lead to comparable similarity values. Furthermore, they have a similar location relative to the liver. Thus, wrong assignments can occur. To avoid this a weighting term $w(g)$ is added to the similarity calculation:

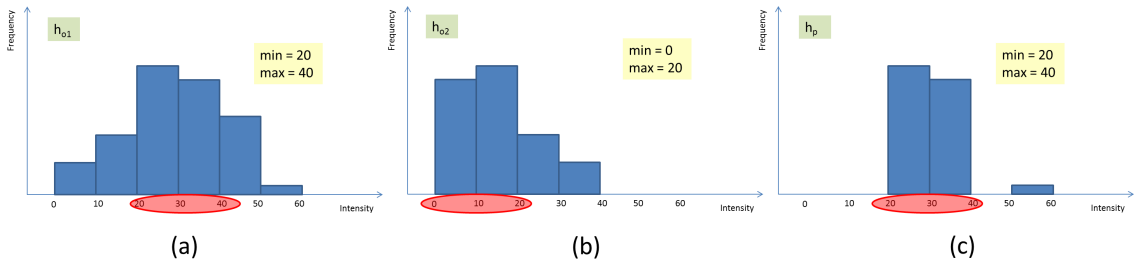

Figure 5.8.: Histograms [OLDW14a]. h_{o_1} and h_{o_2} are the histograms of two organs. h_p is the sample histogram. The red circle shows the bins that contain the most frequently seen intensities.

$$w(g) = \begin{cases} 0.1 & \text{if } min \leq g \leq max \\ 1 & \text{else} \end{cases} \tag{5.4}$$

min and *max* determine the range of bins per organ in which the most frequently seen intensities are contained. g is the bin containing the most frequently seen intensities in h_p. Thus, $w(g)$ favors organs if the most frequent bin of h_p is in its (min, max) range. The red circles in Figure 5.8 show the range of two organs h_{o_1} (a) and h_{o_2} (b) as well as the one for h_p (c).

After introducing those restrictions, the similarity measure finally takes the form:

$$S = w(g) \sum_{bin \in A} (h_{o_i}(bin) - h_p(bin)). \tag{5.5}$$

When the assignment process is over (lines 6 - 10 in Algorithm 13), all Q_i will have a label corresponding to a concrete organ (line 9 in Algorithm 13). However, some of them will be assigned to an incorrect organ. This is mostly noticeable in some areas of the intestine as can be seen in Figure 5.9 (orange circle). A series of voxels that should be labeled as intestine are labeled as ribcage (green). This leads to two areas that are candidate to be adjacent to the ribcage. It can be observed that the correctly labeled area is the one containing the largest amount of voxels. Thus, to overcome the miss-labeling problem the largest connected component per organ is detected (lines 11-13 in Algorithm 13). The voxels that do not belong to it are stored for further reassignment. Once all the organs are identified, a new assignment is carried out to remove outliers. The stored voxels will be assigned to the organ that is most frequently found in their neighborhood (lines 14-16 in Algorithm 13).

5.2. Initial rigid registration

As it was stated by Cash et al. [CMS*05] the chosen rigid registration technique will have an effect on the results of the final deformable registration. Taking into account the clinical scenario of this thesis, there are three possible approaches that could be used to carry out the rigid registration:

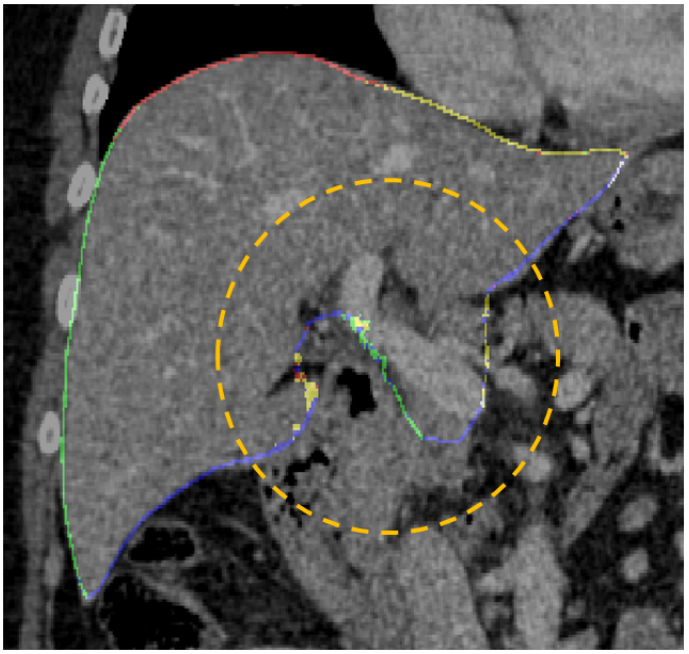

Figure 5.9.: Mismatches happen especially in some areas in which the intestine is adjacent to the liver. These areas are surrounded by an orange circle.

(1) Rigid registration in absence of contrast agent

(2) Rigid registration in presence of contrast agent

(3) Anatomy based rigid registration

5.2.1. Rigid registration in absence of contrast agent

As it was mentioned in Chapter 2 the rigid registration of livers that underwent (extended) hemihepatectomies is especially challenging. In the following a general approach is proposed for the rigid registration of resected livers. This approach is meant to be used also in absence of contrast agent.

All the resection scenarios presented in Belghiti et al. [BCG*00] share the idea that at least segments 2 and 3, or 6 and 7 remain after resection. From this the following idea can derive: **Anatomical landmarks found in segments 2, 3, or 6 can be used as references for initial rigid registration purposes no matter how large the resected area of the liver is.** Note that segment 7 is available but will not be used for the initial rigid registration as no interface between adjacent organs is located in that segment.

The anatomical landmarks that have been traditionally used for liver registration purposes do not lie specifically in the previously mentioned segments. The ligamentum falciforme located in the border between segments 4 and 2/3 cannot be used as landmark when only segments 6 and 7 remain. In spite of the slight movement of the organs adjacent to the liver after a resection, the organ that is located above segment 2 will always be the heart and the organs that appear adjacent to segment 6 are the ribcage and the intestine.

This idea is the basis for the proposed landmark based initial rigid registration. Therefore, the detection of the organs adjacent to the liver introduced in Section 5.1 is used. The organs that are especially interesting for the initial rigid registration method are the ribcage and intestine for left lobe hemihepatectomies and heart and intestine for right lobe hemihepatectomies.

Right lobe (extended) hemihepatectomy Under the assumption that the boundary patches are known (Section 5.1), the following method can be used for initial rigid registration when the left lobe has been resected.

As stated above when the left lobe is resected, segments 2 and 3 will remain. This also holds when an extended hemihepatectomy takes place. The organs that are adjacent to those segments of the liver are the heart and the intestine. The interface between those boundary patches can then be used as landmark for the initial rigid registration. Figure 5.10 illustrates the initial rigid registration steps. Note that the boundary patches form an image that will be used in the remaining section to carry out the initial rigid registration. The first two steps are shown in 2D for visualization purposes but they occur in 3D. These steps are explained in detail as follows:

- For both pre- and post-operative livers all the boundary patches corresponding to organs that do not touch the resected liver will not be considered during the initial rigid registration process, thus, they can be removed from the preoperative boundary patch image. Since the heart will still be adjacent to the liver after right lobe hemihepatectomies, its corresponding boundary patch can be used as reference for this step of the initialization. Therefore, the voxels included in the heart boundary patch are analyzed (first step in Figure 5.10). The leftmost voxel (red circle) among them will then be used as reference and all the voxels with lower x coordinates will be removed from the preoperative boundary patch image (red box).
- The uppermost voxel of the intestine's boundary patches (violet circle in Figure 5.10 step 2) in both datasets are matched by means of translations. After this step both livers are located at similar positions with respect to the x and y axis.
- The 2D slices located in the middle of both boundary patch images (sagittal view) are chosen and the centers of their bounding boxes are calculated. Both centers are matched using translations (third step in Figure 5.10). This step finalizes the initial registration by refining it with respect to the z axis.

Left lobe hemihepatectomy When the left lobe of the liver is resected, the landmark is given by the area in which intestine and ribcage join. It follows the same steps that the previous case with the difference that now the ROI will be calculated using the upper limit of the ribcage. For the initial rigid registration step, the lower limits of both intestine bounding boxes are matched and so are the centers of the middle slice in sagittal view. Figure 5.11 shows visually the steps of the process.

To solve rotation differences this approach can be used in combination with another rigid registration method, e.g., the one proposed by Cash et al. [CSC*04, CMS*05]. Cash

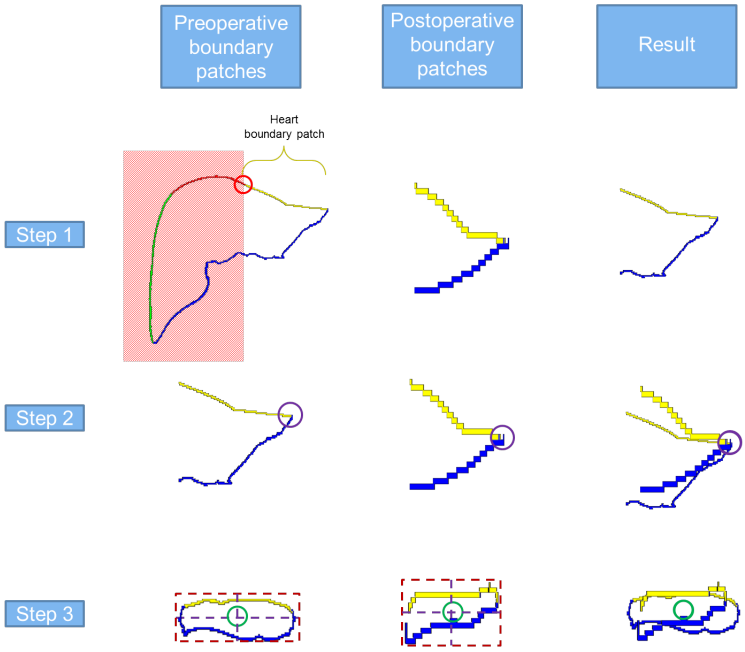

Figure 5.10.: Initialization steps after resection of the right lobe of the liver. Notice that the first two steps are shown in 2D for visualization purposes, but they both happen in 3D.

et al. propose an adaptation of the well-known ICP method for rigid registration. He adds a new term to the general equation of ICP methods to ensure the method to search for the maximum number of points on the surfaces with distances close to zero. The larger the number of points that approach that value, the smaller value the equation will have. Nevertheless, such a method requires a good initial rigid registration that would be provided by the method proposed in this thesis.

5.2.2. Initialization in presence of contrast agent

In addition to the previously proposed method, the internal landmarks (vessel ramification points) can also be used as reference for the rigid registration. The internal landmarks are divided in two sets of points that contain the landmarks that were found in the pre- and post-operative images respectively. Furthermore, the correspondences between both sets of points are known (graph matching). Given two sets of points and their correspondences, the method by Horn[1] [Hor87] can be used to calculate the rigid transformation that brings both sets of points closer from a least square point of view. The higher the distance between both sets of points, the more inaccurate the registration will be. Thus, the calculation of such a transformation minimizes the distance between both sets of points. The transformation that is used for rigid registrations is composed by a translation and a rotation. The main considerations made by Horn to calculate the optimal transformation between two sets of points are the following:

[1] Implementation provided by Visualization Toolkit (VTK). http://www.vtk.org/

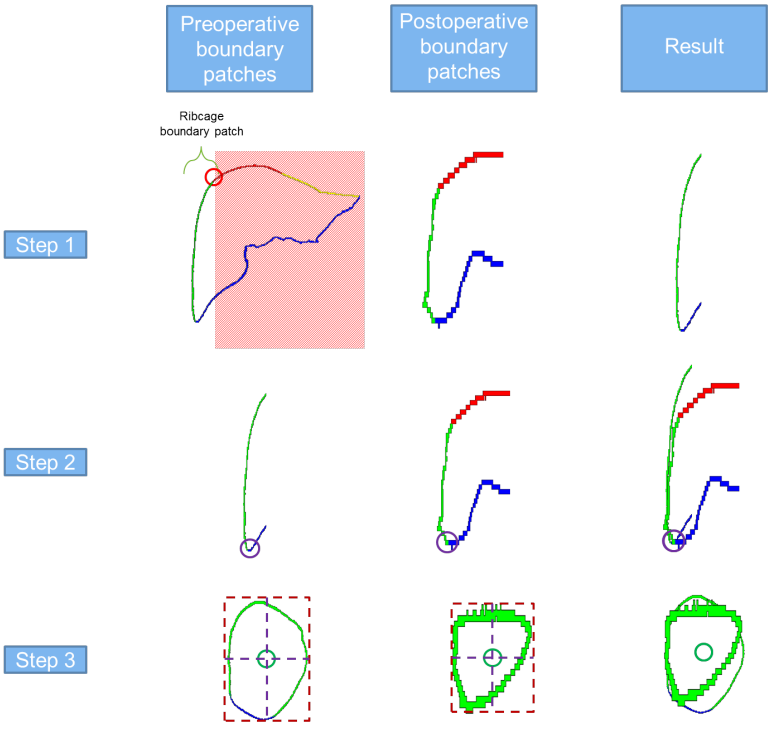

Figure 5.11.: Process of initial rigid registration after resection of the left lobe of the liver. Notice that the first two steps are shown in 2D for visualization purposes, but they both happen in 3D.

- The rotations used during the minimization process are represented by unit quaternions.
- The optimal translation is given by the difference of the centroids of the both sets of points, where one set of points has already been rotated.

Once the transformation is calculated, it is applied to the preoperative image that will be consequently rigidly registered to the postoperative image.

5.2.3. Anatomy based rigid registration

The initial rigid registration method proposed before follows the idea that the closer the initial location of two objects to be registered, the better the results of the subsequent deformable registration. However, this idea does not follow an anatomic based reasoning, which would be more appropriate when a physics-based model is going to be used for the deformations. The goal of a physics based registration method is to take advantage of anatomical information to increase the accuracy of the results. In other words, it tries to accurately deform an organ taking into account the influence of the surrounding organs on it. However, such an approach requires of an initial placement that accurately reproduces the initial spatial location of the organs.

Figure 5.12 shows two rigidly registered CT images of the abdomen acquired at different points in time. The variation of the soft organ positions due to breathing is visible.

The anatomical structure that is less prone to changes regarding breathing deformations or patient movements is the human skeleton. As it was explained in the introduction the ribcage moves during the breathing cycle. Thus, the only structures that are relatively robust against breathing motions are the spine and the pelvis. Nevertheless, the pelvis is not always visible in abdominal CT's and sometimes it will only be visible partially. Thus, although this approach is desirable when the interactions between the liver and its adjacent organs drive the registration process, obtaining an accurate initial placement will not always be straightforward. This approach will therefore not be used in this thesis.

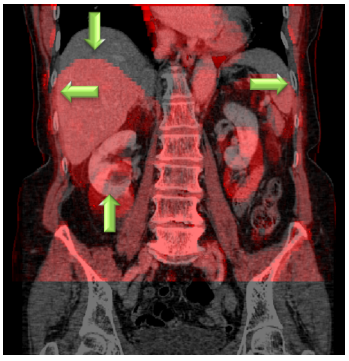

Figure 5.12.: Forces exerted by the lung in the surrounding organs [OLDW14b].

Conclusion The selection of the most appropriate rigid registration approach depends on the deformable registration technique to be used and on the characteristics of the input images. Since the images used for evaluation in this thesis are typically contrast enhanced and therefore internal landmarks are known, the method proposed by Horn (see Section 5.2.2) is used for the rigid registration step.

5.3. FEM-Modelling

Of all available registration techniques, physics based approaches are the most appropriate under the assumption of large deformations. This is the case in the clinical scenarios covered by this thesis: tumor ablation and resection. Livers that have overcome a resection do not only contain deformations due to breathing. The removal of part of the liver makes the surrounding organs slightly move from their original position which will cause additional deformations on the liver.

Finite element methods are used to incorporate all this in the registration of preoperative and postoperative liver CTs. The goal of using finite element methods is to discretize the continuum mechanics problem in the continuous domain. Therefore, the object (the liver in this thesis) is divided into smaller elements. Those elements have a simple geometrical shape, e.g., tetrahedra or hexahedra in 3 dimensions. The nodes that form each element can be moved and this will cause the displacement of its neighboring nodes. The union of all those displacements will result in a deformation of the complete liver volume. After forces have been exerted to the model, a node with coordinates $X = [x, y, z]$ will

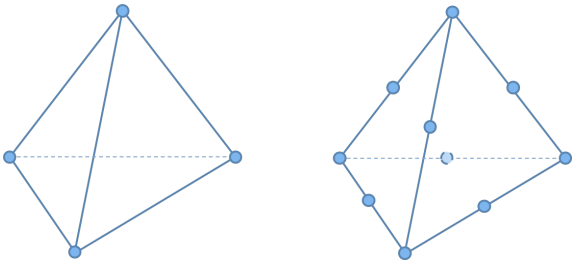

Figure 5.13.: Tetrahedral elements. Left: linear tetrahedral elements contain 4 control points (nodes). Right: quadratic tetrahedral elements contain 6 additional control points (nodes).

change its position

$$X' = HN \tag{5.6}$$

influenced by the nodal coordinates of the rest of the nodes N and the tensorial shape function of the element H [MWTT98].

According to the continuum mechanics, two reference frames can be used to describe the deformations of an object: Lagrangian and Eulerian configurations. The coordinates in the former configuration are referred to the object and change with it (material coordinates). Eulerian coordinates, on the contrary, are fixed in space (spatial coordinates). The latter is often used to model the behavior of fluids. Lagrangian configurations can be further subdivided into Total Langrangian or Updated Lagrangian. In the first configuration the initial state at time t = 0 is taken as reference for the deformation. Thus, it has the advantage that the spatial derivatives of the finite element formulation can be precomputed. In the Updated Lagrangian configuration, however, the spatial derivatives need to be recomputed after every iteration. In this thesis a Total Lagrangian framework is used for the calculations [TCO08] due to its computational efficiency.

The basis for the finite element formulation is the principle of virtual work [MWTT98]

$$\delta \hat{W}^{acc} = \delta \hat{W}^{ext} + \delta \hat{W}^{int}. \tag{5.7}$$

This principle states that there should be an equilibrium between internal and external virtual works. $\hat{W}^{acc}$ is the inertial virtual work

$$\delta \hat{W}^{acc} = \int_V \delta \hat{u}^T \rho_0 \Gamma^V dV \tag{5.8}$$

and it depends on the initial volume mass ρ_0 and the acceleration Γ^V of a point P in the mesh. $\delta \hat{u}^T$ is the local virtual displacement and the inertial virtual work is integrated over the whole object volume V.

The second term of Equation 5.7 is the external virtual work $\hat{W}^{ext}$

$$\delta \hat{W}^{ext} = \int_V \delta \hat{u}^{f^T} f^V dV + \int_R \delta \hat{u}^{f^T} t^R N dR. \tag{5.9}$$

Opposite to the inertial virtual work, the external virtual work consists of two terms. The

first one is integrated over the complete volume V and the second one is integrated over the surface R. The new terms in this equation, namely f^V and t^R, are the external forces applied to the object. f^V is the body force vector and t^R the stress vector at the surface of the object. N contains the vectors normal to the surface at each point of the mesh.

The last term of Equation 5.7 is the internal virtual work ($\delta\hat{W}^{int}$)

$$\delta\hat{W}^{int} = -\int_V \delta\hat{E}^T S dV \tag{5.10}$$

that is calculated using the Lagrangian strain tensor (E) and particularly the virtual strain field ($\delta\hat{E}^T$) as well as the Piola-Kirchoff second stress tensor (S), which are the tensors specifically used in Lagrangian configurations (see Chapter 2).

A discretization of the principle of virtual work derives in the equation of dynamics used for finite element methods

$$M\ddot{U} + D\dot{U} + KU = L. \tag{5.11}$$

The first term is the product of the mass matrix (M) that contains the mass of the nodes in the mesh (see Section 5.3.1) and the acceleration of each point ($\ddot{U}$) in the mesh. The second term is the damping matrix (D) multiplied by the speed of the point displacements ($\dot{U}$). Finally the stiffness matrix (K) is multiplied by the displacement of all the points (U) in the mesh. L represents the external forces applied to each mesh node of the object. Note that each term of the equation is a force, having the first term the form of the well-known Newton's second law of motion ($F = m * a$).

Physical modeling of soft tissue is a highly complex task. The modeling process contains three main challenges:

(1) generation of the volumetric mesh that represents the organ

(2) selection of the model equation that best describes the behavior of the organ and

(3) assignment of values to all parameters

Thus, there are certain aspects that have to be clarified before solving the equation systems of finite element formulation. On the one hand the object (liver) has to be divided into smaller elements. This is done by means of a volumetric mesh generation method that will be introduced in Section 5.3.1. Then, a model that accurately describes the behavior of the liver has to be selected (Section 5.3.2). Furthermore, the parameters describing the stiffness of the liver have to be determined to calculate the previous matrices. The number of parameters to be determined will depend on the complexity of the material that is to be modeled. This will be discussed in Section 5.3.3.

5.3.1. Volumetric mesh generation

The method that is usually used to decompose the object into smaller elements is a mesh generation method. Certain factors have to be considered when it is time to design a mesh generation method:

- Type of the elements

	Element types		Shape functions	
	Hexahedral	Tetrahedral	Linear	Quadratic
Stability	+	+		
Computational cost	+	-	+	-
Complex geometries	-	+	-	+
Stiffness	+	-		

Table 5.2.: Characteristics of hexahedral and tetrahedral elements and linear and quadratic shape functions.

- Single or multi-material
- Additional constraints

Type of the elements: Tetrahedral vs. hexahedral The first aspect to be determined before developing a mesh generation method is the topology of the elements that will form the mesh. To this end, hexahedral and tetrahedral elements are usually considered. In addition to this, the mesh can be designed to handle linear or quadratic shape functions. Table 5.2 summarizes the characteristics that the mesh will have depending on the selection of the element type and the shape functions. The performance of those elements have been specially analyzed to model different parts of the human anatomy from hard tissue, e.g., the femur [Ro06], to soft tissue like kidney [BTPB07], breast [CTH05] or liver [DA04]. In general tetrahedral meshes are preferred against hexahedral meshes due to the fact that human organs contain complex shapes that are difficult to generate using hexahedral meshes. A quantitative evaluation is presented by Bourdin et al. [BTPB07] that concludes that the use of tetrahedral meshes might be appropriate for clinical use except for the higher computational cost of those elements. However, linear tetrahedral meshes behave in a more stiff way than hexahedral meshes, which does not allow their nodes to move as much as they should. To overcome those problems quadratic tetrahedral meshes can be used, which contain 10 nodes instead of the 4 that form the linear ones (Figure 5.13). Both Bourdin et al. and Carter et al. [CTH05] have evaluated the performance of linear and quadratic tetrahedral meshes arriving in both cases to the same conclusion. For meshes with the element density that is necessary to model soft organs almost no differences are appreciated in terms of accuracy [BTPB07], but quadratic meshes have the additional disadvantage of being computationally more expensive (four time higher costs). Thus, within this thesis linear tetrahedral elements are chosen:

- The complex shapes comprised in the liver are hardly recovered by hexahedral elements.
- The computational cost for the studied application is not a limiting factor, nevertheless since quadratic elements do not present advantages in terms of accuracy, linear ones are chosen.

Single or multimaterial Although there are objects that can be modeled using a single material, organs are typically composed of several different tissues. The model can be

created as accurate as desired. Some authors consider the liver to be made uniquely of parenchyma, but the accuracy of the model can be increased by considering additional tissue types or even constructing multi-scale models.

The liver can be assumed to be made of: parenchyma, Glisson's capsule, vessels and tumor. These structures will be studied in detail in the next section. For the time being it suffices to know that the liver will be modeled by several materials. Thus, the generated mesh should be able to handle different tissue types. In addition to this, different tissue types should have different material properties. To this end it is important that each element of the mesh is completely located in a single tissue. In other words, there should not be elements that belong to more than one tissue type. Thus, the mesh should preserve the surfaces between different tissues.

Additional constraints Depending on the application additional constraints have to be taken into account to construct the model. In the current application displacements will not only be exerted in superficial nodes of the model but also in its interior. In addition to this, the locations of those internal displacements are known (see Chapters 3 and 4). Thus, it is desirable that the mesh contains nodes in the exact locations in which those landmarks were detected.

Delaunay based methods Mesh generation methods based on Delaunay refinement have shown to give satisfactory results. In general Delaunay based methods follow the next structure [BYB09a]:

- The structures to be modeled are segmented and a labeled image containing all the structures is generated.
- An initial set of points $E = \{p_1 ... p_n\} \in \mathbb{R}^3$ is randomly selected on the boundaries of the object. Note that in the case of multi-material objects the boundaries do not uniquely consist of the surface of the object, but also the interfaces between different materials. In the registration method proposed in this thesis displacements will be applied to the locations in which landmarks were found (see Chapters 3 and 4). Thus, it is necessary to ensure that the mesh will contain nodes at those exact locations. Therefore, the initial set of points will not only contain points at the boundaries. The spatial locations where landmarks were found will also be added to the initial set of points to ensure that they will be part of the final mesh.
- The restricted Delaunay triangulation of that set of points is generated, $Del_{|\Omega}(E)$. This triangulation is restricted to the object to be meshed Ω. The general Delaunay triangulation $Del(E)$ has the characteristic that the circumball (circumcicles in 2D) of every tetrahedron (triangle in 2D) does not contain any point in E. $Del(E)$ has the additional property of being the geometrical dual of the Voronoi diagram. When the triangulation is restricted to a domain $Del_{|\Omega}(E)$, it contains all tetrahedrons which dual Voronoi intersect with Ω. In other words the circumcentres of all tetrahedrons included in $Del_{|\Omega}(E)$ are inside Ω.
- Refinement of Delaunay triangulation. Points are added iteratively to the set E and the triangulation is updated. The goal of the refinement is that all tetrahedra

included in $Del_{|\Omega}(E)$ fulfill a series of quality criteria: topological and geometrical. The refinement process will continue until this condition is fulfilled.

As the objects to be meshed become more complex (more materials included with complex shapes), more quality criteria have to be fulfilled to use the resulting mesh in finite element simulations. Several authors have tried to improve the quality of multi-material meshes based on restricted Delaunay triangulations. Such a method is used by Pons et al. [PSB*07] to generate high quality meshes. They set as input to the method a labeled image that contains all the materials to be considered. Their method has been extended by Boltcheva et al. [BYB09b] to preserve 1 and 0-junctions. Foteinos et al. [FC11] concentrate their work to improve the quality of the mesh for dihedral angles. The work in this thesis is based on the one by Pons et al. and Boltcheva et al. and focuses on improving the element quality in areas representing thin structures, like vessels. In those areas the aforementioned methods are not able to preserve the complete vessel structure and as consequence some elements that should be labeled as vessel are labeled as parenchyma.

This problem can be found in areas in which a vessel contains a narrowing (Figure 5.14). In those cases it might happen that at some iteration of the refinement process a tetrahedra contains two or three boundary facets (face of the tetrahedra in the interface between two different materials). If the vertex common to those boundary facets is pointing in the direction of the narrowing, the boundary facets could be close enough to the boundary to fulfill the maximum surface distance quality criterion (Figure 5.14 middle). In this case the refinement process will stop in that area and some tetrahedra will be mislabeled. Relaxing the thresholds of the quality criteria does not help in this case: Figure 5.14 left shows the result after lowering the maximum surface distance criteria. But this value cannot be made as small as desired as it is bounded by the resolution of the image. On the other side the effect of this change will be an increase of the density of the mesh in some areas. Thus, the tetrahedra of the mesh will not have homogeneous sizes and this will at the end affect the finite element simulation that is highly dependent on the quality of the mesh.

The proposed solution is to use the skeleton of the liver vasculature for a new criterion that the refinement should take into account (Figure 5.14 right). Thus, the skeleton is extracted using the method by Drechsler et al. [DOL10c]. As result a polyline is obtained

$$B = L_1 \cup L_2 \cup ... \cup Ln, \tag{5.12}$$

where $L_i = m(x_i - x_{i-1})$ is each fragment of the polyline that has a slop of m, and has x_{i-1} and x_i as starting and ending points. This polyline traverses the center of the whole liver vasculature. A new criterion is defined that ensures that no intersections between boundary facets and the skeleton can happen. An intersection would mean that the refinement stopped without covering all the area of the vessel structure. Thus, in addition to the tetrahedra quality criteria, the intersection criterion must be fulfilled for the refinement process to stop. The new criterion is added as a post-processing step:

- Once the mesh is generated all boundary facets are analyzed in search for inter-

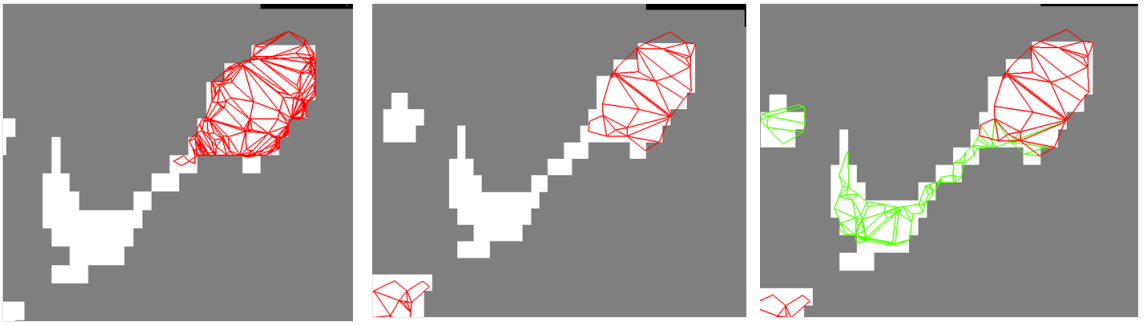

Figure 5.14.: Meshing results in an area in which the vessel contains a narrowing [OLBPDW13]. The image is labeled so that grey represents the liver parenchyma and white the liver vasculature. Note that for visualization purposes the tetrahedra belonging to the parenchyma are not visualized. Left: Results with a very low maximum surface distance. Middle: Narrowing problem without changing the tetrahedra quality criteria. Right: Results using the skeleton as new criteria. In this case the green tetrahedra are added to the mesh.

sections. The set of intersections

$$C = \begin{cases} n_x(x - x_0) + n_y(y - y_0) + n_z(z - z_0) = 0 \\ B = L_1 \cup L_2 \cup ... \cup Ln \end{cases}, \tag{5.13}$$

is given by all intersections between the plane that contains the boundary facet (first equation in the equation system) and B.

- In the same way that it is done for the quality criteria, those boundary facets that contain an intersection are marked as illegal facets.
- The refinement process starts again taking into account the new criterion.
- The process stops when no more intersections occur or the size of the boundary facets is smaller than a certain threshold. The last condition is added to avoid infinite loops when the resolution of the image and the size of the boundary facets are getting close.

5.3.2. Model equation

This section will deal with the second modeling challenge. Depending on the restrictions of the method linear or non-linear models can be used: elastic, hyperelastic or viscoelastic. The organ can be modeled at any scale and its complexity will increase accordingly, e.g., to model the liver in a cellular level the simulation will focus on the interactions between different cells.

As it was motivated in the state of the art a hyperelastic model is used in this thesis. This model has the advantages of being less computationally expensive than viscoelastic models and at the same time more accurate than elastic ones thanks to the introduction of non-linearities. In particular a neo-Hookean hyperelastic model [Hol00] is used for the

registration in which the strain energy function W (see Section 2.3.2.1) takes the form:

$$W = \frac{\mu}{2}\left(\bar{I}_1 - 3\right) + \frac{\kappa}{2}(J-1)^2 \tag{5.14}$$

and depends on the deviatoric first principal invariant $\bar{I}_1$ and the jacobian of the deformation gradient J. Furthermore, it depends on two elastic moduli, namely, the shear (μ) and bulk (κ) moduli.

The first principal invariant [MWTT98]

$$I_1 = \lambda_1^2 + \lambda_2^2 + \lambda_3^2 \tag{5.15}$$

is given by the trace of the Cauchy-Green right dilation tensor and is calculated using the principal stretches λ_1^2, λ_2^2 and λ_3^2. Then

$$\bar{I}_1 = \frac{I_1}{J^{2/3}} \tag{5.16}$$

depends on the jacobian of the deformation gradient $J = det(F)$ (see Chapter 2).

5.3.3. Study of material parameters

Once the equation that describes the behavior of the organ is chosen, values have to be assigned to the parameters of the equation. The elasticity of the organ is not a constant value but it has an inter-patient variability. It also depends on other factors like the health of the organ, and the gender and age of the patient among other. All these factors make the modeling task complex especially in cases in which high accuracy is determinant.

Several groups have focused their research on determining the variability of the liver's elasticity parameters. In the next paragraphs a literature research is done to find out the most appropriate values to be used in the registration.

Parenchyma As it was mentioned before, the liver behavior cannot be considered as purely elastic. An accurate model should consider viscosity and additional properties like porosity as well. Nevertheless, most of the authors describe the behavior of the liver by measuring its elasticity. Table 5.3 summarizes the elasticity values obtained by different authors for the measurement of the liver parenchyma. One can see the great variability of the values. The elasticity of the liver will depend on factors like the pathology of the liver (if it exists). On the other side depending on the fibrosis grade of the liver, the values obtained vary from 1 kPa to 25 kPa. In addition to the values that can be found in Table 5.3, some authors provide additional measures to study the dependency of the liver's elasticity on other factors like gender, weight or habits. Roulot et al. [RCC*08] arrive to the next conclusions in their work:

- Tobacco use has no influence in the stiffness of the liver.
- Stiffness increases with the age but not significantly.
- Stiffness is significantly higher in men.

- Stiffness increases significantly for BMI > 30. However, the difficulty to measure the elasticity in obese patients have been pointed out several times [CFA08, YYM*08].
- Steatosis has no effect in the stiffness of the liver.

Glisson's capsule Glisson's capsule is a very thin layer that covers the liver. Table 5.4 summarizes the elasticity values obtained for Glisson's capsule. One can observe that the studies have been mainly done in animals although Brunon et al. [BBGC10] provide some measurements in human samples. The stiffness of this tissue is much higher than that for the parenchyma showing values in the order of MPa instead of kPa.

Tumor Similarly to the parenchyma, all tumors will not have the same elasticity properties. Even though in general they are stiffer than the parenchyma, their elasticity will also depend on the type of the tumor. Table 5.5 summarizes the mechanical properties of the tumors obtained by 4 authors. One can observe variabilities not only between different pathologies, but also between the measures obtained by different authors and the same pathology.

Vessels The task of measuring the elasticity of the vessel walls is challenging. The extraction of a sample is a very delicate exercise. The measurements of the parenchyma are very often done using non-invasive procedures (MR elastography). However to measure the elasticity of the vessel walls a sample of them has to be extracted and its elasticity is calculated by means of mechanical experiments. Thus, the measurements are carried out in ex-vivo tissue, which adds additional inaccuracies to the measurements. Wuyts et al. [WVL*95] points out the challenges of measuring the elasticity of the vessel's wall. To model vessel walls the elasticity properties of the wall constituents have to be analyzed: elastin (0.1 to 1.0 MPa), smooth muscle (1.38 MPa) and collagen (0.1 to 9.0 GPa).

In the previous sections the large variability of the elasticity parameters has been studied. Thus, unified values are not close to the reality and patient specific values would be necessary for a higher accuracy. To this end MR-elastography images can be acquired each time a liver has to be modeled. Fewer groups try to extract those values from CT or US images of the liver.

Due to the lack of accurate parameter values some authors iteratively change them during the registration process until the solution converges. Nevertheless, the computational cost of this approach might be high as finite element methods are known to be computationally expensive and this way the simulation process is repeated several times. A good alternative could be to let the physician determine the fibrosis level of the liver before the registration takes place. Using this information, in combination to additional information like the weight and gender of the patient, the range of possible values would be reduced. However, only very experienced physicians are able to determine the fibrosis level by visual inspection of the US or MR images.

Depending on the application under study the selection of the most appropriate values can be more critical. This might be the case for open liver surgery. However, when the

Author	No.	Fibrosis grade 0	1	2	3	4	5	FG	Patho.
[YJH*01]	19	1083,55 (3)	2767,52 (1)	1788,5 (2)	1820,51 (3)	2373,56 (7)	4930,71 (3)	M	
[ZLKC05]	251(155)	5500 (88)		6600 (87)	10300 (27)	30800 (49)		M	CH C
[RYD*06]	23	2,7 K (1)	4K (4)	3,2 K (3)	5,7 (3)	19,2 (1)		BL	
[KAR*06]	14				5,77K(1m)				
[GDMR*06]	94(57%)								
Ledinghen	211(116)		<7,1K	7,1K - 9,5 K	9,5 K - 12,5 K	>12,5 K			
[CNPR*06]	101	5,5 K (38)		7,3 K (22)	9,8K (20)	17,3 K (15)		M	
[FCVC05]	711	111		7,2 K (99)	12,5 K (49)	17,6 K (95)		M	
[KHA*07]	5								
[HSS*07]	88	2,1 K (22)	2,4 K (13)	2,5 K (15)	3,1 K (14)	4,3 K (24)		M	
[YHL10]	77()	3,7 K	3,8 K	4,5 K	6,4 K	8,8 K			
[CFA08]				7,1 K (136)	9,5 K (83)	12,5 K (46)		M	CH C
[YYM*08]	97(40)	4,85 k (18)	7,382 K (28), 5,9	9,283 K (24)	13,333 K (18)	25,344 K (9)			NAFLD
[AKH*08]									
[RCC*08]	370	5,3 +- 1,45							NMS
	59	6,25 +- 1,96							MS

Table 5.3.: Summary of the elasticity values obtained by different groups using different mechanical methods. In most of the cases the grading system (FG) used is METAVIR (M). Rouviere et al. [RYD*06] use a different grading called Batts and Ludwig (BL). The pathologies are: Chronic hepatitis C (CH C), non-alcoholic fatty liver disease (NAFLD), non metabolic syndrome (NMS) and metabolic syndrome (MS)

Author	Subject	No. samples	Thickness (μm)	Elasticity (MPa)	
				Low-strain	High-strain
[HNV*06]	Bovine	5	93	1.1 +- 0.2	38.5 +- 4.9
[BBGC10]	Porcine	15			11.6 +- 19.2
	Human	11			16.9 +- 9.9
[UCB*11]	Porcine	30	10-20	8.22 +- 3.42	48.15 +- 4.5

Table 5.4.: Summary of the elasticity values obtained for Glisson's capsule.

Author	Subject	No.	Size	Type	Stiffness (kPa)
[BASLM03]	Human				3.6
[MTY*07]	Human	40	> 5 cm		
		17		HCC	55
		6		CCC	75
		16		Metastases	66.5
		1		Lymphoma	16.9
[VYG*08]	Human	29(16)	1.4 - 11 cm		
		12		HCC	10,3 +- 2 (7,6-14,2)
		14		Metastases	7,6 +- 1,7 (6,2-12,2)
		9		Hemagioma	2,7 +- 0,5 (1,6-3,2)
		5		CCC	16,2 +- 3,4 (10,8-19,6)
		3		Hyperplasia	2,7 +- 0,2 (2,4-2,9)
		1		Adenoma	3.1
[CLHC10]	Human	51			
		17	0.8-3.0 cm	Hemaginoma	35%/23%/41%
		25	1.6-7.9 cm	HCC	52%/24%/24%
		15	0.7-8.4 cm	Metastases	72%/17%/11%
		3	0.7-8.4 cm	CCC	

Table 5.5.: Summary of the elasticity values obtained for tumors. The high variability of the elasticity depends on the pathology observed in the organ: hepatocellular carcinoma (HCC), clear-cell carcinoma (CCC). [CLHC10] present the stiffness results as percentage of tumors with a stiffness higher/equal/smaller than the stiffness of the parenchyma.

patient is closed the movements of the liver are limited. In this thesis it is assumed for the liver to have a METAVIR fibrosis level between 0 (healthy) and 1 (slightly fibrotic). In most of the studies the elasticity values are given by the *Young's modulus* (relation between stress and strain). However several models, for instance, the neo-Hookean hyperelastic model that is used in this thesis, use as parameters in the equations bulk κ (response to uniform compression) and shear μ (relation between shear stress and shear strain) moduli. Thus, those elastic moduli have to be extracted from the Young's modulus value. The equations

$$\kappa = \frac{E}{3(1-2\nu)} \tag{5.17}$$

and

$$\mu = \frac{E}{2(1+\nu)} \tag{5.18}$$

convert Young's modulus into the searched elastic moduli [MWTT98]. ν is Poisson's ratio. This value represents the relation between the compression of the object in the direction in which the force is applied and the expansion of it in the perpendicular direction to the exerted force. Since soft tissue is nearly incompressible, ν approaches 0.5. Thus, a value of about 0.49 is usually given to ν.

In this thesis a series of experiments are carried out to determine which are the most appropriate values for the registration (see Section 5.4). The values given in this section will be used to define the range of values that are incorporated in the experiments.

5.4. FEM-supported Deformable Registration

Once the model has been generated, forces has to be exerted on it to deform it. The deformable registration process will be divided into two steps, as proposed by other groups working on the registration of breast images [CTBN*08, LSR*10]. The first step will serve to overcome the largest deformations using FEM. The second step will consist on a refinement of the results, especially in areas in which fewer landmarks were present, for example, on the surface or in the ablated area. For the simulations included in this section the finite element solver *Nifty Sim* [TCO08] has been used.

External forces The idea is to apply forces at the surface of the liver that simulate the effect that the movement of the rest of the organs cause on it. Forces will derive from the expected movements due to breathing explained in the previous chapter.

The first condition that must hold for this approach is to have an appropriate initial placement of both images, otherwise the magnitude and direction of the forces will be hardly identified. Thus, a so-called anatomy based rigid registration (see Section 5.2.3) has to be used. This initial placement allows to carry out the registration exerting downward (from the lung) and outward (from the ribcage) forces, as it would be expected if the preoperative image was acquired at inhale and the postoperative one at exhale. However, the definition of the magnitude of the forces to be applied to the model remains unknown.

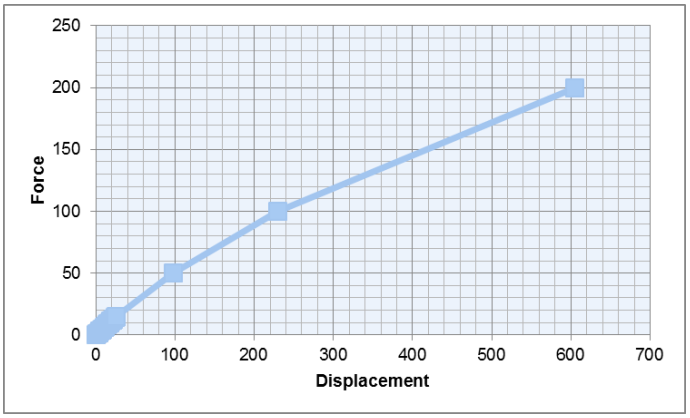

Figure 5.15.: Hyperelastic behavior of the liver.

The first important thing that has to be taken into account to calculate the forces that will be exerted on the liver under changing breathing conditions is how the mathematical

model will react to this forces. As it was previously mentioned a neo-Hookean hyperelastic model has been chosen. Figure 5.15 shows that as theoretically expected the liver model has a non-linear behavior. To prove that, the nodes of the model that belong to the intestine boundary patch (blue nodes according to the previous chapter) have been fixed in the direction in which the force was applied. This simulates the mechanical experiments that are usually done to measure material parameters (Figure 5.16). In those cases samples of a particular shape are taken, usually a cube. Then, forces are exerted on one of the surfaces while the opposite surface is fixed (if the forces are applied outwards) or while it stays on a table (if the forces are applied towards the opposite surface). For the experiment the complete liver has been used. Thus, the intestine nodes are set as fixed in the body-axis (z) direction while an increasing force is applied to a lung node (red labeled node). The displacement of the lung node is measured as the force is increased. The result of this experiment can be seen in Figure 5.15.

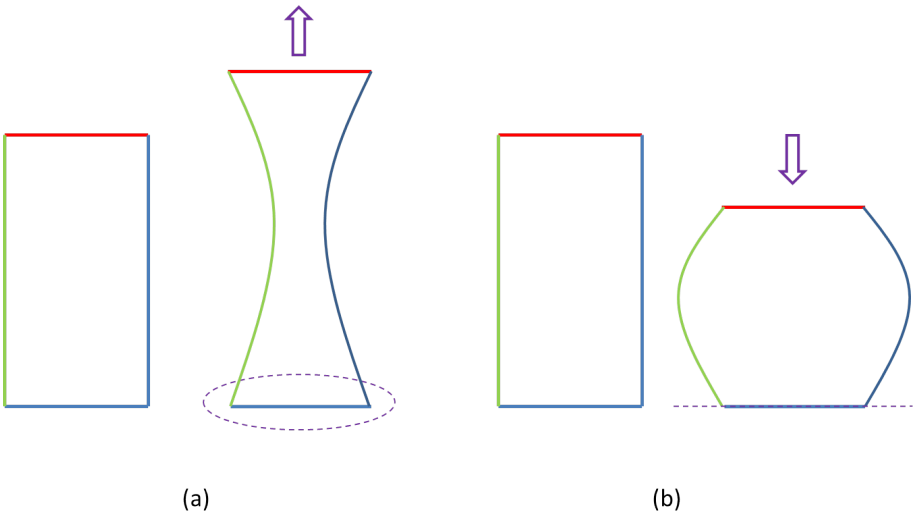

Figure 5.16.: Measurement of material parameters. (a) When the force is applied outwards, the nodes in the opposite surface are fixed. (b) When the force is applied inwards, the object lays on a surface.

However, this stress-strain curve does not contain enough information about the force that has to be applied to the liver in order to register it to the second liver. The node under study will not only be deformed by the force exerted on it, but also by the forces applied to the surrounding nodes (see Equation 5.6). Figure 5.17 shows how the displacement of a point will increase as the number of the points in its neighborhood in which the force is applied increases. New points have been added to the list of displaced nodes according to their distance to the point under study. It can be seen that as the distance between the new point and the point under study increases it arrives a moment in which the induced displacement is imperceptible: The distance between both nodes is larger than the radius of influence of the applied force. Thus, the displacement of a point does not uniquely relate to the force applied to that point. This complicates the process of finding out the forces that caused certain displacements (deformations).

The problem is getting more complex when the effects of the intestine and the ribcage are taken into account. While the ribcage can be simulated introducing contact forces be-

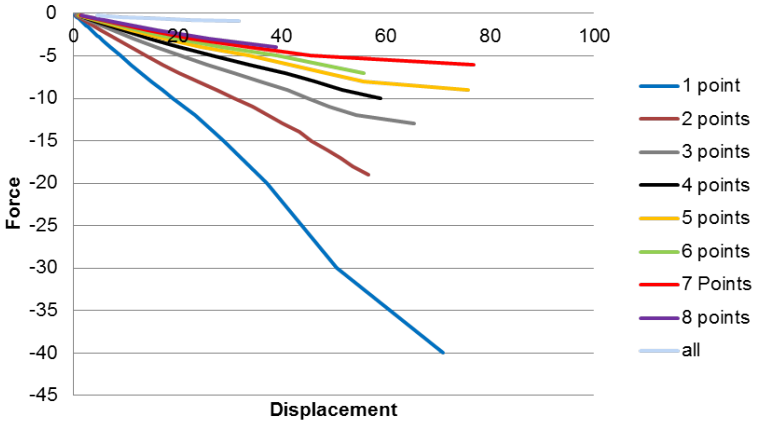

Figure 5.17.: Radius of influence of forces applied in neighboring nodes. As the distance between nodes increase the induced displacement becomes imperceptible.

tween surfaces (ribcage and liver) in the finite element simulation, the resistance exerted by the intestine has to be calculated. It is important to mention that the time required for the simulation when contact forces are included will increase. An iterative process needs to be started to find out which force/resistance combination will bring the liver to its final registered position. Finally, one needs to take into account that the method described holds in the case of inhale. In this case the lung pushes the liver downwards and the intestine exerts a resistance to the movement in that direction. However, in the exhale case the opposite movement can be observed and the liver will move upwards and inwards. The inwards and outwards movement is caused by the ribcage. During inhale contact forces could solve the simulation of the ribcage movements. However, during exhale the ribcage will exert additional forces on the liver surface.

Due to all the aforementioned difficulties it is hard to define the direction and exact magnitude of the forces that have to be applied to the model for an accurate registration by simple inspection of the resulting displacements. Even though in theory this would lead to more accuracy, such a process would require the simulation of all organs in the torso and abdomen, to reconstruct the initial state and deformations of the organs that caused the exact displacements that are visible in the liver.

Internal displacements Anatomical internal landmarks are the only known constraints that can accurately describe the movement and deformations that the liver overcame. The detection of a pair of correspondences implies that a displacement occurred in that position and the liver must be deformed accordingly.

This approach is chosen for the registration in this thesis. Thus, internal displacements will be applied in those locations in which landmarks were detected. The magnitude of the displacement will be given by the euclidean distance between both corresponding landmarks.

For the simulations the liver is assumed to be formed by two materials: parenchyma and Glisson's capsule. In previous sections a literature review of the elasticity parameters of the tissue types present on the liver has been done. However, the values have shown

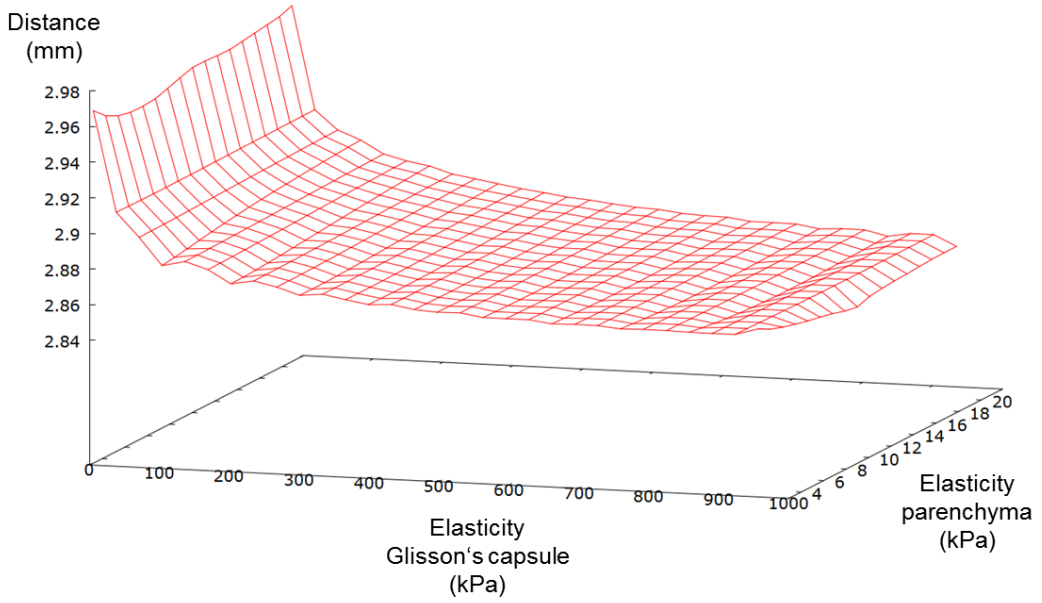

Figure 5.18.: Optimization of the elasticity parameters of Glisson's capsule and parenchyma in one datasets and resulting mean distance between the preoperative (after deformation) and postoperative liver surfaces.

to be changeable and dependable of several factors. The elasticity parameters used for the model have been optimized individually for each patient by means of an exhaustive search within a range of varying elasticity parameters that is detailed as follows. Every preoperative liver model has been deformed using internal displacements. Then, the mean distance between the deformed liver (moving image) and the postoperative liver (reference image) has been calculated. The experiment has been repeated changing the elasticity parameters. The variation range of Glisson's capsule has been set from 1kPa to 1MPa (in steps of 50 kPa), the one of liver parenchyma was set from 1kPa to 10kPa (in steps of 1kPa) to cover all values seen for different METAVIR levels. Figure 5.18 shows the optimization results for one exemplary dataset (all used datasets present similar optimization curves). The z axis represents the mean distance between the preoperative (after deformation) and the postoperative liver surfaces. x and y axes correspond to the elasticity of Glisson's capsule and parenchyma respectively. One can observe that larger values of Glisson's capsule provide better registration results as expected. Nevertheless, in most of the datasets the distance difference between the maximum and minimum distances is still under one millimeter (see z axis). Thus, for registration applications in which the liver remains inside the body (different than open liver surgery) the selected elasticity parameter will not have a significant influence in the results. Consequently, patient specific recalculations of those parameter are not needed. This might not be the case in open liver surgery. However, that scenario is out of the scope of this thesis.

As it was stated in the list of contributions, the goal of this work is not just to add accuracy to the interior of the organ, but also to increase the accuracy in the boundaries of the organ. To this end, appropriate boundary conditions must be applied to the liver. This will be the focus of the next section.

Surface refinement After the first step of the deformable registration has taken place, the largest deformation of the liver is recovered. At this point the areas containing landmarks are correctly registered. However, in some areas near the surface of the liver no internal landmarks can be found. Figure 5.28 shows that the thin vessels that exist near the surface of the liver are not part of the segmented vessels. Thus, there is an area around the surface of the liver that will not contain any correspondences. Figure 5.19 (a) shows some problematic areas that can be mismatched after the first step of the deformable registration.

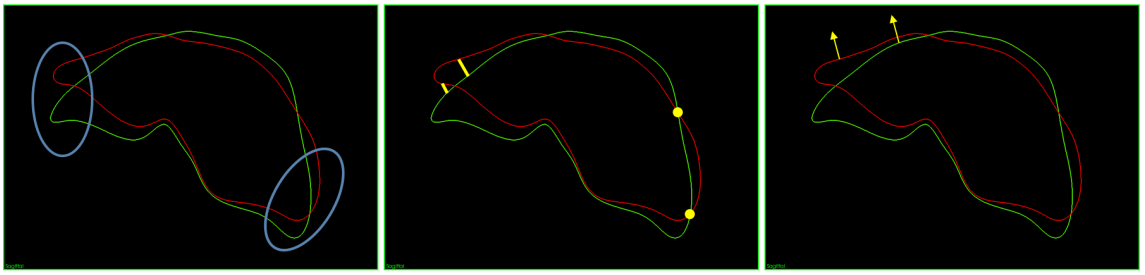

(a) (b) (c)

Figure 5.19.: (a) Inaccuracies in some areas after initial registration. (b) Closest point distance solution. (c) Normal to the surface solution.

To solve for this lack in accuracy, a surface refinement step is applied. In theory the deformed mesh could be used for the new simulation using FEM. However, the capability of finite elements to converge to a solution highly depends on the quality of the mesh. After the first deformation takes place the quality of the initial mesh decreases. It does not necessarily fulfill the quality criteria anymore and a remeshing is needed. Since the expected deformations for this step are small compared to the initial ones, finite element methods are not required. Thus, a different technique is used for the second step of the deformable registration, namely, thin plate splines (see Section 2.3.2.2). Opposite to other techniques like free form deformations, thin plate splines, which consist of a landmark based kernel, allow to freely set a series of landmarks to guide the refinement process. It is specially important for the proposed method to fix the internal landmarks that have been registered in the previous step. Thus, the refinement will improve the registration in the areas with fewer landmarks while it keeps the results in areas that were already correctly registered.

The energy that has to be minimized to find the solution for the registration using thin plate splines was introduced in Chapter 2. As it is expressed by the mathematical form of thin plate splines, the registration will be driven by a series of control points. The displacements applied to the locations of the image that are not part of the set of control points will be the result of an interpolation using the known landmarks. Thus, it is important to find landmarks that accurately describe the deformation of the liver. Since the interior of the liver has already been correctly registered, only landmarks near its surface are required.

Two main techniques have been often used for such a surface registration. One of them is the iterative closest point. Another technique based on the normals to the surfaces was proposed by Niculescu et al. [NNSF09]. Unfortunately, both techniques are inaccurate

to register pre/post operative datasets as can be seen in Figure 5.19 (b) and (c). The first technique matches points that are not real correspondences since the closest point between surfaces is not necessarily a correct correspondence. The same holds when using closest normals directions. In these datasets some areas can still contain deformations. Then, surface points that do not share similar normal directions might be in reality corresponding points.

Another approach that could be used for the refinement purpose is the curvature. The curvature is rotation invariant and thus, does not present the problems of the normals. Gaussian curvature is particularly interesting to take advantage of the fact that measures will not be affected by the orientation of the surfaces. Some other type of curvatures, for example, the mean curvature, would not fulfill this constraint. The Gaussian curvature K can be mathematically formulated as follows:

$$K = \kappa_1 * \kappa_2. \tag{5.19}$$

In this equation κ_1 and κ_2 are the principal curvatures of the surface. Points with a similar curvature (small g_S) could be considered as corresponding points:

$$g_S = K_1 - K_2. \tag{5.20}$$

The curvature has a great potential to serve as refinement metric to find correspondences. Nevertheless, it should be used in combination to a robust outlier detection. The problem is that high curvature points will not only be detected at the desired locations (see red circles in Figure 5.20). This will result in mismatches. In addition to this, the number of landmarks obtained with this metric will be small.

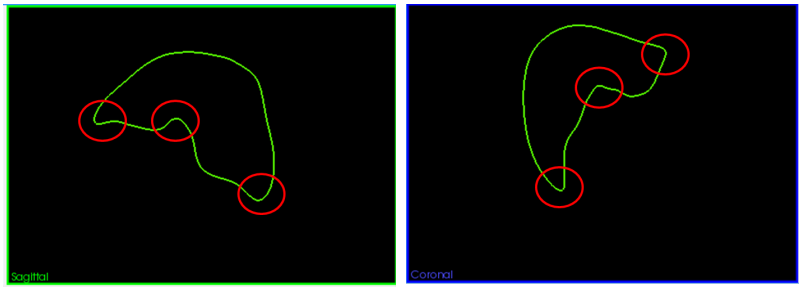

Figure 5.20.: Locations with high curvatures.

In this thesis a novel concept for the surface refinement is introduced to solve for the aforementioned problems. The idea is to apply closest point distances constrained by the boundary patches detected in Section 5.1. This means that for a pair of correspondences to be correct they should belong to corresponding boundary patches. In other words, a surface point of the preoperative image that belong to the lung boundary patch will only be match to a node of the postoperative image's lung boundary patch. This step is carried out using a reduced number of control points and its goal is to bring the areas without internal landmarks close to each other. The final step is a conventional closest point distance method.

This method is also appropriate for resected livers. In presence of resections the sur-

faces should not always perfectly match:

(1) **Patients with a resection prior to the current intervention (Figure 5.21 (a)).** The same resection is visible in both pre- (red) and post-operative (blue) images. Thus, both surfaces should be correctly registered. As it is shown inside the green ellipses of Figure 5.21 (a) the distance between both surfaces after the first step of the deformable registration is relatively close.

(2) **Patients with a new resection (Figure 5.21 (b)).** In the preoperative image the liver is complete, but this is not anymore the case in the postoperative image. Thus, the surfaces in the area of the resection should not be matched. Opposite to the previous case, a large distance can be observed between the surfaces in the area of the resection (green line in Figure 5.21 (b)).

As it was shown in Figure 5.21, the distance between surfaces (after FEM based registration has taken place) in the aforementioned cases varies. With this idea in mind the surface refinement step is restricted to those surfaces that after the first step of the deformable registration are close to each other (distance smaller than 1 cm).

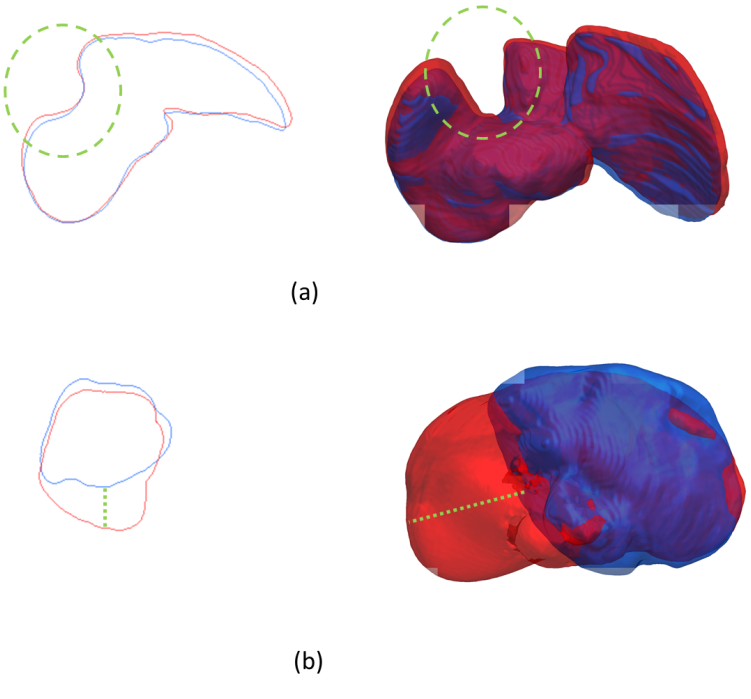

Figure 5.21.: Pre- (red) and post-operative (blue) liver surfaces after FEM based registration. The left images shows the contour of the surfaces corresponding to a 2D axial slice. The right images show a 3D view of the livers. (a) A resection prior to the current intervention exist. (b) A new resection is visible in the postoperative image.

Patient	Type	ID	Resolution (mm)	Model
I	arterial	Ia	1.25	LightSpeed Ultra Thin
	portal	Ib	1.25	LightSpeed Ultra Thin
II	preoperative	IIa	1.25	LightSpeed 16
	postoperative	IIb	5.00	HiSpeed
III	preoperative	IIIa	5.00	LightSpeed 16
	postoperative	IIIb	5.00	HiSpeed
IV	preoperative	IVa	1.25	LightSpeed Ultra Thin
	postoperative	IVb	5.00	HiSpeed
V	arterial	Va	1.25	LightSpeed 16
	portal	Vb	1.25	LightSpeed 16
VI	arterial	VIa	1.25	LightSpeed Ultra Thin
	portal	VIb	1.25	LightSpeed Ultra Thin
VII	arterial	VIIa	1.25	LightSpeed Ultra Thin
	portal	VIIb	1.25	LightSpeed Ultra Thin
VIII	arterial	VIIIa	1.25	LightSpeed Ultra Thin
	portal	VIIIb	1.25	LightSpeed Ultra Thin
IX	arterial	IXa	1.25	LightSpeed Ultra Thin
	portal	IXb	1.25	LightSpeed Ultra Thin
X	arterial	Xa	1.25	LightSpeed Ultra Thin
	portal	Xb	1.25	LightSpeed Ultra Thin
XI	arterial	XIa	1.25	LightSpeed 16
	portal	XIb	1.25	LightSpeed 16
XII	arterial	XIIa	1.25	LightSpeed Ultra Thin
	portal	XIIb	1.25	LightSpeed Ultra Thin

Table 5.6.: Datasets used for evaluation of the method. The z-axial spatial resolution is given in mm. The machines used to acquire the CT datasets are in every case of GE Medical Systems.

5.5. Evaluation

5.5.1. Detection of boundary patches

The evaluation of the organ detection has been done using the 24 clinical CT datasets of the abdomen described in Table 5.6.

To evaluate the organ detection the liver has been segmented in the collected 24 CT datasets and the method has been applied. The accuracy of the results is influenced by two parameters: the number of bins used in the histograms and the number of sampled points k per surface point. When the number of bins is small, each one of them contains a larger number of intensities (less differentiation) and thus, less accuracy is achieved.

For the quantitative evaluation of the method, eight datasets have been selected (VIIIa, IXa, IXb, Xa, Xb, XIa, XIb, XIIb). Notice that as shown in Figure 5.23 there are not substantial differences in the results between different patients. For each liver three slices are chosen, containing in every case at least one with a larger number of mismatches. It can be visually determined which organ is adjacent to the liver at every point. Using this information the number of mismatches has been counted as well as the total number of surface points. The resulting mean error E is the mean of the ratios between the

No. bins	50			100		
No. sampled points	5	10	20	5	10	20
Mean error (%)	16.23	8.92	6.93	17.72	9.63	7.2

Table 5.7.: Effect of the variation in the number of samples per surface point (5, 10 and 20) and in the number of bins per histogram. The results are given as mean percentage of 24 slices from 8 different patients.

mismatches and the total number of points in the three slices:

$$E = \frac{\sum_{i=0}^{s} e(\%)}{s * 100}, \tag{5.21}$$

where $e = m/w$ is the error per slice, with m the number of wrong assignments and w the total number of assignments in that slice. Finally, s is the number of slices used for the evaluation. To evaluate the effect of increasing the number of bins and the number of sampled points the process is repeated varying those factors: 50 and 100 for the number of bins and 5, 10, and 20 for k.

Table 5.7 shows the effect of increasing k. The results are given as the mean percentage of mismatches in the 24 selected slices from 8 different patients. Notice that the same slices were used for calculation of mismatches with 5, 10 and 20 sampled points as well as for 50 and 100 bins. This avoids the results to be influenced by the selection of certain slices. One can see that as k increases the number of mismatches decreases. Additionally, the reduction in the number of mismatches is more prominent when the parameter is changed from 5 to 10 points than when it is changed to 20 points. The results using 100 bins instead of 50 are slightly worst.

Although the results are better using 20 sample points, after careful evaluation of the data one can see that this depends on the area of the liver that one observes. The upper row in Figure 5.22 shows the results of the detection method in the area where the ribcage, the right lung and the liver meet. One can see that the left image, belonging to 20 sample points, contains more mismatches than the second (10 sample points) and the third (5 sample points) images. The reason for this is that as more sample points are taken, more of them belong to the near ribcage, which contain intensity values higher than the lung. This way, some points that should be considered as lung will be matched to the ribcage histogram. Under these circumstances it could be decided to use a small number of sample points. However, as shown in the bottom row of the same figure, in other areas like the one where the right lung, the heart and the liver meet this would not be optimal. There are often segmentation inaccuracies that cause points that belong to the liver-lung union to be matched to the heart histogram. The number of mismatches due to these problems happens to be higher than those due to the high number of sample points.

For the calculation of Table 5.7, three slices per dataset have been selected: One with a larger number of mismatches ($< 15\%$), one with a small number of mismatches ($< 5\%$) and an intermediate slice. The larger mismatches (slices with $\approx 15\%$ of the mismatches) occur when the spine is mismatched, which happens in less than 14 % of the slices and only in those patients for which the spine is not adjacent to the liver. In these cases the

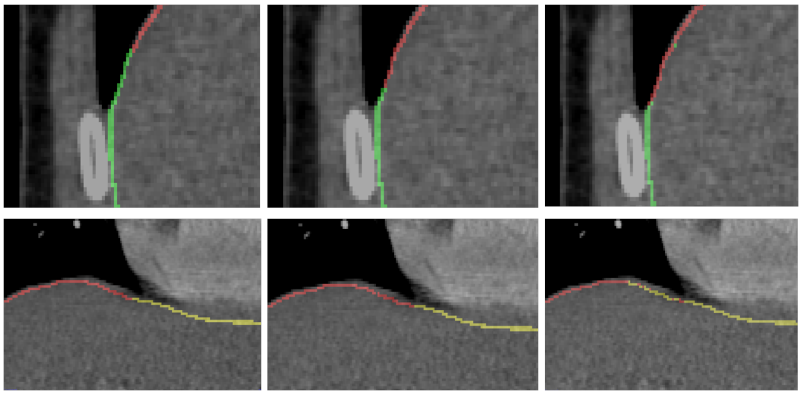

Figure 5.22.: Qualitative evaluation of the effect of decreasing the number of sample points [OLDW14a]. The columns belong to 20, 10 and 5 samples points. The upper row shows the detection results in the area where the ribcage, the right lung and the liver meet. The second row shows the results in the area where the right lung the heart and the liver meet.

method, not being able to find the spine, matches it to the artery.

As it was mentioned before, the method has not only been tested in those 8 datasets used for the quantitative evaluation. Figure 5.23 shows the qualitative results on the remaining 16 datasets. One can see the differences in shapes and resolutions between different datasets. As it was explained in the methods section, the adjacent organs are distinguished by labels: lung (red), heart (yellow), kidney (pink), intestine (blue), ribcage (green) and spine (white).

5.5.2. Mesh generation

The mesh generation method has been evaluated in 23 liver CTs of 17 different patients. Acquisitions from the same patients belong either to pre and postoperative images or to different phases of the same scan. All datasets contain a spatial resolution of 1.25 or 5.00 mm in the z-axis and were acquired using GE Medical Systems machines. The improvements achieved using the new skeleton based criterion are evaluated. To this end special attention will be paid on the vascular structures. To evaluate these improvements, three metrics have been used.

Number of intersections The first metric used is the number of intersections between boundary facets and the skeleton. Figure 5.24 left illustrates an example of this. The red triangle represents a boundary facet that intersects with the skeleton (orange) in the position pointed by the green circle. Due to the narrowing of the vessels the area inside the yellow ellipse will not be labeled as vessel. The results obtained for the evaluation of this metric are shown in Figure 5.25. The number of intersections when the intersection criterion is included (green) or excluded (red) are counted. The metric shows an improvement (reduction) of 65.67% over the number of intersections obtained without using this criterion. One can observe that some intersections are still present. They belong to areas in which the boundary facet reached the minimum tolerable size.

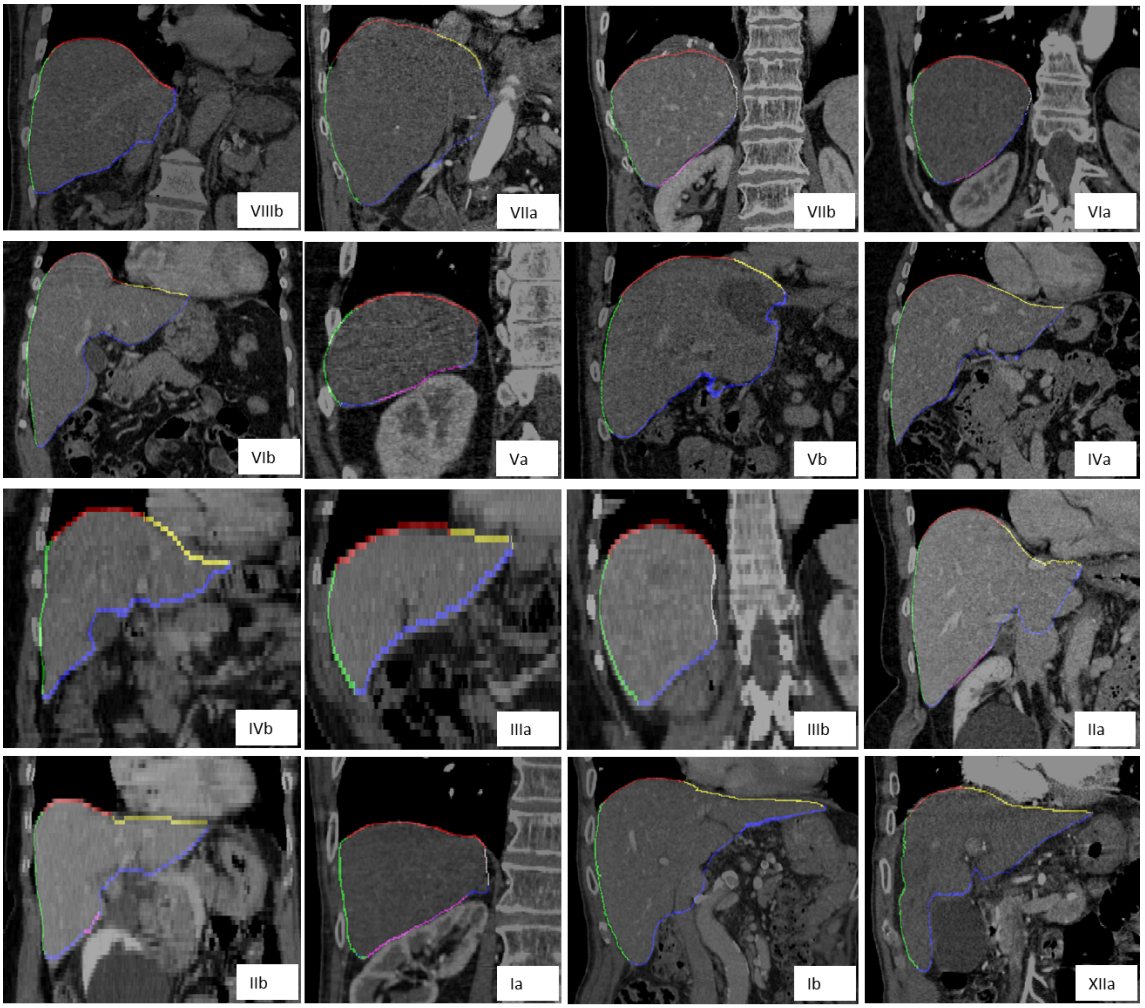

Figure 5.23.: Results of the organ detection method in 16 patients. The different organs adjacent to the liver are labeled with different colors: lung (red), heart (yellow), kidney (pink), intestine (blue), ribcage (green) and spine (white). The ID of each dataset can be seen in the bottom right of each image.

This metric gives an idea of the reduction of the number of mislabeled structures but it does not give any information on how large those structures are. The mislabeled structures can be divided into two groups: those mislabeled when the new criterion is not used and those that are still mislabeled because the minimum allowable tetrahedra size is reached. To evaluate that, two additional metrics are used.

Volume The second metric is the volume of the structures that are detected with and without the new criterion. Figure 5.24 middle illustrates the meaning of this metric. Without using the intersection criterion only the volume before the narrowing will be detected and meshed (blue). When the new criterion is used also the remaining volume (green) will be labeled as vessel. Figure 5.26 shows the quantitative results of the volume metric in the 23 studied datasets. As in the previous evaluation, red shows the volume obtained without the new criterion and green with it. In this case yellow is the ground truth value,

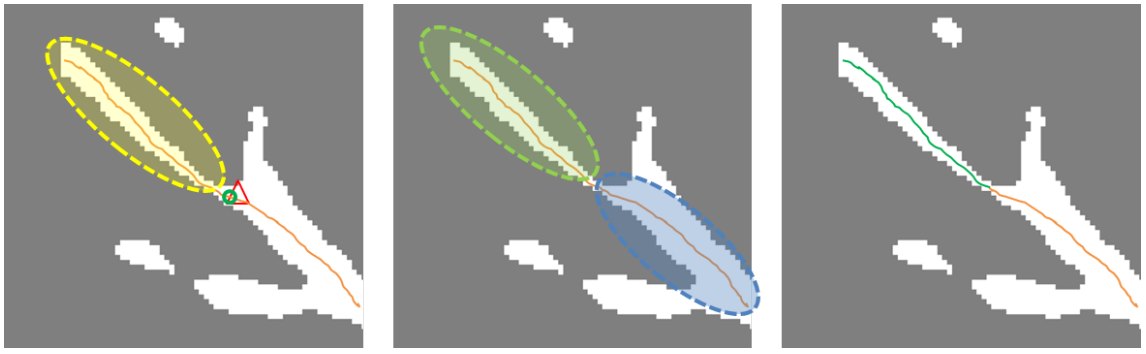

Figure 5.24.: Evaluation metrics [OLBPDW13]. Left: number of intersections (green) between boundary facets (red) triangle and the skeleton (orange). Middle: volume meshed as vessel without using the intersection criterion (blue) and using it (blue + green). Right: length of the skeleton of the meshed vessel without using the intersection criterion (orange) and using it (orange + green).

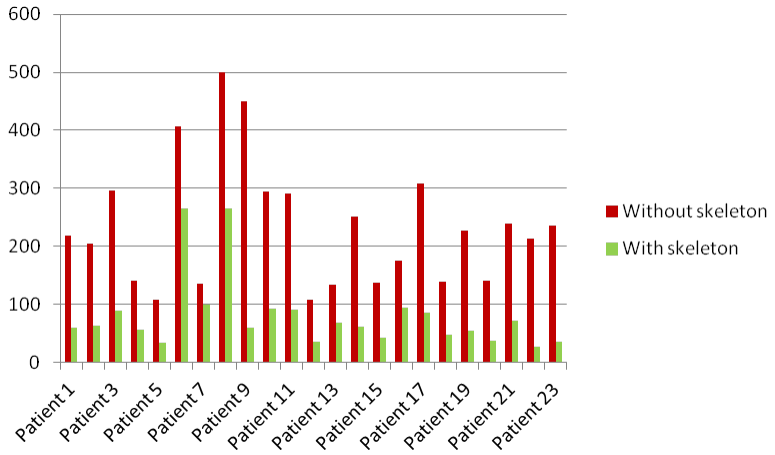

Figure 5.25.: Quantitative evaluation of the number of intersections observed after mesh generation without the intersection criterion (red) and with the new criterion added (green) [OLBPDW13]. An improvement of 65.67% is observed.

namely, the true volume of the liver vasculature. One can see that the improvement is not as significant as it could be expected. However, the reason for this is the volume loss that occur during the conversion from the mesh to an image. In any case an improvement of 4% is observed.

Length of the skeleton The last metric used for the evaluation is the length of the skeleton of the meshed vascular areas. As in the previous cases Figure 5.24 right illustrates the meaning on this metric. In this case thanks to the new criterion the skeleton of the vascular mesh will traverse the complete structure (orange + green) opposite to what occurs without the criterion (only orange detected). Figure 5.27 shows the quantitative results of this metric. With the original method 72.7% of the ground truth skeleton is detected. Thanks to the new criterion a 93.9% of the ground truth is achieved. Thus, there is

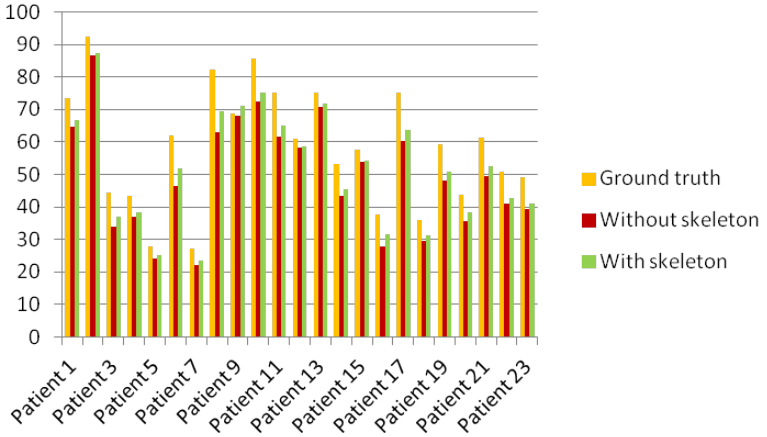

Figure 5.26.: Quantitative evaluation of the number of volume meshed without the intersection criterion (red) and with the new criterion added (green) [OLBPDW13]. Yellow shows the ground truth value, namely, the volume of the liver vasculature.

an improvement of 21.2% over the original method. These values show that even though there is still a number of intersections present in the new meshing results, they belong to small areas of the vasculature while most of the branches are meshed and labeled correctly.

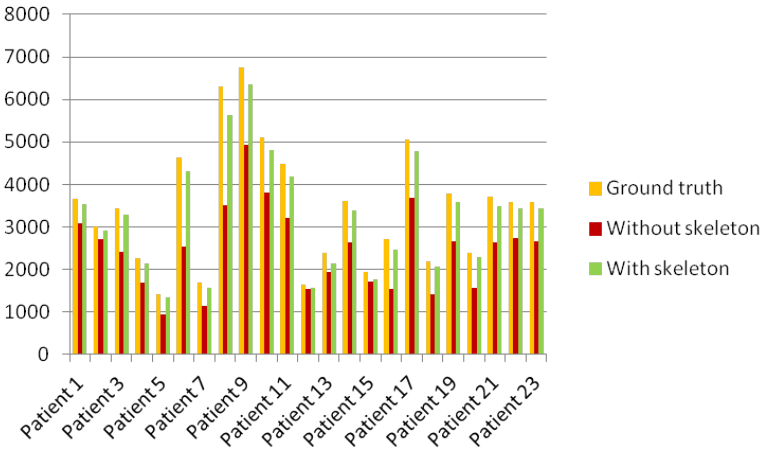

Figure 5.27.: Quantitative evaluation of the length of the vessel skeleton using intersection criterion (red) and with the new criterion added (green) [OLBPDW13]. Yellow shows the ground truth value, namely, the volume of the liver vasculature.

The minimum, maximum and mean values for both compared methods (with and without the skeleton based criterion) are shown in Table 5.9. Those values are obtained as the difference between the ground truth data and the values obtained after meshing. Qualitative evaluation is provided in Figure 5.28. The middle image shows the improvement that the new criterion means. Thanks to this improvement the green branches are

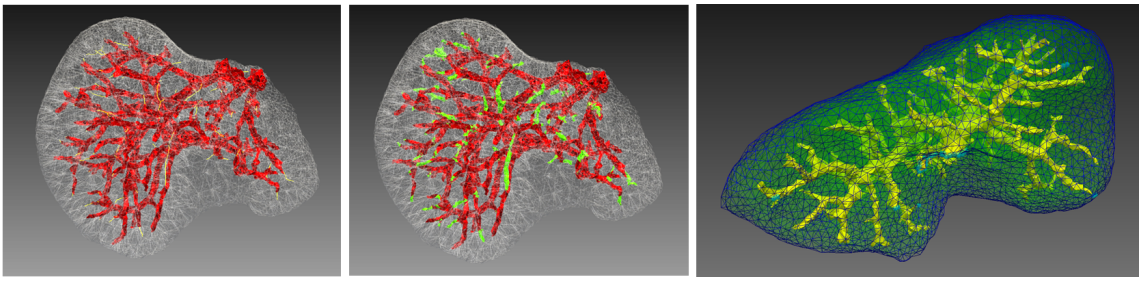

Figure 5.28.: Qualitative evaluation of the method [OLBPDW13]. Left: results without using the skeleton. Middle: Results using the skeleton. The green branches are added to the previous results. Right: Final result of the meshing in one patient. For visualization purposes only the liver and vasculature surfaces are shown.

	Without skeleton			With skeleton		
Metric	Max	Min	Mean	Max	Min	Mean
Volume (%)	25.6	1.3	15.9	16.8	3.5	11.6
Intersections (number)	500	108	232.91	266	27	79.96
Length (%)	44.9	5.4	27.3	10.7	3.4	6.1

Table 5.8.: Maximum, minimum and mean values for the compared methods and the three metrics used. The volume and lengths are given as the percentage of missing volume and length of the vessels compared to the ground truth.

not mislabeled anymore. The right image shows the final volumetric mesh of one patient.

5.5.3. Registration

The registration method has been evaluated in 25 clinical CT datasets. In the following paragraphs the characteristics of the datasets are described and the evaluation results are presented. Table 5.9 summarizes the characteristics of each dataset. In most of the cases the preoperatively gathered image has a better resolution in the z-axis than the post-operatively acquired one. The table points out which of the patients have been treated with radiofrequency ablation and which with tumor resection. In addition to this, the Coinoaud segments that are affected by the therapy are included in the table. 22 of the patients were treated with RF ablation, but in some of them additional factors increased the amount of the deformations visible in the organ. It is well known that there is still a high recurrence rate in patients treated for liver cancer. Patients 7, 8, 16, 21 and 22 are an example of that. Before the current RF ablation, a tumor was treated using resection techniques. There are several other patients that contain substantial fibrosis levels. This is another factor that greatly changes the shape of the liver.

Even though after tumor ablation the liver has undergone additional deformations, the size of the deformations are larger in the case of tumor resection. 4 pairs of datasets have been used for the evaluation of the registration in resected livers. The organs adjacent to the liver will exert pressures on the liver in different positions than those exerted in the preoperative image. Consequently, the liver shape will appear different than the

		Resolution (mm)			
Patient	Type	Pre	Post	Segments	Remarks
1	Ablation	1.25	4	6, 8	
2	Ablation	1	4	5, 7, 8	Fibrosis
3	Ablation	1	4	6, 7	
4	Ablation	1.25	5	1, 7	
5	Ablation	1.25	5	4a, 5, 8	
6	Ablation	1.25	5	6, 7, 8	Fibrosis
7	Ablation	1.25	4	3, 4a, 4b, 5	Resection (5)
8	Ablation	1	4	4a, 5	Resection (2,3)
9	Ablation	4	4	6, 7, 8	
10	Ablation	1.25	4	6, 8	
11	Ablation	1	4	5, 8	
12	Ablation	1	4	6, 7	
13	Ablation	1	4	2	
14	Ablation	1	4	4a, 5, 8	
15	Ablation	1	4	4a	Resection (4b,5,8) + Hypertrophy
16	Ablation	1.25	4		
17	Ablation	1	4	4a, 4b, 8	
18	Ablation	2.5	1.25	8	
19	Ablation	1.25	1.25	2	
20	Ablation	1.25	5	8	Resection (6,7)
21	Ablation	4	4	8	Resection (6,7)
22	Resection	2	0.7	4b	Noisy
23	Resection	0.7	2	6, 7	Resection (4b) + Biliom
24	Resection	6	5	6, 7	
25	Resection	5	5	6	

Table 5.9.: Characteristics of the 25 pairs of clinical CTs used for the evaluation: Type of intervention, resolution in the z axis of the pre- and postoperative acquisitions, treated segments.

preoperative one. Additional causes may further deform the organ. In the examples used within this thesis, one dataset contains a biliom. Nevertheless, the largest deformations can be observed when the liver has regrown. An effect known as hypertrophy. Another example of tumor recurrence can be observed with patients 22 and 23. These datasets belong to the same patient that some time after the first resection had to be treated again with the same technique. Thus, two resections are visible in patient 23.

Internal Accuracy The evaluation of registration methods is a challenging task. When the methods are tested on phantom data ground truth is available, but this is usually not the case with clinical data. To evaluate the internal accuracy of the results some authors propose to use landmarks previously selected by physicians [BDS*06, Bro10]. In this thesis the accuracy of the results inside the liver will also be evaluated using landmarks, namely, correspondences between the vessel trees. Therefore, an evaluation tool has been developed. The vessels from the registered image are segmented [Dre12]. Then both vessel trees (registered and postoperative) are visualized together with a series of

spheres located at bifurcation points along the vessel trees. An example of this is shown in Figure 5.29. The user should select as many landmarks as possible. Then euclidean distances between the selected landmark pairs are calculated.

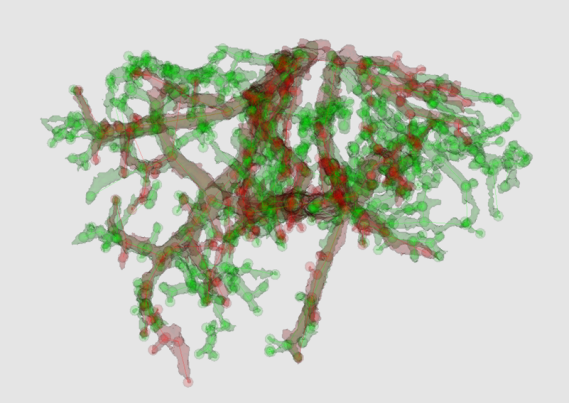

Figure 5.29.: Evaluation of internal accuracy.

Surface accuracy Since vessels are spread in the liver, the internal accuracy can also provide information about the general organ accuracy of the method. Nevertheless, the number of internal landmarks that can be detected during evaluation is not always high. Thus, it is desirable to find an additional metric that complements the previous one. Several metrics have been proposed for that purpose:

- Distances between surfaces
- Dice coefficient
- Volumetric overlap error

While those metrics were mainly designed for evaluation of segmentation results, they can also provide information regarding the accuracy of a registration method. In a perfect registration both livers should completely match, and consequently, there should not exist a volumetric overlap error. Nevertheless, this does not hold in the clinical scenario studied in this thesis. After tumor resection the preoperative and the postoperative livers do not share the same volume. Thus, another metric should be used that is appropriate for all studied cases. The positive predictive value (PPV) is a statistical measure to estimate the precision of a method:

$$PPV = \frac{tp}{tp + fp}. \tag{5.22}$$

The PPV is function of the true positives tp and the false positives fp (errors) of the resulting image. As it is shown in Figure 5.30, this measure can be used to estimate the accuracy of the results also after tumor resection, the area representing the true negatives is not considered in the calculations. The metrics mentioned before (e.g., Dice coefficient) would take into account the area of true negatives for the calculation. This would mean for the registration method that the surface at the resection should be stretched to match the opposite surface. This would result on low volumetric errors and distances, but the registration would not be correct.

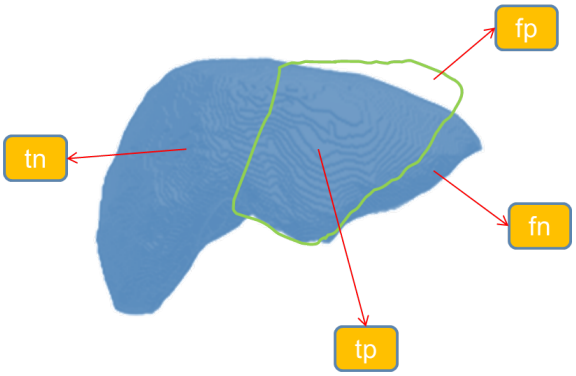

Figure 5.30.: Evaluation of external accuracy. tn: true negatives, tp: true positives, fp: false positives, fn: false negatives.

Registration results Table 5.10 summarizes the quantitative results of the registration method. These results contain the mean, maximum and minimum euclidean distances between selected landmarks as well as the number of landmarks that were used for the evaluation. A higher number of landmarks means that a larger area of the liver was covered by the evaluation, thus, as many landmarks as possible have been selected for each pair of datasets. The PPV has been evaluated before and after the surface refinement to estimate the effect of this step in the global accuracy of the method. The values show that improvements of up to 20 % (Patient 23) can be expected.

In addition to the quantitative evaluation, Figure 5.31 show the qualitative results for every pair of datasets. For each patient a slice containing the ablation/resection has been selected. The checkerboard visualization allows for a better evaluation of the accuracy of the method. In some cases the tumor is not visible in the preoperative image (blue circles in Figure 5.31). Thus, a multiphase registration [ESH*11] can be used as complement to the results of the pre/postoperative registration. The green circles show some examples of patients that underwent a tumor resection previous to the current RF ablation. Note that in those cases the surfaces should match since this resection is common to both the pre and postoperative images. The areas encircled in yellow, on the contrary, belong to new resections. Opposite to the previous case, the preoperative image does not contain this resection. Thus, a correct registration should show a jump between the preoperative and the postoperative images.

In Chapter 2 the multi-institution study by Brock [Bro10] was referenced. In this study 16 liver registration methods were compared. Therefore, liver datasets containing breathing deformations were used. Physicians selected internal landmarks (vessel bifurcations) that were then used to measure the accuracy of the results. Figure 5.32 shows a comparison of the results obtained in that study and the results obtained with the presented method. While this can serve to get an idea of the improvement of using internal and surface landmarks for the registration, it is important to note that the datasets tested in this chapter are not the same that those tested by [Bro10]. The images used by [Bro10] do not contain additional deformations like those observed after a surgery, presenting less difficulties than the studied within this chapter. Thus, the datasets used in the thesis are more challenging. The prove of this is that Brock et al. [BDS*06] achieve a mean

	Landmarks				PPV	
Patient	Mean (mm)	Max (mm)	Min (mm)	No.	Internal	Refinement
1	1.89	8.18	0.35	20	0.91	0.96
2	2.04	8.66	0.79	14	0.94	0.97
3	0.95	2.23	0.21	28	0.95	0.96
4	0.93	2.43	0.25	10	0.96	0.96
5	1.23	2.25	0.52	10	0.97	0.97
6	0.87	4.6	0.14	15	0.99	0.97
7	1.07	2.93	0.37	22	0.9	0.95
8	0.9	2.77	0.09	23	0.94	0.97
9	1.3	4.53	0.22	18	0.86	0.93
10	1.57	3.48	0.45	11	0.89	0.96
11	0.85	1.17	0.14	20	0.95	0.96
12	0.9	1.27	0.49	12	0.96	0.97
13	0.89	3.23	0.29	31	0.93	0.97
14	1.04	3.13	0.5	19	0.98	0.97
15	1.12	1.64	0.45	6	0.95	0.96
16	1.6	5.98	0.37	29	0.96	0.98
17	1.14	3.16	0.21	21	0.92	0.97
18	0.96	2.19	0.21	22	0.81	0.95
19	0.72	2.79	0.21	44	0.91	0.96
20	1.53	5.07	0.34	10	0.89	0.96
21	1.14	1.44	0.95	4	0.82	0.89
22	2.02	9.22	0.64	18	0.89	0.97
23	1.86	6.63	0.53	8	0.76	0.96
24	1.26	2.33	0.63	5	0.75	0.85
25	0.6	0.94	0.22	6	0.83	0.86
Average	1.22	3.71	0.38	17	0.9	0.95

Table 5.10.: Quantitative evaluation of the registration method. Mean, Max and Min refer to the mean, maximum and minimum distances between selected landmarks. No. are the number of landmarks detected in each pair of datasets. Two values of PPV are given the first one corresponds to the results after the initial registration and the second ones after surfaces refinement.

accuracy of 4.2 mm in the registration of pre and postoperative images and an accuracy of 2.3 mm in the multi-institutional study. This gives an idea of the increased difficulty of registering pre and postoperative images over datasets including uniquely breathing deformations.

5.6. Discussion

The quantitative results presented in the previous section represent an improvement over state of the art methods. In this section the results will be analyzed and discussed.

Boundary patches The detection method is able to correctly label all organs adjacent to the liver and as shown in Chapter 5 they serve to improve the accuracy of the registra-

tion method. Nevertheless, it has some limitations that will not influence the results of the registration method but are discussed in the following paragraphs for completeness and as ideas of future work in this field.

The evaluation of the organ detection method has shown its limitations in the areas near the connection between ribcage and lung and between lung and heart. A solution for this problem could be to use 20 as the number of sample points and apply a refinement to the results in the areas known as been problematic like the one near the ribcage. Alternatively, the number of sampled points could dynamically change depending on the direction of the normal to the surface.

The second limitation of the detection part is the mismatch of the spine. This could be improved by setting a threshold so that if the similarity between the histograms does not arrive to the threshold the spine is considered as not adjacent.

The detection of resections is a very challenging task due to their large variability. Chapter 5 contains detailed information about how different liver resections can look like. In general, differences can be observed due to:

- the size of the resection
- the appearance of the area where a part of the liver has been removed

When the resections are located in unusual places related to the organ detection (e.g., extended right hepatectomy), the thresholding proposed to detect non-adjacent spines could be helpful. Therefore, every organ candidate to be adjacent to the liver should have such a threshold. In presence of a extended right hepatectomy the ribcage would appear as non-adjacent organ, which would show the presence of a resection in that area. Nevertheless, this would not work in areas in which the expected adjacent organ remains adjacent after resection (e.g., resection of segment 3).

In addition to this, the resected area is not always occupied by adjacent organs. In some cases a biliom (see Chapter 5) appears in that area. The solution in that case could be to generate an image sample of bilioms and their correspondent histogram. This could be included in the detection process as new histogram for further comparisons. Yet, the billiom can be present anywhere around the liver.

Internal Landmarks For most of the patients the mean euclidean distance of the internal landmarks nears the average of 1.22 mm. There are some exceptions like patients 1, 2, 22 or 23. Those patients present a mean of 1.89, 2.04, 2.02 and 1.86 mm respectively. Those values are still lower than the 4.2 mm obtained by Brock et al. [BDS*06] for pre- and postoperative registration. Nevertheless, in comparison with the rest of the values achieved they are high.

Let's take Patient 1 as example to understand this value. It was shown in Figure 4.33 that in some cases the presented matching method detects certain matches that will be removed by the statistical outlier detection although they are correct. As consequence of this there will be parts of the liver that will not contain landmarks during the registration. The interaction features could be used to refine the results of the outlier detection with the corresponding increase in the accuracy that would be increased to 1.01 mm.

Figure 5.33 shows the results of the registration in the internal structures of six patients. The blue circles shows examples of the deformations that have been slightly mismatched due to the removal of correct matches as explained in the previous paragraphs.

Positive predictive value (PPV) The PPV shows the importance of enhancing the method with a surface refinement. After the refinement step of the method a precision of more than 92 % is achieved for almost all patients (except of three). The maximum improvement of the results thanks to the refinement can be observed in Patient 23 for which the precision increased in 20 % after refinement. Figure 5.34 shows the distances between postoperative and registered surfaces before and after refinement for three patients. The highest distances are represented by red colors. The first images correspond to Patient 23. As it was deduced from the quantitative evaluation the improvement for this patient after refinement (20 %) is visible. The next to images correspond to the datasets that provide the least accurate results: 85 % and 86 % of precision respectively. It can be observed that the most problematic areas are near to sharp edges of the liver. The incorporation of surface landmarks detected using the curvature as metric could improve the registration in those areas. Nevertheless, as explained in the methods, this would require an accurate outlier detector to avoid wrong landmarks.

5.7. Summary

In this chapter, rigid and deformable registration methods for pre- and postoperative CT images have been presented. The proposed methods incorporate the internal landmarks obtained with the methods proposed in Chapters 3 and 4 as well as landmarks on the surface of the liver. The latter are detected with a novel method proposed in this chapter. The results obtained with the proposed methods achieve a higher accuracy than several state of the art methods. This registration method is the basis of the outcome validation tool that is presented in the next chapter.

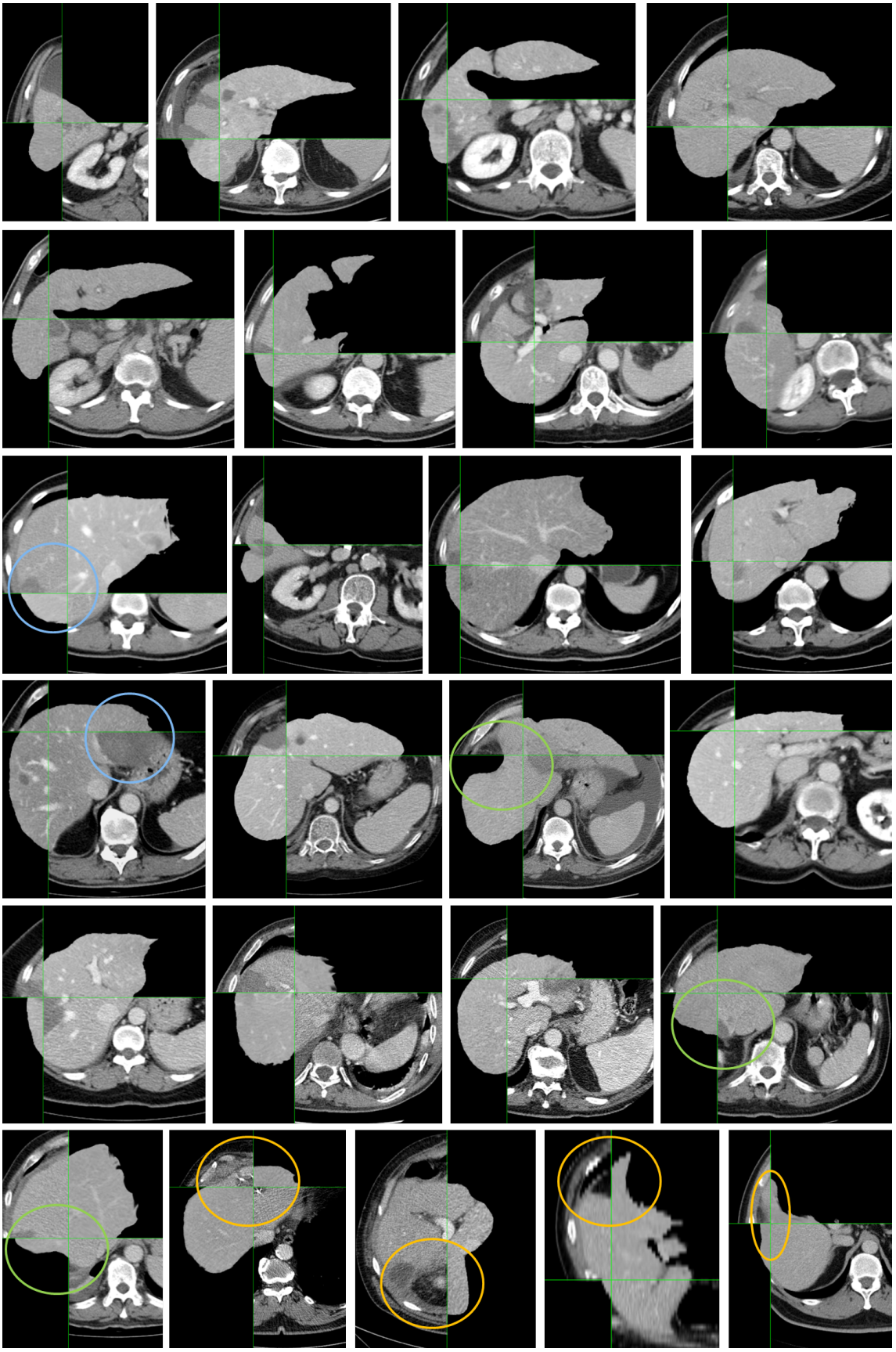

Figure 5.31.: Qualitative evaluation of the results. For every patient an slice in which the ablation/resection is visible has been selected.

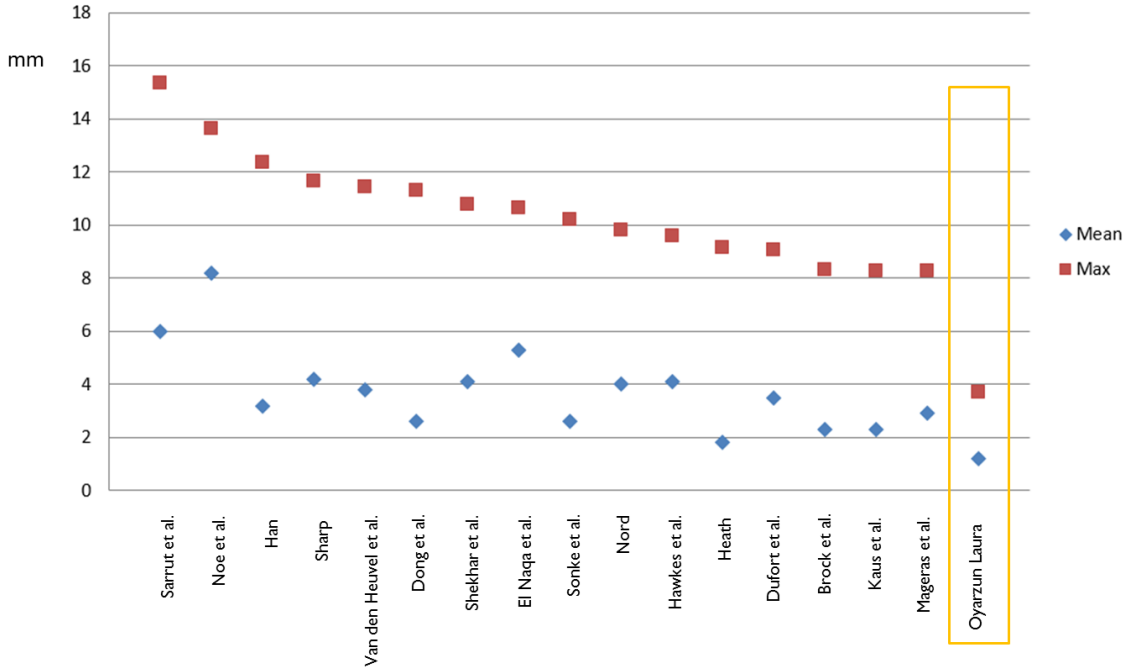

Figure 5.32.: Comparison of mean and maximum distances obtained with the methods proposed in this thesis (yellow rectangle) with the methods studied in [Bro10].

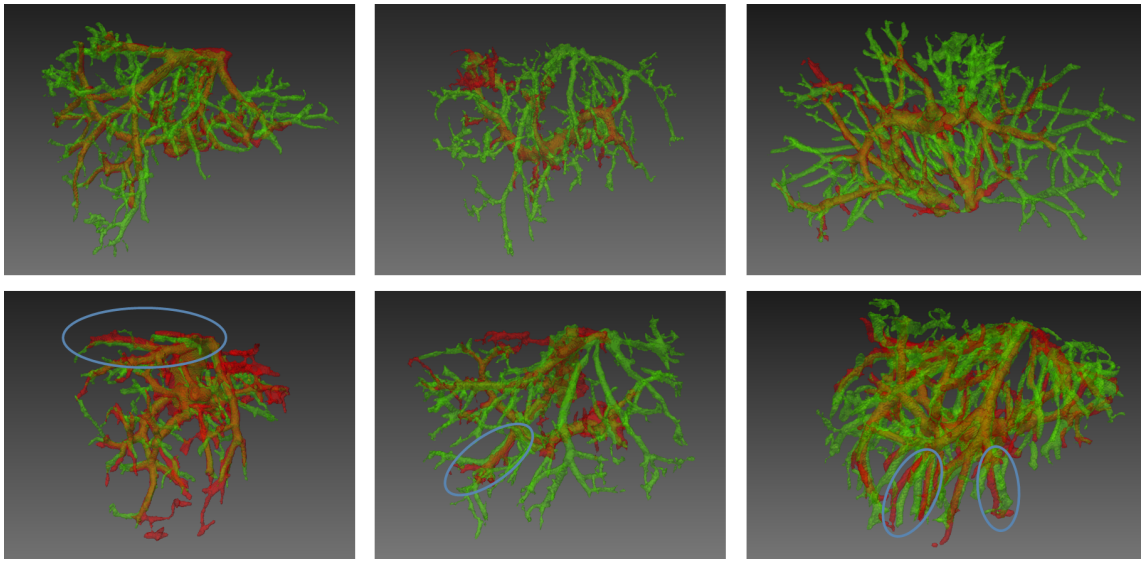

Figure 5.33.: Qualitative evaluation of the results in the internal structures in six patients. Blue circles show locations in which inaccuracies exist.

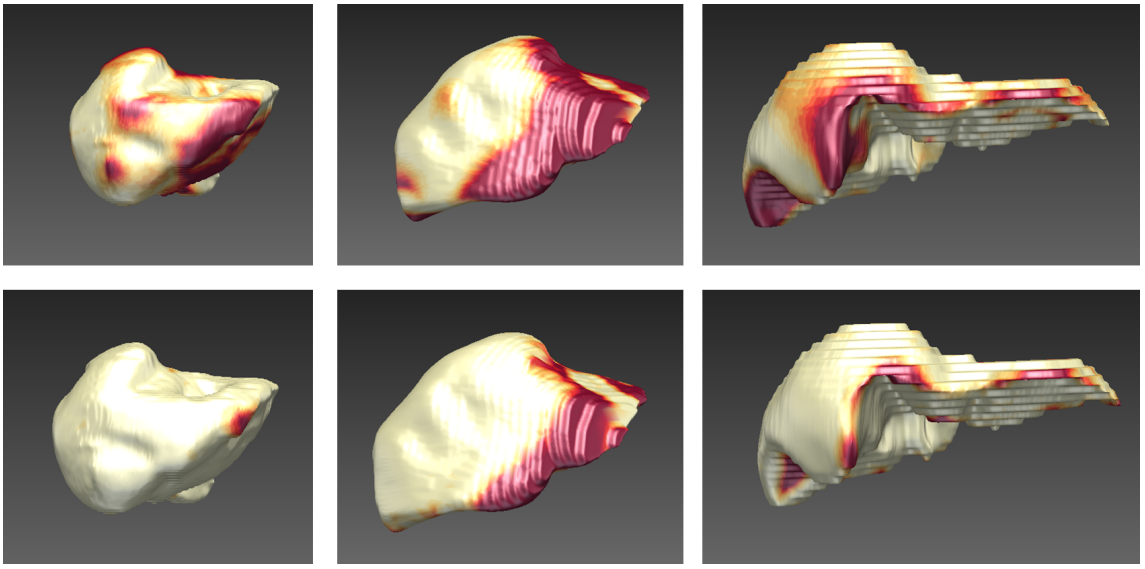

Figure 5.34.: Qualitative evaluation of the results with (bottom) and without (top) surface refinement in patients 23, 24 and 25. Red areas represent larger distances between the preoperative registered surface and the postoperative one.

6. Outcome validation

The goal of this chapter is to provide the physician with a tool for the assessment of liver interventions. In addition, the presented graph matching method can also be used in additional applications, e.g., intra-operative navigation. These applications will be described in the following chapter.

6.1. Outcome validation

The problem of tumor recurrence after RF ablation and tumor resection is well known. In order to reduce the recurrence rate it is necessary to ensure that after treatment all carcinogenic cells have been destroyed. Therefore, once the intervention has been carried out, the physician validates that the outcome of the intervention is satisfactory.

Surgery validation tools provide the physician with qualitative and quantitative measures to evaluated the outcome of the surgery. Two main approaches have been proposed for the validation of liver surgeries. A validation tool for the assessment after RF ablation has been presented by Rieder et al. [RWS*10]. The basis of their validation tool is a manual rigid registration of the images. They assign three different colors to the tumor surface: red to the residual part of the tumor, yellow to the part that has been ablated but has a distance to the necrosis surface smaller than the safety margin, and green to the area that is at least at a safety margin distance from the necrosis surface. In addition, they map the 3D view into a 2D tumor map. Visual inspection is important and so it is to provide the physician with measures that quantify the quality of the intervention results. To this end Passera et al. [PSS*13a] propose a series of volumetric calculations for the assessment of tumor coverage: residual tumor size, tumor free margin, inter-barycentric distance and orientation index. Besides, they visualize the structures of interest in a different way: the tumor in red, the necrosis in green and the safety margin in yellow. In spite of using non-rigid registration techniques as basis for their validation tool, they do not incorporate landmarks in the process. As it was shown in the evaluation of the previous chapter this reduces the achievable accuracy of the registration.

The application presented in this chapter does not only cover RF ablation, but also typical and atypical tumor resection. The assessment tool contains both qualitative and quantitative validation features as proposed by Passera et al. [PSS*13a]. Furthermore, the accuracy of the registration method proposed in this thesis makes the outcome validation tool introduced in this chapter more reliable than the aforementioned ones.

6.1.1. RF ablation

Figure 6.1 summarizes the cases that are covered by the application. A tumor can be completely or partially covered, and the same can happen with the safety margin. The

developed tool allows the physician to select a patient specific safety margin. Nevertheless, in general a safety margin of at least 1 cm is recommended. Thus, this value will be used for all images and tables in this chapter.

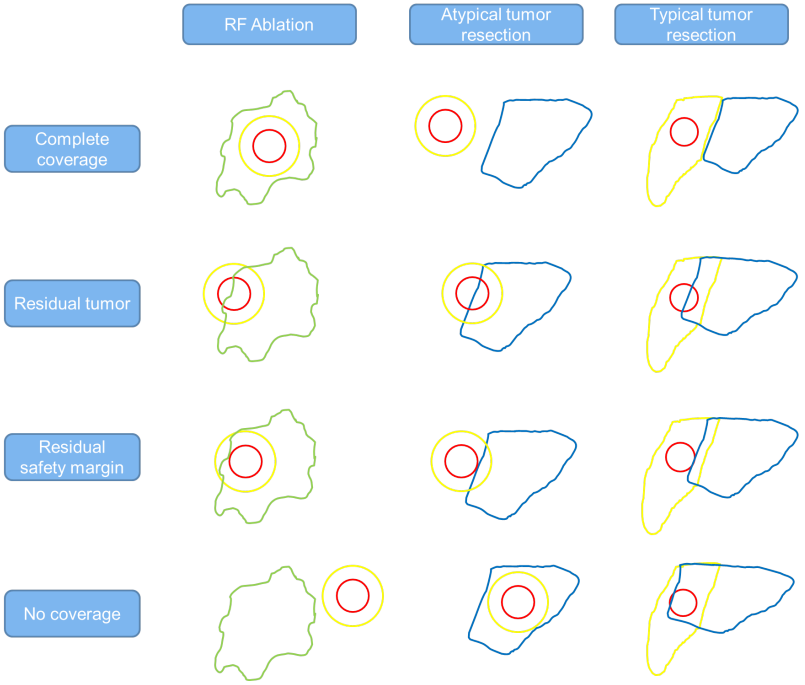

Figure 6.1.: Cases covered by the validation tool. Green: necrosis; Yellow: safety margin or Couinaud segment; Red: tumor; Blue: Liver remnant after resection.

Preprocessing The tumor and necrosis of interest are segmented using the interactive method by Steger and Sakas [SS12] including some manual interaction when needed. Then, the safety margin around the tumor is generated. Therefore, a distance map is calculated and those voxels that are within the safety margin radius selected by the physician are labeled as safety margin voxels.

The outcome validation tool supports the physician during qualitative validation of the surgery and provides him with the following volumetric calculations for assessment of the intervention:

- Tumor volume
- Residual tumor volume: part of the tumor not covered by the necrosis
- Necrosis volume
- Safety margin volume: volume of the margin excluding the tumor
- Residual margin volume: part of the safety margin inside the liver not covered by the necrosis

Figure 6.2 shows the visualization of the outcome validation tool in Patient 13. For this figure a margin of 1 cm around the tumor has been selected as described above. One can observe that a small part of the safety margin remains untreated.

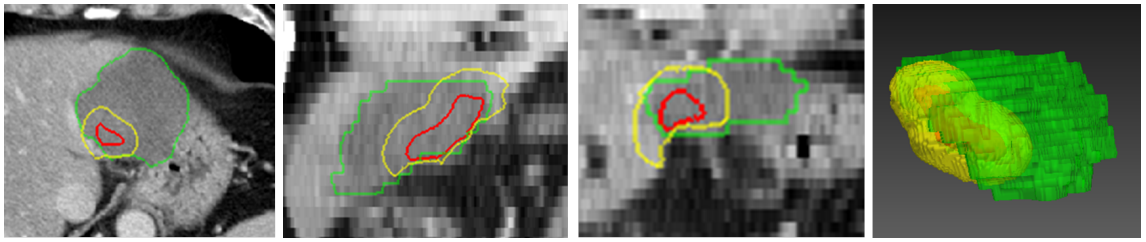

Figure 6.2.: Visualization of the outcome validation results of a RF ablation with a safety margin of 1 cm.

Patient	Tumor	Residual tumor	Necrosis	Safety margin	Residual safety margin
2	10.65	0.12	34.36	25.4	11.79
3	22.22	1.19	57.84	43.05	26.49
4	6.35	0.73	13.03	17.4	10.7
7	12.64	0.00	184.86	31.72	5.12
9	1.50	0.00	11.39	7.93	2.6
10	3.50	1.27	54.46	21.7	12.07
13	2.90	0.07	117.53	22.28	4.81
14	27.93	2.21	50.41	67.17	48.33
17	8.75	0.00	128.54	32.73	2.33
18	16.09	0.33	78.50	29.7	6.87
19	14.71	0.06	75.45	26.74	5.7
20	14.13	4.06	56.19	34.37	14.06

Table 6.1.: Quantitative validation of RF ablations. The presented volumes are given in cm^3.

The results of the quantitative assessment can be found in Table 6.1. One can observe that not all the patients are represented in the table, namely, 9 of the patients are missing. For those patients the tumors are not visible in the CT image acquired during portal phase, but in arterial phase. This is the reason for physicians to use both arterial and portal phase for diagnosis tasks. Hence the importance of multiphase registration techniques like the one presented by Erdt [Erd12]. Such an approach could be combined with the one presented in this thesis to incorporate the arterial phase in the solution.

Only in 25% of the cases the tumor has been completely removed. An additional 33.3% of the patients show a very small residual tumor ($< 0.5\ cm^3$). While this might be in part due to inaccuracies on the segmentations, it does also show that no safety margin was ablated in that area. Residual safety margins exist in every patient. The selected safety margin (1 cm) might not be appropriate for every patient. Thus, in some cases the physician might classify the intervention as satisfactory even if the margin is only partially covered. Nevertheless, the existence of residual tumors in at least 41.7% of the cases highlights the difficulties of the intervention process. The presented application serves the physician to decide if the patient needs further treatment to reduce the risk of tumor recurrence. In addition to this, planning tools like the one presented by Drechsler [Dre12] or intra-operative navigation solutions like the one presented by Keil [Kei13] can improve the outcome of liver surgeries.

6.1.2. Typical tumor resection

As explained in Chapter 5, typical tumor resection aims for the resection of complete Couinaud segments that contain carcinogenic cells. Thus, the goal of the outcome validation tool is to validate that the desired Couinaud segments have been resected. This can be done in combination with the planning tool developed by Drechsler [Dre12]. Thanks to this tool the physician can plan the surgery. The Couinaud segments obtained with that tool are the reference for the assessment of typical tumor resections.

Figure 6.1 shows the possible outcomes of a typical tumor resection. In addition to the volumetry calculations that were provided for validation of RF Ablation the physician will be provided with the residual Couinaud segments, in other words, the volume of the Couinaud segments that has not been resected. Only one dataset for typical tumor resection with a tumor visible in the portal phase is available. The quantitative validation of the surgery returns the following values:

- Tumor volume: 2.07
- Residual tumor volume: 0.00
- Safety margin volume: 372.80
- Residual safety margin: 40.23

Figure 6.3 shows visualization results in that datasets. Instead of the safety margin, the visualization shows the Couinaud segments in yellow and the postoperative liver surface in blue. Note that in this case the residual tumor will be determined by its intersection with the liver surface.

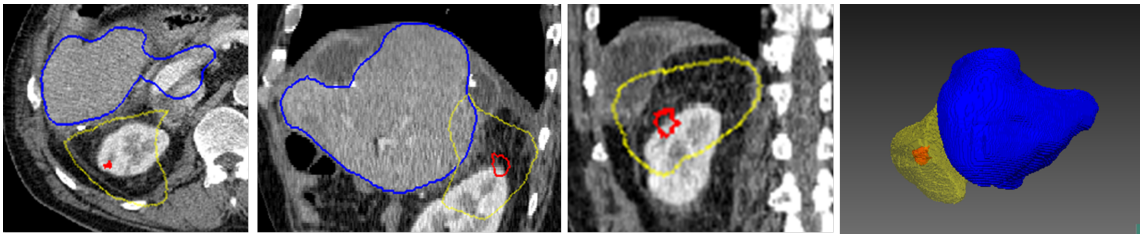

Figure 6.3.: Visualization of the outcome validation results of a typical resection surgery in which Couinaud segments 6 and 7 have been resected.

6.1.3. Atypical tumor resection

Finally, the physician can opt for an atypical tumor resection. In this case the tumor and a margin around it is resected instead of complete Couinaud segments. As shown in Figure 6.1 in the optimal case the tumor and its safety margin will lay completely outside the postoperative liver. Figure 6.4 shows the visualization results in Patient 24. One can observe that the resection fulfilled its goal and both tumor and safety margin were completely removed. This is corroborated by the quantitative measures returned by the validation tool:

- Tumor volume: 1.37
- Residual tumor volume: 0.00
- Safety margin volume: 23.67
- Residual safety margin: 0.00

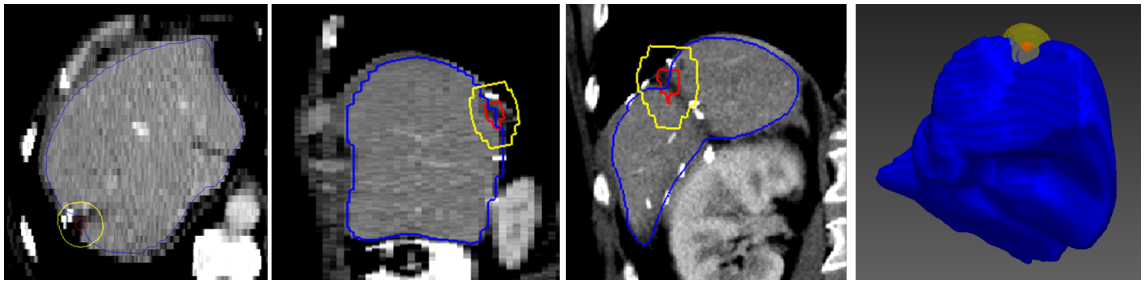

Figure 6.4.: Visualization of the outcome validation results of an atypical tumor resection with a safety margin of 1 cm.

6.2. Minimally invasive intra-operative navigation

As mentioned before, intra-operative navigation tools can improve the outcome of a surgery. Thanks to those applications the physician can plan a surgery using preoperatively acquired CT images and visualize this information during intervention. Similarly to the presented approach, the detection of correspondences between preoperative and intra-operative images can increase the accuracy of the registration needed in this applications. Even though during surgery ultrasound images are often used, there are physicians who prefer to used computer tomography images due their higher resolution.

6.2.1. CT

CT images are preferred by some physicians to ensure that the needle has been correctly placed inside the liver and that the ablation will take place in the correct area. In this sense a monomodal registration is desired. To this end, the methods proposed in this thesis can give accurate results. The additional constraint that have to be taken into account in the case of intervention is that the needles will introduce additional deformations on the liver. However, as the patient is still closed, the organ based surface refinement will correct those deformations.

6.2.2. US

A different registration approach is required when ultrasound images are used during intervention. Such a solution is presented by Keil [Kei13] who uses the graph to graph matching method proposed in this thesis for that application. During intervention efficiency is a crucial factor. Physicians need to have the two registered images (preoperative CT and intra-operative ultrasound) in not more than three minutes. In this case

the low execution time of the proposed matching method helps to speed up the whole process. In addition to this, the fact that no reference correspondences have to be preselected facilitate the process. The ultrasound images show usually a very small area of the vessel tree compared to the CT image. Often the area next to the root of the portal vein is not even visible in it. This makes the task of preselection of nodes needed in most of state of the art methods a hard and time consuming task. A thorough evaluation of the use of this method in such an application can be found in [Kei13].

6.3. Summary

In this chapter, an outcome validation tool has been presented. The basis for this outcome validation is the accurate registration method that was proposed in the previous chapter. This outcome validation tool provides the physician with qualitative and quantitative measures which increases the certainty of their decisions and can result in a decrease of the tumor recurrence rate.

7. Conclusions and Future Work

Cancer is one of the leading causes of death worldwide. Specific treatments are used to reduce this mortality rate. Nevertheless, tumor recurrence after treatment is not uncommon. One of the reasons for that is that not all carcinogenic cells are destroyed during intervention. To improve this, physicians do not destroy only the tumor, but also a safety margin around it. However, postoperative validation of the intervention often reveals only partially covered tumors as result of inaccurate size or location of the ablation/resection, and this is one of the reasons for the high tumor recurrence rate.

The goal of this thesis was to propose a method to support the physician during the outcome validation task after RF ablations and tumor resections.

7.1. Summary of results

This thesis has presented a surgery validation tool that supports physicians in the quantitative and qualitative evaluation of the outcome of an intervention. Therefore the tumor, necrosis/resection and safety margin are visualized in different colors and the volume of the (residual) tumor and (residual) safety margin are provided. Nevertheless, such a tool requires an accurate registration of the preoperative and postoperative liver CT images. Thus, this thesis has proposed a method for the registration of pre and postoperative CT images of the liver. In particular, patients treated with RF ablation and resection have been studied. The method has the novelty of incorporating both internal and external physical landmarks in a physics based registration method. The results confirmed the increased accuracy achieved using this combination.

Two methods have been proposed for the matching of internal landmarks. The first method consists of an efficient tree matching that allows the interaction of the physician to drive the matching. The second method is a fully automatic cyclic graph matching method. Those methods have shown its robustness not only for the cases studied in this thesis, but also to find correspondences between different modalities. The fact that the presented cyclic graph matching method does not require preselection of roots makes it useful during intervention, when time is a hard constraint.

In addition to the aforementioned methods two methods have been presented for the refinement of the resulting correspondences. The first method consist of a series of interaction features that facilitate the task of correction of matches. The second approach is an statistical outlier detection that automatically detects and removes false correspondences. The best results can be obtained using a combination of both approaches.

The detection of landmarks on the surface of the liver has been done by means of an automatic detector of boundary patches. Each boundary patch represent the organ that is adjacent to the liver at each surface point: heart, lung, ribcage, intestine, kidney, and spine.

In addition to the detection of internal and surface landmarks, two methods for the rigid registration of pre and postoperative CTs are presented. The first one solves the alignment problem in presence of non-contrast enhanced CT images. Nevertheless, in the proposed method internal landmarks are usually available and thus, they can be used to align both images. Finally, a physics based deformable registration method is presented for the final overlapping of both images. The required liver model is constructed using an adaptive volumetric mesh generator. The resulting mesh has an improvement of 22 % in presence of vessel narrowing over state of the art methods. A neo-Hookean hyperelastic model has been used to describe the behavior of the liver and FEM incorporating all detected correspondences have been proposed to carry out the final deformation. The method has been tested in 25 patients returning an mean internal accuracy of 1.2 mm and a positive predictive value of 0.95.

7.2. Future work

The presented outcome validation tool has been designed with the valuable comments of medical experts. The results look promising and the next step will be to carry out a thorough clinical evaluation and bring the tool into clinical practice.

While the presented methods for internal landmark detection have shown to be robust, a more robust outlier detection is thinkable. It has been shown that the presented statistical outlier detection does not perform optimally in presence of deformations. In some cases it removes from the final set of matches correspondences that were actually correct. Thus, a method able to detect areas with high deformations and detect outliers accordingly would be more robust. And idea to do so could be a branch- or region-wise outlier detector. This would allow to set different thresholds to areas with different deformation sizes.

In this thesis the registration of pre and postoperative CT images has been studied. In particular, a method able to handle large deformations has been presented. The graph matching method has also shown to be robust and efficient for intra-operative registration during minimally invasive interventions [Kei13]. Nevertheless, there is an additional clinical scenario that could take advantage of such a registration and was not focus of this thesis, namely, open liver surgery. As discussed in Chapter 2, most of state of the art methods carry out the registration using landmarks at the surface of the organ or intensity based methods. Registration methods developed for open liver surgery are not an exception for that. The registration method used by Peterhans et al. [PvBD*11] is driven by four landmarks that are manually selected on the liver's surface near the tumor. Kingham et al. [KSN*12] register CT and US images using salient anatomical features, e.g., the falciform ligament. Instead of using a single US acquisition for the registration Kleemann et al. [KDE*12] acquire a US scan of the complete liver that is then used for a surface registration of the preoperative and intra-operative livers. Rucker et al. [RWO*13, RWC*14] on the contrary, propose to use a laser-range scanned surfaces during intervention. Lange et al. [LPH*09] use a combined landmark and intensity based registration method to register preoperative CT with intra-operative US images acquired during intervention. Therefore, they manually select a series of landmarks along the vessel trees. However, it was shown

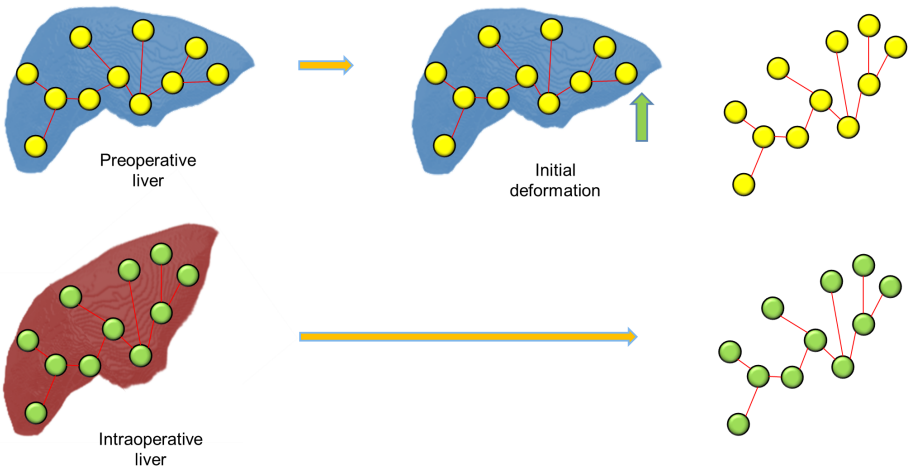

Figure 7.1.: Proposed approach for open liver surgery. The preoperative liver is initially deformed using FEM. The graph extracted after the initial deformation is matched to the intra-operative graph. The internal landmarks are used to increase the accuracy of the registration.

that manual selection of landmarks in minimal invasive surgery is a hard task. This task is even more challenging in open liver surgery when the deformations are much larger than those present during a minimal invasive intervention.

The difficulties to find correspondences between vessel trees increase together with the size of the deformations. The fact that only Lange et al. [LPH*09] proposed to use (manually detected) internal landmarks is a proof of this. Future work in this field could be based on a combination between the proposed method and some existing methods like the one by Kleemann et al. [KDE*12] or the one by Rucker et al. [RWC*14]. The preoperative liver could be initially deformed to fit the intra-operative surfaces using finite element methods. Once the preoperative liver is initially deformed its internal structures could be extracted (Figure 7.1). The vessel trees extracted at this point would have a similar orientation to those of the intra-operative ultrasound and could be matched using a method similar to the one proposed in this thesis.

While it was not focus of research in this thesis, the automatic segmentation of resected livers is still a challenge. Active shape models have been widely used for segmentation of complete livers [ESKW10]. Nevertheless, the variability of the liver's shape highly increase in presence of resections. Under those circumstances a model based segmentation might not be the most appropriate for those purpose. Current work focuses on the segmentation of resected livers using active contours to complete the pipeline presented in this thesis [OOLDW15].

A. Publications

The thesis is partially based on the following publications:

A.1. Publications

A.1.1. Edited proceedings

1. LINGURARU M. G., OYARZUN LAURA C., SHEKHAR R., WESARG S., GONZÁLEZ M. A., DRECHSLER K., SATO Y., ERDT M. (Eds.):. *Clinical Image-Based Procedures. From Planning to Intervention - International Workshop, CLIP 2014, Held in Conjunction with MICCAI 2014* (2015), vol. 8680 of *Lecture Notes in Computer Science*, Springer

2. ERDT M., LINGURARU M. G., OYARZUN LAURA C., SHEKHAR R., WESARG S., GÓNZALEZ M. A., DRECHSLER K. (Eds.):. *Clinical Image-Based Procedures. From Planning to Intervention - International Workshop, CLIP 2013, Held in Conjunction with MICCAI 2013* (2014), vol. 8361 of *Lecture Notes in Computer Science*, Springer

3. DRECHSLER K., ERDT M., LINGURARU M. G., OYARZUN LAURA C., SHARMA K., SHEKHAR R., WESARG S. (Eds.):. *Clinical Image-Based Procedures. From Planning to Intervention - International Workshop, CLIP 2012, Held in Conjunction with MICCAI 2012* (2013), vol. 7761 of *Lecture Notes in Computer Science*, Springer

A.1.2. Journals

1. OYARZUN LAURA C., DRECHSLER K.: Computer assisted matching of anatomical vessel trees. *Computers & graphics 35* (2011)

2. CHEN Y., DRECHSLER K., OYARZUN LAURA C., ZHAO W., Y. L.: A graph description and analysis framework of liver vascular system. *Journal of Computational Information Systems* (2011)

3. DRECHSLER K., OYARZUN LAURA C., CHEN Y., ERDT M.: Semi-automatic anatomical tree matching for landmark-based elastic registration of liver volumes. *Journal of Healthcare Engineering 1*, 1 (2010), 101–124

A.1.3. Conferences and workshops

1. OELMANN S., OYARZUN LAURA C., DRECHSLER K., WESARG S.: Active contour based segmentation of resected livers in CT images. In *SPIE Medical Imaging* (2015)

2. OYARZUN LAURA C., DRECHSLER K., WESARG S.: Two-step FEM-based liver-CT registration: Improving internal and external accuracy. In *SPIE Medical Imaging* (2014)

3. OYARZUN LAURA C., DRECHSLER K., WESARG S.: Anatomical discovery: finding organs in the neighborhood of the liver. In *XIII Mediterranean Conference on Medical and Biological Engineering and Computing* (2014)

4. DRECHSLER K., KNAUB A., OYARZUN LAURA C., WESARG S.: Liver segmentation in contrast enhanced MR datasets using a probabilistic active shape and appearance model. In *IEEE Computer-based medical systems* (2014)

5. KEIL M., KAISLER A., OYARZUN LAURA C., WESARG S.: Refinement and expansion of matched vessel graphs for intraoperative deformable registration of hepatic CT and ultrasound. In *SPIE Medical Imaging* (2013)

6. KEIL M., OYARZUN LAURA C., WESARG S.: Ultrasound B-mode segmentation for registration with CT in percutaneous hepatic interventions. In *MICCAI Workshop on Clinical Image-based Procedures: Translational Research in Medical Imaging* (2013)

7. DRECHSLER K., MEIXNER S., OYARZUN LAURA C., WESARG S.: A framework for validation of vessel segmentation algorithms. In *IEEE Computer-based medical systems* (2013)

8. DRECHSLER K., OYARZUN LAURA C., WESARG S.: Hepatic vein segmentation using wavefront propagation and multiscale vessel enhancement. In *SPIE Medical Imaging* (2013)

9. OYARZUN LAURA C., BUENO PLAZA P., DRECHSLER K.: Comparison of rigid registration methods in four clinical scenarios. In *MICCAI Workshop on Clinical Image-based Procedures: From Planning to Intervention* (2013)

10. OYARZUN LAURA C., BUENO PLAZA P., DRECHSLER K., WESARG S.: Skeleton based refinement of multi-material volumetric meshes. In *SPIE Medical Imaging* (2013)

11. OYARZUN LAURA C., DRECHSLER K., ERDT M., KEIL M., NOLL M., DE BENI S., SAKAS G., SOLBIATI L.: Intraoperative registration for liver tumor ablation. In *MICCAI Workshop on Computational and Clinical Applications in Abdominal Imaging* (2012), vol. 7029

12. ERDT M., OYARZUN LAURA C., DRECHSLER K., DE BENI S., SOLBIATI L.: Improving diagnosis and intervention: a complete approach for registration of liver CT data. In *Abdominal Imaging. Computational and Clinical Applications* (2012)

13. DRECHSLER K., OYARZUN LAURA C., WESARG S.: Interventional planning of liver resections: an overview. In *34th annual conference of the IEEE Engineering in Medicine and Biology Society* (2012)

14. DRECHSLER K., ERDT M., OYARZUN LAURA C., WESARG S.: Multiphase risk assessment of atypical liver resections. In *IEEE Computer-Based Medical Systems* (2012)

15. DRECHSLER K., OYARZUN LAURA C.: Simulation of portal vein clamping and the impact of safety margins for liver resection planning. In *Abdominal Imaging. Computational and Clinical Applications* (2012)

16. KEIL M., OYARZUN LAURA C., DRECHSLER K., WESARG S.: Combining B-mode and color flow vessel segmentation for registration of hepatic CT and ultrasound volumes. In *Eurographics Workshop on Visual Computing for Biology and Medicine* (2012)

17. OYARZUN LAURA C., DRECHSLER K.: Graph to graph matching: Facing clinical challenges. In *IEEE Computer-based medical systems* (2011)

18. OYARZUN LAURA C., DRECHSLER K.: Extracting anatomical landmarks of the liver vasculature using tree matching. In *Biomedical Engineering* (2011)

19. DRECHSLER K., OELMAN S., OYARZUN LAURA C.: Separation of interconnected hepatic veins. In *IEEE Computer-based medical systems* (2011)

20. DRECHSLER K., STROSCHE M., OYARZUN LAURA C.: Automatic ROI identification for fast liver tumor segmentation using graph-cuts. In *SPIE Medical Imaging* (2011)

21. DRECHSLER K., OYARZUN LAURA C.: Closing the gap: From planning to intervention in cardiology. In *Computer Vision, Imaging and Computer Graphics* (2011)

22. CHEN Y., DRECHSLER K., ZHAO W., OYARZUN LAURA C.: A thinning-based liver vessel skeletonization method. In *Internet Computing & Information Services* (2011)

23. CHEN Y., DRECHSLER K., ZHAO W., OYARZUN LAURA C.: Liver vessel tree generation based on skeletonization and graph representation. In *International Conference on Bioinformatics and Biomedical Engineering* (2011)

24. FRIEDL S., DRECHSLER K., OYARZUN LAURA C., KULESCHOW A., KONDRUWEIT M., T. W.: A holistic approach using multimodal image-data for the support of cardiac surgery interventions. In *Computer Assisted Radiology and Surgery* (2011)

25. OYARZUN LAURA C., DRECHSLER K.: Efficient globally optimal matching of anatomical trees of the liver. In *Eurographics Workshop on Visual Computing for Biology and Medicine* (2010)

26. DRECHSLER K., OYARZUN LAURA C.: Dimension reduction based on centroids for multimodal anatomical landmark-based 3D/2D registration of coronary angiograms. In *Proceedings of the International Conference on Information Visualization Theory and Applications* (2010), pp. 173–180

27. DRECHSLER K., OYARZUN LAURA C.: Comparison of vesselness functions for multiscale analysis of the liver vasculature. In *IEEE Information Technology and Applications in Biomedicine* (2010)

28. DRECHSLER K., OYARZUN LAURA C.: Hierarchical decomposition of vessel skeletons for graph creation and feature extraction. In *IEEE International Conference on Bioinformatics and Biomedicine* (2010), pp. 456–461

29. CHEN Y., OYARZUN LAURA C., DRECHSLER K.: Generation of a graph representation from three-dimensional skeletons of the liver vasculature. In *Biomedical Engineering and Informatics* (2009)

30. DRECHSLER K., OYARZUN LAURA C., SAKAS G.: Towards computer assisted cardiac catheterization-how 3D visualization supports it. In *International Joint Conference on Computer Vision, Imaging and Computer Graphics Theory and Applications* (2009)

31. DRECHSLER K., OYARZUN LAURA C.: Registration of cardiac ct data with coronary angiograms using digitally reconstructed radiographs. In *World Congress on Medical Physics and Biomedical Engineering* (2009)

B. Supervising Activities

The following list summarizes the student bachelor, diploma and master thesis supervised by the author. The results of these works were partially used as an input into the thesis.

B.1. Diploma and Master Thesis

1. OELMANN S.: *Adaptation and Comparison of Algorithms for the Segmentation of the Liver in CT Images after a partial Hepatectomy*. Master thesis, Hochschule Darmstadt, 2013

B.2. Bachelor Thesis

1. HABERSTICH T.: *Rigide Registrierung durch automatische Erkennung stark verformter Bereiche der Leber*. Bachelor thesis, Technische Universität Darmstadt, 2011

2. FUCHS R.: *Automatisierte Segmentierung von Strukturen im Bereich der Nasennebenhöhlen auf Basis von CT-Daten*. Bachelor thesis, Hochschule Darmstadt, 2015

C. Curriculum Vitae

Personal Data

Name	Cristina Oyarzun Laura
Birth date & place	04.02.1983 in Irún
Family status	Single
Nationality	Spanish

Education

2001 – 2007	Graduation in Telecommunications Engineering at University of Navarra in San Sebastián, Spain
1999 – 2000	High School at Pío Baroja, in Irún, Spain

Work Experience

2010 – Today	Researcher, Visual Healthcare Technologies, Fraunhofer-Institute for Computer Graphics Research IGD, Darmstadt, Germany
2008–2009	Guest researcher, Visual Healthcare Technologies, Fraunhofer-Institute for Computer Graphics Research IGD, Darmstadt, Germany

Bibliography

[AF11] ASHBURNER J., FRISTON K. J.: Diffeomorphic registration using geodesic shooting and Gauss-Newton optimisation. *NeuroImage 55*, 3 (2011), 954–967.

[AKH*08] ASBACH P., KLATT D., HAMHABER U., BRAUN J., SOMASUNDARAM R., HAMM B., SACK I.: Assessment of liver viscoelasticity using multifrequency MR elastography. *Magnetic Resonance in Medicine 60* (2008), 373–379.

[BASLM03] BRANZAN-ALBU A., SCHWARTZ J.-M., LAURENDEAU D., MOISAN C.: Integrating geometric and biomechanical models of a liver tumour for cryosurgery simulation. In *International Symposium on Surgery Simulation and Soft Tissue Modelling* (2003).

[BBGC10] BRUNON A., BRUYÈRE-GARNIER K., CORET M.: Mechanical characterization of liver capsule through uniaxial quasi-static tensile tests until failure. *Journal of Biomechanics 43* (2010), 2221–2227.

[BCG*00] BELGHITI J., CLAVIEN P. A., GADZIJEV E., GARDEN J. O., LAU W. Y., MAKUUCHI M., STRONG R. W.: The brisbane 2000 terminology of liver anatomy and resections. In *International Hepato Pancreato Biliary World Congress* (2000), vol. 2.

[BDB05] BENTREM D. J., DEMATTEO R. P., BLUMGART L. H.: Surgical therapy for metastatic disease to the liver. In *Annual Review of Medicine* (2005), vol. 56.

[BDS*06] BROCK K. K., DAWSON L. A., SHARPE M. B., MOSELEY D. J., JAFFRAY D. A.: Feasibility of a novel deformable image registration technique to facilitate classification, targeting, and monitoring of tumor and normal tissue. *International Journal of radiation oncology, biology, physics 64*, 4 (2006), 1245–54.

[Ben02] BENGOETXEA E.: *Inexact Graph Matching Using Estimation of Distribution Algorithms*. PhD thesis, Universidad del País Vasco, 2002.

[BGKM98] BAKIRCIOGLU M., GRENANDER U., KHANEJA N., MILLER M. I.: Curve matching on brain surfaces usinf frenet distances. *Human Brain Mapping 6* (1998), 329–333.

[BGP*13] BONNICI V., GIUGNO R., PULVIRENTI A., SHASHA D., FERRO A.: A subgraph isomorphism algorithm and its application to biochemical data. *BMC Bioinformatics 14* (2013).

[Bie53] BIENAYMÉ I. J.: Considérations ŕl'appui de la découverte de laplace. *Comptes rendus des Séances de l'Académie des Sciences 37* (1853), 309–324.

[BK07] BEG M., KHAN A.: Symmetric data attachment terms for large deformation image registration. *IEEE Transactions of Medical Imaging 26*, 9 (2007), 1179–1189.

[BL71] BOURGEOIS F., LASSALLE J.: An extension of the munkres algorithm for the assignment problem to rectangular matrices. *Communications of the ACM 14*, 12 (1971), 802–804.

[BLBP01] BENGOETXEA E., LARRAŃAGA P., BLOCH I., PERCHANT A.: Estimation of distribution algorithms: A new evolutionary computation approach for graph matching problems. In *Proceedings of the Third International Workshop on Energy Minimization Methods in Computer Vision and Pattern Recognition* (2001), vol. 2134, pp. 454–469.

[BLWH06] BÜLOW T., LORENZ C., WIEMKER R., HONKO J.: Point based methods for automatic bronchial tree matching and labeling. In *SPIE Medical Imaging* (2006), vol. 6143.

[BMTY05] BEG M. F., MILLER M. I., TROUVÉ A., YOUNES L.: Computing large deformation metric mappings via geodesic flows of diffeomorphisms. *International Journal of Computer Vision 61*, 2 (February 2005), 139–157.

[BnG96] BRO-NIELSEN M., GRAMKOW C.: Fast fluid registration of medical images. In *Visualization in Biomedical Computing* (1996), pp. 267–276.

[Boo89] BOOKSTEIN F. L.: Principal warps: Thin-plate splines and the decomposition of deformations. *IEEE Transactions on Pattern Analysis and Machine Intelligence 11*, 6 (1989), 567–585.

[BPHF10] BEUTHIEN B., PAPENBERG N., HELDMANN S., FISCHER B.: Volume-constrained image registration for pre- and post-operative ct liver data. In *SPIE Medical Imaging* (2010), vol. 7623.

[Bro10] BROCK K. K.: Results of a multi-institution deformable registration accuracy study (MIDRAS). *International Journal of Radiation Oncology Biology Physics 76*, 2 (2010), 583–596.

[BRS*03] BÖTTGER T., RUITER N. V., STOTZKA R., BENDL R., HERFARTH K. K.: Registration of CT and MRI volume data of the liver. In *Computer assisted radiology and surgery* (2003), vol. 1256, pp. 118–123.

[BTPB07] BOURDIN X., TROSSEILLE X., PETIT P., BEILLAS P.: *Comparison of tetrahedral and hexahedral meshes for organ finite element modeling: an application to kidney impact*. Tech. Rep. 07-0424, INRETS - LBMC (UMR_T9406 INRETS/UCBL1), 2007.

[BvLH*11] BREMM S., VON LANDESBERGER T., HESS M., SCHRECK T., WEIL P., HAMACHER K.: Interactive visual comparison of multiple trees. In *IEEE Symposium on Visual Analytics Science and Technology* (2011).

[BYB09a] BOLTCHEVA D., YVINEC M., BOISSONNAT J.-D.: Feature preserving delaunay mesh generation from 3D multi-material images. In *Eurographics Symposium on Geometry Processing* (2009), vol. 28, pp. 1455–1464.

[BYB09b] BOLTCHEVA D., YVINEC M., BOISSONNAT J.-D.: Mesh generation from 3D multi-material images. In *International Conference on Medical Image Computing and Computer Assisted Intervention* (2009), vol. 5762, pp. 283–290.

[CAM*05a] CHARNOZ A., AGNUS V., MALANDAIN G., FOREST C., TAJINE M., SOLER L.: Liver registration for the follow-up of hepatic tumors. *International Conference on Medical Image Computing and Computer Assisted Intervention 3750* (2005), 155–162.

[CAM*05b] CHARNOZ A., AGNUS V., MALANDAIN G., SOLER L., TAJINE M.: Tree matching applied to vascular system. *Graph-Based Representations in Pattern Recognition 3434* (2005), 183–192.

[CCD*08] CLEMENTS L. W., CHAPMAN W. C., DAWANT B. M., ROBERT L. GALLOWAY J., MIGA M. I.: Robust surface registration using salient anatomical features for image-guided liver surgery: Algorithm and validation. *Medical physics 35*, 6 (2008), 2528–2540.

[CDC*11] CLEMENTS L. W., DUMPURI P., CHAPMAN W. C., DAWANT B. M., GALLOWAY R. L., MIGA M. I.: Organ surface deformation measurement and analysis in open hepatic surgery: method and preliminary results from 12 clinical cases. *IEEE Transactions on Biomedical Engineering 58*, 8 (2011), 2280–2289.

[CDLW00] CARRILLO A., DUERK J. L., LEWIN J. S., WILSON D. L.: Semiautomatic 3-D image registration as applied to interventional MRI liver cancer treatment. *IEEE Transactions on Medical Imaging 19*, 3 (March 2000), 175–185.

[CDOL*11] CHEN Y., DRECHSLER K., OYARZUN LAURA C., ZHAO W., Y. L.: A graph description and analysis framework of liver vascular system. *Journal of Computational Information Systems* (2011).

[CDZOL11a] CHEN Y., DRECHSLER K., ZHAO W., OYARZUN LAURA C.: Liver vessel tree generation based on skeletonization and graph representation. In *International Conference on Bioinformatics and Biomedical Engineering* (2011).

[CDZOL11b] CHEN Y., DRECHSLER K., ZHAO W., OYARZUN LAURA C.: A thinning-based liver vessel skeletonization method. In *Internet Computing & Information Services* (2011).

[CFA08] CASTERA L., FORNS X., ALBERTI A.: Non-invasive evaluation of liver fibrosis using transient elastography. *Journal of Hepatology 48* (2008), 835–847.

[CFSV04] CONTE D., FOGGIA P., SANSONE C., VENTO M.: Thirty years of graph matching in pattern recognition. *International Journal of Pattern Recognition and Artificial Intelligence 18*, 3 (2004), 265–298.

[CJLG08] CHENGCHENG R., J. Z., LIMIN L., GUOGANG C.: Fast non-rigid image registration using viscous fluid model and b-spline. In *The 2nd International Conference on Bioinformatics and Biomedical Engineering, 2008* (2008), pp. 2450 – 2453.

[CKB03] CONTI F., KHATIB O., BAUR C.: Interactive rendering of deformable objects based on a filling sphere modeling approach. In *IEEE International Conference on Robotics & Automation* (2003), pp. 3716–3721.

[CLHC10] CHO S. H., LEE J. Y., HAN J. K., CHOI B. I.: Acoustic radiation force impulse elastography for the evaluation of focal solid hepatic lesions: preliminary findings. *Ultrasound in Medicine and Biology 36*, 2 (2010), 202–208.

[CLRS09] CORMEN T. H., LEISERSON C. E., RIVEST R. L., STEIN C.: *Introduction to Algorithms*. The MIT Press, 2009.

[CMS*05] CASH D. M., MIGA M. I., SINHA T. K., GALLOWAY R. L., CHAPMAN W. C.: Compensating for intraoperative soft-tissue deformations using incomplete surface data and finite elements. *IEEE Transactions on Medical Imaging 24*, 11 (2005), 1479–1491.

[CNPR*06] CORPECHOT C., NAGGAR A. E., POUJOL-ROBERT A., ZIOL M., WENDUM D., CHAZOUILLÈRES O., DE LÉDINGHEN V., DHUMEAUX D., MARCELLIN P., BEAUGRAND M., POUPON R.: Assessment of biliary fibrosis by transient elastography in patients with PBC and PSC. *Hepatology 43*, 5 (2006), 1118–1124.

[COLD09] CHEN Y., OYARZUN LAURA C., DRECHSLER K.: Generation of a graph representation from three-dimensional skeletons of the liver vasculature. In *Biomedical Engineering and Informatics* (2009).

[CR00] CHUI H., RANGARAJAN A.: A new algorithm for non-rigid point matching. In *IEEE Conference on Computer Vision and Pattern Recognition* (2000), vol. 2, pp. 44 – 51.

[CRC*12] CIFOR A., RISSER L., CHUNG D., ANDERSON E. M., SCHNABEL J. A.: Hybrid feature-based log-demons registration for tumour tracking in 2-D liver ultrasound images. In *International Symposium on Biomedical Imaging* (2012), pp. 724–727.

[CRM96] CHRISTENSEN G. E., RABBITT R. D., MILLER M. I.: Deformable templates using large deformation kinematics. *IEEE Transactions on Image Processing 5*, 10 (1996), 1435–1447.

[CSC*04] CASH D. M., SINHA T. K., CHEN C.-C., DAWANT B. M., CHAPMAN W. C., MIGA M. I., GALLOWAY R. L.: Identification of deformation using invariant surface information. In *SPIE Medical Imaging* (2004), vol. 5367, pp. 140–150.

[CSRK10] CRIMINISI A., SHOTTON J., ROBERTSON D. P., KONUKOGLU E.: Regression forests for efficient anatomy detection and localization in ct studies. In *Medical Computer Vision. Recognition Techniques and Applications in Medical Imaging* (2010), vol. 6533, pp. 106–117.

[CSS06] COUR T., SRINIVASAN P., SHI J.: Balanced graph matching. In *Advances in Neural Information Processing Systems* (2006).

[CTBN*08] CARTER T. J., TANNER C., BEECHEY-NEWMAN N., BARRATT D. C., HAWKES D.: Mr navigated breast surgery: Method and initial clinical experience. In *International Conference on Medical Image Computing and Computer Assisted Intervention* (2008), Metaxas D. N., Axel L., Fichtinger G., Székely G., (Eds.), vol. 5242 of *Lecture Notes in Computer Science*, Springer, pp. 356–363.

[CTH05] CARTER T. J., TANNER C., HAWKES D. J.: A comparison of linear and quadratic tetrahedral finite elements for image-guided surgery applications. In *MIAS-IRC* (2005).

[CWDP12] COMMOWICK O., WIEST-DAESSLÉ N., PRIMA S.: Block-matching strategies for rigid registration of multimodal medical images. In *International Symposium on Biomedical Imaging* (2012), pp. 700–703.

[CWH97] CROSS A. D. J., WILSON R. C., HANCOCK E. R.: Inexact graph matching using genetic search. *Pattern Recognition 30*, 6 (1997), 953–970.

[DA04] DELINGETTE H., AYACHE N.: Soft tissue modeling for surgery simulation. In *Computational Models for the Human Body*. 2004, pp. 453–550.

[DBB08] DAGON B., BAUR C., BETTSCHART V.: A framework for intraoperative update of 3D deformable models in liver surgery. In *30th Annual International Conference of the IEEE Engineering in Medicine and Biology Society* (2008), pp. 3235–3238.

[DCL*09a] DUMPURI P., CLEMENTS L. W., LI R., WAITE J. M., STEFANSIC J. D., GELLER D. A., MIGA M. I., DAWANT B. M.: Comparison of pre/post-operative CT iamge volumes to preoperative digitization of partial hepatectomies: a feasibility study in surgical validation. In *SPIE Medical Imaging* (2009), vol. 7261.

[DCL*09b] DUMPURI P., CLEMENTS L. W., LI R., WAITE J. M., STEFANSIC J. D., GELLER D. A., MIGA M. I., DAWANT B. M.: Comparison of pre/post-operative CT image volumes to preoperative digitization of partial hepatectomies: a feasibility study in surgical validation. In *SPIE Medical Imaging* (2009), vol. 7261.

[DEL*13] DRECHSLER K., ERDT M., LINGURARU M. G., OYARZUN LAURA C., SHARMA K., SHEKHAR R., WESARG S. (Eds.):. *Clinical Image-Based Procedures. From Planning to Intervention - International Workshop, CLIP 2012, Held in Conjunction with MICCAI 2012* (2013), vol. 7761 of *Lecture Notes in Computer Science*, Springer.

[DEOLW12] DRECHSLER K., ERDT M., OYARZUN LAURA C., WESARG S.: Multiphase risk assessment of atypical liver resections. In *IEEE Computer-Based Medical Systems* (2012).

[DHLH11] DARKNER S., HANSEN M. S., LARSEN R., HANSEN M. F.: Efficient hyper-elastic regularization for registration. In *Proceedings of the 17th Scandinavian conference on Image analysis* (2011), pp. 295–305.

[Dij59] DIJKSTRA E. W.: A note on two problems in connexion with graphs. *Numerische Mathematik 1*, 1 (1959), 269–271.

[DKFH97] DAVIS M., KHOTANZAD A., FLAMIG D., HARMS S.: A physics-based coordinate transformation for 3-D image matching. *IEEE Transactions on Medical Imaging 16*, 3 (1997), 317–28.

[DKOLW14] DRECHSLER K., KNAUB A., OYARZUN LAURA C., WESARG S.: Liver segmentation in contrast enhanced MR datasets using a probabilistic active shape and appearance model. In *IEEE Computer-based medical systems* (2014).

[DMOLW13] DRECHSLER K., MEIXNER S., OYARZUN LAURA C., WESARG S.: A framework for validation of vessel segmentation algorithms. In *IEEE Computer-based medical systems* (2013).

[DMVS02] D'AGOSTINO E., MAES F., VANDERMEULEN D., SUETENS P.: A viscous fluid model for multimodal non-rigid image registration using mutual information. In *International Conference on Medical Image Computing and Computer-Assisted Intervention* (2002), pp. 541–548.

[DOL09] DRECHSLER K., OYARZUN LAURA C.: Registration of cardiac ct data with coronary angiograms using digitally reconstructed radiographs. In *World Congress on Medical Physics and Biomedical Engineering* (2009).

[DOL10a] DRECHSLER K., OYARZUN LAURA C.: Comparison of vesselness functions for multiscale analysis of the liver vasculature. In *IEEE Information Technology and Applications in Biomedicine* (2010).

[DOL10b] DRECHSLER K., OYARZUN LAURA C.: Dimension reduction based on centroids for multimodal anatomical landmark-based 3D/2D registration of coronary angiograms. In *Proceedings of the International Conference on Information Visualization Theory and Applications* (2010), pp. 173–180.

[DOL10c] DRECHSLER K., OYARZUN LAURA C.: Hierarchical decomposition of vessel skeletons for graph creation and feature extraction. In *IEEE International Conference on Bioinformatics and Biomedicine* (2010), pp. 456–461.

[DOL11] DRECHSLER K., OYARZUN LAURA C.: Closing the gap: From planning to intervention in cardiology. In *Computer Vision, Imaging and Computer Graphics* (2011).

[DOL12] DRECHSLER K., OYARZUN LAURA C.: Simulation of portal vein clamping and the impact of safety margins for liver resection planning. In *Abdominal Imaging. Computational and Clinical Applications* (2012).

[DOLCE10] DRECHSLER K., OYARZUN LAURA C., CHEN Y., ERDT M.: Semi-automatic anatomical tree matching for landmark-based elastic registration of liver volumes. *Journal of Healthcare Engineering 1*, 1 (2010), 101–124.

[DOLS09] DRECHSLER K., OYARZUN LAURA C., SAKAS G.: Towards computer assisted cardiac catheterization-how 3D visualization supports it. In *International Joint Conference on Computer Vision, Imaging and Computer Graphics Theory and Applications* (2009).

[DOLW12] DRECHSLER K., OYARZUN LAURA C., WESARG S.: Interventional planning of liver resections: an overview. In *34th annual conference of the IEEE Engineering in Medicine and Biology Society* (2012).

[DOLW13] DRECHSLER K., OYARZUN LAURA C., WESARG S.: Hepatic vein segmentation using wavefront propagation and multiscale vessel enhancement. In *SPIE Medical Imaging* (2013).

[DOOL11] DRECHSLER K., OELMAN S., OYARZUN LAURA C.: Separation of interconnected hepatic veins. In *IEEE Computer-based medical systems* (2011).

[Dre12] DRECHSLER K.: *Extraction of Hepatic Veins in Contrast Enhanced CT with Application to Interventional Planning*. PhD thesis, Technische Universität Darmstadt, 2012.

[dSGMMH10] DOS SANTOS T. R., GERGEL I., MEINZER H., MAIER-HEIN L.: Fast correspondences search in anatomical trees. In *SPIE Medical Imaging* (2010), vol. 7623.

[DSOL11] DRECHSLER K., STROSCHE M., OYARZUN LAURA C.: Automatic ROI identification for fast liver tumor segmentation using graph-cuts. In *SPIE Medical Imaging* (2011).

[dSSMMH10] DOS SANTOS T. R., SEITEL A., MEINZER H., MAIER-HEIN L.: Correspondences search for surface-based intra-operative registration. In *International Conference on Medical Image Computing and Computer Assisted Intervention* (2010), vol. 6362, pp. 660–667.

[DTZ*10] DENG K., TIAN J., ZHENG J., ZHANG X., DAI X., XU M.: Retinal fundus image registration via vascular structure graph matching. *International Journal of Biomedical Imaging 2010* (2010).

[DVCL*06] DARKNER S., VESTER-CHRISTENSEN M., LARSEN R., NIELSEN C., PAULSEN R. R.: Automated 3D rigid registration of open 2D manifolds. In *MICCAI Workshop from statistical atlases to personalized models* (2006), pp. 19–22.

[EKB*12] EHRHARDT J., KRÜGER J., BISCHOF A., BARKHAUSEN J., HANDELS H.: Automatic correspondence detection in mammogram and breast tomosynthesis images. In *SPIE Medical Imaging* (2012), vol. 8314.

[ELOL*14] ERDT M., LINGURARU M. G., OYARZUN LAURA C., SHEKHAR R., WESARG S., GÓNZALEZ M. A., DRECHSLER K. (Eds.):. *Clinical Image-Based Procedures. From Planning to Intervention - International Workshop, CLIP 2013, Held in Conjunction with MICCAI 2013* (2014), vol. 8361 of *Lecture Notes in Computer Science*, Springer.

[EOLD*12] ERDT M., OYARZUN LAURA C., DRECHSLER K., DE BENI S., SOLBIATI L.: Improving diagnosis and intervention: a complete approach for registration of liver CT data. In *Abdominal Imaging. Computational and Clinical Applications* (2012).

[Erd12] ERDT M.: *Non-uniform deformable volumetric objects for medical organ segmentation and registration*. PhD thesis, Technische Universität Darmstadt, 2012.

[ESH*11] ERDT M., SAKAS G., HAMMON M., BENI S. D., SOLBIATI L., CAVALLARO A.: Automatic shape based deformable registration of multiphase contrast enhanced liver CT volumes. In *SPIE Medical Imaging* (2011).

[ESKW10] ERDT M., STEGER S., KIRSCHNER M., WESARG S.: Fast automatic liver segmentation combining learned shape priors with observed shape deviation. In *IEEE Computer-Based Medical Systems* (2010).

[ESW12] ERDT M., STEGER S., WESARG S.: Deformable registration of MR images using a hierarchical patch based approach with a normalized metric quality measure. In *International Symposium on Biomedical Imaging* (2012), pp. 1347–1350.

[Fan12] FAN W.: Graph pattern matching revised for social network analysis. In *International Conference on Database Theory* (2012), pp. 8–21.

[FC11] FOTEINOS P., CHRISOCHOIDES N.: High-quality multi-tissue mesh generation for finite element analysis. In *MeshMed, Workshop on Mesh Processing in Medical Image Analysis* (2011), pp. 18–28.

[FCVC05] FOUCHER J., CHANTELOUP E., VERGNIOL J., CASTÉRA L.: Diagnosis of cirrhosis by transient elastography (FibroScan): a prospective study. *Gut 55* (2005), 403–408.

[FDOL*11] FRIEDL S., DRECHSLER K., OYARZUN LAURA C., KULESCHOW A., KONDRUWEIT M., T. W.: A holistic approach using multimodal image-data for the support of cardiac surgery interventions. In *Computer Assisted Radiology and Surgery* (2011).

[FHI*06] FUJIOKA C., HORIGUCHI J., ISHIFURO M., KAKIZAWA H., KIGUCHI M., MATSUURA N., HIEDA M., TACHIKAKE T., ALAM F., FURUKAWA T., ITO K.: A feasibility study: Evaluation of radiofrequency ablation therapy to hepatocellular carcinoma using image registration of preoperative and postoperative ct. *Academic Radiology 13*, 8 (2006), 986–994.

[FPO*12] FERAGEN A., PETERSEN J., OWEN M., LO P., THOMSEN L. H., WILLE M. M. W., DIRKSEN A., DE BRUIJNE M.: A hierarchical scheme for geodesic anatomical labeling of airway trees. In *Medical Image Computing and Computer-Assisted Intervention* (2012), vol. 7512, pp. 147–155.

[FT87] FREDMAN M. L., TARJAN R. E.: Fibonacci heaps and their uses in improved network optimization algorithms. *Journal of the ACM 34*, 3 (1987), 596–615.

[FTGL04] FISCHER B., THIES C. J., GULD M. O., LEHMANN T. M.: Content-based image retrieval by matching hierarchical attributed region adjacency graphs. In *SPIE Medical Imaging* (2004), vol. 598.

[Fuc15] FUCHS R.: *Automatisierte Segmentierung von Strukturen im Bereich der Nasennebenhöhlen auf Basis von CT-Daten*. Bachelor thesis, Hochschule Darmstadt, 2015.

[Fun93] FUNG Y. C.: *Biomechanics Mechanical Properties of Living Tissues*. Springer, 1993.

[FWG*99] FERRANT M., WARFIELD S. K., GUTTMANN C. R. G., MULKERN R. V., JOLESZ F. A., KIKINIS R.: 3D image matching using a finite element based elastic deformation model. In *International Conference on Medical Image Computing and Computer Assisted Intervention* (1999), vol. 1679, pp. 202–209.

[Gal06] GALLAGHER B.: *The State of the Art in Graph-Based Pattern Matching*. Tech. Rep. UCRL-TR-220300, Lawrence Livermore National Laboratory, 2006.

[GDMR*06] GÓMEZ-DOMÍNGUEZ E., MENDOZA J., RUBIO S., MORENO-MONTEAGUDO J. A., GARCÍA-BUEY L., MORENO-OTERO R.: Transient elastography: a valid alternative to biopsy in patients with chronic liver disease. *Alimentary Pharmacology & Therapeutics 24* (2006), 513–518.

[GH06a] GRAHAM M. W., HIGGINS W. E.: Globally optimal model-based matching of anatomical trees. In *Medical Imaging* (2006), vol. 6144.

[GH06b] GRAHAM M. W., HIGGINS W. E.: Optimal graph-theoretic approach to 3d anatomical tree matching. *IEEE International Symposium on Biomedical Imaging* (2006), 109–112.

[GML*09] GIESEL F. L., MEHNDIRATTA A., LOCKLIN J., MCAULIFFE M. J., WHITE S., CHOYKE P. L., KNOPP M. V., WOOD B. J., HABERKORN U., VON TENGG-KOBLIGK H.: Image fusion using CT, MRI and PET for treatment planning, navigation and follow up in percutaneous rfa. *Experimental Oncology 31*, 2 (2009), 106–14.

[GR96] GOLD R., RANGARAJAN A.: A graduated assignment algorithm for graph matching. *IEEE Transactions of Pattern Analysis and Machine Intelligence 18*, 4 (April 1996), 377–388.

[Gra08] GRAHAM M. W.: *Robust methods for human airway-tree segmentation and anatomical-tree matching*. PhD thesis, The Pennsylvania State University, 2008.

[GWJS13] GUO Y., WU G., JIANG J., SHEN D.: Robust anatomical correspondence detection by hierarchical sparse graph matching. *IEEE Transactions on Medical Imaging 32*, 2 (2013), 268–277.

[GZN09] GROHER M., ZIKIC D., NAVAB N.: Deformable 2D-3D registration of vascular structures in a one view scenario. *IEEE Transactions on Medical Imaging 28*, 6 (2009), 847–860.

[Hab11] HABERSTICH T.: *Rigide Registrierung durch automatische Erkennung stark verformter Bereiche der Leber*. Bachelor thesis, Technische Universität Darmstadt, 2011.

[HEM*99] HARIS K., EFSTRATIADIS S. N., MAGLAVEROS N., GOURASSAS J., LOURIDAS G.: Model-based morphological segmentation and labeling of coronary angiograms. *IEEE Transactions on Medical Imaging 18*, 10 (1999), 1003–1015.

[HGWG12] HOSSBACH M., GREGORI J., WESARG S., GÜNTHER M.: Head motion compensation for arterial spin labeling using optical motion tracking. In *Workshop on Clinical Image-based Procedures: From Planning to Intervention* (2012).

[HGWG13] HOSSBACH M., GREGORI J., WESARG S., GÜNTHER M.: Design and analysis of a calibration-method for stereo-optical motion tracking in MRI. In *SPIE Medical Imaging* (2013), vol. 8668.

[HHM*11] HAN L., HIPWELL J., MERTZANIDOU T., CARTER T., MODAT M., OURSELIN S., HAWKES D.: A hybrid fem-based method for aligning prone and supine images for image guided breast surgery. In *IEEE International Symposium on Biomedical Imaging: From Nano to Macro* (2011).

[HHP*13] HAMPSHIRE T., HELBREN E., PLUMB A., ROTH H., HALLIGAN S., HAWKES D. J.: Spatial correspondence between prone and supine ct colonography images: Creating a reference standard. In *Abdominal Imaging* (2013), pp. 39–45.

[HHS*99] HERLINE A. J., HERRING J. L., STEFANSIC J. D., CHAPMAN W. C., GALLOWAY R. L., DAWANT B. M.: Surface registration for use in interactive image-guided liver surgery. *MICCAI 1999 1679* (September 1999), 892–899.

[HNV*06] HOLLENSTEIN M., NAVA A., VALTORTA D., SNEDEKER J., MAZZA E.: Mechanical Characterization of the Liver Capsule and Parenchyma. 2006, pp. 150–158.

[Hol00] HOLZAPFEL G. A.: *Nonlinear solid mechanics : a continuum approach for engineering*. Wiley, Chichester, New York, 2000. Réimpression avec corrections en 2001, 2004, 2005, 2007, 2008 et 2010.

[Hol08] HOLDEN M.: A review of geometric transformations for nonrigid body registration. *IEEE Transactions on Medical Imaging 27*, 1 (2008), 111–128.

[Hor87] HORN B. K. P.: Closed-form solution of absolute orientation using unit quaternions. *Journal of the Optical Society of America A 4*, 4 (1987), 629–642.

[HRH*11] HAMPSHIRE T., ROTH H., HU M., BOONE D., SLABAUGH G. G., PUNWANI S., HALLIGAN S., HAWKES D. J.: Automatic prone to supine haustral fold matching in ct colonography using a markov random field model. In *Medical Image Computing and Computer-Assisted Intervention* (2011), pp. 508–515.

[HRH*13] HAMPSHIRE T., ROTH H., HELBREN E., PLUMB A., BOONE D., SLABAUGH G. G., HALLIGAN S., HAWKES D. J.: Endoluminal surface registration for ct colonography using haustral fold matching. *Medical Image Analysis 17*, 8 (2013), 946–958.

[HRM*10] HU Y., RIJKHORST E.-J., MANBER R., HAWKES D., BARRATT D.: Deformable vessel-based registration using landmark-guided coherent point drift. In *MIAR* (2010).

[HSS*07] HUWART L., SEMPOUX C., SALAMEH N., JAMART J., ANNET L., SINKUS R., PEETERS F., TER BEEK L. C., HORSMANS Y., BEERS B. E. V.: Liver fibrosis: Noninvasive assessment with mr elastography versus aspartate aminotransferase–to-platelet ratio index. *Radiology 245*, 2 (2007), 458–466.

[HU13] HAMAMCI A., UNAL G.: Registration of brain tumor images using hyperelastic regularization. In *Computational Biomechanics for Medicine* (2013), pp. 101–114.

[Hum03] HUMPHREY J. D.: Review paper: Continuum biomechanics of soft biological tissues. In *Proceedings of the Royal Society of London* (2003), vol. 459, pp. 3–46.

[HVK*07] HILSMANN A., VIK T., KAUS M., FRANKS K., BISSONETTE J.-P., PURDIE T., BEZIAK A., AACH T.: Deformable 4DCT lung registration with vessel bifurcations. In *International Conference of Computer Assisted Radiology and Surgery* (2007).

[IPL*11] IM K., PIENAAR R., LEE J., CHOI J. S. Y. Y., LEE K. H., GRANT P. E.: Quantitative comparison and analysis of sulcal patterns using sulcal graph matching: a twin study. *NeuroImage 57* (2011), 1077–1086.

[JTT*11] JOHNSEN S., TAYLOR Z., THOMPSON S., HU M., GURUSAMY K., DAVIDSON B., HAWKES D., OURSELIN S.: Explicit FEM tissue simulation for surgical image-guidance. In *Living Imaging* (2011).

[KAR*06] KLATT D., ASBACH P., RUMP J., PAPAZOGLOU S., SOMASUNDARAM R., MODROW J., BRAUN J., SACK I.: In vivo determination of hepatic stiffness using steady-state free precession magnetic resonance elastography. *Investigative Radiology 41*, 12 (2006), 841–848.

[KD11] KOTSAS P. D., DODD T.: A review of methods for 2D/3D registration. *World Academy of Science, Engineering and Technology 59* (2011), 606–609.

[KDE*12] KLEEMANN M., DEICHMANN S., ESNAASHARI H., BESIREVIC A., SHAHIN O., BRUCH H.-P., LAUBERT T.: Laparoscopic navigated liver resection: Technical aspects and clinical practice in benign liver tumors. In *Case Reports in Surgery* (2012).

[Kei13] KEIL M.: *Ultraschallbasierte Navigation für die minimalinvasive onkologische Nieren- und Leberchirurgie*. PhD thesis, Technischen Universität Darmstadt, 2013.

[KHA*07] KLATT D., HAMHABER U., ASBACH P., BRAUN J., SACK I.: Noninvasive assessment of the rheological behavior of human organs using multifrequency MR elastography: a study of brain and liver viscoelasticity. *Physics in Medicine and Biology 52* (2007), 7281–7294.

[KHB*08] KASHANI R., HUB M., BALTER J. M., KESSLER M. L., DONG L., ZHANG L., XING L., XIE Y., HAWKES D., SCHNABEL J. A., MCCLELLAND J., JOSHI S., CHEN Q., LU W.: Objective assessment of deformable image registration in radiotherapy: A multi-institution study. *Medical Physics 35*, 12 (2008), 5944–5953.

[KKNN06] KAFTAN J. N., KIRALY A. P., NAIDICH D. P., NOVAK C. L.: A novel multipurpose tree and path matching algorithm with application to airway trees. *SPIE Medical Imaging 6143* (2006), 215–224.

[KKOLW13] KEIL M., KAISLER A., OYARZUN LAURA C., WESARG S.: Refinement and expansion of matched vessel graphs for intraoperative deformable registration of hepatic CT and ultrasound. In *SPIE Medical Imaging* (2013).

[KLK*11] KIM K. W., LEE J. M., KLOTZ E., KIM S. J., KIM S. H., KIM J. Y., HAN J. K., CHOI B. I.: Safety margin assessment after radiofrequency ablation of the liver using registration of preprocedure and postprocedure CT images. *American journal of roentgenology 196* (2011), 565–572.

[KLL07] KAINMUELLER D., LANGE T., LAMECKER H.: Shape constrained automatic segmentation of the liver based on a heuristic intensity model. In *MICCAI Workshop on 3D Segmentation in the Clinic: A Grand Challenge* (2007), pp. 109–116.

[KMQH*12] KUKLISOVA-MURGASOVA M., QUAGHEBEUR G., HAJNAL J. V., NOBLE J. A., SCHNABEL J. A.: Towards 3D registration of fetal brain MRI and ultrasound. In *IEEE International Symposium on Biomedical Imaging* (2012), pp. 346–349.

[Kob98] KOBBELT L.: Fairing by finite difference methods. In *Mathematical Methods for Curves and Surfaces* (1998).

[KOLDW12] KEIL M., OYARZUN LAURA C., DRECHSLER K., WESARG S.: Combining B-mode and color flow vessel segmentation for registration of hepatic CT and ultrasound volumes. In *Eurographics Workshop on Visual Computing for Biology and Medicine* (2012).

[KOLW13] KEIL M., OYARZUN LAURA C., WESARG S.: Ultrasound B-mode segmentation for registration with CT in percutaneous hepatic interventions. In *MICCAI Workshop on Clinical Image-based Procedures: Translational Research in Medical Imaging* (2013).

[KRS01] KOHLRAUSCH J., ROHR K., STIEHL H. S.: A new class of elastic body splines for nonrigid registration of medical images. In *Bildverarbeitung für die Medizin* (2001), vol. 36, pp. 164–168.

[KS80] KINDERMANN R., SNELL J. L.: *Markov Random Field and Their Applications*. American mathematical society, 1980.

[KSG01] KUMAR S., SALLAM M., GOLDGOF D.: Matching point features under small nonrigid motion. *Pattern Recognition 34* (2001), 2353–2365.

[KSN*12] KINGHAM T., SCHERER M., NEESE B., CLEMENTS L., STEFANSIC J., JARNAGIN W.: Image-guided liver surgery: intraoperative projection of computed tomography images utilizing tracked ultrasound. *HPB: the official journal of the International Hepato Pancreato Biliary Association 14* (2012), 594–603.

[KSP07] KLEIN S., STARING M., PLUIM J. P.: Evaluation of Optimization Methods for Nonrigid Medical Image Registration using Mutual Information and B-splines. *IEEE Transactions on Image Processing 16*, 12 (2007), 2879 – 2890.

[KW11] KIRSCHNER M., WESARG S.: Active shape models unleashed. In *SPIE Medical Imaging 2011* (2011), vol. 7962.

[LCL*08] LEPORÉ N., CHOU Y., LOPEZ O. L., AIZENSTEIN H. J., BECKER J. T., TOGA A. W., THOMPSON P. M.: Fast 3D fluid registration of brain magnetic resonance images. In *SPIE Medical Imaging* (2008), vol. 6916.

[LGPC11] LOMBAERT H., GRADY L., POLIMENI J. R., CHERIET F.: Fast brain matching with spectral correspondence. In *Information Processing in Medical Imaging* (2011), vol. 6801, pp. 660–673.

[LH05] LEORDEANU M., HEBERT M.: A spectral technique for correspondence problems using pairwise constraints. In *IEEE International Conference on Computer Vision* (2005), pp. 1482–1489.

[LKZ*08] LOHE T., KRÖGER T., ZIDOWITZ S., PEITGEN H., JIANG X.: Hierarchical matching of anatomical trees for medical image registration. In *International conference on Medical biometrics* (2008), pp. 224–231.

[LLF08] LEE H.-P., LIN M. C., FOSKEY M.: Physically-based validation of deformable medical image registration. In *International Conference on Medical Image Computing and Computer-Assisted Intervention* (2008), pp. 830–838.

[LMVS04] LOECKX D., MAES F., VANDERMEULEN D., SUETENS P.: Nonrigid image registration using free-form deformations with a local rigidity constraint. In *International Conference on Medical Image Computing and Computer Assisted Intervention* (2004), vol. 3216, pp. 639–646.

[LOLS*15] LINGURARU M. G., OYARZUN LAURA C., SHEKHAR R., WESARG S., GONZÁLEZ M. A., DRECHSLER K., SATO Y., ERDT M. (Eds.):. *Clinical Image-Based Procedures. From Planning to Intervention - International Workshop, CLIP 2014, Held in Conjunction with MICCAI 2014* (2015), vol. 8680 of *Lecture Notes in Computer Science*, Springer.

[LPH*09] LANGE T., PAPENBERG N., HELDMANN S., MODERSITZKI J., FISCHER B., LAMECKER H., SCHLAG P. M.: 3D ultrasound-CT registration of the liver using combined landmark-intensity information. *International Journal of Computer Assisted Radiology and Surgery 4*, 1 (2009), 79–88.

[LR10] LEE J., REEVES A. P.: Segmentation of individual ribs from low-dose chest CT. In *SPIE Medical Imaging* (2010).

[LRQG13] LIN X., RUAN S., QIU T., GUO D.: Nonrigid medical image registration based on mesh deformation constraints. *Computational and Mathematical Methods in Medicine 2013* (2013).

[LSR*10] LEE A. W. C., SCHNABEL J. A., RAJAGOPAL V., NIELSEN P. M. F., NASH M. P.: Breast image registration by combining finite elements and free-form deformations. In *International conference on Digital Mammography* (2010), pp. 736–743.

[LWRS09a] LANGE T., WÖRZ S., ROHR K., SCHLAG P. M.: Landmark-based 3D elastic registration of pre- and postoperative liver CT data. In *Bildverarbeitung für die Medizin* (2009).

[LWRS09b] LANGE T., WÖRZ S., ROHR K., SCHLAG P. M.: Landmark-based 3D elastic registration of pre- and postoperative liver CT data. In *Bildverarbeitung für die Medizin* (2009).

[LZZ*08] LING H., ZHOU S. K., ZHENG Y., GEORGESCU B., SÜHLING M., COMANICIU D.: Hierarchical, learning-based automatic liver segmentation. In *Computer Vision and Pattern Recognition* (2008).

[MBB08] MA F., BAJGER M., BOTTEMA M. J.: Temporal analysis of mammograms based on graph matching. In *Digital Mammography* (2008), pp. 158–165.

[MBZ13] MERIGGI F., BERTOCCHI P., ZANIBONI A.: Management of potentially resectable colorectal cancer liver metastases. *World Journal of Gastrointestinal Surgery 5*, 5 (2013), 138–145.

[MCS*02] MÄKELÄ T., CLARYSSE P., SIPILÄ O., PAUNA N., PHAM Q. C., KATILA T., MAGNIN I. E.: A review of cardiac image registration methods. *IEEE Transactions on Medical Imaging 21*, 9 (2002), 1011–1021.

[MHC*10] MARCHESSEAU S., HEIMANN T., CHATELIN S., WILLINGER R., DELINGETTE H.: Fast porous visco-hyperelastic soft tissue model for surgery simulation: Application to liver surgery. *Progress in Biophysics and Molecular Biology 103*, 2-3 (2010), 185–196.

[MHV*03] MATTES D., HAYNOR D. R., VESSELLE H., LEWELLEN T. K., EUBANK W.: PET-CT image registration in the chest using free-form deformations. *IEEE Transactions on Medical Imaging 22*, 1 (2003), 120–128.

[MJM06] MCLOUGHLIN J. M., JENSEN E. H., MALAFA M.: Resection of colorectal liver metastases: current perspectives. In *Cancer Control* (2006), vol. 13.

[MKS*07] METZEN J. H., KRÖGER T., SCHENK A., ZIDOWITZ S., PEITGEN H.-O., JIANG X.: Matching of tree structures for registration of medical images. *Graph-Based Representations in Pattern Recognition 4538* (2007), 13–24.

[MTY*07] MASUZAKI R., TATEISHI R., YOSHIDA H., SATO T., OHKI T., GOTO T., YOSHIDA H., SATO S., SUGIOKA Y., IKEDA H., SHIINA S., KAWABE T., OMATA M.: Assessing liver tumor stiffness by transient elastography. *Hepatology International 1* (2007), 394–397.

[MV98] MAINTZ J. B. A., VIERGEVER M. A.: A survey of medical image registration. *Medical Image Analysis 2*, 1 (1998), 1–36.

[MWTT98] MAUREL W., WU Y., THALMANN N. M., THALMANN D.: *Biomechanical Models for Soft Tissue Simulation*. Springer, 1998.

[NFN07] NICULESCU G., FORAN D. J., NOSHER J.: Non-rigid registration of the liver in consecutive CT studies for assessment of tumor response to radiofrequency ablation. In *Annual International Conference of the IEEE Engineering in Medicine and Biology Society* (2007), pp. 856–859.

[NKL*12] NAM W. H., KANG D.-G., LEE D., LEE J. Y., RA J. B.: Automatic registration between 3D intra-operative ultrasound and pre-operative CT images of the liver based on robust edge matching. *Physics in Medicine and Biology 57* (2012), 69–91.

[NNSF09] NICULESCU G., NOSHER J. L., SCHNEIDER M. D. B., FORAN D. J.: A deformable model for tracking tumors across consecutive imaging studies. *Journal of Computer Assisted Radiology and Surgery 4*, 4 (2009), 337–347.

[NTL*08] NOE K., TANDERUP K., LINDEGAARD J., GRAU C., SŘRENSEN T.: Gpu accelerated viscous-fluid deformable registration for radiotherapy. *Studies in Health Technology and Informatics 132* (2008).

[OBB*10] OU Y., BESBES A., BILELLO M., MANSOUR M., DAVATZIKOS C., PARAGIOS N.: Detecting mutually-salient landmark pairs with MRF regularization. In *IEEE International Symposium on Biomedical Imaging: From Nano to Macro* (2010), pp. 400–403.

[Oel13] OELMANN S.: *Adaptation and Comparison of Algorithms for the Segmentation of the Liver in CT Images after a partial Hepatectomy*. Master thesis, Hochschule Darmstadt, 2013.

[OLBPD13] OYARZUN LAURA C., BUENO PLAZA P., DRECHSLER K.: Comparison of rigid registration methods in four clinical scenarios. In *MICCAI Workshop on Clinical Image-based Procedures: From Planning to Intervention* (2013).

[OLBPDW13] OYARZUN LAURA C., BUENO PLAZA P., DRECHSLER K., WESARG S.: Skeleton based refinement of multi-material volumetric meshes. In *SPIE Medical Imaging* (2013).

[OLD10] OYARZUN LAURA C., DRECHSLER K.: Efficient globally optimal matching of anatomical trees of the liver. In *Eurographics Workshop on Visual Computing for Biology and Medicine* (2010).

[OLD11a] OYARZUN LAURA C., DRECHSLER K.: Computer assisted matching of anatomical vessel trees. *Computers & graphics 35* (2011).

[OLD11b] OYARZUN LAURA C., DRECHSLER K.: Extracting anatomical landmarks of the liver vasculature using tree matching. In *Biomedical Engineering* (2011).

[OLD11c] OYARZUN LAURA C., DRECHSLER K.: Graph to graph matching: Facing clinical challenges. In *IEEE Computer-based medical systems* (2011).

[OLDE*12] OYARZUN LAURA C., DRECHSLER K., ERDT M., KEIL M., NOLL M., DE BENI S., SAKAS G., SOLBIATI L.: Intraoperative registration for liver tumor ablation. In *MICCAI Workshop on Computational and Clinical Applications in Abdominal Imaging* (2012), vol. 7029.

[OLDW14a] OYARZUN LAURA C., DRECHSLER K., WESARG S.: Anatomical discovery: finding organs in the neighborhood of the liver. In *XIII Mediterranean Conference on Medical and Biological Engineering and Computing* (2014).

[OLDW14b] OYARZUN LAURA C., DRECHSLER K., WESARG S.: Two-step FEM-based liver-CT registration: Improving internal and external accuracy. In *SPIE Medical Imaging* (2014).

[OOLDW15] OELMANN S., OYARZUN LAURA C., DRECHSLER K., WESARG S.: Active contour based segmentation of resected livers in CT images. In *SPIE Medical Imaging* (2015).

[OT12] OLIVEIRA F. P. M., TAVARES J. M. R. S.: Medical image registration: a review. *Computer Methods in Biomechanics and Biomedical Engineering* (2012).

[PBC06] PHANG S. S., BOLES W. W., COLLINS M. J.: Tracking iris surface deformation using elastic graph matching. In *Twenty-first International Conference, Image and Vision Computing New Zealand* (2006).

[PEY*11] PACE D., ENQUOBAHRIE A., YANG H., AYLWARD S., NIETHAMMER M.: Deformable image registration of sliding organs using anisotropic diffusive regularization. *International Symposium on Biomedical Imaging* (03 2011), 407–413.

[PGC*11] PAULY O., GLOCKER B., CRIMINISI A., MATEUS D., MÖLLER A. M., NEKOLLA S., NAVAB N.: Fast multiple organ detection and localization in

whole-body MR dixon sequences. In *International Conference on Medical Image Computing and Computer-assisted Intervention* (2011), pp. 239–247.

[Pin13] PINHEIRO M. A.: Graph and point cloud registration for tree-like structures:survey and evaluation. In *International Student Conference on Electrical Engineering* (2013).

[PMV03] PLUIM J. P. W., MAINTZ J. B. A., VIERGEVER M. A.: Mutual-information-based registration of medical images: A survey. *IEEE Transactions on Medical Imaging 22*, 8 (2003), 986–1004.

[PNA11] PACE D., NIETHAMMER M., AYLWARD S.: Sliding geometries in deformable image registration. In *Abdominal Imaging. Computational and Clinical Applications* (2011), vol. 14, pp. 141–48.

[PSB*07] PONS J. P., SÉGONNE F., BOISSONNAT J. D., RINEAU L., YVINEC M., KERIVEN R.: High-quality consistent meshing of multi-label datasets. In *International conference on Information processing in medical imaging* (2007), vol. 20, pp. 198–210.

[PSS*13a] PASSERA K. M., SELVAGGI S., SCARAMUZZA D., GARBAGNATI F., VERGNAGHI D., MAINARDI L. T.: Radiofrequency ablation of liver tumors: quantitative assessment of tumor coverage through CT image processing. *BMC Medical Imaging 13* (2013), 3.

[PSS*13b] PINHEIRO M. A., SZNITMAN R., SERRADELL E., KYBIC J., MORENO-NOGUER F., FUA P.: Active testing search for point cloud matching. In *Information Processing in Medical Imaging* (2013), pp. 572–583.

[PSZ99] PELILLO M., SIDDIQI K., ZUCKER S. W.: Matching hierarchical structures using association graphs. *IEEE Transactions on Pattern Analysis and Machine Intelligence 21*, 11 (1999), 1105–1119.

[PvBD*11] PETERHANS M., VOM BERG A., DAGON B., INDERBITZIN D., BAUR C., CANDINAS D., WEBER S.: A navigation system for open liver surgery: design, workflow and first clinical applications. *The international journal of medical robotics and computer assisted surgery 7* (2011), 7 – 16.

[RB01] RAHM E., BERNSTEIN P. A.: A survey of approaches to automatic schema matching. *The International Journal on Very Large Data Bases 10* (2001), 334–350.

[RBNF07] RUSKÓ L., BEKES G., NÉMETH G., FIDRICH M.: Fully automatic liver segmentation for contrast-enhanced CT images. In *MICCAI Workshop on 3D segmentation in the clinic* (2007), pp. 143–150.

[RCC*08] ROULOT D., CZERNICHOW S., CLÉSIAU H. L., COSTES J., VERGNAUD A., BEAUGRAND M.: Liver stiffness values in apparently healthy subjects:

Influence of gender and metabolic syndrome. *Journal of Hepatology 48* (2008), 606–613.

[RCLW12] ROLFF H. C., CALATAYUD D., LARSEN P. N., WETTERGREN A.: Good results after repeated resection for colorectal liver metastases. *Danish Medical Journal 59*, 2 (2012).

[RCRMOZ04] ROHLFING T., CALVIN R. MAURER J., O'DELL W. G., ZHONG J.: Modeling liver motion and deformation during the respiratory cycle using intesity-based nonrigid registration of gated MR images. *Medical Physics 31*, 3 (2004), 427–432.

[RFS99] ROHR K., FORNEFETT M., STIEHL H. S.: Approximating thin-plate splines for elastic registration: Integration of landmark errors and orientation attributes. *Information Processing in Medical Imaging 1613* (1999), 252–265.

[RHMS12] RISSER L., HEINRICH M. P., MATIN T. N., SCHNABEL J. A.: Piecewise-diffeomorphic registration of 3D CT/MR pulmonary images with sliding conditions. In *International Symposium on Biomedical Imaging* (2012), pp. 1351–1354.

[RLNN07] RHEE T., LEWIS J. P., NEUMANN U., NAYAK K.: Soft-tissue deformation for in-vivo volume animation. In *Pacific Graphics* (2007), pp. 435–438.

[RLNN08] RHEE T., LEWIS J. P., NAYAK K., NEUMANN U.: Adaptive non-rigid registration of 3D knee MRI in different pose spaces. In *IEEE International Symposium on Biomedical Imaging* (2008), pp. 1111–1114.

[RMPO*02] RIVIÈRE D., MANGIN J.-F., PAPADOPOULOS-ORFANOS D., MARTINEZ J.-M., FROUIN V., RÉGIS J.: Automatic recognition of cortical sulci of the human brain using a congregation of neural networks. *Medical Image Analysis 6* (2002), 7792.

[Ro06] RAMOS A., OES J. S.: Tetrahedral versus hexahedral finite elements in numerical modelling of the proximal femur. *Medical Engineering & Physics 28* (2006), 916–924.

[RPD09] ROY A. S., PATIL U., DAS B.: Non-rigid registration framework for bronchial tree labeling using robust point matching. In *SPIE Medical Imaging* (2009), vol. 7259.

[RSH*99] RUECKERT D., SONODA L. I., HAYES C., HILL D. L. G., LEACH M. O., HAWKES D. J.: Nonrigid registration using free-form deformations: Application to breast MR images. *IEEE Transactions on Medical Imaging 18*, 8 (1999), 712–721.

[RSS*01] ROHR K., STIEHL H. S., SPRENGEL R., BUZUG T. M., WEESE J., KUHN M. H.: Landmark-based elastic registration using approximating thin-plate splines. *IEEE Transactions on Medical Imaging 20*, 3 (2001), 526–534.

[RW02] RAYMOND J. W., WILLETT P.: Maximum common subgraph isomorphism algorithms for the matching of chemical structures. *Journal of Computer-Aided Molecular Design 16* (2002), 2002.

[RWC*14] RUCKER D. C., WU Y., CLEMENTS L. W., ONDRAKE J. E., PHEIFFER T. S., SIMPSON A. L., JARNAGIN W. R., MIGA M. I.: A mechanics-based nonrigid registration method for liver surgery using sparse intraoperative data. *IEEE Transactions on Medical Imaging 33* (2014), 2014.

[RWO*13] RUCKER D. C., WU Y., ONDRAKE J. E., PHEIFFER T. S., SIMPSON A. L., MIGA M. I.: Nonrigid liver registration for image-guided surgery using partial surface data: a novel iterative approach. In *SPIE Medical Imaging* (2013).

[RWS*10] RIEDER C., WEIHUSEN A., SCHUMANN C., ZIDOWITZ S., PEITGEN H.-O.: Visual support for interactive post-interventional assessment of radiofrequency ablation therapy. *Computer Graphics Forum 29*, 3 (2010), 1093–1102.

[RWS*12] RIEDER C., WIRTZ S., STREHLOW J., ZIDOWITZ S., BRUNERS P., ISFORT P., MAHNKEN A. H., PEITGEN H.-O.: Automatic alignment of pre- and post-interventional liver CT images for assessment of radiofrequency ablation. In *SPIE Medical Imaging* (2012).

[RYD*06] ROUVIÈRE O., YIN M., DRESNER M. A., ROSSMAN P. J., BURGART L. J., FIDLER J. L., EHMAN R. L.: MR elastography of the liver: Preliminary results. *Radiology (RSNA) 240*, 2 (2006), 440–448.

[SAC*12] SERAG A., ALJABAR P., COUNSELL S. J., BOARDMAN J. P., HAJNAL J. V., RUECKERT D.: LISA: Longitudinal image registration via spatio-temporal atlases. In *International Symposium on Biomedical Imaging* (2012), pp. 334–337.

[SB94] SALLAM M., BOWYER K. W.: Registering time sequences of mammograms using a two-dimensinal image unwarping technique. In *Proceedings of the Second International Workshop on Digital Mammography* (1994), pp. 121–130.

[SBC*08] SÖHN M., BIRKNER M., CHI Y., WANG J., DI Y., BERGER B., ALBER M.: Model-independent, multimodality deformable image registration by local matching of anatomical features and minimization of elastic energy. *Medical Physics 35*, 3 (2008), 866–878.

[SBK10] SMEETS D., BRUYNINCKX P., KEUSTERMANS J.: Robust matching of 3D lung vessel trees. In *Workshop on pulmonary image analysis* (2010), pp. 61–70.

[SDP12] SOTIRAS A., DAVATAZIKOS C., PARAGIOS N.: *Deformable Medical Image Registration: A Survey*. Tech. Rep. 7919, INRIA, 2012.

[Sed83] SEDGEWICK R.: *Algorithms*. Boston: Addison-Wesley Publishing Company, Inc, 1983.

[SEW*03] STIPPEL G., ELLSMERE J., WARFIELD S. K., WELLS W. S. M., PHILIPS W.: A new technique for multi-modal 3D image registration. *Biomedical Image Registration 2717* (2003), 244–253.

[SGG*12] SILESS V., GLAUNES J., GUEVARA P., MANGIN J., POUPON C., BIHAN D. L., THIRION B., FILLARD P.: Joint T1 and brain fiber Log-Demons registration using currents to model geometry. In *International Conference on Medical Image Computing and Computer Assisted Intervention* (2012), pp. 57–65.

[SGK*12] SERRADELL E., GLOWACKI P., KYBIC J., MORENO-NOGUER F., FUA P.: Robust non-rigid registration of 2D and 3D graphs. In *IEEE International Conference on Computer Vision and Pattern Recognition* (2012), pp. 996 – 1003.

[Sin64] SINKHORN R.: A relationship between arbitrary positive matrices and doubly stochastic matrices. *The Annals of Mathematical Statistics 35*, 2 (1964), 876–879.

[SK10] STEGER S., KEIL M.: Automated initialization and region of interest detection for successful head registration of truncated CT/MR head & neck images. In *IEEE International Conference on Information Technology and Applications in Biomedicine* (2010).

[SKH*12] SMEETS D., KEUSTERMANS J., HERMANS J., VANDERMEULEN D., SUETENS P.: Feature-based piecewise rigid registration in 2-D medical images. In *International Symposium on Biomedical Imaging* (2012), pp. 696–699.

[SKMNF12] SERRADELL E., KYBIC J., MORENO-NOGUER F., FUA P.: Robust elastic 2D/3D geometric graph matching. In *SPIE Medical Imaging* (2012), vol. 8314.

[SLH91] SCOTT G., LONGUET-HIGGINS H.: An algorithm for associating the features of two images. In *Biological Sciences* (1991), vol. 244, pp. 21–26.

[SRD*11] SUWELACK S., ROEHL S., DILLMANN R., WEKERLE A., KENNGOTT H., MÜLLER-STICH B., ALT C., SPEIDEL S.: Quadratic corotated finite elements for real-time soft tissue registration. In *MICCAI workshop: Computational Biomechanics for Medicine* (2011).

[SREWH09] SCHMIDT-RICHBERG A., EHRHARDT J., WERNER R., HANDELS H.: Slipping objects in image registration: Improved motion field estimation with direction-dependent regularization. In *International Conference on Medical Image Computing and Computer-Assisted Intervention* (2009), pp. 755–762.

[SRWHE12] SCHMIDT-RICHBERG A., WERNER R., HANDELS H., EHRHARDT J.: Estimation of slipping organ motion by registration with direction-dependent regularization. *Medical Image Analysis 16*, 1 (2012), 150–159.

[SS12] STEGER S., SAKAS G.: FIST: Fast interactive segmentation of tumors. In *International Workshop on Computational and Clinical Applications in Abdominal Imaging* (2012).

[STR*11] SUWELACK S., TALBOT H., RÖHL S., DILLMANN R., SPEIDEL S.: A biomechanical liver model for intraoperative soft tissue registration. In *SPIE Medical Imaging* (2011), vol. 7964.

[SWZS94] SHASHA D., WANG J. T.-L., ZHANG K., SHIH F. Y.: Exact and approximate algorithms for unordered tree matching. *IEEE Transactions on Systems, Man, and Cybernetics 24*, 4 (1994), 668–678.

[SZP*12] SHI W., ZHUANG X., PIZARRO L., BAI W., WANG H., TUNG K.-P., EDWARDS P. J., RUECKERT D.: Registration using sparse free-form deformations. In *International Conference on Medical Image Computing and Computer Assisted Intervention* (2012), vol. 7511, pp. 659–666.

[TC06] TANG W. H., CHUNG A. C. S.: Cerebral vascular tree matching of 3D-RA data based on tree edit distance. In *Third international conference on Medical Imaging and Augmented Reality* (2006), pp. 116–123.

[TCO08] TAYLOR Z. A., CHENG M., , OURSELIN S.: High-Speed Nonlinear Finite Element Analysis for Surgical Simulation Using Graphics Processing Units. *IEEE Transactions on Medical Imaging 27*, 5 (2008), 650–663.

[TFV*13] TSUI A., FENTON D., VUONG P., HASS J., KOEHL P., AMENTA N., COEURJOLLY D., DECARLI C., CARMICHAEL O.: Globally Optimal Cortical Surface Matching With Exact Landmark Correspondence. In *Information Processing in Medical Imaging* (2013).

[Thi98] THIRION J.-P.: Image matching as a diffusion process: an analogy with Maxwell's demons. *Medical Image Analysis 2*, 3 (1998), 243–260.

[TJ04] TANG S., JIANG T.: Nonrigid registration of medical image by maxwell model of viscoelasticity. In *IEEE Symposium Biomedical Imaging: From Nano to Macro* (2004), pp. 1443–1446.

[TMP*05] TSCHIRREN J., MCLENNAN G., PALÁGYI K., HOFFMAN E. A., SONKA M.: Matching and anatomical labeling of human airway tree. *IEEE Transactions on Medical Imaging 24*, 12 (2005), 1540–1547.

[TU00] THEVENAZ P., UNSER M.: Optimization of mutual information for multiresolution image registration. *IEEE Transactions on Image Processing 9* (2000), 2083–2099.

[UCB*11] UMALE S., CHATELIN S., BOURDET N., DECK C., DIANA M., DHUMANE P., SOLER L., MARESCAUX J., WILLINGER R.: Experimental in vitro mechanical characterization of porcine glisson's capsule and hepatic veins. *Journal of Biomechanics 44* (2011), 1678–1683.

[Ull76] ULLMANN J. R.: An algorithm for subgraph isomorphism. *Journal of the ACM 23*, 1 (1976), 31–42.

[Ume88] UMEYAMA S.: An eigendecomposition approach to weighted graph matching problems. *IEEE Transactions on Pattern Analysis and Machine Intelligence 10*, 5 (1988), 695–703.

[vDVH*04] VAN DALEN J. A., VOGEL W., HUISMAN H. J., OYEN W. J. G., JAGER G. J., KARSSEMEIJER N.: Accuracy of rigid ct-fdg-pet image registration of the liver. *Physics in Medicine and Biology 49*, 23 (2004), 5393–5405.

[VJ04] VIOLA P., JONES M. J.: Robust real-time face detection. *International Journal of Computer Vision 57*, 2 (2004), 137–154.

[VYG*08] VENKATESH S. K., YIN M., GLOCKNER J. F., TAKAHASHI N., ARAOZ P. A., TALWALKAR J. A., EHMAN R. L.: MR elastography of liver tumors: Preliminary results. *American Journal of Roentgenology 190*, 6 (2008), 1534–1540.

[WCZ*98] WILSON D. L., CARRILLO A., ZHENG L., GENC A., DUERK J. L., LEWIN J. S.: Evaluation of 3D image registration as applied to MR-guided thermal treatment of liver cancer. *Journal of magnetic resonance imaging 8* (1998), 77–84.

[WDYPB07] WIEST-DAESSL´E N., YGER P., PRIMA S., BARILLOT C.: Evaluation of a new optimisation algorithm for rigid registration of MRI data. In *SPIE Medical Imaging* (2007).

[WPU*12] WANG S., PETRICK N., UITERT R. L. V., PERIASWAMY S., WEI Z., SUMMERS R. M.: Matching 3-D prone and supine CT colonography scans using graphs. *IEEE Transactions on information technology in biomedicine 16*, 4 (2012), 676–682.

[WR06] WÖRZ S., ROHR K.: Physics-based elastic image registration using splines and including landmark localization uncertainties. *International Conference on Medical Image Computing and Computer Assisted Intervention 4191* (2006), 678–685.

[WR07] WÖRZ S., ROHR K.: Hybrid spline-based elastic image registration using analytic solutions of the navier equation. In *Bildverarbeitung für die Medizin* (2007), pp. 151–155.

[WRK*07] WEIHUSEN A., RITTER F., KRÖGER T., PREUSSER T., ZIDOWITZ S., PEITGEN H.-O.: Workflow oriented software support for image guided radiofrequency ablation of focal liver malignancies. In *SPIE Medical Imaging* (2007), vol. 6509.

[WS00] WANG Y., STAIB L. H.: Physical model-based non-rigid registration incorporating statistical shape information. *Medical Image Analysis 1* (2000), 35–51.

[Wu10] WU Y.: *Extending Graph Homomorphism and Simulation for Real Life Graph Matching*. PhD thesis, University of Edinburgh, 2010.

[WVL*95] WUYTS F. L., VANHUYSE V. J., LANGEWOUTERS G. J., DECRAEMER W. F., RAMAN E. R., BUYLE S.: Elastic properties of human aortas in relation to age and atherosclerosis: a structural model. *Physics in Medicine and Biology 40* (1995), 1577 – 1597.

[YHL10] YIN Y., HOFFMAN E. A., LIN C.-L.: Lung lobar slippage assessed with the aid of image registration. In *International conference on Medical image computing and computer-assisted intervention* (2010), pp. 578–585.

[YJH*01] YEH W.-C., JENG Y.-M., HSU H.-C., KUO P.-L., LI M.-L., YANG P.-M., LEE P. H., LI P.-C.: Young's modulus measurements of human liver and correlation with pathological findings. In *IEEE Ultrasonics Symposium* (2001), vol. 2, pp. 1233 – 1236.

[YK09] YANG F., KRUGGEL F.: A graph matching approach for labeling brain sulci using location, orientation, and shape. *Neurocomputing 73* (2009), 179–190.

[YW05] YI Z., WAN J.: *Viscoelastic registration of medical images*. Tech. Rep. CS-2005-36, 2005.

[YYM*08] YONEDA M., YONEDA M., MAWATARI H., FUJITA K., ENDO H., IIDA H., NOZAKI Y., YONEMITSU K., HIGURASHI T., TAKAHASHI H., KOBAYASHI N., KIRIKOSHI H., ABE Y., INAMORI M., KUBOTA K., SAITO S., TAMANO M., HIRAISHI H., MAEYAMA S., YAMAGUCHI N., TOGO S., NAKAJIMA A.: Noninvasive assessment of liver fibrosis by measurement of stiffness in patients with nonalcoholic fatty liver disease (NAFLD). *Digestive and Liver Disease 40* (2008), 371–378.

[ZCL13] ZHANG K., CHENG Y., LEOW W. K.: Dense correspondence of skull models by automatic detection of anatomical landmarks. In *Computer Analysis of Images and Patterns* (2013), pp. 229–236.

[ZGC09] ZHENG Y., GEORGESCU B., COMANICIU D.: Marginal space learning for efficient detection of 2D/3D anatomical structures in medical images. In *International conference on Information Processing in Medical Imaging* (2009), vol. 5636, pp. 411–422.

[ZIW*11] ZHENG Y., III A. A. H., WU J., WANG H., GAO J., MAGUIRE M. G., GEE J. C.: Landmark matching based automatic retinal image registration with linear programming and self-similarities. In *International Conference on Information Processing in Medical Imaging* (2011), vol. 6801, pp. 674–685.

[ZLKC05] ZIOL M., LUCA H. A., KETTANEH A., CHRISTIDIS C.: Noninvasive assessment of liver fibrosis by measurement of stiffness in patients with chronic hepatitis C. *Hepatology 41*, 1 (2005), 48–54.

[ZNSY12] ZHANG P., NIETHAMMER M., SHEN D., YAP P.-T.: Large deformation diffeomorphic registration of diffusion-weighted images. In *International Conference on Medical Image Computing and Computer Assisted Intervention* (2012).

[ZZC07] ZHOU S. K., ZHOU J., COMANICIU D.: A boosting regression approach to medical anatomy detection. In *Computer Vision and Pattern Recognition* (2007).

[ZZPK08] ZHAN Y., ZHOU X. S., PENG Z., KRISHNAN A.: Active scheduling of organ detection and segmentation in whole-body medical images. In *International Conference on Medical Image Computing and Computer Assisted Intervention* (2008), pp. 313–321.